Surface acoustic wave-induced dielectrophoresis: Lab on a Chip cell sorting technology for autologous cell therapies

Alban Smith

School of Electronic and Electrical Engineering

University of Leeds

A thesis submitted for the degree of

Doctor of Philosophy

September 2017

The candidate confirms that the work submitted is his/her own, except where work which has formed part of jointly authored publications has been included. The contribution of the candidate and the other authors to this work has been explicitly indicated below. The candidate confirms that appropriate credit has been given within the thesis where reference has been made to the work of others.

Publication (Journal Article): Smith, A.J., O'Rorke, R.D., Kale, A., Rimša, R., Tomlinson, M.J., Kirkham, J., Davies, A.G., Wälti, C. and Wood, C.D. (2017) Rapid cell separation with minimal manipulation for autologous cell therapies. *Scientific Reports*, **7**.

The experimental work in this publication was conducted primarily by the candidate, with contributions from the other authors. Material from this publication has been included in Sections 4.3, 4.5, 5.3, 5.5, and 6.2.

Publication (Patent): Wälti, C., Smith, A.J., O'Rorke, R., Davies, A.G. and Wood, C.D., University Of Leeds. *Method and apparatus for manipulating particles.* Issued Feb 19, 2015. GB PCT/GB2014/051409.

The candidate contributed to some of the drawings and discourse featured in this publication. The following patent drawings (all contributed by the candidate) have been included in this thesis (thesis reference in brackets): Figure 10 (Section 4.3, Figure 4.7), and Figures 12A, 12B, 13C (Section 4.5, Figure 4.19).

This thesis is dedicated to my mum and dad, Regine and Ken, and my sister, Melanie.

Acknowledgements

My thanks to my primary supervisors, Dr. Christopher Wood and Prof. Christoph Wälti, who were always fun and supportive throughout the course of this work, and played an active part through weekly meetings and more. Further appreciation goes to my secondary supervisor, Prof. Jennifer Kirkham, for her help and expertise in all things biology.

My warmest gratitude extends to Dr. Richard O'Rorke, the researcher who got this work off the ground, and who was the first to patiently train me as I shattered my way though those first piezoelectric wafers; similarly, Dr. Matthew Tomlinson, who convivially trained and advised me in cell culture and related matters throughout this PhD. I also express my sincere thanks to Dr. Adam Davison, Dr. Michal Szymonik, Dr. Rajan Sharma, Dr. Sarah Myers, Jackie Hudson, Dr. Scott Finlay, and Dr. Jing Kang for advice and assistance on various parts of this project.

My special thanks to Roberts Rimša, who was always there as my sounding board, personal advisor, and general partner-in-crime/law abidance. Finally, my kindest regards to the rest of my colleagues in Bioelectronics and Oral Biology for being lovely to work and hang out with. Thank you all.

Abstract

The ability to isolate specific cells from a heterogeneous population using label-free methods, and subsequently extract these cells at high throughput, is a key step in the advancement of autologous cell-based therapies in the field of regenerative medicine. Surface acoustic wave-based dielectrophoresis (SAW-DEP) utilises a standing shear horizontal SAW to provide a non-uniform electric field in which cells can be separated by dielectrophoresis. Due to the absence of electrodes in contact with the solution, this method overcomes many disadvantages of current dielectrophoretic technologies, allowing cell separation at high continuous throughput (<500 cells/second) and in high conductivity solutions (<0.4 S/m).

This thesis describes the design and application of several iterations of SAW-DEP devices. After demonstrating the alignment of latex beads (1 - 10 µm) by negative DEP, the force exerted on latex beads is studied by particle tracking, and is shown to closely match a theoretical model for dielectrophoretic trapping.

Following this, the separation of viable from non-viable yeast cells and mammalian cells is demonstrated. To ascertain whether SAW-DEP has any adverse effect on cells, primary human mesenchymal stromal cells (dental pulp stromal cells) are tested for viability and differentiation capability following exposure to the SAW-DEP electric field, with the results showing that the electric field had no effect, compared to controls where the cells were not exposed to the electric field.

Finally, the ability to tune the liquid conductivity is investigated as a means to separate live from dead mammalian cells to high fidelity (live and dead cells were enriched into lines of 97% and 99% purity, respectively), as well as separating live mammalian cells of different lineages.

Abbreviations

ABS (plastic)	acrylonitrile butadiene styrene
AC	alternating current
ALP	alkaline phosphatase
AM (calcein –)	acetoxymethyl
ARF	acoustic radiation force
BAW	bulk acoustic wave
BMS (cell)	bone marrow stem cell
BSA	bovine serum albumin
CAD	computer-aided design
CCD	charge coupled device
CM (factor)	Clausius-Mossotti
CMOS	complementary metal-oxide-semiconductor
DC	direct current
DI	deionised
DEP	dielectrophoresis
DMEM	Dulbecco's modified Eagle's medium
DNA	deoxyribonucleic acid
DPS (cell)	dental pulp stromal
EDTA	ethylenediaminetetraacetic acid
EU	European Union
FCS	foetal calf serum
FDA	Food and Drug Administration (of the United States)
FACS	fluorescence-activated cell sorting
FFF	field flow fractionation
GIF	Graphics Interchange Format
GP	general practitioner
HBE (cell)	human bronchial epithelial
HEPES	4-(2-hydroxyethyl)-1-piperazineethanesulfonic acid
ID	inner diameter
IDT	interdigitated transducer
LED	light-emitting diode
LoC	Lab on a chip
MACS	magnetic-activated cell sorting

MCF7 (cell)	Michigan Cancer Foundation-7 (referring to where this breast cancer cell line was established)
MEM	minimal essential medium
MSC	mesenchymal stem cell
nDEP	negative dielectrophoresis
P1, P2, P3, etc	passage 1, passage 2, passage 3, etc
PBS	phosphate-buffered saline
PCB	printed circuit board
pDEP	positive dielectrophoresis
PDMS	polydimethylsiloxane
PEEK	polyether ether ketone
PEG	polyethylene glycol
PI	propidium iodide
PTFE	polytetrafluoroethylene
OD	outer diameter
R-SAW	Rayleigh surface acoustic wave
SAW	surface acoustic wave
SAW-DEP	surface acoustic wave-induced dielectrophoresis
SH-SAW	shear horizontal surface acoustic wave
SMA (connector)	SubMiniature version A
SMD	surface-mount device
UV	ultraviolet
UVO (cleaner)	ultraviolet ozone

Contents

List of Figures

Chapter 1

Literature Review

This chapter summarises the motivation for this research, and describes why new technologies must be developed in the field of medical cell sorting. An overview of traditional cell-separation methods is presented, alongside a discussion of more recent developments in microfluidic cell sorting techniques. Finally, a detailed review of various eminent methods of dielectrophoretic cell sorting techniques is presented, which have formed a basis for the research and technology presented in this thesis.

1.1 Motivation

1.1.1 Definition and applications of cell sorting

Cell sorting refers to the separation of a heterogeneous mixture of biological cells, generally human cells, into more defined sub-populations. The main uses for this are as follows: (1) Isolation of specific cells for biological research, (2) Identification of cell types for medical diagnostic purposes, and (3) Enrichment of a desired cell type for therapeutic applications i.e. cell therapies.

Isolation of specific cells for biological research

The most obvious application of this, as a researcher, is to isolate a specific cell type from a raw tissue sample for analysis and research. Indeed, every cell culture currently growing in a cell biologist's laboratory has been isolated originally from a biopsy sample, which may include for example, cancer cells in a tumour, dental pulp cells from an extracted tooth, mammary fibroblasts from breast reduction surgery, white blood cells from a blood donation. Following extraction and separation, these cells may be then genetically engineered such that they can be expanded indefinitely, cryogenically stored, and sent to other labs - this is particularly useful when a tissue is difficult to obtain, like neural matter.

Identification of cell types for medical diagnostics

Being able to identify the different cell types present in a sample is also important for some medical diagnostic procedures. For example, drug screening requires cell sorting and analysis of large numbers of patient samples, typically via flow cytometry (1). Scaling-down and simplifying the apparatus required for flow cytometry, one could imagine, would be of great interest to pharmaceutical companies.

Enrichment of specific cell types for cell therapies

Cell sorting will also be vital to the advancement of cell therapy, which is a focus of this research thesis. Cell therapy is linked to the fields of regenerative medicine and tissue engineering, and refers to treatments which involve the transplantation of cells to the sites where they are needed. These may be the patients own cells (an autologous graft) or someone else's (allogeneic).

Cell therapy has long existed in the form of blood transfusions (Figure 1.1**a**); for modern transfusions, the components of whole donor blood are separated into its constituent parts (red blood cells, white blood cells, plasma, platelets, etc). This is typically achieved through apheresis, a centrifugation-based cell sorting

method that is discussed further in Section 1.2.1 (2).

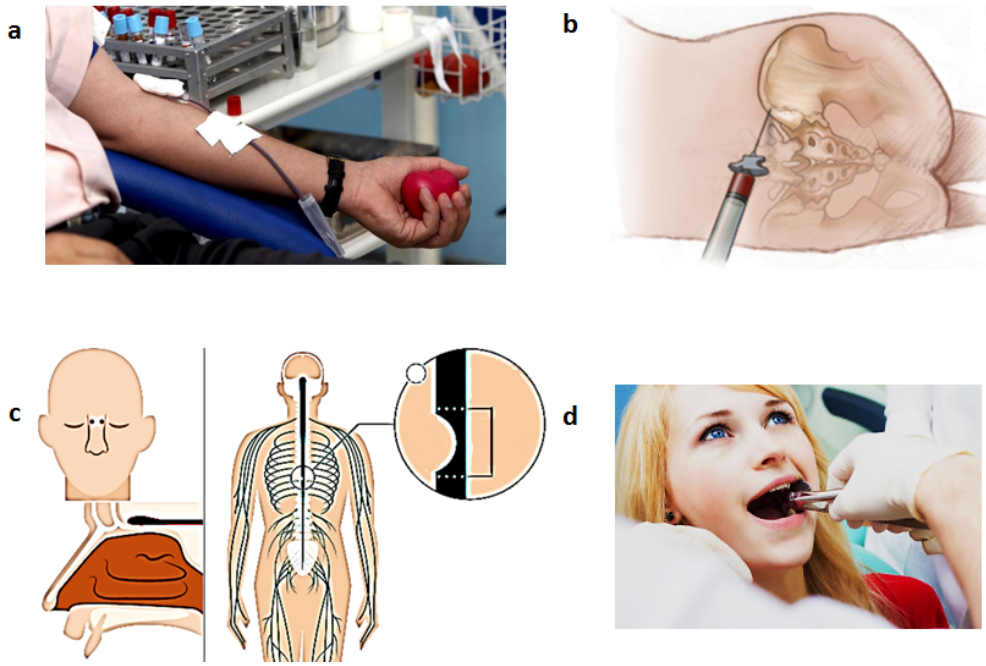

Figure 1.1: Examples of donation/biopsy methods for cell therapy. **a** Blood transfusions (3) and **b** bone marrow aspirate from iliac crest (4) are common treatments, while **c** the first transplantation of olfactory (nasal) neuronal stem cells to successfully treat spinal cord injury was performed in 2015 (5); **d** mesenchymal stromal cells can be found in the dental pulp, which have a range of potential therapeutic applications (6).

Another established cell therapy is the use of stem cells harvested from bone marrow aspirate (Figure 1.1**b**), known as hematopoietic stem cells, typically used to repopulate a deficit of cells in patients suffering from blood or bone marrow cancer (7). These multipotent stem cells can differentiate into a range of cell types, and have recently been used in other new treatments, namely myocardial regeneration in patients with heart disease (8), but also for anaemia, chronic myelogenous leukaemia, and myodysplasia, amongst others (9).

Indeed, many treatments are on the horizon that utilise stem cells transplanted

from one part of the body to another. In 2014, a man previously paralysed by a knife injury to the spine gained the ability to walk again (5), a year after doctors transplanted olfactory neuronal cells (taken from inside the nose) into his spine (see Figure 1.1**c**) (10).

An alternative source of stem cells for cell therapy are those found within teeth, dental pulp stromal cells (Figure 1.1**d**). These stem cells are predisposed to form bone-like osteoblasts, making them a potential candidate for cell therapy in bone regeneration; however, they have much the same differentiation capabilities of mesenchymal stem cells, which appear early in embryonic development to differentiate into a variety of cells/tissues including neurons (brain), cardiomyocytes (heart), chondrocytes (cartilage), hepatocytes (liver), and islet β-cells (pancreas) (11); thus, cells which are relatively easy to come by (due to the prevalence of wisdom tooth extractions) could have a host of possible applications in regenerative medicine.

Having discussed the scope of the possible biotechnology and medical applications of cell sorting, one specific application will be examined in more detail - the use of sorting cells intra-operatively for bone graft surgery. The purpose and market for the procedure will be discussed, followed by some technical considerations and ways in which intra-operative cell sorting can improve the current technology.

1.1.2 Case study: Cell sorting in bone graft surgery

Bone grafting refers to a surgical procedure used to treat abnormalities or disease in bones or joints (15). It is the most commonly transplanted tissue after blood, with 2.2 million grafting procedures being carried out annually across the world[1] (16).

[1] Given that these are largely in developed countries with an increasingly ageing population (e.g. the USA and UK), we can expect this to increase massively in the next 20 years, not to mention the potential for demand in emerging economies such as those in the Far East and South America.

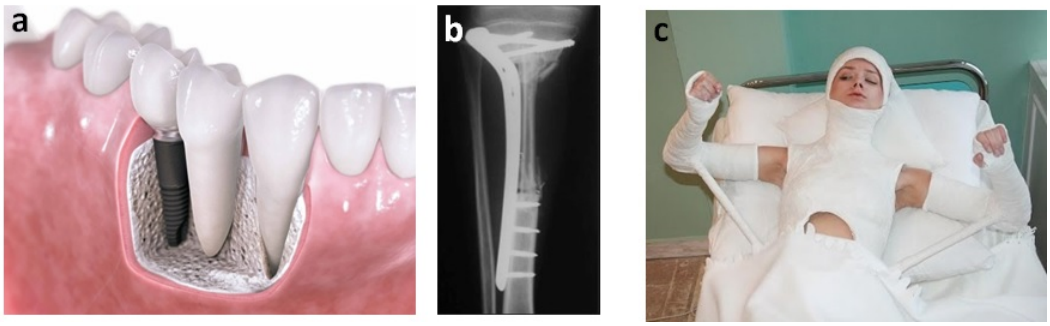

Figure 1.2: Examples of medical treatments that involve bone grafting, including **a** dental implants (12), **b** fibular shaft operations (13), **c** enhanced fracture recovery (14).

The main areas for grafting are orthopaedics, neurosurgery, and dentistry (16). The most common use of bone grafts is in dental implants (Figure 1.2**a**), where bone must be grafted underneath the dental implant such that it will grow round and support it (17). Bone grafts are also commonly used in fibular shaft operations (Figure 1.2**b**), which aim to restore function in the long bones of the limbs which may be affected by congenital defects, trauma, or malignant tumour invasion (18).

Other procedures, which may become more common with greater streamlining and understanding of stem cell therapy, include enhancing the recovery of broken bones, particularly those which do not heal well naturally (19), such as injuries in older people. With an aging population in many developed countries such as the UK, there is also much interest in this therapy to treat age-related disease like osteoporosis (20) and osteoarthritis (21). Ideally autologous bone from the iliac crest is used (Figure 1.3), because this area is easy to access and provides a large amount of tissue which is capable of both differentiating into bone-specialist cells (osteogenic) and stimulating the surrounding host cells to do likewise (osteoinductive) (16).

There are two typical issues when using harvested cells: 1.) Harvest methods are traumatic and cause cell death in the tissue to be transplanted; 2.) harvested

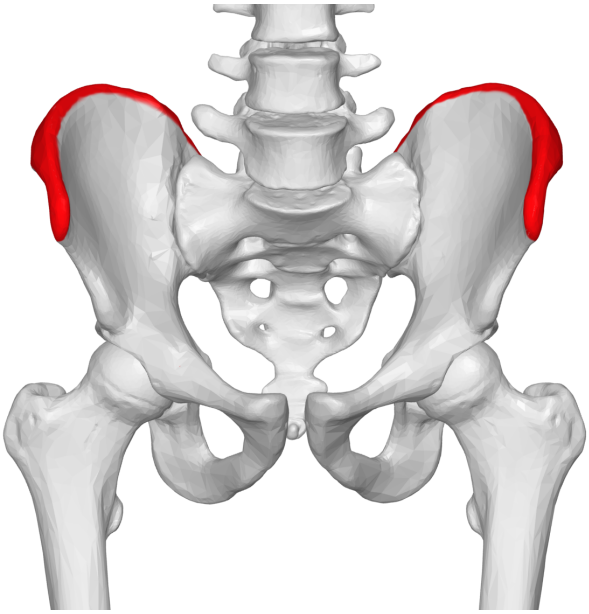

Figure 1.3: Schematic of pelvic girdle, with iliac crest in red (22).

cells are almost always a heterogeneous mix - as well as mesenchymal stem cells, a sample from the iliac crest will invariably contain a high proportion of differentiated cells and unnecessary cells, particularly adipose (fat) tissue. Typically, 1 ml of bone marrow aspirate will contain ~ 10 million mononuclear cells (subpopulation that excludes cells with no or multiple nuclei) , of which only about 8,000 (0.08%) are mesenchymal stromal cells (23).

Issues with cell death in grafted cells

Typical death rates in bone marrow from iliac crest are ~ 50 % (24). There has also been concern regarding cell death in most other major grafting procedures, including osteochondral grafts, neuronal grafts (25, 26), pancreatic islet cells (27, 28), fat grafting for breast augmentation (29).

Not only are dead cells incapable of re-populating a diseased site and releasing beneficial growth factors and bioactive molecules (30), but they can also cause the release of harmful cytokine molecules which initiate an immune response;

subsequently, this can lead to transplant rejection, contributing negatively to operation success rates (31, 32). Some grafting procedures, such as taking adipose tissue from the buttocks for breast augmentation, utilise a centrifugation step to enrich a sample for viable cells (exploiting the lower density of dead adipose cells). However, for many reasons (such as the presence of other cells of various densities, or where the densities of viable/non-viable cells are too similar), this is not possible for all grafting procedures. In the case of bone grafts, most effort into improving sample viability has focussed on optimising the harvest technique. However, these typically involve a very invasive drilling or scooping procedure, for which it is difficult to minimise graft cell death and collateral tissue damage (30).

1.1.3 Considerations for a minimally-manipulative, intra-operative cell sorter

Within this context, this work aims to develop a technology that can rapidly separate a target from a heterogeneous mixture of cells, in a time frame that would not significantly increase the length of time of an operation. Another consideration, which will be discussed more in the proceeding sections, is that the cell separation step must not adversely affect cells (with regards to their viability and subsequent differentiation potential) as many current technologies are known to.

In the ideal case, the device developed can be classed as 'minimally manipulative, as described in EU directive No 1394/2007 (Advanced therapy medicinal products) (33). This is because little is known about the medium and long-term behaviour of cells that have been 'manipulated', and there is a concern they may cause deleterious effects within the body. Deleterious effects may be caused, for example, due to the addition of chemical labels used to sort cells that may be potentially harmful in the body (label based sorting techniques are discussed in Section 1.2.2), or an immune response triggered by poor graft cell viability. For this reason, special consideration to the effect on cells must be made when

considering methods for cell isolation and sorting.

Having outlined the motivation and goals for this work, the rest of the remainder of the chapter will provide a technical analysis of current cell-separation methods and of current research into the field of cell sorting, with reference to the considerations necessary to develop a minimally-manipulative, intra-operative cell sorter.

1.2 Traditional methods of cell sorting

1.2.1 Density-based methods: Centrifugation

Differences in the density of different cell types can be exploited for various fractionation-techniques, including sedimentation (34), and field-flow fractionation (Sections 1.3.3). The most commonly used density-based method is centrifugation.

Centrifugation is used in the laboratory to concentrate cells. A cell solution in a test tube is put into a fast rotor, typically spinning at ~ 1000 rpm, depending on rotor arm length (exerting accelerations of >200 g), such that the densest and largest particles in the solution concentrate at the bottom of the tube. The rate at which particles sediment determines how they can fractioned off from each other, and is given by the following equation:

$$v = \frac{d^2(p - L) \cdot g}{18n} \tag{1.1}$$

where v is the sedimentation velocity, d is the cell diameter, $pandL$ are the densities of the particle and the suspending liquid respectively, g is the graviational force and n is the viscosity of the medium.

By experimenting with the spin speed and the density of the suspension medium used (generally with sugar solutions), cell types with distinct size and density profiles can be separated into different areas of the test tube and fractioned off separately. Indeed, the separation of blood cells is commonly carried out by such a method, known as aphaeresis (from the Greek “a taking away”) (Figure 1.4). This is because the relative constituents of blood (namely plasma, platelets, white, and red blood cells) have distinct density profiles, making separation by centrifugation relatively straightforward.

The advantages of differential centrifugation as a separation technique are that the equipment is relatively cheap (~ $10,000), it can process large volumes, and

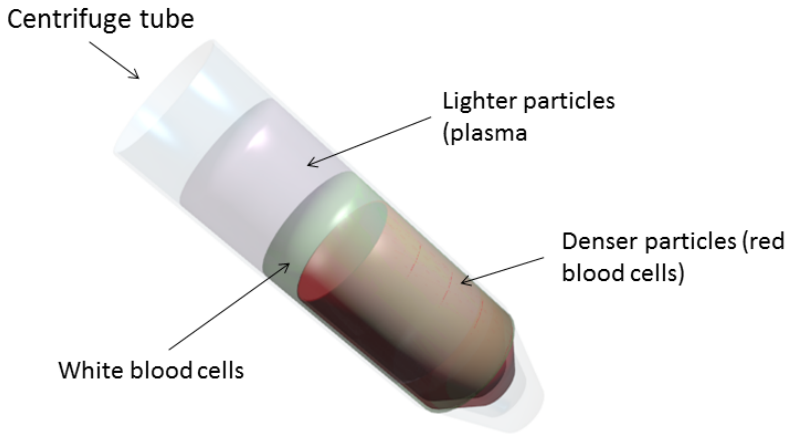

Figure 1.4: Schematic of a centrifuge tube containing a blood sample, that has been fractionated into heavier and lighter portions following centrifugation.

that the reagent costs are very low. No labelling of cells is needed (see Section 1.2.2), and so the processing speed is relatively quick. For example, to fractionate the red blood cells (as well as white blood cells and platelets) used in this thesis (Appendix A.1), 10 ml of blood (~ one billion white blood cells, ~ fifty billion red blood cells) was processed using normal tissue culture plastic tubes and a benchtop centrifuge, by passing it through a density gradient medium at 300 g centrifugal force for 20 minutes, which can be regarded as an intra-operative timescale (although further washing steps are often performed to increase purity).

However, one can appreciate that this technique only works for cells with very distinct density profiles. Even for blood, with its massive differences in white and red cells (~ 1.06-1.08 g/cm^3 (35) and ~ 1.10-1.20 g/cm^3 (36), respectively), the best fully-automated aphaeresis procedures typically yield no greater than 90% purity for the target population (37).

1.2.2 Antibody-based

A very different and far more selective approach to detection and separation of cell types is seen in antibody-based techniques, currently the gold standard

method for research. Cells express a variety of proteins on their outer membrane, with many unique to their particular cell type and gene expression, and these can be thought of as cell-specific 'markers'. By injecting quantities of these proteins into model animals such as rats or rabbits, the animal's immune system will generate molecules that specifically bind to these proteins (known as antibodies) as a signal for its immune defence to get rid of it.[1] (A schematic of antibodies binding to surface markers on a cell can be seen in Figure 1.5.) Subsequently, animal lymphocyte cells which secrete the antibody can be isolated and immortalised, such that the antibody can be grown and harvested *in vitro*. These antibodies can then be 'tagged' (often via secondary antibodies) with labels such as fluorescent molecules or magnetic molecules (38), forming the basis for fluorescence- and magnetic-activated cell sorting (FACS and MACS, respectively), which will be explained in the proceeding paragraphs.

From this it can be surmised that antibody-based selection is both inherently excellent for discerning biological phenotypes, but inherently manipulative to the cells it sorts. The former is because surface protein expression presents a highly variable landscape to use for discerning different cell types, resulting in exquisite selectivity and specificity. However, labelling a cell with a fluorescent or magnetic tag inherently modifies the cells (39) making their subsequent behaviour unpredictable, and may interfere with subsequent expansion and differentiation of cells (40). While it is possible to separate cells without physically attaching the tag to them (for example, using negative selection, in which binders are used against all the non-target cells in a heterogeneous population, thus enabling separation without binding to the target cell), the cells will still have to be incubated in the antibody solution (to tag the other cells), and this, therefore, would be unlikely to meet guidelines on minimal manipulation.

[1] This is the basis of mammalian 'adaptive immunity', in which the immune system adapts to specifically target a new pathogen. The ability of lymphocyte cells to rapidly mutate before being able to secrete a molecule that is specific to the foreign surface marker is thought to have been evolutionarily acquired through the insertion of a virus into a part of the mammalian genome.

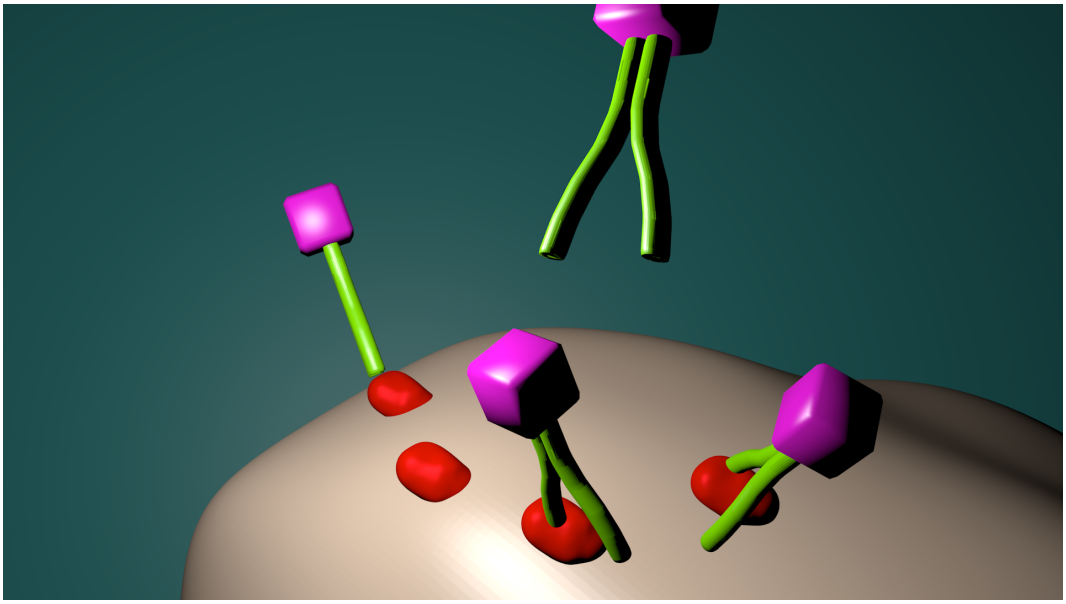

Figure 1.5: Illustration of antibodies binding to antigens on a cell surface. The purple cubes represent molecular labels (e.g. fluorescent or magnetic) attached to antibodies which allow subsequent detection or extraction of cells.

This highlights a second issue: before cells are sorted, they require a labelling-step in which they are incubated in the antibody solution, typically for around 30 minutes (41). This time must be added on to the time taken for actual sorting, a consideration for assessing the duration of any procedure against accepted intra-operative timescales.

Whilst there are other antibody-based methods which will be discussed in Section 1.2.3, the two main methods, FACS and MACS, are explained in detail below, followed by a discussion on their relative advantages and disadvantages.

Fluorescence-activated cell sorting

A flow cytometer is a staple, if expensive, piece of equipment for many laboratories. The concept is shown schematically in Figure 1.6. Cells labelled with fluorescent dyes are hydrodynamically focused into a single stream, such that

each cell can be probed using lasers (typically one laser per dye). Their fluorescence emission is detected to give information as to what label they were carrying. For traditional flow cytometry, this is the end of the story. For FACS, however, a piezo crystal vibrates to break the fluidic stream carrying the cells into one droplet per cell. Information from the detectors determines the charge that the droplets are pulsed with, as shown in Figure 1.6, which is used to sort the cells/droplets as they pass through charged deflection plates.

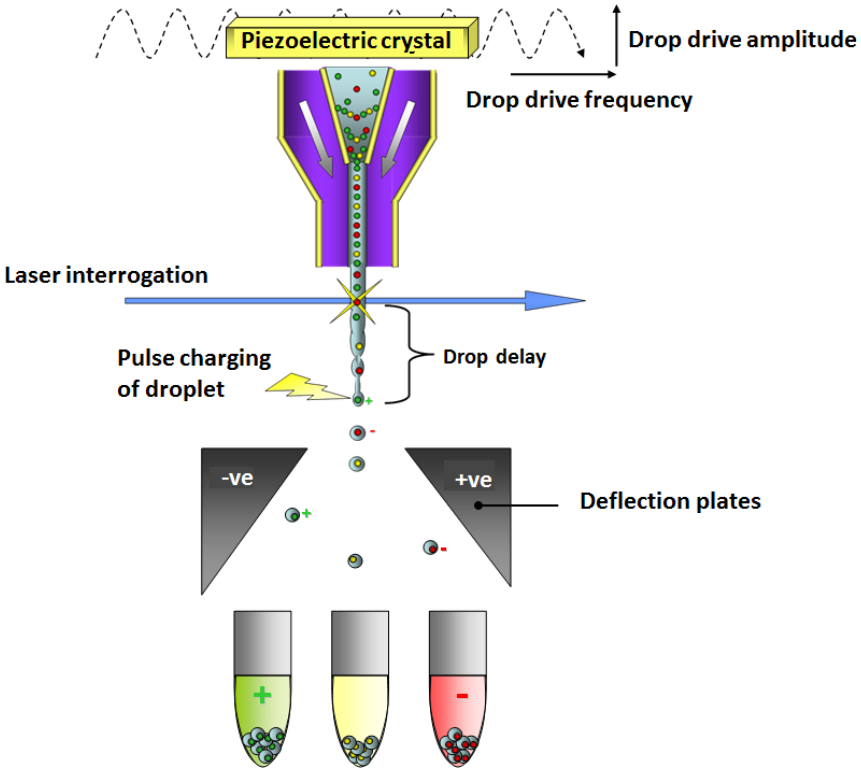

Figure 1.6: Schematic showing how a fluorescence-activated cell sorter operates (42). A heterogeneous mixture of cells is labelled with cell-specific antibodies, which fluoresce at different wavelengths (i.e. red, green, and yellow colours in the diagram). Labelled cells are passed single-file in front of a laser that interrogates the specific label/cell type. This is passed to a feedback loop, and cells receive a charge downstream of the laser (+, -, or none, according to the interrogation feedback). The presence of negative and positively charged deflection plates at the collection phase determines where cells are collected.

Magnetic-activated cell sorting

The apparatus required for MACS (Figure 1.7) is far simpler than that used for FACS. In this method, cells are incubated with magnetic nanoparticles coated with an antibody, following which they are passed through a column which is subject to a strong magnetic field. Bound cells (positively selected) can be washed out by removing the column from the magnetic field.

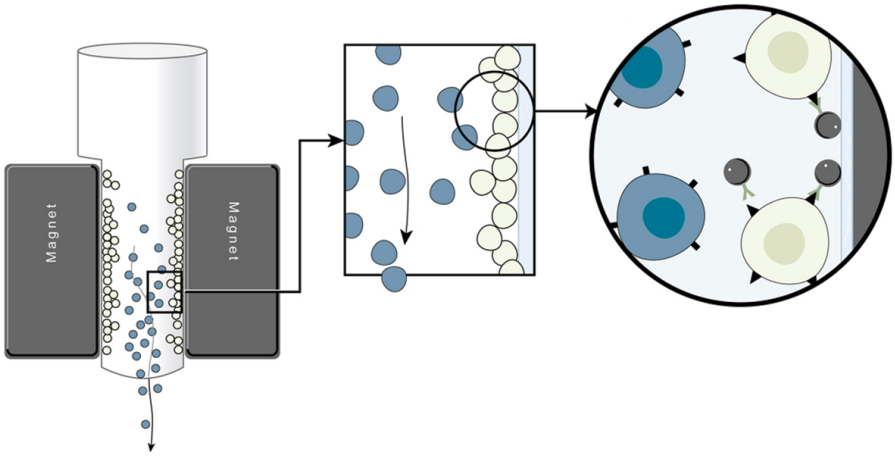

Figure 1.7: Schematic showing the concept behind magnetic activated cell sorting (43). Magnetically-tagged antibodies are incubated to bind to a target cell type (white). These are then passed into a column flanked by magnets, thus retaining the target cell, and allowing other cells (blue) to pass through.

The ability of FACS to probe one cell at a time in conjunction with sophisticated optical detection ports (whose sensitivity can be automatically or manually tuned via a computer) makes it a more specific technique with capability to get more analysis out of a sample while it is being sorted (44). However, the equipment required for MACS is significantly cheaper, with basic separation columns for manual starting out at £200 (45).

Importantly, MACS is considered to be far superior at providing high, therapeutically-relevant throughput. While FACS is generally accepted as providing the highest enrichment purity of the target cell type, MACS is simpler and quicker to carry

out large-throughput separations (46), with standard benchtop equipment capable of carrying out throughput upwards of 10^9 cells per hour (47).

1.2.3 Other methods

Whilst centrifugation and antibody-based separation methodologies are by far the most prevalent cell sorting techniques available to cell biologists, affinity chromatography, adherence, and panning are alternative established approaches, which have been outlined below.

Affinity chromatography

Affinity chromatography is a column-based antibody-binding technique similar to MACS, which is more commonly used for purifying smaller molecules like proteins (48). For cell sorting, target cells are passed through a cryogel matrix functionalised with an antibody. However, functionalising a matrix with an antibody causes misorientation of the antibody which reduces the specificity (49). Kumar *et al.* (2010) (49) improved the efficiency of this method by labelling cells before passing them through the matrix, which was functionalised with a less orientation-specific affinity molecule, 'proteinA' (see Figure 1.8). However, the main problem arising from this method is that non-specific binding of cells occurs, such that they are difficult to remove (50).

Adherence

Adherence is typically used in isolating cells from a raw biopsy sample (44). In this method, a heterogeneous mixture of cells is seeded into a tissue culture flask and incubated for a certain amount of time, typically 1-2 days (see Figure 1.9). Non-adherent cells can be washed off (and kept if they are of interest). If left for longer, cell types which grow better on the surface will outcompete other adherent cells, and thus further enrichment can be achieved. This is used, for example, in the isolation of dental pulp stromal cells from the extracted periodontal ligament (outcompeting cells like neurons and monocytes) (51), or of monocytes from blood (52).

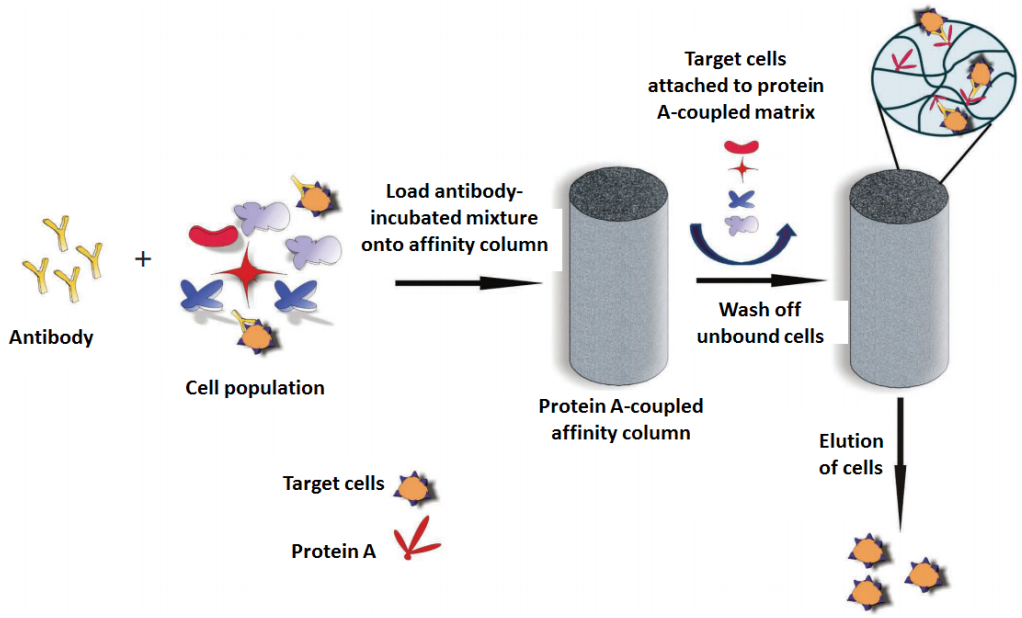

Figure 1.8: Example protocol for antibody-based affinity chromatography procedure (49). In this case, cells are labelled with an antibody prior to being passed through the matrix ('affinity cryogel column'). The matrix has been functionalised with 'Protein A' which the antibody (already bound to target cells) binds to, thus retaining the target cells.

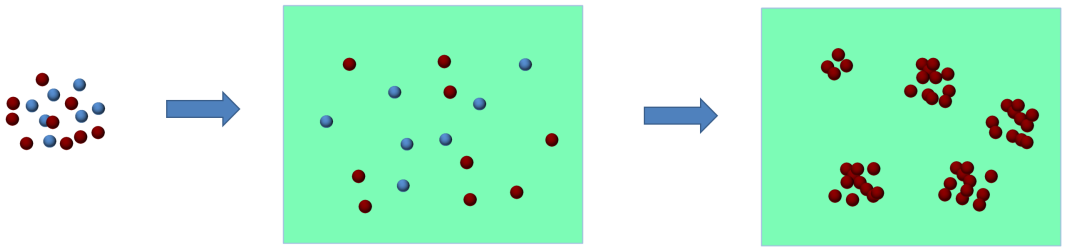

Figure 1.9: Schematic showing adherence-based cell sorting. A heterogeneous mixture of cells (red and blue) is plated onto a surface (green) (for example, a surface-treated polystyrene tissue culture flask) onto which one cell type preferably adheres and proliferates (red cells, in this case).

Various surfaces can be used to select for a range of cell types. Polymer brushes have been investigated for adherence-selection, because it is easy to tune the

brush length to accommodate for the cell of interest. For example, Nagase *et al.* (2012) (53) used this method to discern a variety of cells from endothelial, dermal, and muscle origin.

Panning

Panning, also known as immunoabsorption, is a versatile antibody-based method which is useful when commercial magnetic and fluorescent labels are not available for the requisite antibody (54). A surface, typically gold, is functionalised with an antibody, following which cells are flowed onto the surface and allowed to sediment. After an incubation step for antibody-binding, the unbound cells are washed off (see Figure 1.10.)

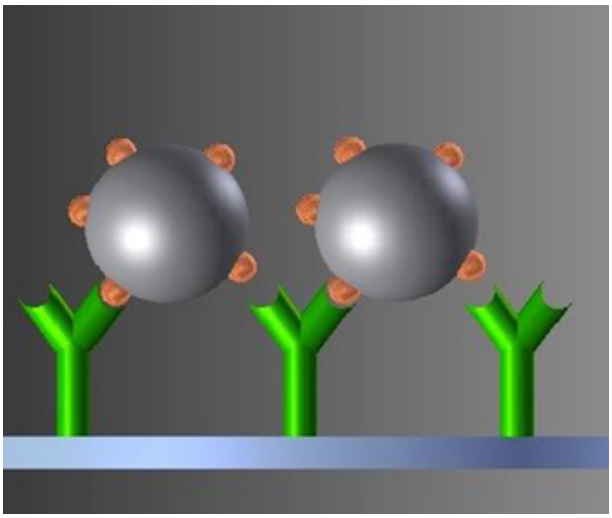

Figure 1.10: Schematic depicting "panning"/immunoabsorption (55). The surface is functionalised with antibodies (green) that bind to surface markers (orange) on the target cells (grey).

While this method is fine at negatively selecting cells which do not bind to the antibody, detachment of bound cells (which are typically the target cell) generally requires undesirably forceful methods, such as scraping in ice cold buffer (56).

1.3 Methods of cell sorting: Lab on a chip

1.3.1 Concept and central themes

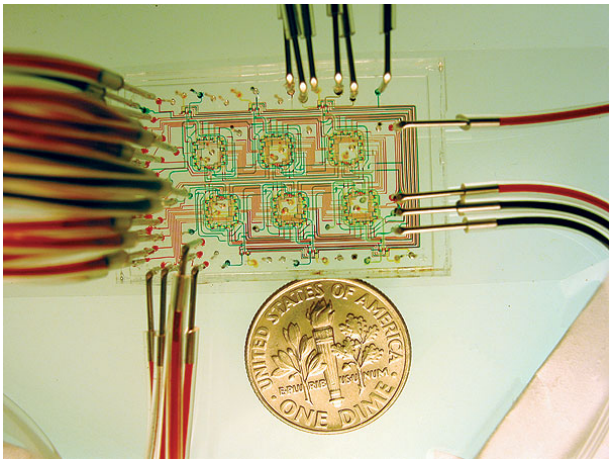

Figure 1.11: Photograph of a LoC chemostat device (57).

Lab on a chip (LoC) is a technological device or platform which enables a laboratory assay, that would normally require large equipment or facilities, to be performed on a handheld chip. It is often envisaged that the assay can be carried out away from a laboratory, for example in a GP clinic, operating theatre, environmental sampling, or in the home. Typical procedures that are being developed include chemical synthesis and analysis (58), biosensing for monitoring the environment (59), and medical diagnostics (60).

The ability for academic and biomedical institutions to design and fabricate such miniaturised devices has no doubt been spurred on by the computer industry, and investment into development of smaller and smaller CMOS[1] systems by lithographic techniques (61). Techniques such as photolithography and electron beam lithography allow electrodes of micrometre to nanometre dimensions to be patterned onto the surface of a chip (typically a thin 0.5 mm-thick crystal wafer, such as quartz or silicon) (62). As well as being able to scale down electric circuits, this same technology can be used to pattern fluidic channels (often in

[1] complementary metal-oxide-semiconductor

glass, PDMS, and plastic (63, 64)) that scales down the conventional test tubes and other glassware common to most bioscience and chemical experiments.

There are several obvious advantages of developing devices on this hand-held scale[1], which are listed below:

1. The device is transportable and can be used in various out-of-lab settings, including for medical applications
2. The scaling down of a reaction reduces the cost of both materials for the devices and the cost of reagent
3. Reagents travel shorter distances, thus speeding up reaction times
4. Design and manufacture of such devices has been made simpler and cheaper due to advances made in microfabrication by the computer chip industry, namely via photolithography, and more recently by the advance of 3D printing.

In reviews of the field, there has been some consternation that, while there has been much research, there are still very few commercial products or devices which are LoC. George Whitesides, a prominent researcher and proponent, asks *"Why is every biochemistry laboratory not littered with 'lab on chips'? Why does every patient not monitor his or her condition using microfluidic home-test systems? The answers are not yet clear."* (65).

In the ten years since this statement, progress has still been rather slow. Most biology and chemistry labs still run their assays on large equipment with many tedious manual components (e.g. pipetting), with the exception of some innovative groups, notably the de Mello group, currently in ETH Zurich (who run large-scale chemical assays using automated microfluidic apparatus (58)).

[1] An added commercial incentive to investigating LoC alternatives is that it suits a central trend in product development, of making things cheap and disposable

Whilst it is rare that LoC options are seen as the 'gold standard' for a given test, they have already found in use in developing world diagnostics (66, 67), where often price is more of a limiting factor than accuracy and sensitivity.

In the commercial world, perhaps the largest (and one of the few) companies utilising *Lab on a chip* technology for retail services is Theranos. This is a home testing company, where customers can send minute swab and blood samples in the post to the company's laboratory, and await a notification of their disease status via the internet. However, in the 2016, the firm (then worth $9 bn) was prohibited from running a diagnostics lab for two years (having only received FDA approval in 2015); this sanction was issued because the company was found to be misleading investors, in that the technology was not working as well as it was claiming (68). Now worth $800 m (and temporarily barred from retail services), the company is focusing on developing its as-yet unproven *Lab on a chip* technology (69, 70).

The only commercial point-of-care diagnostic platform is currently the Veritor System, a flu-testing platform by Becton, Dickinson & Co, one of the two manufacturers of flow cytometers(71), currently sold to healthcare providers.

Figure 1.12: BD Veritor System (71).

A possible reason for this slow progress is that LoC fabrication procedures and innovation typically requires detailed engineering knowledge, while the end users of such devices are often biologists and chemists. This cross-disciplinary field therefore requires either engineers and microfabrication specialists to learn about the biochemical experiments that would benefit from miniaturisation, or for the biologists and chemists to learn the skills necessary to design and manufacture the devices they need. Until these devices are prevalent in the laboratory, the idea that medical testing can be done at home is probably still too big a leap of the imagination for many investors.

To demonstrate how a cell sorting method can be scaled down to the microscale, the following sections will describe novel LoC sorting methods which have been made available through the advance of microfluidic and microelectronic technology.

1.3.2 FACS on a chip

Several research groups have scaled down FACS technology onto a chip. The earliest was by Stephen Quake's group in the California Institute of Technology in 1999 (72). Figure 1.13 shows the sorting chamber - the wells are 2 mm in diameter, and the channels are 100 µm wide, narrowing to 3 µm at the sorting junction, and a depth of 4 µm. However, the schematic showing the whole setup (Figure 1.14) reveals this was far from a handheld device.

Since then, efforts have been made to further scale down the components. Reductions in pump size have included using electro-osmotic flow and incorporating mini-peristaltic pumps on the chip (73). Indeed, the need for small-scale pumps is a limitation to all microfluidic/Lab on a chip systems. Similarly, effort has been made to scale down the optical components, with LEDs and laser pointers being used to excite fluorescence, which is then collected used fibre optics (73).

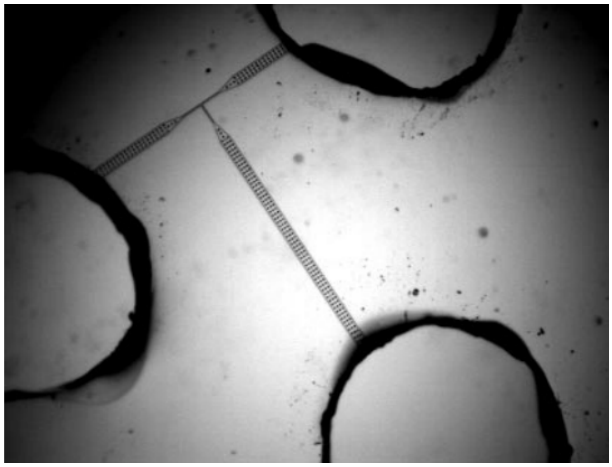

Figure 1.13: Photograph of the microfluidic component of the first 'FACS on a chip' (72). The large circles show the tubing input holes (2mm), feeding into 100 μm wide (4 µm deep) microchannels, which narrow to 3 µm at the sorting junction. This 3 µm channel sorts cells into single-file, without the need for the hydrodynamic focusing applied in conventional FACS machines.

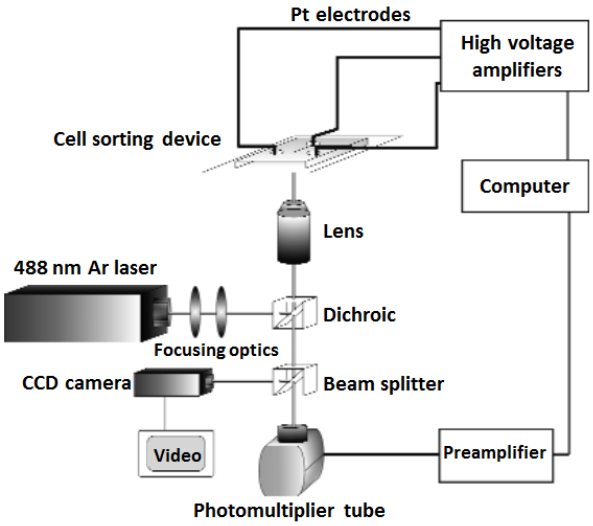

Figure 1.14: Schematic showing the experimental setup in (72).

It is worth noting that while academics make improvements to 'FACS on a chip', any big advances in scaling down FACS is either going to be made by or bought by one of the two major flow cytometer manufacturers, Beckman Coulter and

Becton Dickinson (74). One of the smallest FACS machines currently available is the benchtop BD FACSJazz (see Figure 1.15), taking up just 50 x 50 cm^2 of bench space (75), and selling for between $200,000 - $300,000, depending on the number of lasers installed (76).

Figure 1.15: The new FACSJazz machine, available from BD Biosciences (75).

1.3.3 Field flow fractionation

The concept behind field flow fractionation (FFF) is that cells are flowed through a channel, typically microfluidic, to which a field is applied perpendicular to the fluid flow (Figure 1.16). Cell types react differently to the field and travel through it at different speeds, such that they can be fractionated downstream. This can be an external field such as magnetic, thermal, or electrical (77), but the most commonly used are sedimentation-based methods, where the field comes from gravitational pull. Thus, while FACS-on-a-chip is an example of how antibody-based detection can be reduced to the microfluidic scale, field flow fractionation (FFF) is an on-chip method for density-based separation, akin to centrifugation.

In the case of gravity separation, particles of different weight are flown into the channel. Heavier particles experience greater gravitational force (in a direction perpendicular to flow), while lighter particles are more affected by the flow; the

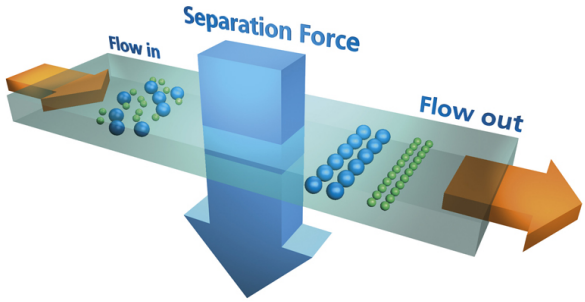

Figure 1.16: Schematic illustrating the concept of Field Flow Fractionation-based cell separation (78). Two cell types are flowed into a channel (green and blue, 'Flow in'); they then experience a separation force which is perpendicular to the direction of flow, and is stronger towards one cell type (blue in this case); subsequently, this cell type travels more slowly through the perpendicular field, and the other cell type (green) can be fractioned off from the outflow separately before the (blue) cells.

lighter particles reach the end of the channel earlier and can be fractionated off.

Following conceptualisation by JC Giddings in the late 1960s, FFF was developed gradually over the following 30 years to separate particles from 10 nm - 100 µm (77, 79). This included the fractionation of human from animal red blood cells, and red blood cells from HeLa (breast cancer) cells (80). While this method offers (perhaps) greater sensitivity than centrifugation, the main limitations listed for the latter remain (Section 1.2.1). Indeed, while gravity-based FFF was central to most early FFF research due to simplicity and availability of the field, most recent interest in the technique has been with a dielectrophoretic field, and this will be discussed further in Section 1.4.7.

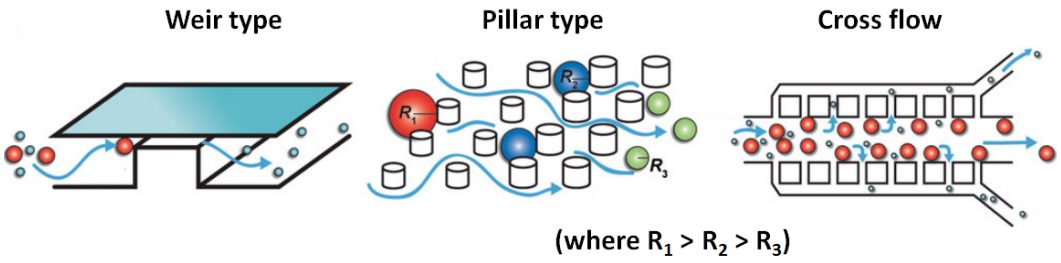

Figure 1.17: Schematics of the three main types of micro-filter for size-based exclusion of cells that are found in the literature, from (40). Wier-type and Pillar-type filters are similar in concept, offering very simple size-based exclusion, and one is typically favoured over the other depending on the fabrication facilities of the research institute. Cross-flow filters are slightly more elaborate, offering a route out for the larger 'excluded' cells so that the channel does not get blocked up.

1.3.4 Size-exclusion

Various types of microscale filters have been used to separate cell types based on their size (see Figure 1.17). Pillar-type filters have poor throughput (due to clogging-up), but can also be used to separate cells based on deformability with better sensitivity (40). Cross-flow methods are similar to pillar-type, but are designed to reduce clogging up (40), and thus could offer the high throughput necessary for therapeutic sorting applications.

These filters have been used primarily for blood-based sorting (40), due to the relatively distinct size of blood cell types: red blood cells are ~ 8 µm in diameter, while white blood cells vary from 12-25 µm according to function/type (81). Whilst the throughput is unlikely to ever exceed that of centrifugation for blood-based separation, there is the possibility that devices such as these could be used to filter out non-blood cells, such as circulating tumour cells, for sensitive detection in blood samples (82).

1.3.5 Hydrodynamic filtration

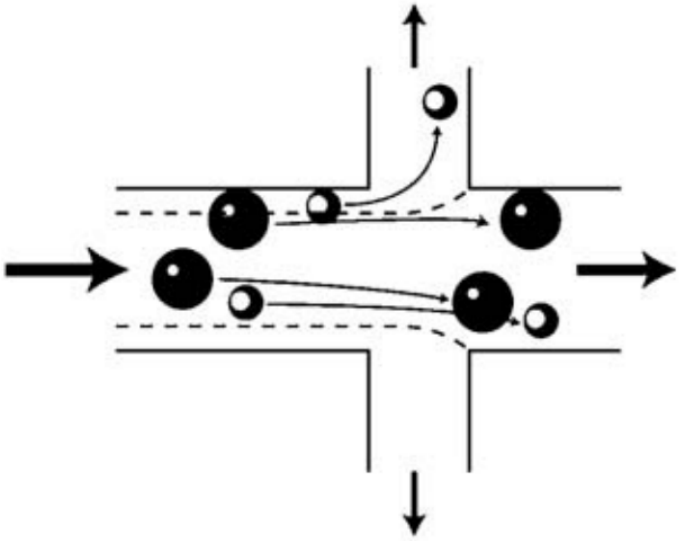

Figure 1.18: Schematic of particle separation by hydrodynamic focusing (83). The dashed lines flanking the channel show the boundary of where the flowlines flow into the side channels. For cells with a larger radius than this boundary width, their centre will always trace the flow lines parallel to the main channel, while smaller cells may get filtered through the side channels.

Hydrodynamic filtration exploits microfluidic phenomena, whereby at low Reynolds number (i.e. in microfluidic channels) the centre of a particle will trace the flowlines in the fluid (40). Due to laminar flow, it is relatively straightforward to achieve uniform patterning of the flowlines in such a channel (84). An example for how this can separate particles based on their size is shown in Figure 1.18, as used in (83), where smaller particles will follow the flow lines into the side channels, to be separated from larger particles. In this case, if the centre of the particle is on the wall-side of the dashed line, it will flow into the side channel; the distance of the dashed line from the wall can be tuned by modulating the flow rate, thus modulating the threshold size for cells to be directed into the side channels. Yamada *et al.* (83), who invented this technique (40) used it to demonstrate the enrichment of leukocytes from blood, and the separation of

liver cells based on size (85). Variations include 'pinched flow fractionation', put forward by the same group (86), whereby a constriction within the channel 'pinches' the flowlines. As a result, cells of different size travel different regions within the channel, to be separated off downstream.

Hydrodynamic filtration is in fact very similar to the size-exclusion filters built in the previous section (1.3.4), but for the fact that the size-exclusion filters in this case are based on flow profile rather than mechanical channel geometry. The advantage of hydrodynamic filtration is that the channel structural features can be many times greater than the cells it separates (unlike for size-exclusion filters), such that far better throughput can be achieved (85). However, the drawbacks given in Section 1.3.4 still apply.

1.3.6 Optical tweezers

Differences in the refractive index of cells allows light-based separation, commonly known as 'optical tweezers'. This harnesses the change in momentum that light experiences as it is bent by an object (e.g. a cell with a characteristic refractive index), to exert an equal and opposite change in momentum on the object (due to conservation of momentum), thus giving rise to a force (87, 88). Most optical tweezers use a focused Gaussian laser beam (see Figure 1.19) which features a high electric field gradient in the beam waist, to which dielectric particles are attracted (with force proportional to the displacement, x). Because the laser focal point can typically be moved around in 2 or 3 dimensions, this makes optical tweezers excellent as a single cell trap, and it is often a relatively straightforward and delicate method of moving single cells on a chip when this has been required (for example Hochstetter *et al.* (2015) (89) used the method to transport individual trypanasome cells into chambers on a microfluidic chip for drug testing).

With regards to cell sorting, Wang *et al.* (91) used optical tweezers for a FACS-on-chip, in which a fluorescent label was detected (here using a CCD camera),

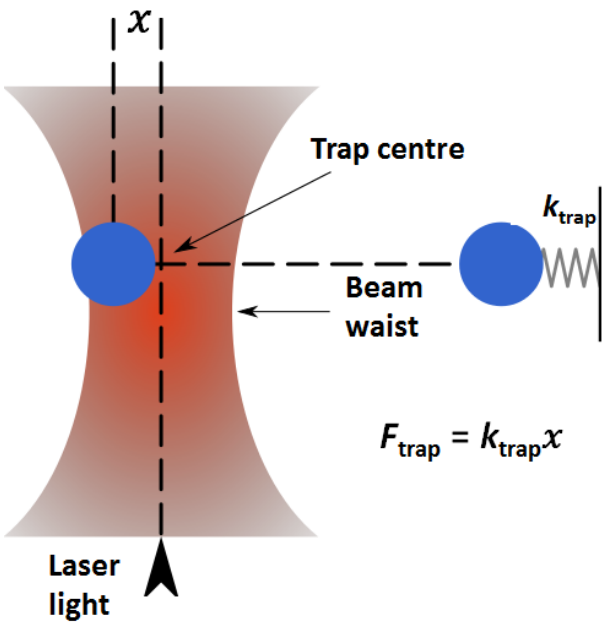

Figure 1.19: Schematic depicting particle trapping in a Gaussian beam for 'optical tweezers (from (90)). Dielectric particles such as cells are attracted to high electric field gradient in the beam waist, allowing them to be trapped.

sending a signal for the tweezers to put them in an appropriate channel downstream. However, it has also been used for label-free separation, most notably by Macdonald *et al.* (2003) (92), who used a laser to pattern an optical lattice onto a microchannel surface (Figure 1.20); two particle types (microbeads in this case) could subsequently be separated based on differences in size and refractive index through a fractionation approach in which particles were deflected more or less depending on their refractive index and size. The research group published a subsequent paper in 2005, in which they used an optical trap to separate lymphocytes from red blood cells (93); however, the optical lattice/fractionation approach was discarded and exchanged for a more conventional single-cell method. While optical trapping offers an interesting, creative solution, it can be presumed that the refractive index difference between cell types is not sufficient for consistent, high throughput cell sorting.

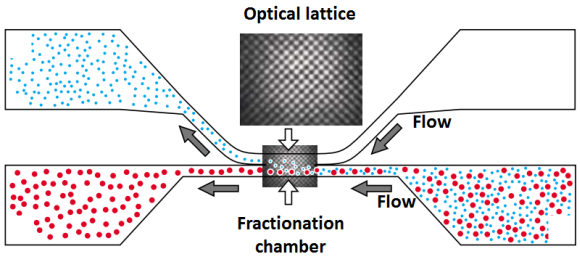

Figure 1.20: Schematic depicting the optical lattice used to separate particles in (92).

1.3.7 Acoustic sorting

Acoustic sorting involves coupling a mechanical wave into a fluidic channel, which exerts a pressure on cells known as an acoustic radiation force (94). Acoustic sorting methods are generally split up by the two basic methods used to couple the acoustic wave into the fluid: bulk acoustic waves (BAWs) and surface acoustic waves (SAWs), principally Rayleigh surface acoustic waves (R-SAWs) (95). Special attention will be paid to R-SAWs, because the technology is very similar to that used for this research.

Bulk acoustic waves

A standard BAW acoustic trap involves putting a block of piezoelectric material (commonly the ceramic lead zirconate titanate, PZT) at a liquid interface. Application of an alternating electric field sends a BAW through the material, which couples into the adjacent liquid to produce pressure waves of the same frequency of the alternating field (96). Particle trapping is achieved by setting the length of the chamber to match the frequency of the pulse (typically $\lambda/2$) such that it resonates and creates a standing wave. Particle trapping occurs at the nodes of the standing wave via acoustic radiation forces.

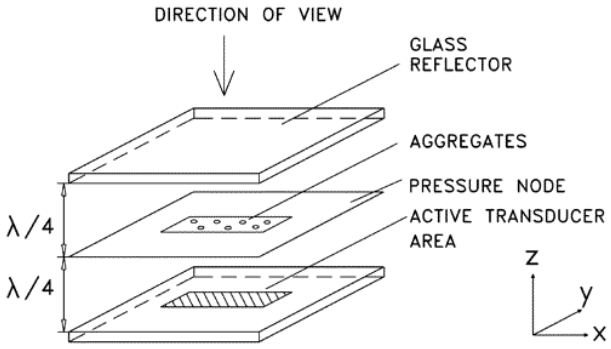

Figure 1.21: Schematic showing a typical acoustic trap using BAWs (96). A transducer sends a BAW pulse via an alternating electrical signal, which sends a travelling wave into a channel. By locating a glass reflector at $\lambda/2$, a standing wave is formed, which resonates with the frequency of the transducer. A pressure node forms in the middle of the channel, which can be used to trap particles.

Surface acoustic waves

SAWs were first described by Lord Rayleigh in 1885 (97), and the most commonly observed example would be that of earthquake seismic waves that propagate along the surface similar to waves on water (98). A full description of SAW motion can be found in Section 2.1.2.

SAWs can be generated on a chip by patterning electrodes on top of a piezoelectric[1] substrate (e.g. lithium niobate, lithium tantalate, gallium arsenide, quartz) (see Figure 1.22) such that an electronic ac signal can be turned into a mechanical propagation along the surface. These were first developed by the US military in the 1970s to delay a pulse to improve the efficiency of radar, and have subsequently been used as filters for receiving signals in televisions and phones (99).

The two types of SAW that are predominantly used in engineering and research are Rayleigh SAWs (R-SAWs) (Figure 1.22**a**) and shear horizontal SAWs (SH-SAWs) (Figure 1.22**b**), which differ in that R-SAWs displace the substrate in the

[1]Defined fully in Section 2.1.2.

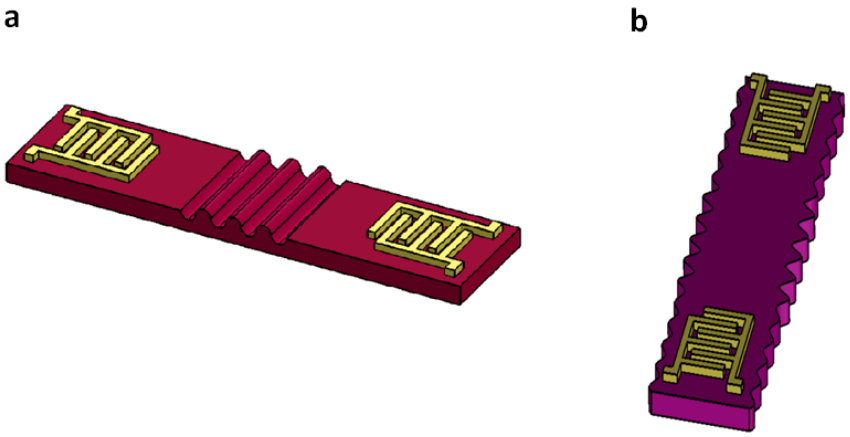

Figure 1.22: Schematic of how IDTs on a piezoelectric substrate can produce SAWs. **a** Rayleigh standing SAW, where the principle direction of mechanical displacement is perpendicular to the plane of the substrate (with the substrate surface moving up and down) **b** Shear horizontal standing SAW, where the principle direction of mechanical displacement is within the plane of the substrate (where the substrate moves from side to side)

vertical plane, while SH-SAWs displace it in the horizontal plane. Because of this, R-SAWs cause mechanical coupling into the liquid, known as a 'leaky SAW', and it is this that is utilised to manipulate particles (like cells) in the liquid. (SH-SAWs, on the other hand, are not generally used for particle manipulation, and instead are mainly used for biosensing applications.)

Similar to nodal trapping by BAWs, SAW IDTs form a standing wave on the substrate, which couples to form a standing wave in the overlying liquid, with regions and gradients of high and low pressure; particles are thus trapped by acoustic radiation forces, similar to in BAWs.

The main advantage of using SAWs over BAWs for acoustic trapping is that they are far lower power (the wave only propagates within one wavelength of the surface - typically <100 µm), and also allow for neater integration for lab

on a chip purposes. In this case, a standing wave is formed between the two transducers, and this couples into the overlying fluid to form an array of pressure nodes and antinodes according to the SAW wavelength.

First described to trap particles by Wood *et al.* (100) in 2008, it has since been used to manipulate and separate cells based on differences in their size, with larger cells moving faster due to the acoustic radiation force. Typical devices (e.g. shown in Figure 1.23) consist of pressure node in the middle of the channel; the cells are flowed through the acoustic field at such a rate that the larger/denser particles align at the node, while the other particle type does not, such that they can be directed into separate sub-channels downstream.

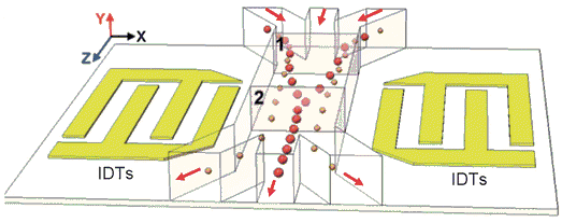

Figure 1.23: Schematic demonstrating particle separation by standing SAWs via a time of flight method (101). Acoustic radiation forces direct particles into the pressure node and the middle of the channel. Because larger particles experience greater acoustic radation forces, the flow rate can be tuned such that only they have time to move into the middle of the channels, so the smaller particles can be separated out.

The shortcomings of acoustic trapping are comparable to those of centrifugation-based cell sorting methods, namely that size and density are not often the best ways of distinguishing cell types. On the other hand, the well-established microfabrication techniques used to make SAW-devices and their accompanying microfluidics has the advantage of precision, such that time-of-flight based separation methods can be finely tuned. It should also be noted that SAW devices offer an excellent opportunity for general manipulation and control of cells on

chips.

1.4 Methods for cell sorting: Dielectrophoresis

Dielectrophoresis (DEP) is a label-free lab-on-a-chip method of sorting cells, much like those discussed in the last section. However, since the technology developed in this thesis exploits a novel, remote dielectrophoretic cell-sorting technique, this section therefore provides a review of competing techniques which utilise DEP-based separation. Whilst DEP has been used to separate many diverse cell types, to measure biophysical characteristics, and to manipulate single cells, the focus here will be on methods for cell sorting with potential application in medical diagnostics or high-throughput cell selection. The chapter concludes with a discussion of the principle limitations of DEP which have thus far prevented clinical uptake, and which the work in this thesis aims to overcome.

1.4.1 Overview on dielectrophoresis for cell sorting

Dielectrophoresis is a way of separating cells based on their dielectric properties using non-uniform electric fields (either DC or AC). The basic mechanisms for DC and AC dielectrophoresis will be briefly described here, although a more thorough description can be found in Section 2.2.2.

DC dielectrophoresis

Dielectric materials (electrical insulators) become polarised in the presence of an electric field. Dielectrophoresis features two dielectric materials: a small particle (dielectric 1) suspended in an aqueous electrolyte solution (dielectric 2), positioned within a non-uniform (asymmetric) electric field (see Figure 1.24, where the field asymmetry is arises from the pin-to-plate electrode design, and blue and red colours represent negative (-) and positive (+) potential/charge respectively).

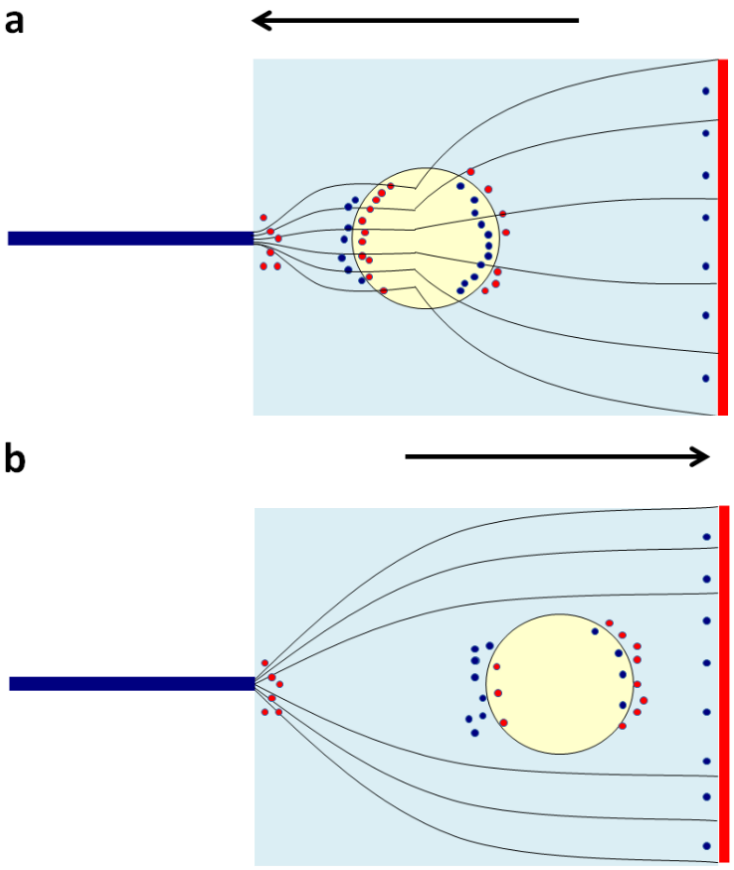

Figure 1.24: Schematic describing the differences beteen negative DEP (nDEP) and postive DEP (pDEP) forces. The Figure shows a cell (light yellow) situated in an aqueous electrolyte solution (light blue) within an asymmetric electric field, whereby the field asymmetry arises from the pin-to-plate electrode design (blue and red bars, respectively). The small blue and red dots represent ionic charges both inside the cell and in the surrounding fluid, gathering at the cellular interface in response to field-induced polarisation of the cell. Blue represents negative (-) potential/charge, and red represents positive (+) charge. **a** pDEP: Due to more charges inside the cell than the surrounding liquid, the electric field lines are drawn towards the cell, pulling it towards the electrodes on both sides; because the field intensity is higher on the left side (shown by higher density of field lines), the cell moves towards the left electrode. **b** nDEP: This time, the liquid has more charges than inside the cell, so the field lines bend around the cell and the cell is repulsed from the electrodes. Again, the force is highest at the left side of the cell due to the higher field intensity; because the force is now repulsive, the cell travels to the right.

As shown in Figure 1.24**a**, if the cell contains more polarisable entities than the surrounding fluid, the electric field lines bend into the cell and it experiences an attractive force towards either electrode. Because the force is stronger where the field intensity is highest (i.e. the left side of the cell), the cell moves towards the left electrode - this is known as positive DEP (pDEP). Conversely (Figure 1.24**b**, if the cell is less polarisable than the surrounding liquid the electric field lines bend around the cell and it experiences a repulsive force from the electrodes; the net force pushes it to the right side, due to the field asymmetry.

AC dielectrophoresis

In the case for AC dielectrophoresis, it must be envisaged that the potentials of the blue and red electrodes in Figure 1.24 are constantly changing between positive and negative. The charges inside and around the cell are therefore constantly switching sides.

In AC dielectrophoresis, the polarisability of different cell types and the surrounding liquid is dependent not only on the density of charge carriers, but also of the mobility of the charge carriers, i.e. how long it takes for them to switch polarity according to the changing direction of the electric field. A more thorough description of the nature of polarisation of different charge carriers at different frequencies is given in Section 2.2.2.

Advantages of DEP as a cell-sorting method

DEP allows cell types to be separated by exploiting differences in their dielectric properties - this is a characteristic which is dependent on many properties, including the frequency of the applied electric field, the conductivity of the surrounding liquid, conductivity and permittivity of the cell cytoplasm, and the thickness and capacitance of the cell membrane[1] (102). Because researchers can easily tune

[1]These are in fact all the properties which are taken into account when theoretically calculating or predicting DEP behaviour based on the 'single shell model' (see Section 2.2.2). In

the frequency of the electrical field (and, to an extent, the conductivity of the surrounding fluid), the parameters can be set such that the permittivity of the medium is less than that of one cell type, and more than that of the other, thus enabling separation of the two cell types.

There are two reasons that make DEP a particularly good label-free sorting method: Firstly, the ability to exert a positive *or* a negative force on cells, according to type, makes it much easier to spatially separate two cell types on a chip (compared to, say, acoustic sorting, density sorting, which works on the basis that one cell or particle type gets slightly less force exerted on it). Secondly, the ability to distinguish cells by dielectric properties has proven to be a more sensitive and discerning method that other label-free approaches. In a review on LoC cell sorting, Gossett *et al.* (40) suggest that this could be because the biological state of a cell is typically defined by the presence of entities like large, charged protein complexes, dynamic ion gradients across a membrane, and internal organelle structures, which consequently may heavily impact upon the dielectric properties.

Limitations of using DEP to sort cells

It can be argued that the dielectric properties of a cell population are just as arbitrary as sorting cells based on other label-free characteristics such as size, density, refractive index etc; that is to say, researchers are generally not interested in separating a cell because it is different in any physical characteristics, but because of it's unique function - for example, a stem cell compared to a differentiated cell. This is defined generally by its protein expression profile, and thus sorting cells by surface protein-specific antibodies (Section 1.2.2) is therefore a more direct and specific approach to separation, while sorting cells by an arbitrary physical characteristic is limited when cells of different biological

reality, many other factors play a part in influencing the polarisability of a cell; for example, the nucleus to cytoplasm ratio is a key biophysical characteristic of a cell which will influence its dielectric properties; however, it is accounted for in the calculation for cytoplasm conductivity. Similarly, the presence of ion channels or gradients in the membrane are accounted for by the membrane capacitance of the cell.

phenotypes have very similar physical characteristics. However, the range of clinically useful cell types already separated by DEP method - including viable from non-viable (103, 104, 105), stem cells from differentiated cells (106) and cancer from non-cancer/other cancers (107), as well as the common model of blood cell types (108) - is testament to the superiority of DEP in label-free separation.

In terms of building a practical, high-throughput cell sorting device, DEP has been limited mainly by the fact that the electrodes are in contact with the fluid, from which several problems arise:

Firstly, this limits the composition of buffers (i.e. the surrounding liquid) in which the cells are suspended to those of very low conductivity, generally 0.001 - 0.03 S/m. A higher conductivity leads to significant coupling of the electric current into the liquid, causing joule heating of the fluid, which damages cells and disrupts trapping by convection currents. Because the conductivities of physiological fluids are typically 0.5 - 2 S/m (109), this poses a concern as to the viability and usefulness of cells after having been suspended in low-conductivity liquids (110). This is investigated further in Section 5.4.

Another significant problem is that the cells are typically trapped on or around the electrodes, such that the throughput of the device is limited by the area of the electrodes (typically ~ 500 cells per 1 mm^2 of surface area). As well being low-throughput, cells trapped at the electrodes (i.e. those attracted to areas of high field gradient by pDEP) are subjected to a strong electric field for prolonged periods, again raising concerns regarding the viability and usefulness of cells following separation.

Furthermore, cells which are trapped at the electrodes are generally difficult to remove afterwards (known as electrode fouling), which limits the device lifespan and introduces contamination (111). Other reported issues include bubble formation at the electrodes, disrupting trapping of cells (111).

Major DEP designs are discussed in the remainder of this chapter, many of which attempt to address the issues presented here. Early devices and typical electrode designs are discussed in Sections 1.4.2 through to 1.4.7, continuous throughput designs in Sections 1.4.9 and 1.4.10, followed by novel efforts to remove the electrodes from the liquid (Sections 1.4.11 and 1.4.12). Finally, efforts to trap particles by the novel method of SAW-DEP are described (Section 1.4.13 (a variation of which is used in this work), before summarising the key issues that will be addressed in the DEP designs used for this thesis (Section 1.4.14).

1.4.2 Early DEP devices

Pohl in the 1950's (112) showed that in a non-uniform electric field, cells suspended in a liquid experience different forces depending on their dielectric properties and hence on their type. Pohl's early experiments of particle separation in the 1960s (113, 114) used simple designs such as the pin-plate design (Figure 1.25).

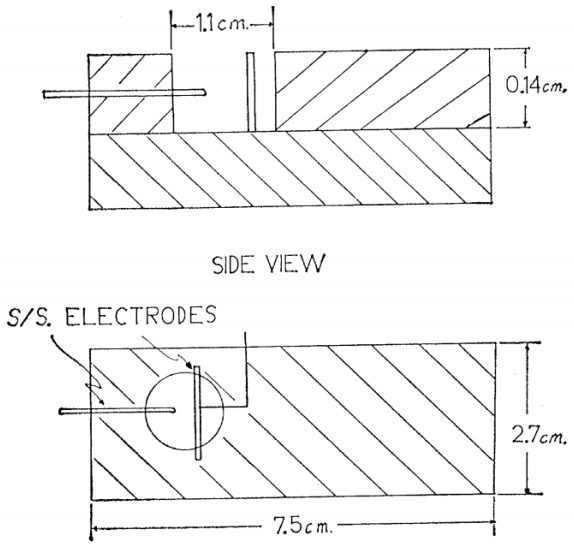

Figure 1.25: Schematic of the pin-plate design used in (114), the first demonstration of DEP to separate live and dead cells.

This is a practical realisation of the electrode design shown in Figure 1.24, so it can be imagined where the field lines are. This setup was used by Pohl and Hawk in 1966 (114) to separate live and dead yeast cells, which has since become a model example to demonstrate DEP. Dead cells are significantly less polarisable than live cells, due to ionic content being released from their more permeable cell membrane. Thus, the dead cells are directed to the low gradient at the 'plate', whereas live cells are attracted towards the 'pin'. Pohl *et al.*'s work throughout this period used relatively thick wires (0.258-1.59 mm diameter), for which electrical biases up to 11 kV were required in order to generate sufficient electric field strengths to produce the force necessary to locomote cells (102) (this value is accepted to be about 10 V/m for a 10 µm cell (115)). The problem with having

to use such high voltages is that this led to significant thermal effects within the fluid, leading to disruptive currents, and potential damage to cells (102).

This led to a dry spell in DEP research throughout the 1980s, before microfabrication techniques became readily accessible for academic groups in the 1990s. By fabricating electrodes on a chip (using the microfabrication methods described in Section 1.3), a reduction in spacing between electrodes from 10s of mm to 10s of µm can lead to a 1000-fold increase in electric field intensity.

These advances, coupled with greater ease of delivery and extraction of cells afforded by microfluidics, allowed for researchers to separate a range of mammalian cell types, as discussed previously. Notable proponents of DEP cell sorting in the 1990s include the Morgan group in Glascow (116, 117, 118, 119), the Gascoyne group in Houston (108, 120, 121, 122), and the Pethig group in Bangor, Wales (108, 123, 124, 125, 126).

Modern DEP-based LoC devices use electrodes in height range 50-100 nm, which are typically fabricated using metallic vapor deposition. The electrode width is usually chosen to be 5-10 times the diameter of the particles to be selected (e.g. 10 - 150 µm (102). The following sections introduce the more widely used electrode designs, namely "polynomial", "castellated", and "interdigitated" (115), before extending the discussion to more novel DEP device designs.

1.4.3 Electrode design: Polynomial

Polynomial electrodes are so-called because the electrical potential of any point in the system can be defined by a polynomial that obeys Laplace's equation (102). The most common arrangement is that seen in Figure 1.26, which is typically used for trapping single cells (in the middle) to measure their dielectric properties.

This is usually achieved through electrorotation, in which the alternating potential applied to the electrodes is 90 degrees out of phase with the adjacent

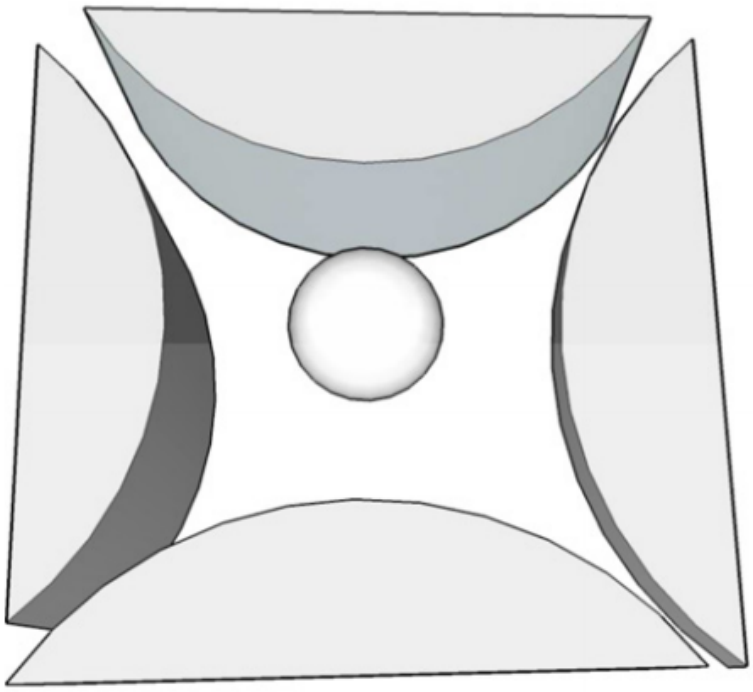

Figure 1.26: Schematic showing a cell trapped in a typical quadrupole electrode design (102).

electrode, such that the resultant electric field at the centre of the electrodes rotates either clockwise or anti-clockwise. The resultant DEP-force causes the particle to spin with or against the field rotation, according to whether it is experiencing positive or negative DEP. These experiments are typically carried out such that the frequency of the applied bias is increased from low frequency (where the cell experiences nDEP, 10-100 KHz) to medium frequency (where cell experiences pDEP, 100 KHz - 100 MHz) to high frequency (where the cell again experiences nDEP, >100 MHz (102), as shown in Figure 1.27.

1.4.4 Electrode design: Castellated

First used in 1992 by Pethig *et al.* (115, 125), the castellated electrode design and the resulting trapping is shown in Figure 1.28. It features parallel wires with

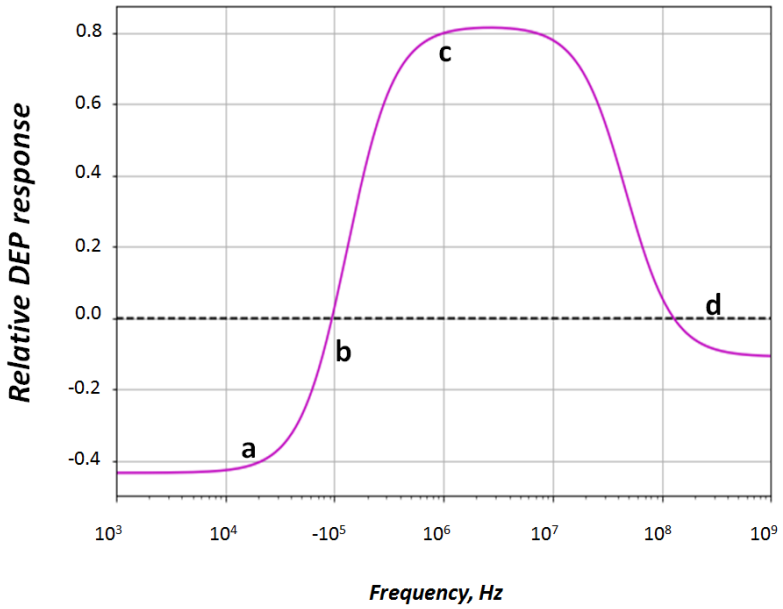

Figure 1.27: Graph showing typical DEP response (positive or negative) of a typical mammalian cell, as a function of frequency, (102), as can be found by observing the direction of cellular rotation in polynomial electrodes. **a** Below 100 KHz, cells experience negative DEP (nDEP). **b** At about 100 KHz (though this can vary greatly depending on the dielectric properties of the cell and fluid), the cell experiences no DEP force and can be observed to stop rotating at all. **c** Between 100 KHz and 100 MHz, the cell can be observed to rotate in the opposite direction - it is now experiencing positive DEP (pDEP). **d** At 100 MHz the cell stops rotating, and above 100 MHz the direction of rotation changes again, back to nDEP.

'teeth' patterned at an even mark-to-space ratio. The field gradient is highest between the corners of the teeth, and lowest in the space between teeth, resulting in positive and negative DEP trapping at these areas, respectively. Separation was first demonstrated by Markx *et al.* (1996) (115, 126) using live and dead bacterial cells; this is typically achieved, as for most DEP devices, by trapping one cell type (e.g. live cells) by positive dielectrophoresis, and flowing liquid to dislodge negatively trapped cells (e.g. dead cells), which are repelled from the field and so washed away more easily. Following this, the electric field can be

switched off in order to release the pDEP cells.

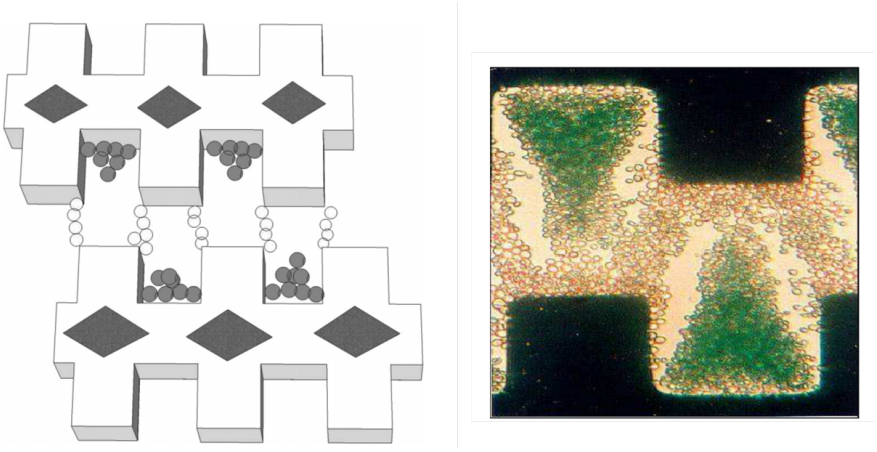

Figure 1.28: Schematic showing typical castellated IDT electrode geometry (left), and a microscope image showing typical positive/negative cell trapping in such a device (right) (102).

The problem with these two-step separation techniques is that switching between steps is often time consuming, and the throughput is limited by the area of the electrodes; consequently scaling it up would defeat many of the key objectives of LoC technology (see Section 1.3.1). Many DEP technologies attempt to combine hydrodynamic force with DEP to allow for continuous throughput devices. For example, Yasukawa *et al.* (127) aligned the teeth of castellated electrodes (Figure 1.29), and used nDEP to separate polystyrene beads based on their size (3 µm and 10 µm).

By applying a 2 MHz frequency, both particles experience nDEP, however the larger 10 µm particles are subject to a stronger force. This allows an enrichment of smaller particles into 'weaker' nDEP lines (Line A) and larger into the stronger nDEP regions (Line B). Despite the precedence this work was given by reviews such as (102), the authors note that in practice line B still contained 35% if the 3 µm particles. Furthermore, although line A exhibited 100% enrichment of the smaller particles, the flow rate was limited to only 10 particles/second.

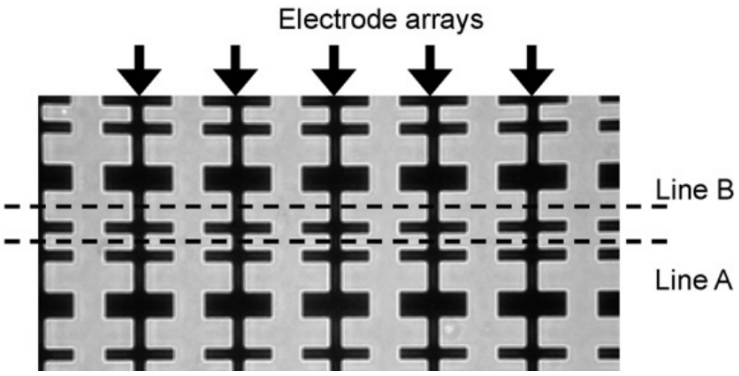

Figure 1.29: Microscope image showing the aligned IDT electrode geometry used in (127). The asymmetry in the pattern (from top to bottom) is exploited such that larger beads (10 µm) are repulsed most strongly into Line B, while some smaller particles (3 µm) may flow into Line A (as well as Line B).

1.4.5 Electrode design: Interdigitated

The interdigitated electrode design is analogous to the transducer electrodes used to generate surface acoustic waves. It is a very simple design in which alternating bars of ground and signal electrodes are aligned alongside each other, such that positive cells are trapped along the electrode edges, while negative cells levitate between the electrodes where the electric field gradient is lowest (see Figure 1.30).

Due to negative cells being levitated rather than trapped between electrodes (in castellated geometries), this configuration lends itself better to separation (115), and its simplistic design is more readily combined with hydrodynamic forces and gravity-based approaches in, for example, field flow fractionation (DEP-FFF) and travelling wave DEP (twDEP), which shall be discussed in the next two subsections.

1.4.6 Travelling wave DEP

Travelling wave DEP was first described by Hagedorn *et al.* (129), and is also used frequently by the Morgan group (130, 131, 132, 133). In this approach,

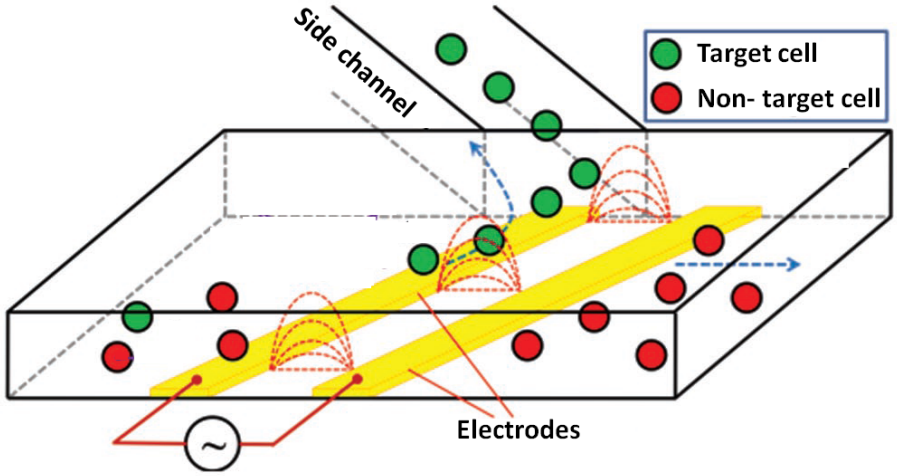

Figure 1.30: Schematic demonstrating particle trapping around electrodes (yellow/gold colour) by dielectrophoresis (128). One cell type ('Target cell') experiences pDEP and is attracted to the high field gradient areas at the electrode edges. Non-target cells are repulsed and may be flowed away without disrupting the target cells.

individual interdigitated electrodes are subjected to sequentially phase-shifted potentials to produce a travelling electric field. This allows nDEP-experiencing particles to be moved along the array, with typical particle velocities of 10 µm/s (although this is rather slow) (Figure 1.31).

Because of differences in the nDEP force experienced by particles, owing to e.g., their size (131), the speed at which they travel can differ, thus allowing fractionation to occur. An interesting advantage of this technique is that unlike most LoC microfluidics, it does not require a syringe pump (or similar) because particles can be transported independent of fluid flow (115).

1.4.7 DEP-FFF

DEP-FFF is a form of field flow fractionation (Section 1.3.3) in which the discriminating field is an electric field. Cells are levitated away from the electrodes

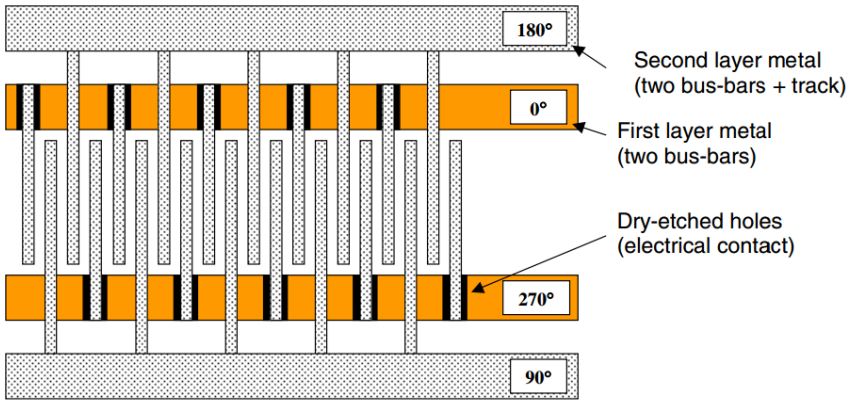

Figure 1.31: Schematic showing a typical travelling wave DEP electrode design (to be fabricated using multilayer methods) (131). By having four different points of electrical contact, the potential can be phase shifted along each finger to move particles along the electrodes by nDEP.

(via nDEP), until the DEP-force is balanced by the sedimentary force commonly used in FFF, as shown in Figure 1.32 (120). Thus cells which experience a greater nDEP force (i.e. those that are less polarisable by the electric field) are levitated higher into the faster fluid streams (at middle of the channel height), such that they are fractionated downstream. This method is commonly used for DEP separation by the Gascoyne group in Houston (120, 121, 122).

Again, this is a multi-step process; after being flown into the chamber, cells are left for ~ ten minutes (120) to reach their equilibrium height, before taking a roughly equivalent amount of time to flow the separate cell populations out. While Wang *et al.* (2000) (120) reported impressive enrichment of 92-99.99%, recovery was only 55-75%, presumably due to electrode/channel fouling while the cells are left in the chamber for an extended time period. Perhaps more critically, the long amount of time that cells are exposed to the electric field is concerning with regards to cell viability/manipulation, although this can be said about many DEP methods where cells are fractionated off (i.e. not performed under continuous flow). Indeed, one advantage that could be said of DEP-FFF is that, by primarily exploiting nDEP (and therefore locating the cells at areas

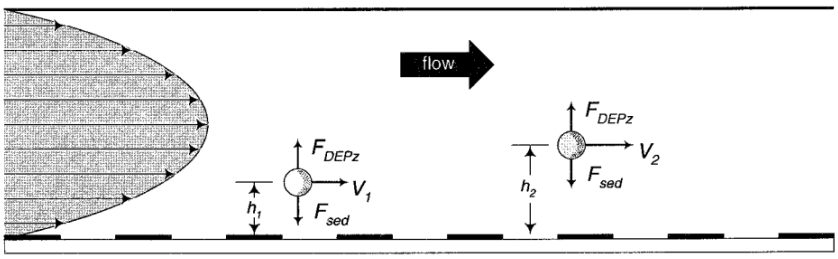

Figure 1.32: Schematic showing the operating principle for DEP-FFF (120). Due to differences in dielectric properties, two particles types (left and right spheres) are levitated to different heights within the channel. Because the flow profile (shaded area) results in faster flow in the middle of the channel height, particles which are levitated closest to this can be fractioned off early, and thus separated from the other particle type.

lowest field gradient and intensity), and possible harm cause to cells experiencing electric fields for prolonged periods is minimised (134).

One way to avoid the incubation step was demonstrated by Holmes *et al.* (2003) (56, 135), whereby pre-separation electrodes focused cells into the middle of the channel (Figure 1.33). Focusing cells in microfluidics systems is a common step, though it is more often achieved using hydrodynamic or SAW-based methods (136). Whilst the device shown in Figure 1.33 would efficiently collect cells into separate bands on the chip (for example, to be counted), it is not suitable for subsequent extraction of separated cell types because there is no way of flowing off the two bands separately.

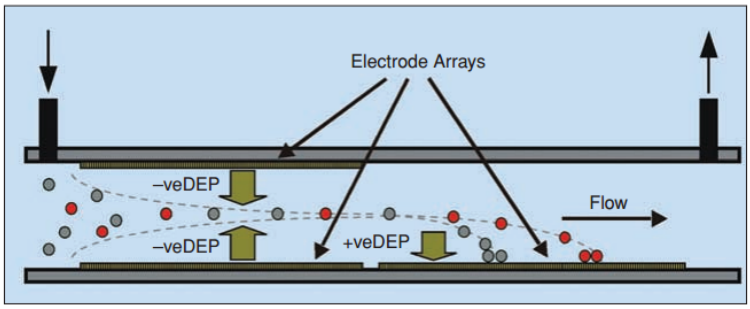

Figure 1.33: Schematic showing the DEP-FFF used by (56, 135), whereby particles are focused by nDEP before separation. Separation occurs by cell types experiencing different amounts of pDEP attraction to the second electrode (set to a pDEP-inducing frequency), such that different cell types collect in different bands along the chip.

1.4.8 Funneling DEP

A variation on the nDEP-focusing method presented by Holmes *et al.* (56, 135) can be seen in the work of Fiedler *et al.* (1998) (134). The authors used a 'funnel' electrode design (Figure 1.34), with the primary aim of focusing and concentrating particles to the middle of the fluidic channel.

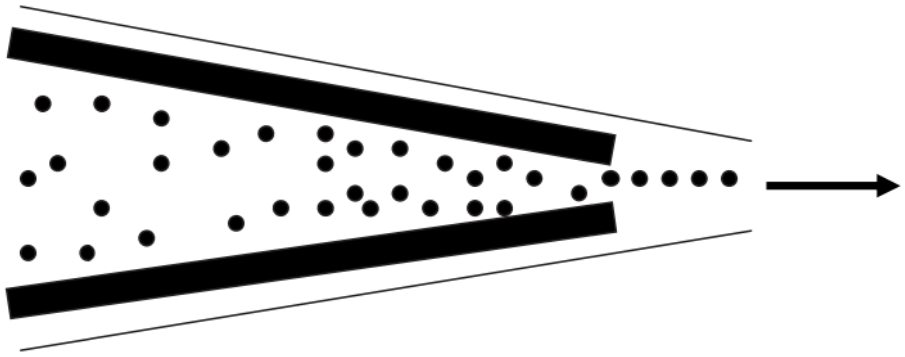

Figure 1.34: Schematic showing a funnelling electrode design to concentrate particles with nDEP. Particles (black spheres) are repelled by nDEP from electrodes (black lines) within a microchannel, which are angled so as to focus them (102).

Due to the greater DEP force experienced by larger cells, this has also been used for size-based sorting (by fractionating off smaller cells first) (137), again similar to the capabilities of centrifugation. The typical cell velocities reported by Fiedler *et al.* (134) were an impressive (for microfluidics) 10 mm/s; however, it is still hard to envisage this technique as ever matching centrifugation for throughput, though its specificity is likely to be roughly equivalent. It is also worth noting that this method is very similar to travelling wave DEP (Section 1.4.6).

One obvious disadvantage of the techniques discussed thus far is that they are not continuous-flow devices, i.e., sorted cells either have to be fractionated off in repeated steps in order to achieve high throughput. This is in contrast to the SAW-based sorting device presented by Shi *et al.* (101) (Figure 1.23), in which the two cell types are continuously directed into two separate channels. This

brings us to two novel methods, 'Hydrodynamic' and 'Isomotive' DEP, which offer similar continuous sorting capabilities.

1.4.9 Hydrodynamic DEP

Doh *et al.* (2005) proposed a 'Hydrodynamic DEP' sorter for continuous flow and higher throughput particle separation (138). Electrodes flank the sides of the channel in a similar way to Funneling DEP, and hydrodynamic focusing of the cells as they enter is achieved by sheath flow (Figure 1.35).

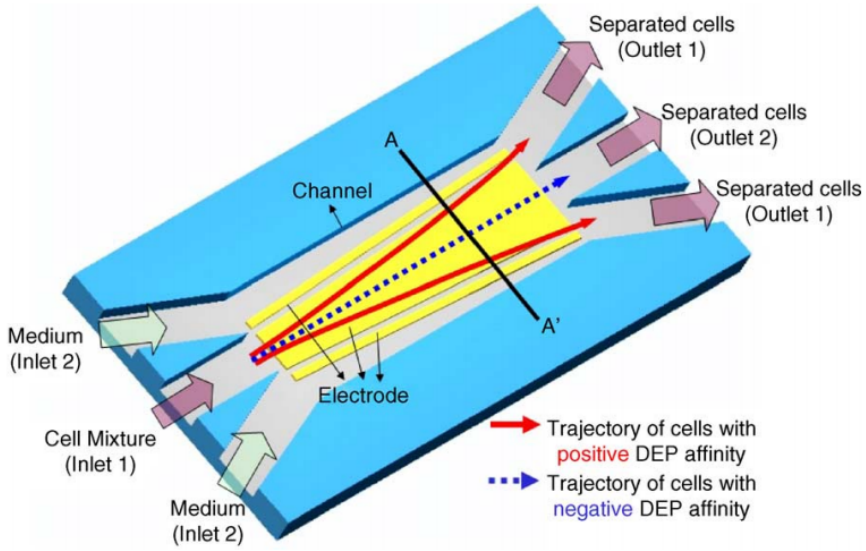

Figure 1.35: Schematic showing the design used for continuous hydrodynamic DEP by Doh *et al.*, 2005 (138). Cells are directed into the middle of the channel by hydrodynamic focusing. As they travel through the channel, electrodes flanking the channel attract one cell type by pDEP, such that they move into 'Outlet 1' regions. Conversely, cells experiencing negative DEP are repelled by the electrodes and stay in the middle of the channel, to be extracted by Outlet 2.

This technique also makes use of both pDEP and nDEP, by tuning the parameters such as that one cell type (live yeast cells) receives pDEP and is attracted

to the flanking electrodes, while the other (dead yeast cells) are repelled to the centre. Thus, pDEP cells are collected by channels at the sides, and nDEP cells in a central channel. This method demonstrated a good throughput of ~650 cells/second, similar to FACS, and purity of 97% and 75% for pDEP and nDEP cells, respectively.

1.4.10 Isometric DEP

Isomotive DEP is another continuous-throughput separation method, presented by Li *et al.* (2007) (139). In their setup (Figure 1.36), the electrodes are designed such that the magnitude of force experienced by a cell (whether experiencing pDEP or nDEP) is the same irrespective of its position in the channel (hence movement is 'isomotive' (140)). The cell moves to the left or right channel depending on whether it receives positive or negative DEP.

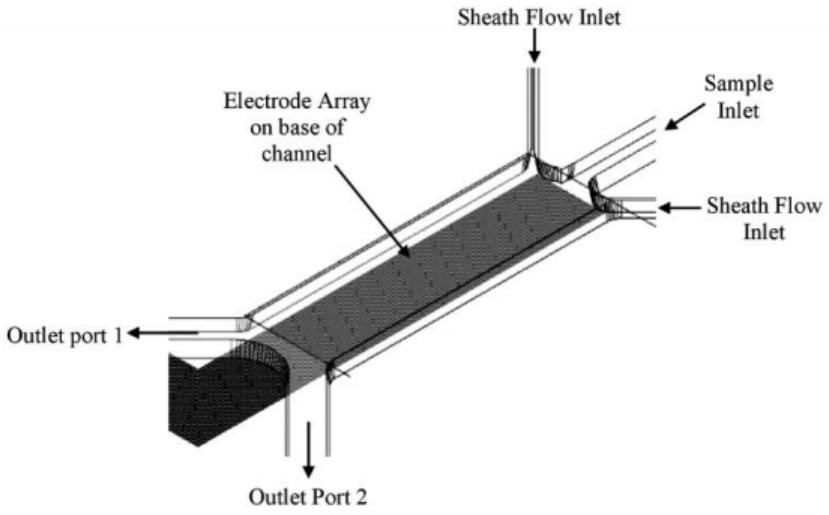

Figure 1.36: Schematic showing the isomotive DEP channel and electrode design used in (139). An electrode array at the base of the channel is designed such that cells experience the same amount of force (pDEP or nDEP) throughout the channel, with pDEP-experiencing cells moving to the right, and nDEP-experiencing cells moving to the left.

This seems like an incredibly neat solution to give continuous flow, while utilising the discretion of positive and negative DEP forces. However, the results of the paper (139) were disappointing: enriching live yeast from a live/dead sample, the target outlet only had a ~ 10% greater proportion of the target cell (e.g. live). It can only be speculated, for example, that the field produced is not sufficiently non-uniform to exert a sizeable force on cells, as a possible reason why the method was not more successful.

A major limitation of all the techniques considered so far is that the requirement to have electrodes in contact with the fluid. This imposes limitations on the medium conductivity, which must be kept low (0.001 - 0.03 S/m) for reasons discussed in Section 1.4.1, such that cells are kept in potentially harmful buffer conditions. Other problems also arise from the presence of the electodes, such as fouling, and the observation that this requirement does not lend itself readily to continuous-throughput designs. The remainder of this section will look at steps researchers have taken to minimise the effect of, or remove, electrodes from the fluid in DEP devices.

1.4.11 Electrodeless DEP

An electrodeless DEP device can be produced by passing the field directly into the fluid if it is suitably ionic (such as that of a typical cell buffer or culture medium) (102, 141). In order to create the asymmetry required to produce a DEP force, the channel features constrictions made of insulating material, that distort or warp the electric field. Figure 1.37 shows the constriction design used by (141); in this case, the areas of high field gradient are at the centre of the constriction, with low field gradient regions formed at either side.

The suggested application of this is more of a diagnostic tool rather than a high-throughput separator. Cell sorting achievements have included the separation of blood cells from *E. coli* (142), in which the *E. coli cells* are trapped in the

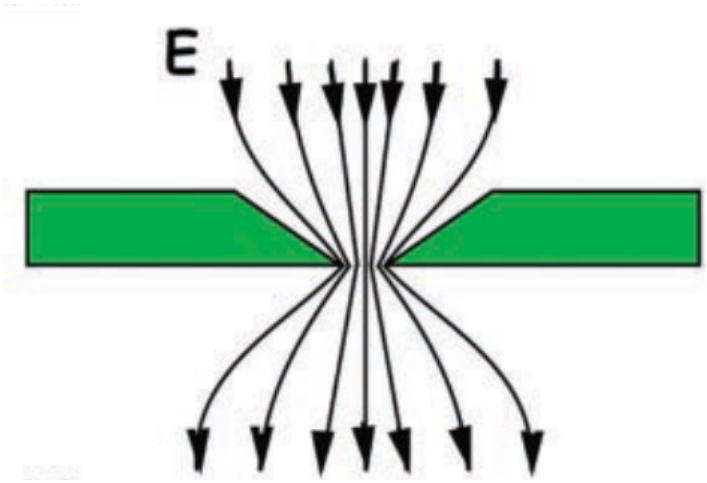

Figure 1.37: Schematic showing an electrodeless DEP design, where constrictions in an insulating material within the microchannel creates non-uniformity in the electric field (thus exerting a DEP force on particles passing through it). A current is passed directly into a high conductivity fluid, such that a field is formed in the liquid; the field is subsequently shaped by dielectric obstacles etched into a microchannel (in this case quartz) (141).

channel as the blood cells flow on.

While this is a novel and creative solution to removing the electrodes from the liquid, it is difficult to see how cells can be differentially extracted afterwards, at least with high throughput. Another issue with this method is that while some problems caused by the electrodes are solved, passing the current directly into the ionic fluid generates a substantial increase in temperature (111).

1.4.12 Contactless DEP

Contactless DEP was developed by Shafiee *et al.* in 2009 (111). In this case, the electrodes are separated from the fluid by a thin dielectric material (see Figure 1.38), which capacitively couples the field from the electrodes into the main channel.

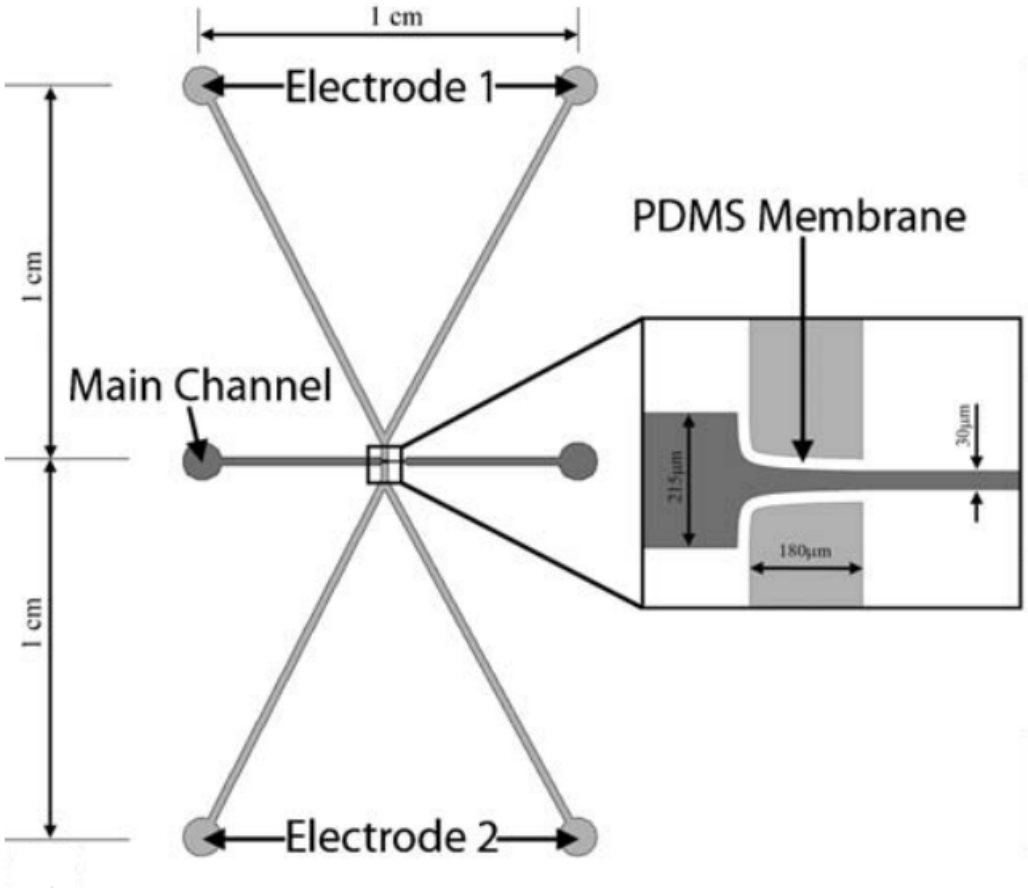

Figure 1.38: Schematic and dimensions for contactless DEP, from (111), in which the electrodes are capacitively coupled to the cell solution by separating them with a thin dielectric layer (i.e. the PDMS membrane), thus avoiding direct contact of the electrodes.

This method was used to separate live and dead mammalian (leukaemia) cells (143) as well as plasma from whole blood (144). While this may seem like a simple solution to the problem of having electrodes in contact with the fluid, the same issues of joule heating and hence the need for low conductivity fluids remains; likewise, the electrodes can only be on either side of the channel, and separation of cells depends on a fractionation technique, in which the throughput is limited by the area of the (capacitive) electrode surface. The main advantage of this technique is that the electrodes can be added separately and the

intricate, micro-scale features of the device can be made through insulator-based technologies with relative "ease of fabrication" (for example, commercial devices could ultimately be made by injection-moulding). However, the claim that making 30 µm wide microchannels in PDMS is any harder that vapour-depositing microelectrodes is a contentious one, and it could be similarly argued that micropatterning electrodes (particularly on a large scale) has been made relatively straightforward thanks to its utility to the computer/smart phone industry.

1.4.13 SAW-DEP

In the SAW devices mentioned in Section 1.3.7, a non-uniform electric field is formed relative to the nodes and antinodes of the standing wave (high and low electric field gradient, respectively). This is due to the compression and rarefaction of the charge centres within the crystal lattice of the substrate. Thus, theoretically, cells can be lined up at the nodes and antinodes between the transducers by positive and negative DEP. In practice, however, the use of Rayleigh SAWs to produce the standing wave means DEP forces are competing with much stronger acoustic radiation forces, and cells will always tend to line up at the nodal (low pressure) regions of the leaky SAW (Figure 1.39).

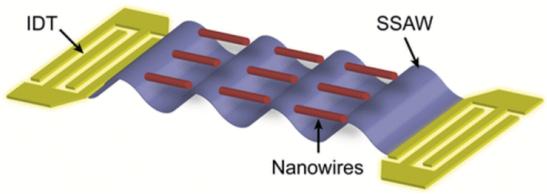

Figure 1.39: Schematic showing nanowire alignment by SAW-induced DEP, from (145). The nanowires, which are made of a conductive material, experience dielectrophoretic force that causes them to align at the antinodes of the underlying SAW (the low gradient regions), in a formation parallel to the SAW propagation axis. The dielectrophoretic force is sufficiently strong to overcome acoustic forces from the leaky SAW pressure wave in the channel, which otherwise would cause the nanotubes to align perpendicular to the SAW propagation axis at the nodes of the pressure wave.

The DEP effect from SAWs has been used, however, to align particles with enhanced conductivity, such as metallic microtubules (146). Kong *et al.* (2010) used Rayleigh SAWs on $LiNbO_3$ to align conducting microtubules (see Figure 1.40). As can be seen in this figure, the microtubes align along the SAW axis of propagation; to prove this was caused by dielectrophoretic effects (not acoustic forces, for example, via misleading reflections in the channel), the field was screened and no alignment was observed (146).

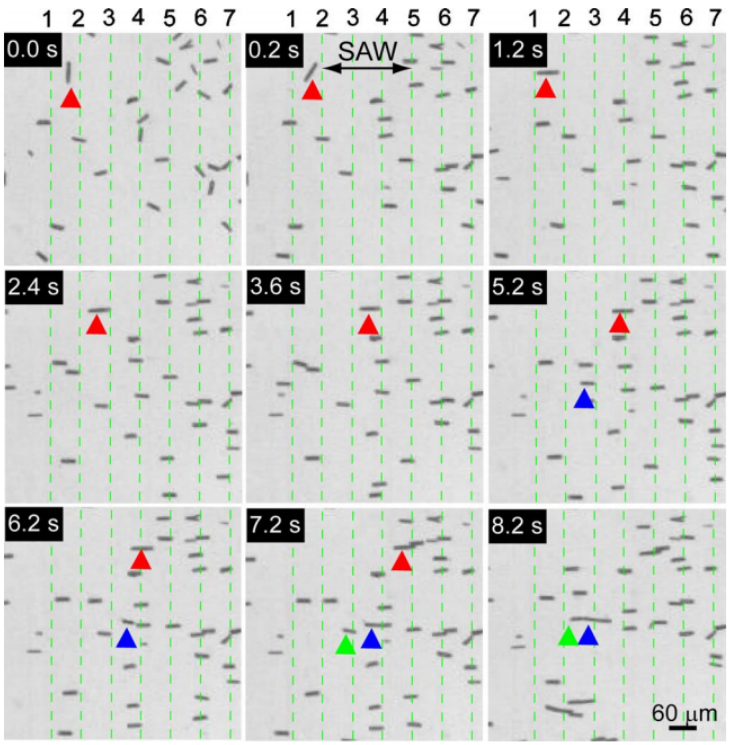

Figure 1.40: Time series of Cr microtubules aligned using SAWs on a $LiNbO_3$ substrate, from (147). The coloured triangles are markers on individual nanotubes.

A similar experiment was done by the Huang group in 2013 (145). This experiment used a similar setup to generate arrays of nanowires at the SAW antinodes, separated from microspheres at the nodes (see Figure 1.41).

Even for applications such as separating nanowires from microspheres, or simply patterning nanowires, the acoustic forces are both strong, but also produce unpredictable flow and can generate significant heat within the fluid. The position of pressure nodes depends not only on the position of the standing wave in the substrate, but also on the channel geometry, as the wave couples into the overlying liquid in the form of a leaky SAW which subsequently reflects according to the channel geometry. This non-uniformity of patterning is evidenced by the uneven arrangment of particles seen in Figure 1.41.

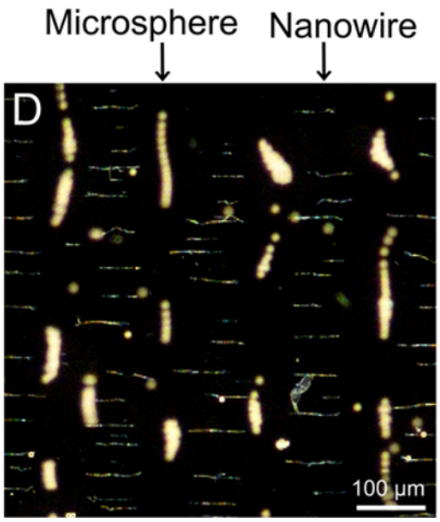

Figure 1.41: Schematic showing nanowire alignment by SAW-induced DEP, from (145).

1.4.14 Dielectrophoresis summary and considerations for a SAW-DEP cell sorter

A corollary of the preceding section would be that if the acoustic effects could be successfully removed from SAW-based devices, the dielectrophoretic forces would dominate and possibly be sufficient to align cells. This thesis builds on early work (by those mentioned in the Acknowledgements section) that suggests the use of shear horizontal (SH-) SAWs to achieve this. SH-SAWs are similar to Rayleigh SAWs, but with the displacement in the horizontal plane of the surface (Figure 1.42), such that there is no mechanical coupling into the liquid. Lithium tantalate ($LiTaO_3$) is a common substrate to generate SH-SAWs for use, e.g. in biosensing applications (148).

In this work, a method is proposed that could overcome several key issues with DEP techniques discussed in this subsection (see Figure 2.6):

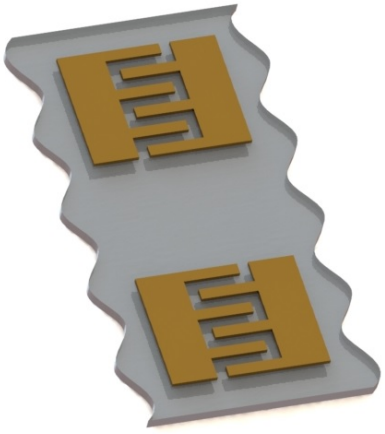

Figure 1.42: Schematic showing a SAW chip with a shear horizontally-propagating SAW standing wave, as opposed to the Rayleigh waves discussed earlier.

- This method would allow sorting of cells into both positive and negative dielectrophoresis, for high fidelity separation of cell types
- By placing the fluidic channel between the electrodes, the fluid can be kept apart from the electrodes. Because the electric field effect arises from static charges on the surface, there will be no current passed into the liquid, meaning that high conductivity liquids can be used without negative effects such as heating and convection currents
- Cells can be flown through the electric field and sorted, to be diverted into separate channels. This would allow for both high-throughput, continuous separation, and avoids fouling of electrodes.

A detailed and mathematical description of the mechanism behind our proposed technology is described in the following section.

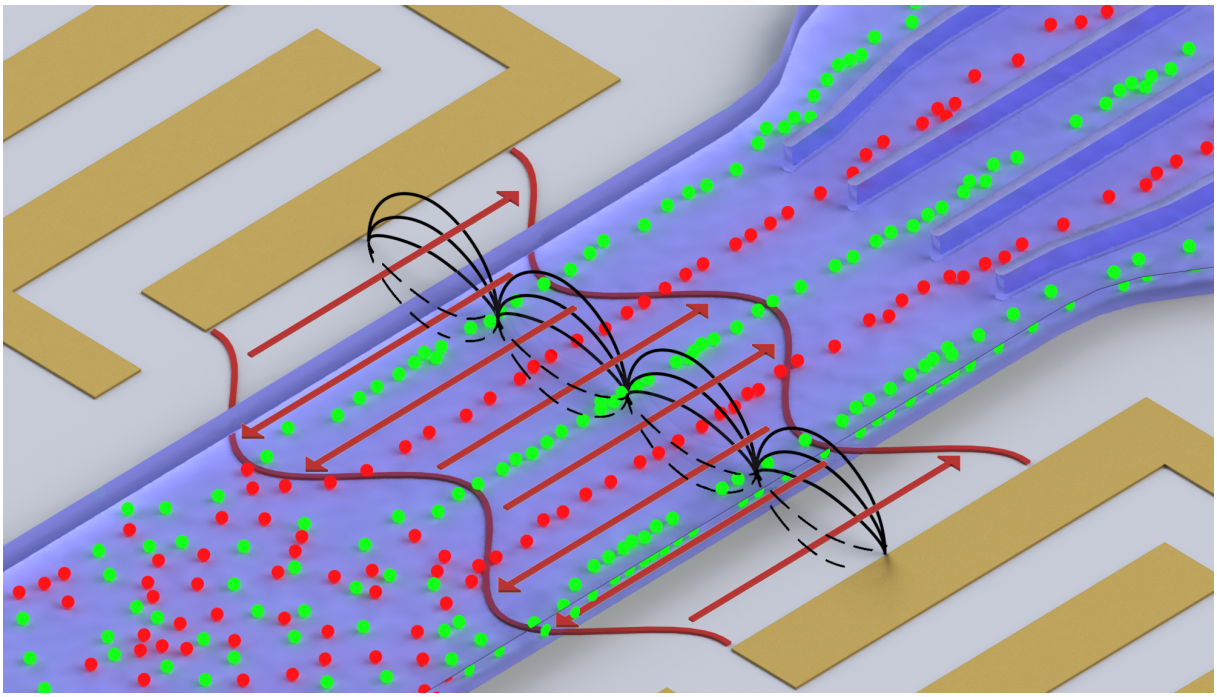

Figure 1.43: Schematic showing cell separation of a SAW chip (149). IDTs either side of a microfluidic channel produce a standing SH-SAW between them (red arrows, side-to-side movement). This in turn produces a non-uniform electric field (black lines). By flowing in a heterogeneous mixture of particles (green and red spheres, left), the particles can be dielectrophoretically separated into discrete lines by the induced non-uniform electric field, and flowed into structurally separated sub-channels for subsequent extraction.

Chapter 2

Theory of surface acoustic waves and dielectrophoresis

2.1 SAWs

2.1.1 Description of mechanical waves

A mechanical wave can be described as a periodic oscillation of matter that travels, and therefore transfers energy, through a medium. An illustration of the most basic types of mechanical (or "acoustic") wave can be seen in Figure 2.1. Surface acoustics waves (SAWs) are a special subset of mechanical wave, in which the travelling mechanical oscillations are confined to the interface between two materials - in this case, at the surface of a piezoelectric crystal substrate. Whilst a bulk acoustic wave (BAW) travels through the body of a material, the mechanical perturbations of a SAW are generally confined to within one wavelength of the substrate surface. Two of the most common types of SAW are: the shear-horizontal SAW (SH-SAW), in which the mechanical oscillations are parallel to the substrate surface and perpendicular to the direction of propagation (analogous to Figure 2.1**b**); and the Rayleigh wave, which exhibits components both along the direction of wave propagation, and normal to the surface plane (a complex convolution of Figure 2.1**a** and **c**). The most well known SAWs are the Rayleigh waves that propagate through the earth's surface following a seismic event. Both types of SAW are elastic waves, i.e. they propagate through

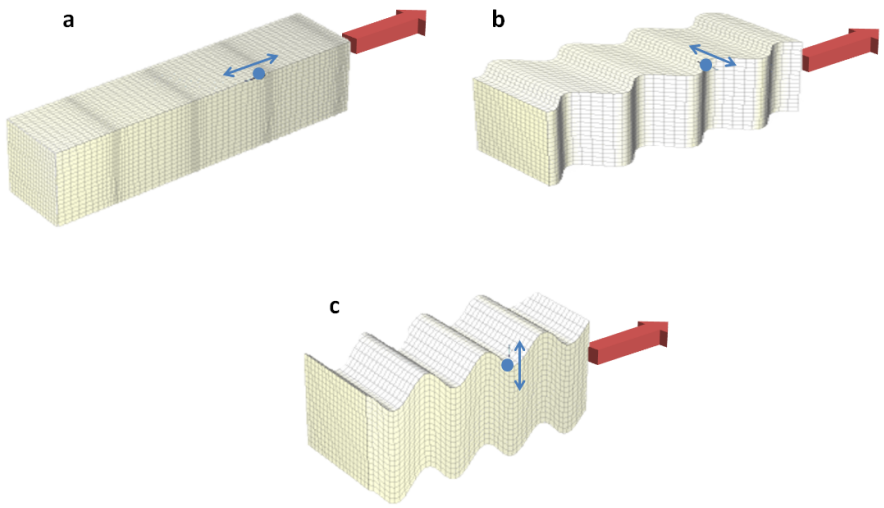

Figure 2.1: Schematic of mechanical wave types propagating along a substrate. Red arrows indicate the direction of propagation, and blue arrows indicate the movement (i.e. the mechanical displacement) of individual particles (blue circle) within the substrate. **a** Pressure, or longitudinal, wave, where particles are displaced parallel to the surface plane in the direction of propagation **b** Shear (or "transverse") horizontally polarized wave, where particles are displaced parallel to the surface plane, perpendicular to the direction of propagation **c** Shear vertically-polarized wave, where particles are displaced perpendicular to the surface plane, perpendicular to the direction of propagation (150).

a material without resulting in a permanent deformation.

2.1.2 Creating surface acoustic waves on a piezoelectric substrate

Piezoelectric materials are those that become electrically polarized in response to mechanical perturbation. For example, they are used for the spark-generating components of cigarette lighters and gas cooker lighters, which discharge electricity when mechanical pressure is applied. For a material to exhibit the piezoelectric effect, the unit cell of the material's crystal structure must lack

inversion symmetry (Figure 2.2). When mechanical pressure is applied along the axis of asymmetry, the charge centres of the crystal are misaligned such that there is a change in dipole, δP, caused by the movement of charge in the crystal, which is exhibited by a change in charge density at the crystal suraces and a corresponding electric field is established between the crystal faces. The larger the applied force, the larger the generated field.

Similarly, applying a potential across a section of piezoelectric material can induce an expansion or compression proportional to the applied bias. By applying an alternating bias, the compression and expansion alternates with the electric field, and propagates through the material as a travelling wave.

A typical transducer geometry for generating SAWs is shown in Figure 2.3. These comb-like electrodes are known as interdigitated transducers (IDTs), where one 'comb' is grounded, while an AC voltage is applied to the other. These transducers must be made of a conductive material, generally gold or aluminium. Upon application of the alternating bias, the electrical potential difference creates an undulation of compressions and rarefactions of the underlying crystal that oscillate with the same period as the applied potential.

If the spacing between finger pairs is an integer number of SAW wavelengths (e.g. for a 50 µm SAW wavelength, finger spacings of 50, 100, or 150 µm, etc), then subsequent finger pairs will amplify the SAW as it propagates, allowing it to travel further along the substrate beyond the IDT (typically <1 cm). The SAW wavelength is described in Equation 2.1:

$$f = \frac{v}{\lambda} \tag{2.1}$$

where f is the applied frequency, v is the wave speed/speed of sound in the substrate, and λ is the SAW wavelength.

For example, a 10 MHz acoustic wavelength in a lithium tantalate substrate ($LiTaO_3$) where the speed of sound is ~ 4,000 m/s would have a wavelength of

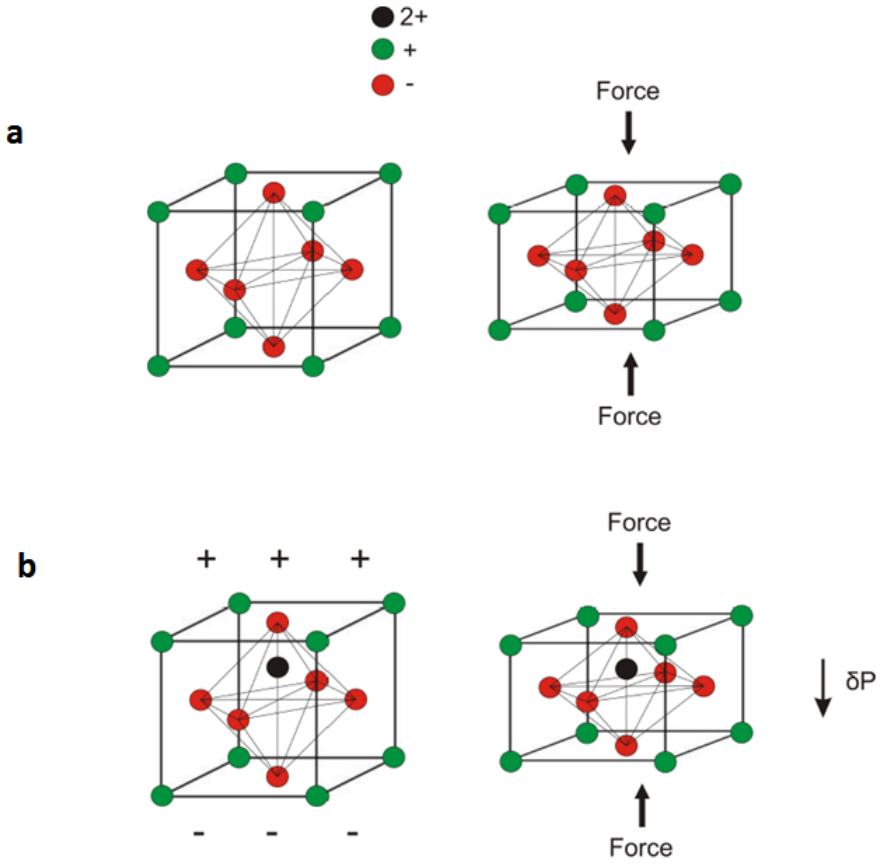

Figure 2.2: Schematic showing a face centred cubic unit cell **a** with and **b** without inversion symmetry. Positive charges (+) are shown in green, negative (-) in red (the charges of molecules are arbitrary). In **a**, the centres of positive and negative charge are coincident, and there is no net polarisation; when force (or stress) is applied, the crystal lattice becomes strained but the charge symmetry remains; there is therefore no change in the polarisation of the crystal. In **b** an additional charge (2+, black) means that the centres of positive and negative charge are not perfectly coincident, such that there is a net polarisation. When a strain is applied, the relative positions of the centres of negative and positive charge are altered, generating a change in the dipole, δP, of the unit cell and therefore a change in the electric field between the faces (151).

400 µm. In order to generate an acoustic wave at this frequency, the pitch of the IDT would be designed to match the wavelength (i.e. 400 µm, λ in Figure 2.3).

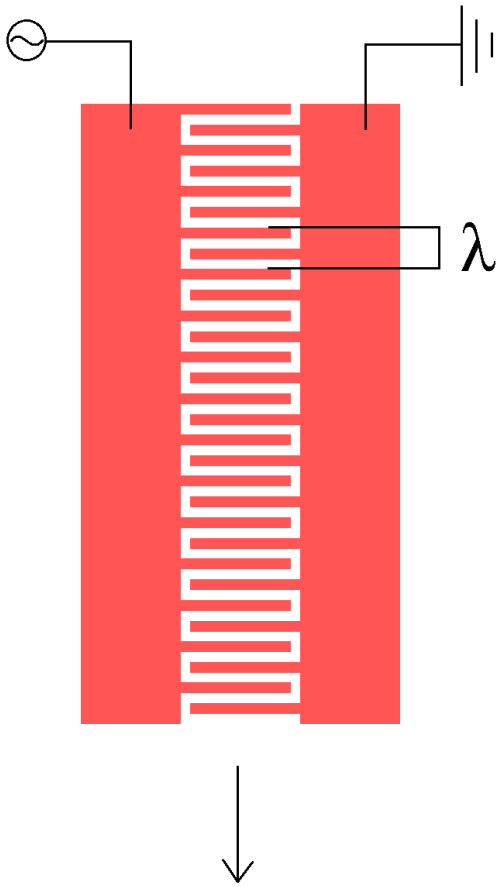

Figure 2.3: An example interdigitated transducer (IDT) design to produce SAWs. An oscillating potential is applied to one set of transducers while the other set is grounded, generating an acoustic wave that propagates along the surface of the underlying piezoelectric substrate. The wavelength of the wave produced is defined by the pitch of the IDTs indicated by λ.

By applying a phase-locked driving signal to transducers at both ends of the substrate, two travelling waves travelling in opposite directions along the same axis will overlap and combine to form a standing wave, as illustrated in Figure 2.4. Figure 2.4 also depicts the two types of SAW that can be produced - Rayleigh

(Figure 2.4**a**) or shear horizontal (Figure 2.4**b**) - according to the crystal cut of the substrate.

The rest of this subsection will provide a mathematical description of the waves that are formed in SAW devices. Detailed mathematical treatments can be found in references (152, 153, 154, 155), from which the majority of the discussion presented here was derived.

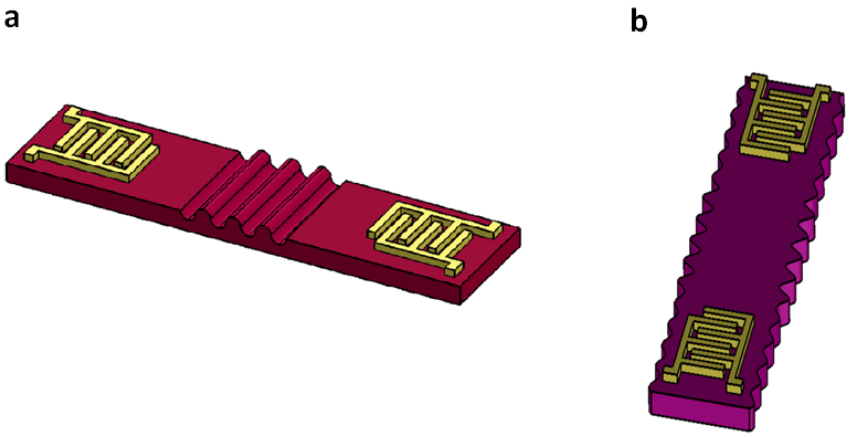

Figure 2.4: Schematic of how IDTs on a piezoelectric substrate can produce SAWs. **a** Rayleigh standing SAW, where the principle direction of mechanical displacement is perpendicular to the plane of the substrate (with the substrate surface moving up and down) **b** Shear horizontal standing SAW, where the principle direction of mechanical displacement is within the plane of the substrate (where the substrate moves from side to side)

2.1.3 Terminology

Stress and Strain

Wave propagation in elastic media is described in terms of *Stress* and*Strain* tensors within a Cartesian coordinate system. The stress (T) is a measure of the internal forces within a material (N/m^2), while the strain (S) is a measure of the deformation of the material per unit length (dimensionless). They are both expressed as tensors, T_{ij} and S_{kl} respectively, where i, j, k, and l each have x, y, and z coordinate directions. The second order stress tensor T_{ij} is depicted graphically within a Cartesian coordinate system in Figure 2.5.

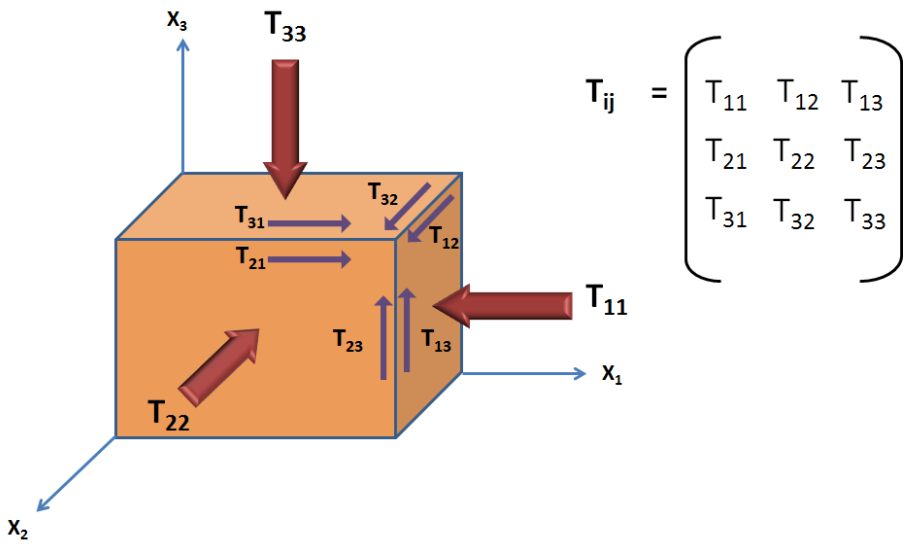

Figure 2.5: Schematic depicting how stress forces in a material are represented within a Cartesian coordinate system. The directions 1, 2 and 3 correspond to the orthogonal coordinates x, y, and z. $\mathbf{T}$ represents the stress force on the substrate, defined by force per unit area; $\mathbf{X}_1$, $\mathbf{X}_2$, and $\mathbf{X}_3$ correspond to the coordinate axes x, y, and z, respectively.

Figure 2.5 shows the forces acting on a unit cube in three dimensions. The stress tensor (or stress 'state') T_{ij} can be decomposed into 9 components written as a matrix (T_{11} etc in Figure 2.5). The subscripts i and j denote orthogonal

directions; T_{ij}, therefore, is the the force (per unit area) on the i-face in the j direction. As can be seen in Figure 2.5, this leads to three normal stresses where $i = j$ (T_{11}, T_{22}, and T_{33}), and six shear stresses where $i \neq k$. To relate this to the matrix in Figure 2.5, i (1,2, or 3) denotes the row number of the matrix, while j denotes the column number. (A full example of one stress component is given after a description of *Strain*.)

To describe the strain (S) a particle (or point) is considered within the material which is displaced from its equilibrium state by deformation by a distance U. Strain is also described as a second order tensor, S_{kl}, which is given by:

$$S_{kl} = \frac{1}{2}\left(\frac{\partial U_k}{\partial l} + \frac{\partial U_k}{\partial l}\right) \tag{2.2}$$

where k and l each have x, y, and z components.

Stress and strain are linearly proportional to one another by a constant tensor, C. Stress and strain are both second order tensors, so their relationship must be described by a fourth order tensor, denoted here with the subscripts i, j, k, and l:

$$T_{ij} = C_{ijkl} S_{kl} \tag{2.3}$$

Each of i, j, k, and l can have values for x, y, and z, such that there are therefore ($3^4 =$) 81 stiffness constants. However, in elastic non-ferroelectric materials, the stress matrix is symmetric and so $T_{ij} = T_{jk}$, which in turn means that the stiffness constants are related by:

$$C_{ijkl} = C_{jikl} = C_{ijlk} = C_{klij} \tag{2.4}$$

This reduces the number of stiffness constants to 21. Due the symmetry of the tensors in question, the subscripts can be abbreviated as shown in Table 2.1.

Table 2.1: Abbreviation of subscripts

Label	ij
1	xx
2	yy
3	zz
4	yz,zy
5	xz,xy
6	xy,yx

To illustrate, this is how the second order strain tensor can be represented in matrix form (note the $i = j$ symmetry):

$$\mathbf{S} = \begin{vmatrix} S_{xx} & S_{xy} & S_{xz} \\ S_{yx} & S_{yy} & S_{yz} \\ S_{zx} & S_{zy} & S_{zz} \end{vmatrix} = \begin{vmatrix} S_1 & \frac{1}{2}S_6 & \frac{1}{2}S_5 \\ \frac{1}{2}S_6 & S_2 & \frac{1}{2}S_4 \\ \frac{1}{2}S_5 & \frac{1}{2}S_4 & S_3 \end{vmatrix}$$

By notating the stress and stiffness constants in similar form, Equation 2.3 becomes:

$$\begin{vmatrix} T_1 \\ T_2 \\ T_3 \\ T_4 \\ T_5 \\ T_6 \end{vmatrix} = \begin{vmatrix} c_{11} & c_{12} & c_{13} & c_{14} & c_{15} & c_{16} \\ c_{12} & c_{22} & c_{23} & c_{24} & c_{25} & c_{26} \\ c_{13} & c_{23} & c_{33} & c_{34} & c_{35} & c_{36} \\ c_{14} & c_{24} & c_{34} & c_{44} & c_{45} & c_{46} \\ c_{15} & c_{25} & c_{35} & c_{45} & c_{55} & c_{56} \\ c_{16} & c_{26} & c_{36} & c_{46} & c_{56} & c_{66} \end{vmatrix} \cdot \begin{vmatrix} S_1 \\ S_2 \\ S_3 \\ S_4 \\ S_5 \\ S_6 \end{vmatrix}$$

Stress component example

To illustrate, below is an example of one of the stress components:

$$\begin{aligned} T_{xx} = C_{xxxx}S_{xx} + C_{xxxy}S_{xy} + C_{xxxz}S_{xz} + C_{xxyx}S_{yx} + C_{xxyy}S_{yy} \\ + C_{xxyz}S_{yz} + C_{xxzx}S_{zx} + C_{xxzy}S_{zy} + C_{xxzz}S_{zz} \end{aligned} \tag{2.5}$$

which, using the abbreviations of Table 1, becomes:

$$T_1 = C_{11}S_1 + C_{12}S_2 + C_{13}S_3 + 2C_{14}S_4 + 2C_{15}S_5 + 2C_{16}S_6 \tag{2.6}$$

The proceeding section will discuss how these terms fit into general equations for motion in order to describe piezoelectric wave propagation.

2.1.4 Wave propagation

Equation for motion

The total force exerted on a material (modelled as a cube, as in Figure 2.5) can be described by:

$$F = \frac{\partial T_{ij}}{\partial X_j} \tag{2.7}$$

where F is the force density per unit volume, T_{ij} is the stress tensor, and X_j is the length in X_1, X_2, and X_3. F must be equal to the mass ($m = \rho V$, where ρ is the density and V is the volume) times the acceleration ($\partial^2 U_i / \partial t^2$); because F in this case is per unit volume, Newton's second law becomes:

$$F = \rho \frac{\partial^2 U_i}{\partial t^2} \tag{2.8}$$

This can be substituted into Equation 2.7 to give a wave equation to describe displacements in isotropic media[1], as well as elastic, homogenous anisotropic media:

$$\rho \frac{\partial^2 U_i}{\partial t^2} = \frac{\partial T_{ij}}{\partial X_j} \tag{2.9}$$

[1]Isotropic media has the same characteristics in all directions, while anisotropic media exhibits different characteristics in different dimensions

Relating to stress and strain

Recalling Equation 2.3, the Stress component (S_{kl}) can be substituted for $\partial U_l/\partial X_k$ (where U is the displacement and X is the unit length) such that Equation 2.3 becomes:

$$T_{ij} = C_{ijkl}\frac{\partial U_l}{\partial X_k} \tag{2.10}$$

The wave equation (2.9) can now be re-written to include the stiffness constants of a given material (C_{ijkl}) by substituting T_{ij} on the right side, and dividing the left side by a further ∂X component:

$$\rho\frac{\partial^2 U_i}{\partial t^2} = C_{ijkl}\frac{\partial^2 U_l}{\partial X_j \partial X_k} \tag{2.11}$$

This gives a set of three equations (for U_x, U_y, and U_z). $ijkl$ takes all possible combinations of X, Y, and Z, and thus is related to how many stiffness constants there are for the material.

2.1.5 Considerations for piezoelectric medium

Piezoelectric components

As described partially in Section 2.1.2, piezoelectricity is a phenomenon of certain anisotropic materials that couples elastic stress and strain to electric fields. In a piezoelectric material, the stress components T_{ij} are therefore dependent not only on the stiffness (C) and strain (S) components, but also the electric field,

E, described by:

$$D_i = \epsilon_{ij} E_j \tag{2.12}$$

where D is the electric displacement field vector, ϵ is the permittivity matrix, and E is the electric field vector.

A mechanical wave propagating in a piezoelectric medium will partially dissipate energy into an electric signal, described by (using Equation 2.3):

$$T_{ij} = C_{ijkl} S_{kl} - e_{kij} E_k \tag{2.13}$$

where e_{kij} is the third order piezoelectric tensor, and E_k is the electric field in three directions.

Similarly, an electric field dissipates energy into a mechanical stress (S), as shown by (using Equation 2.12):

$$D_i = e_{ikl} S_k l + \epsilon_{ik} E_k \tag{2.14}$$

where D_i is the component of the electric displacment, and ϵ_{ik} is the symmetric permittivity matrix.

Wave propagation in a piezoelectric medium

Using Equations 2.13 and 2.14 and substituting in the terms for the previously-shown equation for wave motion (Equation 2.11), it is possible to get a system of coupled wave equations to describe wave propagation in consideration of the piezoelectric effects.

Considering Equation 2.13, T_{ij} and S_{kl} can be substituted (as for Equation 2.11) to give:

$$\rho\frac{\partial^2 U_i}{\partial t^2} - C_{ijkl}\frac{\partial^2 U_k}{\partial X_j \partial X_l} - e_{kij}E_k \tag{2.15}$$

In the case of acoustic waves, the electric field can be described as the negative gradient of the scalar potential (153):

$$E = -\nabla\phi \tag{2.16}$$

The term $-\nabla\phi$ can be written as the differential $\frac{\partial^2\phi}{\partial X_k \partial X_j}$. Substituting this for E_k, Equation 2.15 becomes:

$$\rho\frac{\partial^2 U_i}{\partial t^2} - C_{ijkl}\frac{\partial^2 U_k}{\partial X_j \partial X_l} - e_{kij}\frac{\partial^2\phi}{\partial X_k \partial X_j} = 0 \tag{2.17}$$

Finally, the S_{kl} and E_k components in Equation 2.14 can be substituted as for the above, to give:

$$e_{ikl}\frac{\partial^2 U_k}{\partial X_i \partial X_l} - \epsilon_{ik}\frac{\partial^2\phi}{\partial X_i \partial X_k} = 0 \tag{2.18}$$

2.2 Dielectrophoresis

2.2.1 Formation of a non-uniform electric field by a standing SAW

A standing SAW formed on a piezoelectric substrate will oscillate the charge centres back and forth so as to produce an electric field emanating from bound charges in the substrate; because the degree of oscillation varies along the standing wave (i.e. more towards the antinodes, less towards the nodes), this electric field will be non-uniform. The electric field associated with a piezoelectric standing SAW is represented diagrammatically in Figure 2.6. A more thorough description of this phenomena, with modelling and experimental results from force tracking, will be presented in Section 4.4. The remainder of this section will describe how non-uniform electric fields can be used to move particles by dielectrophoresis. A more thorough description of dielectrophoresis can be found in the references (102, 115, 156), from which the majority of this section is based on.

2.2.2 Brief description of dielectrophoresis

DC dielectrophoresis

All the dielectrophoretic experiments used in this work (and most other works pertaining to manipulation of cells by dielectrophoresis) pertains to AC dielectrophoresis, that is, the movement of dielectric particles in a non-uniform AC electrical field. It is logical to begin by describing DC dielectrophoresis (i.e. the movement of dielectric particles in a DC electric field), before explaining the differences between it and AC dielectrophoresis.

Dielectric materials (electrical insulators) become polarised in the presence of an electric field. Polarisation can be thought of as the movement of charged entities within the dielectric material to maximise attraction or minimise repulsion in their interaction with the surrounding electric field.

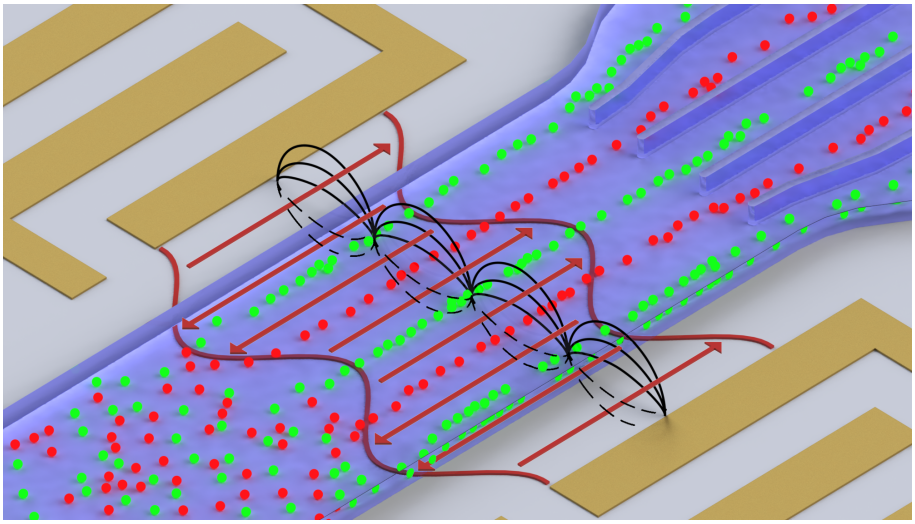

Figure 2.6: Schematic showing how a standing SAW formed on a piezoelectric substrate produces an associated non-uniform electric field. The mechanical movement of a shear standing wave in the substrate is represented by red lines and arrows; the black lines represent the associated electric field component. The greatest compression and rarefraction of the substrate occurs at the standing SAW nodes; these are the regions of highest electric field intensity (represented by the widest point of the three black electric field lines). Similarly, the lowest field intensity is found at the SAW antinodes. The green and red spheres represent cells in an overlying microchannel, flowing from the bottom left to the top right of the image, which receive a dielectrophoretic force from the non-uniform field.

Dielectrophoresis concerns the polarisation of two dielectric materials: a small particle, such as a cell or latex bead, suspended in an aqueous electrolyte (such as sodium chloride, NaCl). The polarisation of the two materials within a uniform DC electric field (formed by two 'plate' electrodes) is shown diagramatically in Figure 2.7.

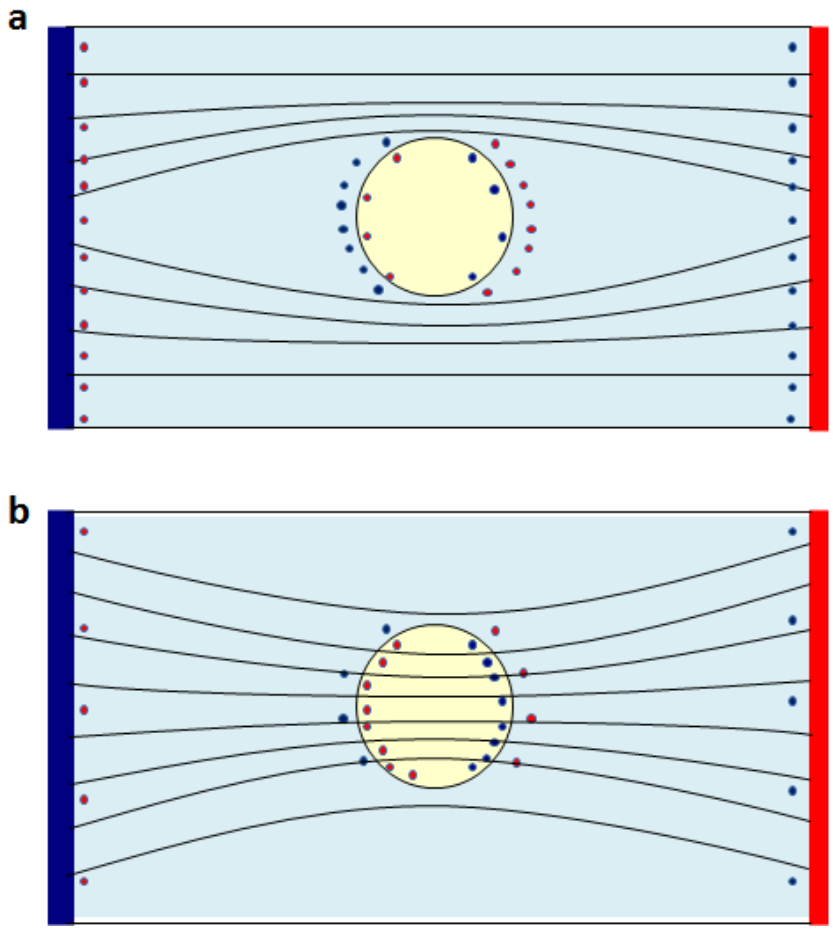

Figure 2.7: Schematic showing how a particle (yellow circle) and aqueous electrolyte solution (pale green liquid surrounding the particle) become polarised in a (uniform) DC electric field. The blue and red bars represent negative and positive ('plate') electrodes, respectively. Blue and red dots represent negative and positive charge carriers (for example, Cl^- and Na^+ ions), respectively. The polarisation force is the same on both sides of the particle (because it is in a uniform electric field), and so there is no net movement of the particle. **a** There is a greater concentration of charge carriers in the surrounding liquid than in the the particle, such that the liquid is more polarisable than the particle. Because of this, the electric field lines bend around the particle. **b** There is a greater concentration of charge carriers inside the particle than in the surrounding liquid, such that the particle is more polarisable than the liquid; now, the field lines bend into the particle.

Figure 2.7 shows that, when in a DC electric field, the field lines will go through whichever medium (the liquid or the particle) that has the highest concentration of charge carriers. This figure shows the case for a uniform electric field, which polarises dielectric particles such that a net dipole forms, but leads to no net movement of the particle because the polarisation force is the same on both sides of the particle.

Figure 2.8 shows a dielectric particle in an aqueous solution in a non-uniform DC electric field. Similar to the case for a uniform field, the direction of the net dipole of the particle depends whether it is more or less polarisable than the surrounding liquid, such that the particle experiences a repulsive force from the electrodes if it less polarisable than the surrounding liquid, or an attractive force if it is more polarisable. However, because the field is non-uniform, there is a stronger force (attractive or repulsive) from the regions of high field intensity (i.e. the blue electrode in Figure 2.8). The result of this is that if the particle is less polarisable than the surrounding liquid (Figure 2.8**a**), it is will be pushed away from the regions of high field intensity (known as negative dielectrophoresis, or 'nDEP'), while it is attracted towards the regions of highest field intensity if it is more polarisable than the surrounding liquid (positive dielectrophoresis, or 'pDEP').

AC dielectrophoresis

AC dielectrophoresis can also be illustrated by looking at Figure 2.8, but it must be considered that the electrode potentials (illustrated by blue and red colours) are constantly alternating. In response to the alternating potential, the charge carriers inside and outside of the particle are moving to alternating sides of the particle, with a slight time delay that depends on the mobility of the charge carriers. For AC dielectrophoresis, therefore, the direction of the net dipole of the particle depends therefore not only on the density of charge carriers inside and outside the particle, but also on the mobility of charge carriers. The types of charge carriers and the factors that affect their mobility are discussed in the

next sub-section.

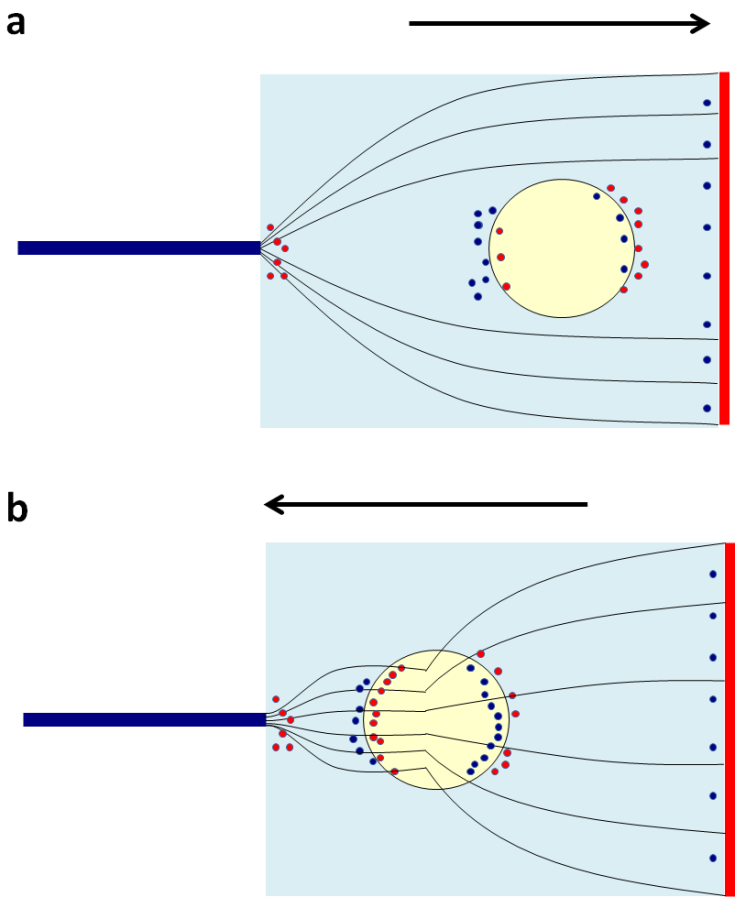

Figure 2.8: Schematic showing a particle surrounded by an aqueous electrolyte solution, similar to Figure 2.7, only in the presence of a non-uniform electric field instead of a uniform electric field. The black arrow represents the resulting direction of particle movement. **a** The particle is less polarisable than the surrounding liquid, such that the field lines bend around the particle to travel through the liquid. Because of the dipole formed by the electric field (where the red, positive charge carriers group to the left of the particle, and blue, negative charge carriers group to the right), opposite charge carriers in the liquid group round the outside of the particle. This forms a net dipole across the particle such that there is a repulsive force from either electrode; because there is a strong force from the regions of higher field intensity (i.e. from the blue, negative electrode), the particle is pushed in the direction away from the high field intensity regions. **b** Similar to **a**, except the particle has a higher concentration of charge carriers such that it is now more polarisable than the surrounding medium. As a result, the net dipole is such that either side of the particle experiences attractive forces towards the electrodes. Because there is a stronger force attracting it to the regions of high field intensity/blue electrode, it moves towards these regions.

2.2.3 Types of polarisation

It has been mentioned that by applying an electric field, a dielectric becomes polarised. Polarisation can be thought of as when the negative and positive charges in a dielectric are displaced in opposite directions. When the electric field is turned off, it takes a certain amount of time for the charges to revert back to their non-polarised state - this is known as the 'relaxation time', and is a measure of the mobility of charge carriers. The types of polarisation that can occur to various charge carriers in a dielectric are detailed below:

Electronic polarisation

Electronic polarisation occurs when the centre of charge of an electron cloud is skewed by an electric field, such that it is displaced with respect to the charge centre of the nucleus (see Figure 2.9. The relaxation time for electronic polarisation is on the order of 10^{-14} seconds.

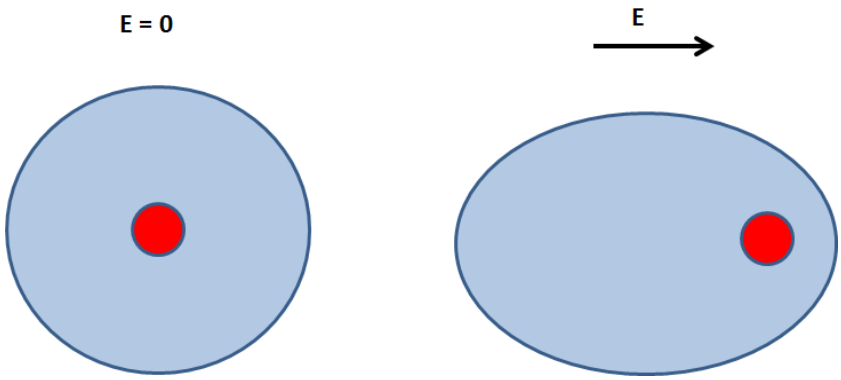

Figure 2.9: Schematic showing the movement of the centre of an electron cloud (simplified into a light blue circle) relative to the centre of charge of a nucleus (red), in response to an electric field.

Atomic polarisation

In ionic lattices (such as crystalline NaCl), the ions move in opposite directions in response to the electric field, as detailed in Figure 2.10. This is known as atomic

polarisation, and has a relaxation time of 10^{-12} s.

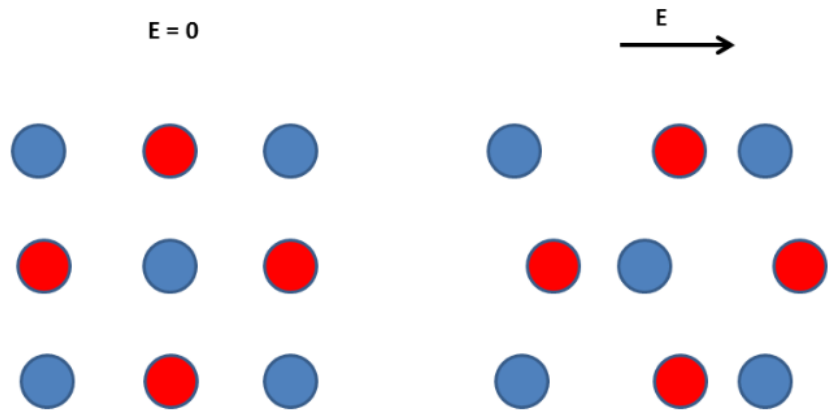

Figure 2.10: Schematic showing atomic polarisation. Oppositely-charged ions bound in a solid lattice move in different directions upon application of an electric field.

Orientational polarisation

Orientational polarisation occurs when molecules with a permanent molecular dipole (e.g. H_2O) switch from a random alignment in the absence of an electric field, to orienting themselves parallel to an applied field (see Figure 2.11). The relaxation time of this polarisation varies with temperature, and the size and structure of the molecule in question. At room temperature, water has a relaxation time of 2×10^{-10} s.

Interfacial polarisation

Interfacial polarisation happens at the interface between two dielectrics, for example, a latex bead (dielectric 1) suspended in water (dielectric 2). This is depicted in Figures 2.7 and 2.8. For particles like cells, the polarisation is caused by the migration of solubilised ions; in stronger insulators like latex beads, it is predominantly caused by migration of surface charges. In the case of interfacial polarisation, the relaxation time is much longer, on the order of 10^{-2} to 10^{-4} s.

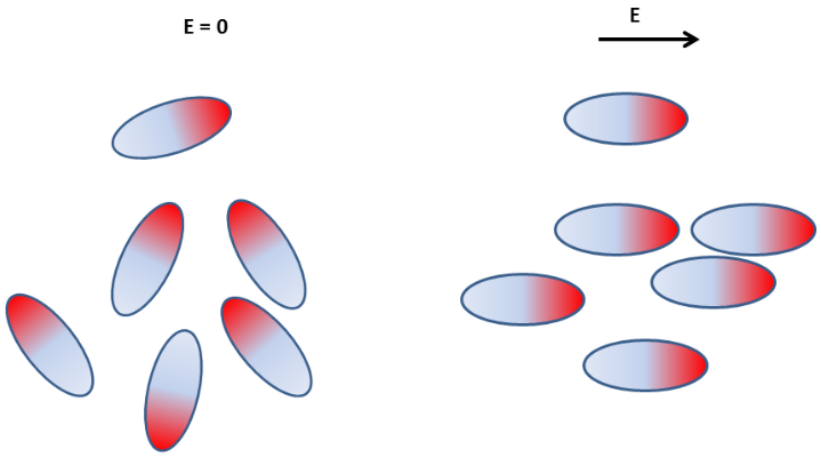

Figure 2.11: Schematic of orientational polarisation. Molecules with permanent molecular dipoles switch from a random to a unifom alignment, upon application of an electric field.

Relationship between frequency of an alternating electric field and the mechanisms of dielectric polarisation

When dealing with an alternating electric field, the mechanisms of polarisation vary with the frequency of the field, and this has a corresponding effect on the DEP response. It can be said that at low frequencies, the DEP force depends on the conductivity properties of the dielectrics, while at higher frequencies the values for permittivity are most important.

For example, imagine a latex bead suspended in de-ionised (low conductivity) water. At low frequencies (e.g. $< 10^4$ Hz), migration of surface charges on the latex beads makes it more polarisable than the water, and so the particle experiences positive DEP. At higher frequencies, however ($> 10^6$ Hz), the mobility of surface charges is too low to respond to the alternating field, and the particle permittivity dominates the dielectrophoretic response (for instance, by re-orientation of dipoles). For water, the relative permittivity is about 80, while for latex it is about 2.5 (115). Thus, at higher frequencies, the liquid is now more polarisable than the particle, and the latter experiences negative DEP.

2.2.4 Mathematical description of dielectrophoresis

Dielectrophoretic force

The dielectrophoretic force on a spherical particle is described by:

$$\vec{F}_{DEP} = 2\pi r^3 \epsilon_m Re[F_{CM}] \nabla E_{rms}^2 \tag{2.2.19}$$

where r is the particle radius, ϵ_m is the permittivity of the liquid, $Re[F_{CM}]$ is the real part of the Claussius-Mossotti factor (see below), E is the amplitude (root mean square) of the electric field, and ∇ represents the gradient operator. For this work, F_{CM} is important because it can be tuned by modulating the frequency of the field, and/or conductivity of the liquid, such that cell types have a distinct F_{CM} based on their dielectric signature.

Polarisability and complex permittivity

Polarisability is defined as the ability of a dielectric to become polarised in response to an electric field, in order to reduce the total electric field in the medium. Whether a particle experiences positive or negative dielectrophoresis depends on its relative polarisability with respect to the surrounding medium. This is determined using the Clausius-Mossotti (or CM) factor, F_{CM}:

$$F_{CM} = \frac{\epsilon_p^* - \epsilon_m^*}{\epsilon_p^* + 2\epsilon_m^*} \tag{2.2.20}$$

where ϵ^* refers to the complex permittivity, and $_p$, $_m$ denote the particle and medium, respectively. By analysing Equation 2.2.20, it is clear that when the permittivity of the particle is greater than that of the medium (it can also be

said that "the *polarisability* of the particle is greater than that of the medium"), $0 < F_{CM} \leq 1$ and the particle will experience positive dielectrophoresis. Conversely, when $\epsilon_p^* < \epsilon_m^*$, then $-0.5 \leq F_{CM} < 0$, and the particle will experience negative dielectrophoresis.

Dependence of permittivity on conductivity and frequency

For AC fields, permittivity shows a frequency-dependent response. It is expressed as a complex number because field-induced polarisation occurs *after* the application of the field, such that there is a phase lag. The complex permittivity ϵ^* is given by:

$$\epsilon^* = \epsilon + \frac{j\sigma}{\omega} \tag{2.2.21}$$

where σ refers to the conductivity, ω the angular frequency, j is $\sqrt{-1}$, and ϵ is the relative permittivity of the medium. It can be observed that at either high conductivity or low frequency, the imaginary component of the complex permittivity becomes dominant and *vice versa*. For example, when ω approaches 0 or infinity, F_{CM} becomes, respectively:

$$F_{CM} = \frac{\sigma_p - \sigma_m}{\sigma_p + 2\sigma_m}, for \quad \omega \to 0 \tag{2.2.22}$$

$$F_{CM} = \frac{\epsilon_p - \epsilon_m}{\epsilon_p + 2\epsilon_m}, for \quad \omega \to \infty \tag{2.2.23}$$

This indicates that at lower frequencies, the Claussius-Mossotti factor is dominated by the conductivity of the particle and medium. As we increase frequency, however, their respective permittivity begins to dominate.

2.2.5 Modelling F_{CM} for microparticles and cells

To calculate F_{CM}, ϵ_p must be calculated for the microparticles in question. Below is a description of how the particles used in this work were modelled:

Latex beads

Latex beads are strong insulators, therefore their conductive properties are dominated by their surface charge, K_s (157). The conductivity of these beads, σ_p is given by:

$$\sigma_p = \frac{2K_s}{r} \tag{2.2.24}$$

where r is the particle radius, and K_s is the particle surface conductivity, given by:

$$K_s = \frac{r}{4}(-\sigma_m + [9\sigma_m^2 - 4((\epsilon_p - \epsilon_m)(\epsilon_p + 2\epsilon_m)(2\pi f_0)^2)]^{\frac{1}{2}}) \tag{2.2.25}$$

in which f_0 is the bead crossover frequency.

Using Equations 2.2.25 and 2.2.24 to calculate the particle conductivity for Equation 2.2.20 can produce plots of the CM factor, F_{CM}. Figure 2.12 shows the CM factor for 1 µm latex beads as a function of frequency, in different liquid conductivities.

By first examining the plots for low liquid conductivity in Figure 2.12, (e.g. 0.1 mS/m, red line), it can be observed that latex beads experience positive DEP

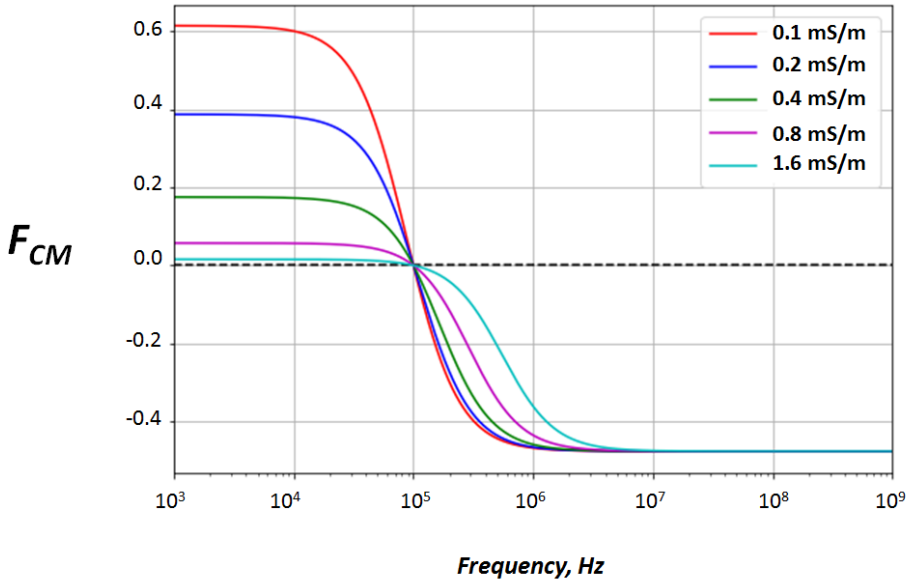

Figure 2.12: Plot of CM factor of 1 µm latex beads as a function of frequency. The different lines are for beads in different liquid conductivities, for 0.1 mS/m to 1.6 mS/m.

(due to a positive F_{CM} value) at lower frequencies of 1-100 KHz, but experience negative DEP at frequencies above 100 KHz. As discussed in Sections 2.2.3 and 2.2.4, this is because the polarisability at lower frequencies is largely determined by the mobile charge carriers of the latex beads (which are relatively polarisable compared to those of 0.1 mS/m water), while at higher frequencies it is dominated by their permittivity, which is far lower than that of water.

Figure 2.12 also shows that <10 MHz, increasing the conductivity of water from 0.1 mS/m to 1.6 mS/m produces a dramatically lower F_{CM} value. This is because the polarisability of water has increased through the addition of ions (which act as charge carriers), thus the polarisability of the latex beads is lower relative to the liquid.

Mammalian cells

Mammalian cells are roughly spherical and generally 10-30 μm in diameter; they consist of a lipid membrane ~ 8 nm thick surrounding the cytoplasm (115). The cytoplasm consists of an aqueous suspension of numerous organelles (the 'organs' or 'machinery' of the cell), which are in turn generally surrounded by their own lipid membrane. Figure 2.13 shows a labelled cross-section of a cell cytoplasm.

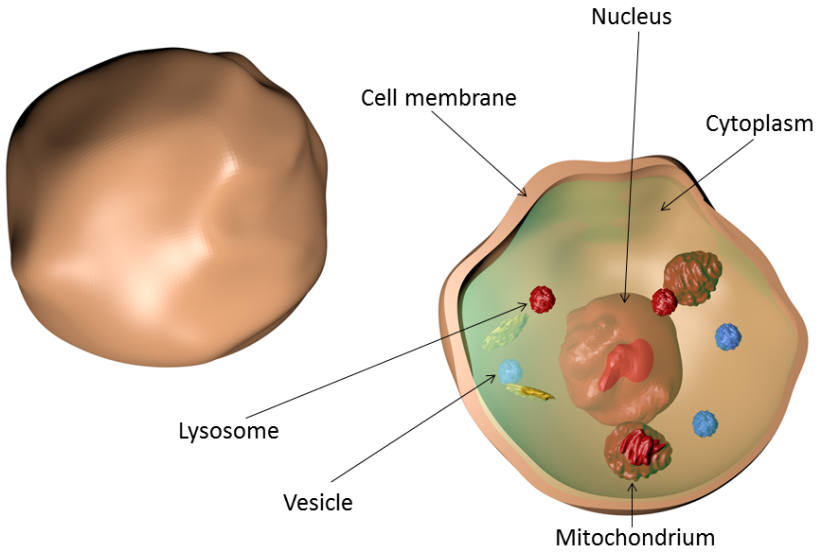

Figure 2.13: Schematic of a mammalian cell (left) and a cross section (right). A mammalian cell consists of a lipid membrane, surrounding a cytoplasm containing the nucleus and other smaller organelles, in an aqueous suspension.

When modelling the polarisability of mammalian cells, it is therefore much simpler to consider the dielectric properties (namely the permittivity and conductivity) of only the membrane and the cytoplasm, known as the "Single-Shell Model" (108). Strictly speaking, this does consider the organelles and other cytoplasmic contents, but all averaged as one entity. Furthermore the cell is modelled as a perfect sphere, as illustrated in Figure 2.14.

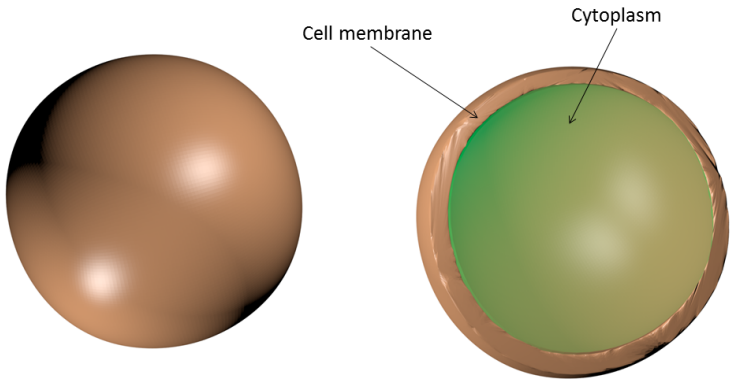

Figure 2.14: In the Single Shell Model, a mammalian cell is considered as a perfect sphere, constituting an insulating membrane and a conductive, aqueous cytoplasm.

Because of the insulating nature of the cell membrane, it is more accurate to measure the membrane capacitance (rather than the conductance), and use this to give the permittivity (108, 158). The complex permittivity of the cell, ϵ_c is given by:

$$\epsilon_c^* = \frac{C_{mem}^* \cdot r \cdot \epsilon_{cyt}^*}{C_{mem}^* \cdot r + \epsilon_{cyt}^*} \tag{2.2.26}$$

where C_{mem}^* is the complex membrane capacitance, r is the radius, and ϵ_{cyt}^* is the complex permittivity of the cytoplasm. C_{mem}^* is given by:

$$C_{mem}^* = C_{mem} + j\frac{G_{mem}}{\omega} \tag{2.2.27}$$

where C_{mem} is the membrane capacitance, j is $\sqrt{-1}$, G_{mem} is the membrane conductance, and ω is the angular frequency. G_{mem} is given by:

$$G_{mem} = \frac{\sigma_{mem}}{d} \tag{2.2.28}$$

where σ_{mem} is the membrane conductivity, and d is the membrane thickness.

For completeness, ϵ^*_{cyt} is given by:

$$\epsilon^*_{cyt} = \epsilon_{cyt} + j\frac{\sigma_{cyt}}{\omega} \tag{2.2.29}$$

where ϵ_{cyt} is the permittivity of the cytoplasm, σ_{cyt} is the cytoplasm conductivity, and ω is the angular frequency.

These equations enable the calculation for the F_{CM} of mammalian cells, while accounting for biophysical differences between cell types, as shown in Figure 2.15.

By first examaning the plot for 'normal' mammalian cells in Figure 2.15, it can be observed that, in 0.03 S/m conductivity liquid, the cells experience negative DEP up to 100 KHz and after 100 MHz, but positive DEP at the intermediate frequencies. This is because, firstly, at lower frequencies the DEP response of cells is dominated by the properties of the cell membrane, because the electric field does not penetrate into the cytoplasm at low frequencies (161), and the polarisability of the cell membrane is typically less than that of the surrounding liquid (at 0.03 S/m, for example). The F_{CM} becomes positive above 100 KHz

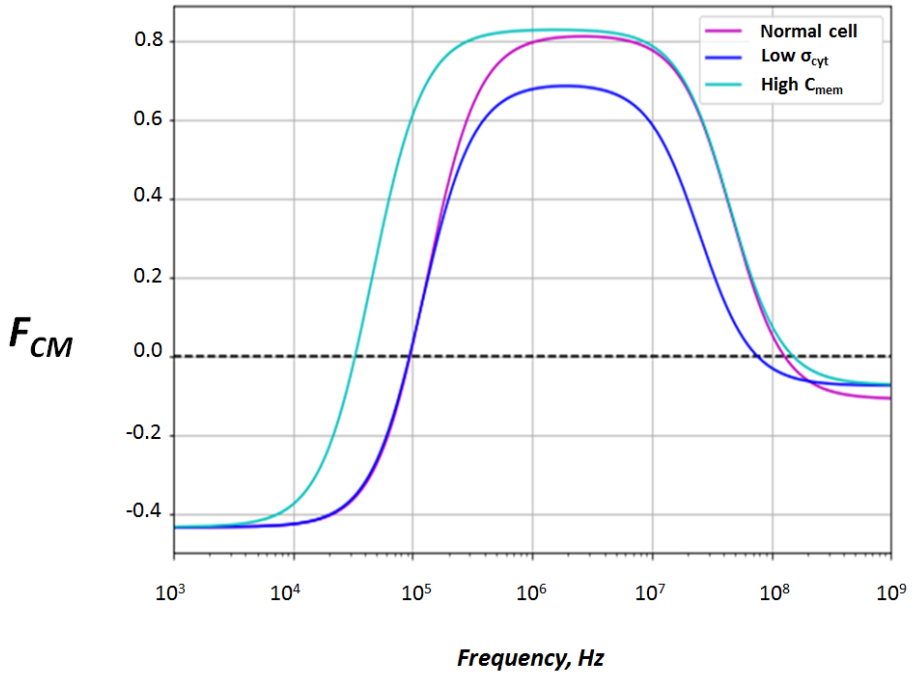

Figure 2.15: CM factor for mammalian cells as calculated with the single shell model, in a liquid conductivity of 0.03 S/m. The biophysical values for 'Normal cell' (magenta line) are derived from the reported values for erythrocytes (108), with a 'typical' cytoplasm conductivity of 0.5 S/m (159), and a typical cell radius of 15 µm. For 'Low σ_{cyt}' (i.e. low cytoplasm conductivity), this value was reduced to 0.25 S/m (e.g. reported values for breast cancer cells (160); for 'High C_{mem}' (i.e. high specific membrane capicitance), the specific membrane capacitance was increased from 9 mF/m^2 ('typical' value) to 26 mF/m^2 (e.g. reported value for another cell type in (108)). The graph shows a clear distinction in the DEP profile of cells with a high membrane capacitance at 10 -1,000 KHz. Conversely, the cells with low cytoplasm conductivity (blue line) are similar to 'normal' cells in this frequency range, but become more distinct at higher frequencies (above 1,000 KHz).

because the electric field can now penetrate into the cytoplasm, which is typically more conductive than the surrounding medium. Finally, as the frequency exceeds 10 MHz, the permittivity increasingly dominates the DEP response more so than the conductivity (discussed in Section 2.2.4), and the relatively high permittivity

of water makes the liquid more polarisable than the cell, such that above 100 MHz the cells get negative DEP.

Figure 2.15 also illustrates how differences in the cytoplasm conductivity or membrane capacitance of cells (blue and cyan lines, respectively), can alter the F_{CM} of cells at various frequencies. Just below 100 KHz, for example, it can be observed that 'normal' cells get negative DEP, while cells with high membrane capacitance get positive DEP. At this frequency (and 0.03 S/m liquid conductivity), therefore, the two cell types could be separated on a DEP device. Similarly, it can be seen that at 100 MHz 'normal' cells would get positive DEP, while cells of lower cytoplasm conductivity would get negative DEP.

The equations described in this section can also be used to plot the F_{CM} of cells as a function of liquid conductivity. This is shown in Figure 2.16.

Figure 2.16 shows that as liquid conductivity increases, the F_{CM} of the cell decreases, as it becomes less polarisable with respect to the liquid. Furthermore, cells with a low cytoplasm conductivity (blue line) always have a lower F_{CM} than normal cells (magenta line). Between 0.23 S/m and 0.50 S/m (light blue shading), normal cells will get positive DEP while cells with low cytoplasm conductivity will get negative DEP, meaning that they can be separated in a DEP device.

Yeast cells

Yeast cells differ to mammalian cells in that they have an additional cell wall that surrounds the cytoplasm and membrane. To describe the dielectrophoretic behaviour of yeast cells, a Dual Shell Model is often used (103). This considers the nucleus, cell membrane and cell wall as separate entities. In this model, the complex permittivity of the cell, ϵ_c^*, is given by:

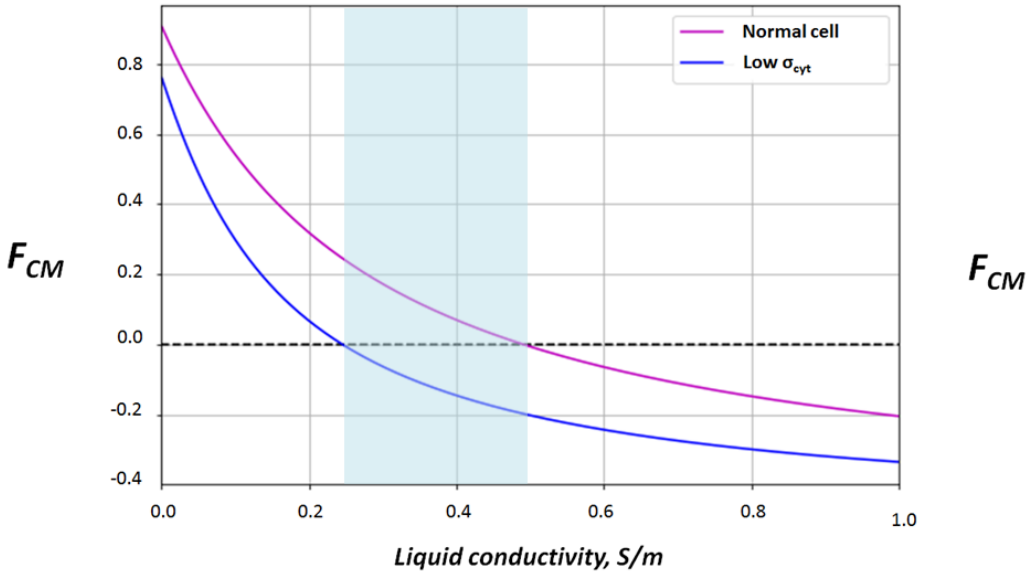

Figure 2.16: F_{CM} for mammalian cells using the same values described in Figure 2.15, but plotted as a function of liquid conductivity at 10 MHz frequency. The plot shows that, at 10 MHz, increasing liquid conductivity leads to a lower F_{CM} of cells, as the polarisability of the cell decreases relative to the liquid. Cells with a lower cytoplasm conductivity (blue line, 0.25 S/m) are always less polarisable than 'Normal cells' (magenta line, 0.5 S/m).

$$\epsilon_c^* = \epsilon_1^* \frac{\left(\frac{r_1}{r_2}\right)^3 + 2\left(\frac{\epsilon_{23}^* - \epsilon_1^*}{\epsilon_{23}^* + 2\epsilon_1^*}\right)}{\left(\frac{r_1}{r_2}\right)^3 - \left(\frac{\epsilon_{23}^* - \epsilon_1^*}{\epsilon_{23}^* + 2\epsilon_1^*}\right)} \tag{2.2.30}$$

and:

$$\epsilon_{23}^* = \epsilon_2^* \frac{\left(\frac{r_2}{r_3}\right)^3 + 2\left(\frac{\epsilon_3^* - \epsilon_2^*}{\epsilon_3^* + 2\epsilon_2^*}\right)}{\left(\frac{r_1}{r_2}\right)^3 - \left(\frac{\epsilon_3^* - \epsilon_2^*}{\epsilon_3^* + 2\epsilon_2^*}\right)}, \tag{2.2.31}$$

where $\epsilon^*_{1,2,3}$ are the complex permittivities of the cell wall, cytoplasm and nucleus, respectively. ϵ^*_{23} is the average complex permittivity of the cell wall + nucleus. In this case, complex permittivity ϵ^* is given by the more generic formula, as in Equation 2.2.21.

These equations for yeast produces plots of F_{CM} similar to those shown for mammalian cells. Using biophysical values derived by Patel *et al.* (2012) (162), the F_{CM} as a function of conductivity of live and dead yeast cells (at 10 MHz) is plotted in Figure 2.17. The figure shows that at 10 MHz, dead yeast cells always get negative DEP (due principally to their low cytoplasm conductivity), while live cells get positive DEP between 0 and 0.125 S/m liquid conductivity.

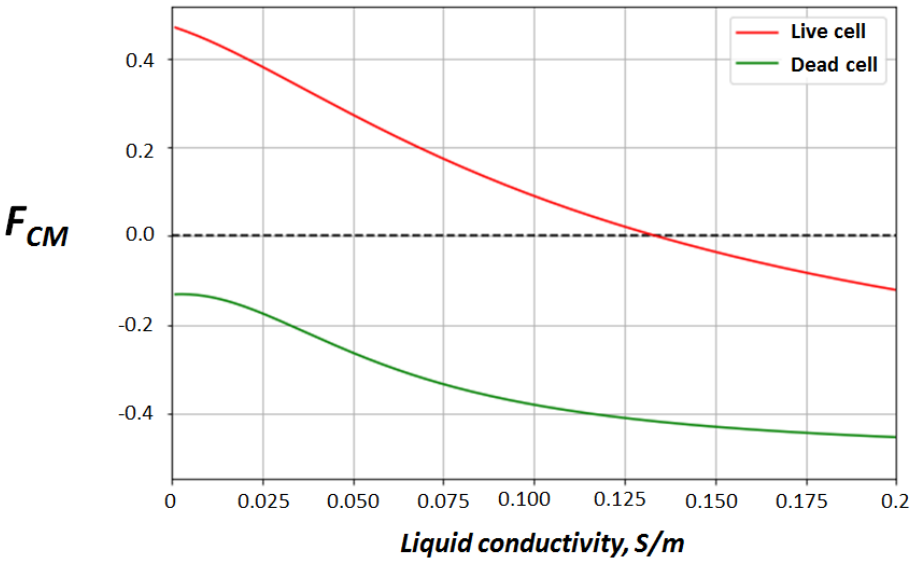

Figure 2.17: F_{CM} for live and dead yeast cells as a function of liquid conductivity (at 10 MHz). Dead yeast cells (green line) always get negative DEP at 10 MHz, while live cells get positive DEP from 0 to 0.125 S/m liquid conductivity.

Chapter 3

Methods

This methods chapter will introduce the reader to all the major investigative techniques used in this work, as well as providing step by step instructions to repeat any of the experimental results discussed in the further chapters. It will begin with a description of the fabrication methods used to make SAW devices and fluidic flow cells, before describing the investigative protocols in the order in which they appear in the subsequent experimental chapters.

3.1 Fabrication

This section will discuss the fabrication of surface acoustic wave (SAW) devices, the microfluidic component and the surrounding flow cells, as well as the electrical and fluidic connections required for device operation.

3.1.1 Surface acoustic wave device fabrication

To summarise, SAW devices (Figure 3.1) were fabricated by standard cleanroom photolithography methods. The general procedure is as follows: Firstly, a mask of the microelectrode design is drawn up on CAD software and sent off to be made by a manufacturer. Upon receiving the mask, it is used as a stencil to pattern gold electrodes onto a substrate ($LiTaO_3$ in this case). Patterning is done in a

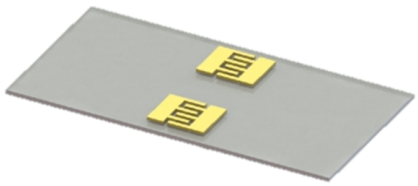

Figure 3.1: Schematic of a typical surface acoustic wave (SAW) device chip, consisting of Au interdigitated transducers (IDTs) (gold colour) patterned on top a $LiTaO_3$ substrate (grey).

cleanroom, that is, a specialist electronics fabrication laboratory where the air is kept free of particulates.[1] The main reasons for this is that in semiconductor manufacturing, if the substrate is dirty before electrodes are deposited (typically Au), adherence and subsequent electrical connections are poor.

Designs

Background to the design consideration of SAW devices can be found in Section 2.1.2. The designs for 20 MHz and 10 MHz devices used in this work are shown in Figure 3.2. A 1:1 mark to space ratio was used. Recalling that the speed of sound in the $LiTaO_3$ substrate is 4,022 m/s, the 20 MHz device finger pitch was set to 50 µm (giving an anticipated resonant frequency of 20.11 MHz), and the 10 MHz device to 100 µm finger pitch (anticipated 10.055 MHz resonant frequency).

In general, the more finger pairs a device has, the greater the amplification. The number of finger pairs was set to 15; this was because, considering the 10 MHz device, more finger pairs would have required a larger chip to fit the transducers on, which proves costly. The aperture (for acoustic manipulation) was set to 1 mm - this was chosen as a good dimension to image cells under 5X and 10X

[1] An ISO 5 cleanroom was used in this work, meaning that a maximum of 3,520 >0.5 µm particles may be found per 1 m^3 (a typical urban environment contains around 35,200,000 particulates per 1 m^3). A full description of the maximum number of various particle sizes permitted in different cleanroom classes (ISO 1, 2, etc) can be found in the literature (163).

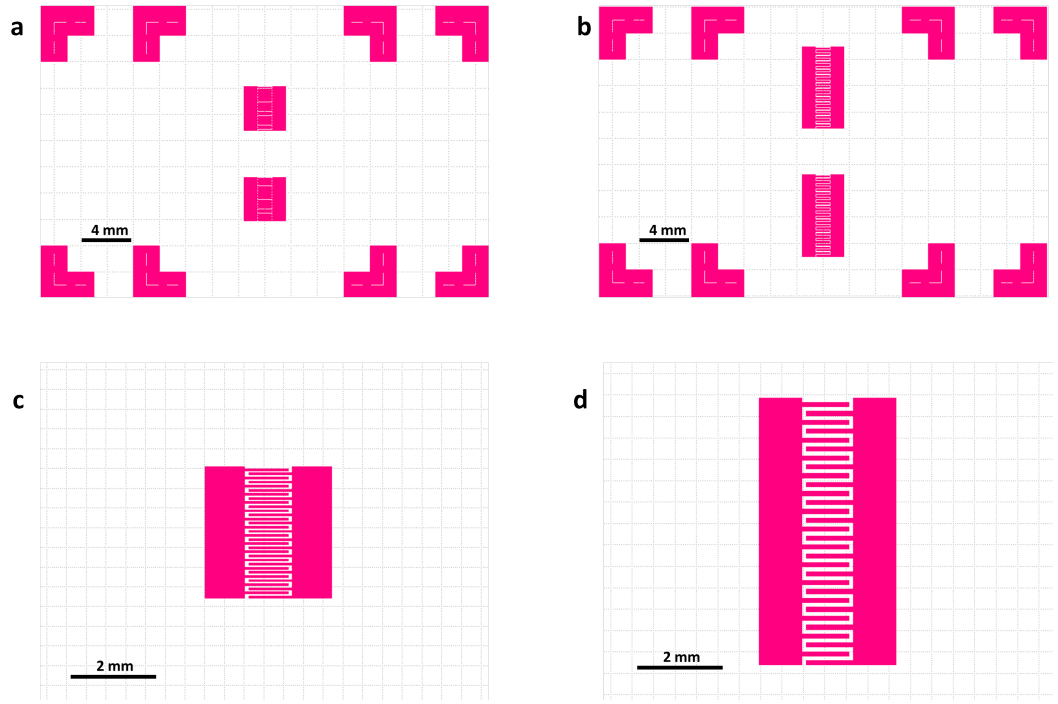

Figure 3.2: Schematic showing the mask design for the SAW devices used in this work. Note that the masks were darkfield/negatives - that is, the background of the mask was opaque, and the detail (of IDTs, etc) was transparent (380-780 nm) to allow UV through. **a** and **b** show the overall chip layouts for 20 and 10 MHz, respectively. IDTs can be seen in the centre, and alignment marks around the outside for two different chip sizes). **c** and **d** show 20 MHz and 10 MHz (respectfully) IDT designs, zoomed in.

microscope objectives. The gap between electrode pairs was 3 mm - this was to allow a 1 mm channel flanked by 1 mm of PDMS either side to prevent fluid contact with the electrodes.

Finally, electrodes were flanked by 1 mm-wide bond pads to allow straightforward electrical contacts via wire-bonding or pogo-pins.

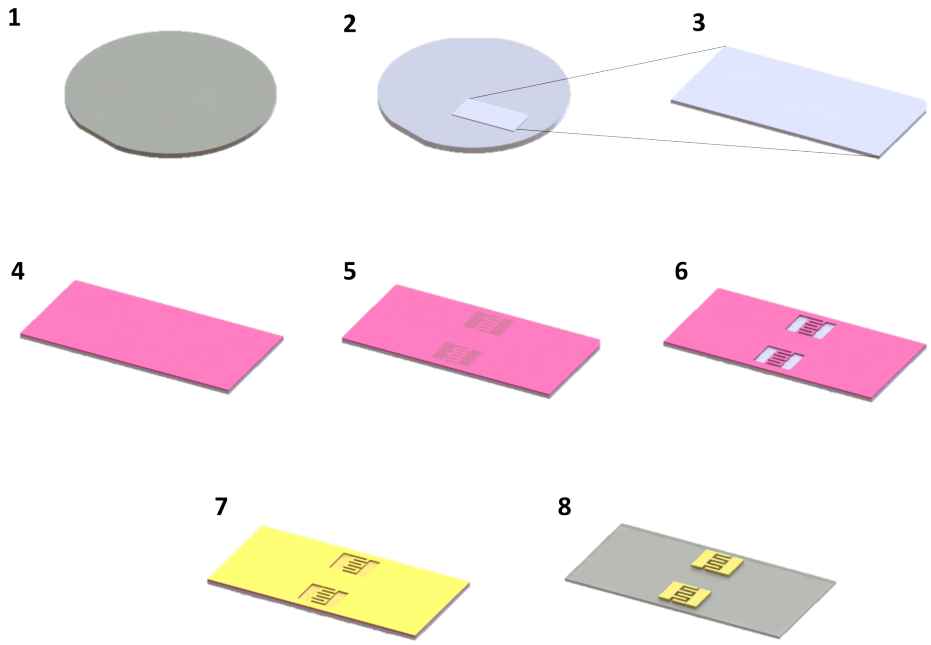

Figure 3.3: Schematic showing the steps involved in SAW device fabrication on $LiTaO_3$. (1) Wafer (2) Al deposition (3) Dicing the wafer into chips (4) Adding a photoresist layer (5) Exposing the photoresist through a mask to define the pattern (6) Developing the resist (7) Au deposition (8) Lift off.

Fabrication protocol: $LiTaO_3$

A fabrication protocol was developed just prior to this project by Richard O'Rorke and Mark Rosamond. Figure 3.3 is a schematic showing the sequence of fabrication steps. Cleanroom processing of $LiTaO_3$ is made tricky by its pyroelectric properties - that is, heating it up during processing steps generates an electrical potential difference across the chip, which can lead to shattering (and painfully discharging onto the researcher, as was discovered!).

To address this, the first step in processing was to deposit a 200 nm sacrificial layer of Al over the wafer (1 and 2), to dissipate charge across the chip. This is achieved by electrode beam evaporation - the wafer is put into a vacuum chamber

with a crucible containing Al; an electron beam is steered into the crucible such that the Al vapourises, coating the the wafer in an even layer. Following this, the wafer is diced into chips by a wafer saw (3).

Overview

The process of photolithography begins by spreading a 1 µm layer of positive photoresist via a vacuum chuck spinner (4) and exposing the resist to UV light through the mask (5). The mask allows the UV light to expose certain regions of the resist to define the electrode pattern. A solvent developer removes the exposed regions of the photoresist (6). The exposed Al is then removed via an etch solution and etched a little more to produce an undercut (for more efficient subsequent deposition of Au) (also 6). The removal of selected regions of the photoresist and Al layers means that part of the underlying substrate (the $LiTaO_3$ chip) is exposed, in the pattern of the prospective electrodes. A layer of gold (80 nm) is deposited onto the chips by electron beam evaporation (8), and the remaining resist and Al (along with the unwanted overlying Au) can then be removed (8) with a 'lift off' solvent.

Detailed description

Full details of the procedure are as follows: (Note that the frequent steps of sonicating in acetone and isopropanol, and plasma-ashing, are all too ensure the substrate is kept clean.)

1. (Photomasks (darkfield) for interdigitated transducers were designed on L-edit software, and ordered from JD Phototools, UK, as 4 x 4" Soda Lime "Super High Resolution".) $LiTa_O3$ 3" wafers, Y-axis 42° rotated, were purchased from PM Optics, MA.

2. Wafers were cleaned by sonicating at 50% power in acetone followed by isopropanol, for ten minutes each, after which they were O_2 plasma-ashed

at 50W for ten minutes. A 200 nm layer of aluminium (Al) was deposited by electron beam evaporation at < 2 x 10^{-6} mbar.

3. Before dicing up the wafer into chips, a protective layer of S1813 was spun on at 3,000 rpm, then soft baked by ramping the temperature on a hot plate, from room temperature to 115°C at 5°C per minute. It was then cleaved into 18 x 20 mm chips (for Flow Cell Design 1: Perspex Lid) or 36 x 20 mm chips (for Flow Cell Design 2: 3D-printed) (20 mm being the axis perpendicular to SAW propagation) with a Microace 66 Wafer Saw.

4. Chips were cleaned by sonicating in acetone followed by isopropanol at 50% power for ten minutes each time, then blow dried under N_2. Microposit-S1813 positive photoresist (Shipley, MA) was spun on at 5,000 rpm for 30 seconds, and soft baked by ramping the temperature to 115°C.

5. Chips were aligned and brought into contact with the mask, and UV-exposed at ~ 30 mW/cm^2 for 2 s.

6. MF-319 was used to develop away the UV-exposed resist for 30-60 s, before they were rinsed under a jet of DI water, then dried under N_2. The Al under the exposed photoresist was now exposed, and this was etched away with a solution of 85% phosphoric acid, DI water, 70% nitric acid, and 100% acetic acid at a ratio of 50:10:2:2. This took ~ 3 minutes to etch down 200 nm to the $LiTa0_3$ substrate, and the chips were then left for a further 3 minutes to develop an undercut.

7. Chips were plasma-ashed at 50 W for 40 s, before being deposited with 20 nm titanium and 80 nm gold in an electron beam evaporator at < 2 x 10^{-6} mbar.

8. To lift off, the S1813 was stripped by leaving the chips in acetone for 15 minutes, and then the Al was stripped by leaving them in the etch solution described above for ~ 3 minutes, after which they were rinsed with DI water and dried by N_2. Chips were stored by coating in S1813 and leaving in a cleanroom storage box.

Fabrication protocol: Black $LiTaO_3$

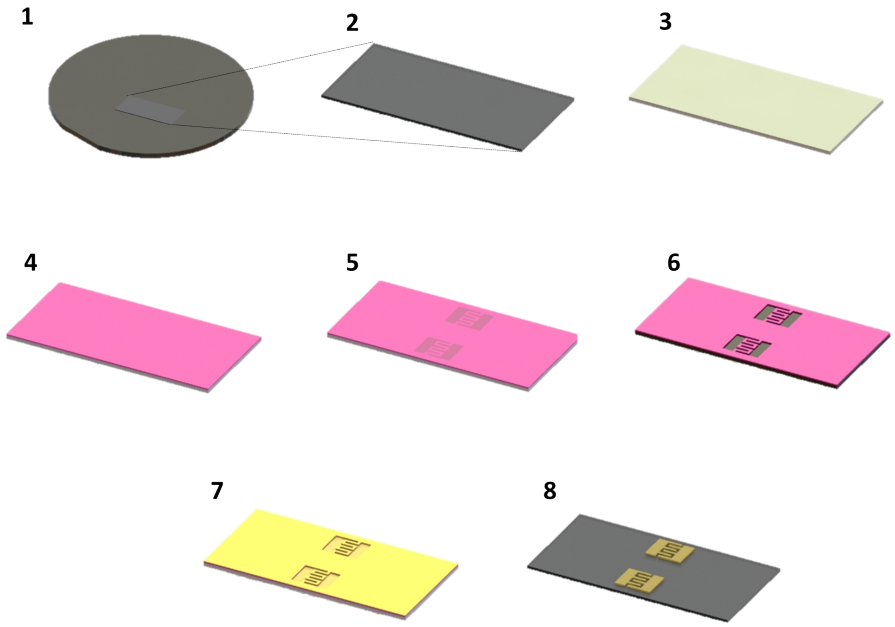

Figure 3.4: Schematic showing the steps involved in SAW device fabrication on Black $LiTaO_3$. (1) Wafer (2) Dicing the wafer into chips (3) Adding a resist underlayer (4) Adding a positive photoresist top layer (5) Exposing the photoresist to UV light through a mask (6) Developing the photoresist and underlayer, to expose the Black $LiTaO_3$ substrate (7) Au deposition (8) Lift off.

Some devices were made when Black $LiTaO_3$, when it became available from a supplier - Black $LiTaO_3$ has been doped to minimise pyroelectric discharge,

which allows higher temperatures to be used in the fabrication process. A more typical photolithographic fabrication protocol was used (see Figure 3.4: Wafers (1) were diced up (2) and coated with a resist underlayer (3). As before, a positive photoresist is then added (4) and this is exposed to UV light through a mask (5). The top and bottom resist layers are then developed, exposing the substrate (Black $LiTaO_3$) (6) for subsequent deposition of Au (7). Finally, the resist layers and overlying gold are lifted off by a solvent (8).

1. Black $LiTa_O3$ 4" wafers, Y-axis 42° rotated, were purchased from PM Optics, MA.

2. These was diced into chips by wafer SAW, as with normal $LiTaO_3$.

3. Chips were cleaned in piranha solution (7:3 concentrated H_2SO_4: 35% H_2O_2 solutions) for 10 minutes, following which they O_2-ashed for at 50W for 5 minutes, and dehydration-baked on a hot plate at 185 °C (after ramping the temperature up from 50 °C for a total of 3 minutes). LOR resist (Shipley, MA) was spun on at 4,000 rpm for 45 s and baked at 185 °C for 3 minutes, using the ramping method described previously.

4. After cooling the chips for 3 minutes, S1813 photoresist was spun on at 4,500 rpm for 45 s and baked at 115 °C for 3 minutes, ramping the temperature up from 50 °C for 1 minute.

5. Chips were aligned and brought into contact with the mask, and UV-exposed at ~ 30 mW/cm^2 for 2 s.

6. Following this they were developed in MF-319 for 60-70 s - typically the first 45 s develops the S1813, and the rest develops the LOR and produces an undercut. The chips were then rinsed in DI water and dried with N_2.

7. Chips were plasma-ashed at 50 W for 40 s, before being deposited with 20 nm titanium and 80 nm gold in an electron beam evaporator at < 2 x 10^{-6} mbar.

8. Metal lift-off was carried out using 1165 developer, heated to 80 °C, following which chips were rinsed in isopropanol and dried under N_2, and stored as mentioned previously.

Fabrication protocol: Non-SAW DEP device

For control DEP experiments, discussed briefly in Chapter 4.2.1, a non-SAW DEP device was made by fabricating Au IDT electrodes onto a glass substrate (these electrodes could thus be used for DEP without any SAW effect). The protocol for these was the same as for the Black $LiTaO_3$ described above (using the 20 MHz IDT design), with two differences: (1) The substrate used was a glass microscope slide, scribed to 20 x 20 mm with a diamond-tipped scribe and a ruler; (2) Ramping the temperature was not necessary - e.g. after spinning on LOR resist, chips were put straight onto a 185 °C hotplate for 3 minutes.

Matching networks

After fabrication, SAW devices were characterised in a Network Analyzer (Agilent, CA), using a Perspex Lid flow cell (Section 3.7) for electrical contacts. A sample transmission parameter (S21), showing characteristic SAW peaks around 10 MHz is shown in Figure 3.5. The S-parameters were used to design matching networks in AWR Environment software. Matching networks were made by soldering SMD components (from Farnell, UK) onto a copper co-planar waveguide. These constituted a 1.8 μH series inductor, and a 20-120 pF parallel variable capacitor (aiming for 113 pF). This was shown to improve the insertion loss at 10 MHz from about - 30 dBm (unmatched) to about - 20 dBm (matched).

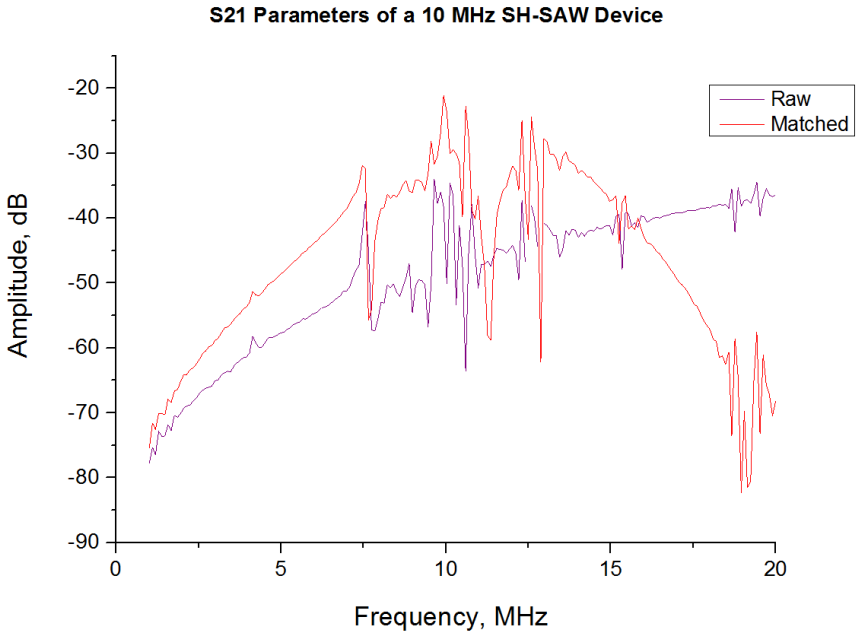

Figure 3.5: S21 transmission parameters of a 10 MHz device, showing how much power is transmitted between the device ports (i.e. the two sets of IDTs) from 1 MHz to 20 MHz. The two lines show a device without matching networks (purple line) and a device with matching networks (red line).

3.1.2 Cover slip prototype device

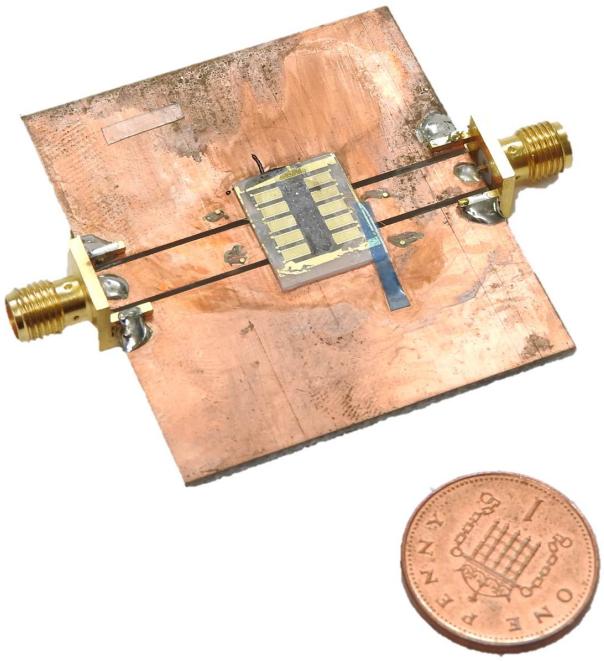

Figure 3.6: Photograph of the device used for early experiments - a 2 ul drop of particle solution (e.g. latex beads) would be put between the transducers - a thin strip of cover slip (typically 3 x 3 mm) would be laid on top of the droplet to confine it to the surface (and therefore the electric field). NB the design of the SAW chip in the photograph is slightly different to that used in this work.

Overview

Figure 3.6 shows the earliest device used to demonstrate Remote DEP. A SAW chip is glued onto a copper-surface coplanar waveguide, and connections are made by wire bonding the IDTs to the appropriate ground or conducting planes. For experiments, a 2 µl droplet of latex bead solution was put in between transducers, and confined to the surface by overlaying the droplet with a small strip of glass cover slip (typically 4 x 10 mm).[1] The movement of particles in response to the

[1] A note on the channel height: Supposing that 2 µl spreads out perfectly evenly under a 4 x 10 mm coverslip and does not flow out, the channel height would be 50 µm (4 mm x 10

SAW-DEP field could then be imaged by an upright microscope.
The precise steps to mounting the chip in this way are as follows:

Waveguides

Waveguides were made by chopping Cu-epoxy PCB into 4 x 4 cm squares in a workshop guillotine. Coplanar strips (the two etched lines visible in Figure 3.6) were etched by coating PCBs in S1813 (5,000 rpm 30 s), soft-baking at 115 °C for 2 minutes, exposing through a home-made acetate mask (made using an office printer) at ~ 30 mW/cm^2 for 2 s, and developed in MF319 for 30 s. Finally, the exposed copper was etched away using Cu-etch solution.

Gluing the bond pads and chip

Four Au bond pads were glued to the PCB (ground and conducting plane, either side of where the chip sits) using Ag-loaded epoxy (RS, UK). Devices were glued into the middle of the waveguide with black wax - the black wax is left in the middle of the waveguide, and melted at 100 °C on a hotplate, after which the SAW chip can be pushed on top and taken off the heat to set.

Electrical connections

The Au bond pads were wire bonded to the corresponding IDTs. To minimise the chance of pyroelectric discharge, the wire bonder is set to room temperature (the risk of discharge is increased by the wire bonder exerting force onto the chip, therefore generating piezoelectric current). Finally, SMA connectors were soldered on to the edges of the waveguide.

mm x 50 µm = 2 mm^3/µl volume). This is, however, a rough approximation (experimental observations indicated the height in this 'channel' was probably <50 µm).

3.1.3 Flow Cell Design 1: Perspex Lid

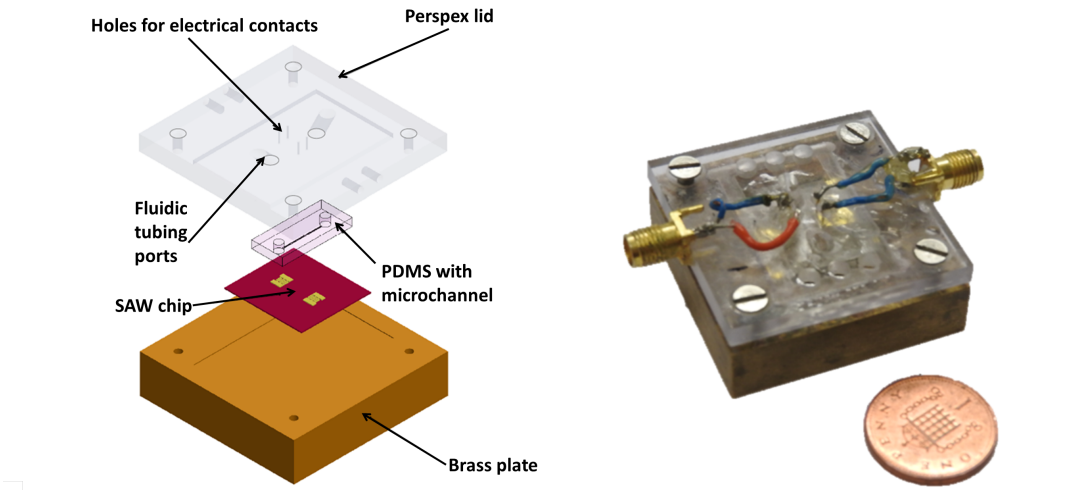

Figure 3.7: Labelled schematic of 'Perspex Lid' flow cell design (left), and a photograph of the device (right).

Overview

Figure 3.7 shows the first flow cell design. It consisted of a PDMS microchannel that was temporarily sealed to the chip by pressing it down via a Perspex 'lid'. The Perspex lid was screwed down into a brass base, chosen for sturdiness and reflectivity for imaging.

The lid had holes above the PDMS channel inlet and outlets, where silicone tubing ($\frac{1}{8}''$ OD) could be pushed into. The tubing was connected to a 1 ml syringe which could be filled with beads or yeast cells for delivery onto the chip; the transparency of Perspex allowed for imaging of particle behaviour on the chip surface.

This device had the advantage over the earlier coverslip device because the liquid was properly confined from the electrodes by the PDMS microchannel, meaning that higher fluid conductivities could be used without shorting the electrodes.

The main drawback was Perspex did not provide a good fluidic seal to tubing that was pushed into it, so it was difficult to get a steady flow rate and therefore do investigations into throughput of particles.

Detailed procedure:

PDMS microchannel fabrication

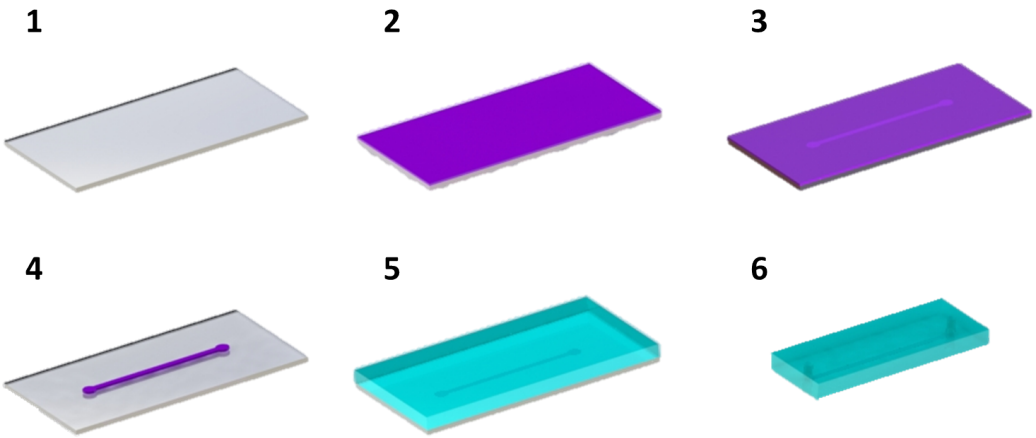

Figure 3.8: Process of fabricating PDMS microchannels. A substrate (typically a glass microscope slide) (1) is covered with a negative polymer resist (2) which is exposed through a photomask (3) and developed to leave the channel defined in the exposed resist (4), which can now be used as a mould. Liquid PDMS is poured onto the mould and cured to solidify (5). After this, the PDMS is peeled off, cut to fit the chip, and hole-punched for fluidic contacts (6).

PDMS for microfluidics

Polymethoxysilane (PDMS) is a rubbery polymer which is one of the most common materials used for microfluidics, along with glass (SiO_2). Both substances are transparent, allowing imaging of the microchannel; PDMS microfluidics has the advantage of being easier to fabricate because it can be patterned without the need for dangerous hydrofluoric acid (HF)-etching.

SU8, a polymer negative photoresist, should also be mentioned as a possible candidate material for constructing microfluidics. SU8 can be patterned onto a chip using photolithography, at a range of heights suitable for microfluidics (e.g. from 1 to 200 µm). The channel is then sealed by wafer-bonding another chip on top, for example, a glass coverslip for transparency. This final processing step is quite unsuitable for piezoelectric materials, because the bonding process involves both heat and high mechanical pressure, leading to charge generation and shattering of the piezoelectric substrate.

Because of its soft, rubbery nature, PDMS can be sealed reversibly to the substrate by applying gentle pressure. This was used to seal this flow cell design by screwing a Perspex lid on top of the PDMS channel while it was laid over the substrate. A stronger fluidic seal can be achieved, however, by irreversibly bonding the PDMS to the substrate, typically by plasma bonding, a process used for the second flow cell design, described in Section 3.1.4.

Process overview

The process of fabrication (summarised in Figure 3.8) involves using cleanroom photolithography to pattern a polymer resist with a photomask that defines the channel geometry in x and y dimensions (the channel height, z, is defined by the resist thickness). Instead of depositing metal at this stage, the chip with patterned resist is used as a negative to pour liquid PDMS onto and cure. The PDMS can then be peeled off and cut to fit the SAW chip. Holes for tubing can be made with a leather punch.

Adaptions to process - avoiding T-topping

When exposing a thick, negative resist like SU8-50, it is desirable to expose it from the back to avoid T-topping. T-topping occurs when high energy photons of ~ 250 nm wavelength react particularly strongly with the first few nm of resist layer. This generates acid, which spreads to the upper regions of non-exposed resist regions, and results in unexposed regions in the upper resist becoming cross-linked. By exposing from the back, the excess cross-linking occurs only in the lower layers, which does not significantly deform the subsequent microfluidic channel.

To expose from the back, the mask was directly patterned onto glass slides in chrome (i.e. before Step 1 of Figure 3.8). Thus for the exposure step (Step 3), the substrate was flipped upside down in the mask aligner, and the chrome pattern ensured that the resist was selectively exposed.

The whole procedure in detailed is given below:

Patterning the glass slides in chrome

1. Photomasks (brightfield) for were designed in L-edit software. The designs used in this work are shown in Figure 3.9. These were made into a 4 x 4″ Soda Lime mask ("Super High Resolution", from JD Phototools, UK).

2. Half microscope slides were cleaned by sonicating the slides in acetone, then isopropanol, at 50% power for 5 minutes, drying under N_2, then UVO for five minutes, followed by a dehydration bake (5 minutes on a 175° hotplate).

3. After cooling, S1813 was spun on at 3,000 rpm for 40 s, and soft baked at 110°C for three minutes.

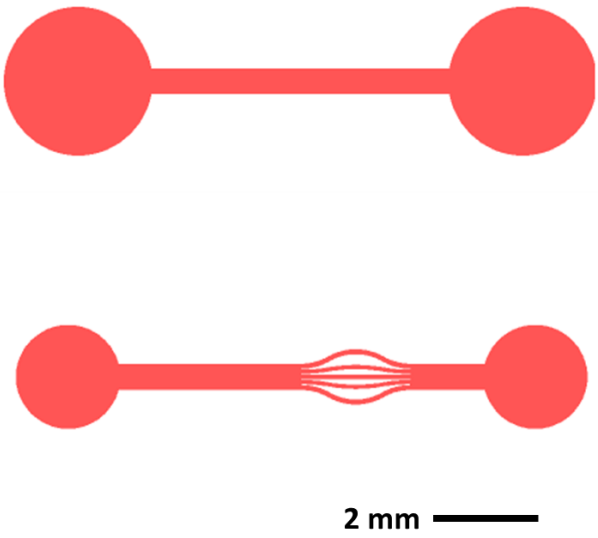

Figure 3.9: Mask design for the two microfluidic channels used with Perspex Lid flow cell. The upper design is for a simple straight channel, which was used to observed and photograph DEP behaviour of particles in the SAW-DEP aperture. The lower design branches off into five separate sub-channels in the middle of the channel (i.e. within the SAW-DEP aperture), and was used to demonstrate how different cell types (namely live and dead yeast cells) could be directed into different subchannels during SAW-DEP separation.

4. Slides were put in contact with the mask and UV-exposed at ~ 30 mW/cm^2 for 2 s.

5. After this, they were soaked chlorobenzene for five minutes (to harden the upper layer of resist to the developer, so as to produce an undercut), and rinsed with isopropanol.

6. The resist was developed in MF-319 for 60-90 s, rinsed in DI water and dried under N_2.

7. The slides were then cleaned by plasma-ashing at 50 W for 40 s, before being deposited with 70 nm of chrome by electron beam evaporation at < 2×10^{-6} mbar.

8. To lift off, slides were left in acetone for 15 minutes, then rinsed in isopropanol and dried. This produced the reverse of the mask (now darkfield) on the glass slides, such that the moulds could be produced by spinning a negative resist and exposing from the back.

SU8 mould fabrication

1. Chrome-plated slides were now cleaned by soaking in piranha solution (100 % H_2SO_4 and 35% H_2O_2 at a 7:3 ratio) for 30 minutes, followed by UVO for five minutes, and then a dehydration bake (ten minutes on a hotplate at 175°C).

2. The substrate was left to cool, before spinning on SU8-50 (500 rpm for 10 seconds, then 2,000 rpm for 40 seconds) to produce a 50 μm thick layer. The resist was soft baked on a hotplate for 65°C for five minutes then 95°C for fifteen minutes.

3. Slides were then UV-exposed from the back, at ~ 30 mW/cm^2 for 8 s. They were post-exposure baked at 65°C for 1 minute and 95°C for 4 minutes.

4. The resist was then developed in EC solvent (6-8 minutes) or SU8 developer (4-6 minutes), normally with two baths (a 'dirty' bath and a 'clean' bath).

5. To define the outer dimensions of the PDMS, gaskets were cut out of 2 mm Perspex in a laser cutter. This is to ensure that the dimensions of the cured PDMS block are 12 x 18 x 2 mm. These were stuck onto the glass slides (around the SU8 mould) with double-sided sticky tape.

Casting PDMS
PDMS was mixed at a 10:1 ratio of elastomer:cross-linker, and degassed at ~ 5 mBar for 30 minutes, poured into the gaskets, and degassed for a further 15 minutes before being cured by baking on a hotplate at 70°C for 1 hour. The PDMS, with microfluidic channels, could now be removed from the mould with a scalpel. Finally, the fluid entry/exit holes were made with a 1.5 mm diameter leather punch.

Flow cell assembly

Perspex lid and brass plate
The lid and brass plate was designed on SolidWorks 3D CAD software (Dassault Systémes, France) and machined by Brian Gibbs (Physics and Astronomy Workshop, University of Leeds, UK).

Fluidic connections
Silicone tubing (1/8 ″ OD, 1/16″ ID) was purchased from Cole-Palmer, IL, as were plastic hose-barb to luer connectors. The luer connector attaches to a syringes (generally 1 ml), which allows solutions to be infused into the microfluidics.

Electrical contacts
To provide electrical contacts to the SAW transducers, spring contacts (purchased from Signalin, MA) measuring 7 mm long and 0.3 mm diameter were fitted into specific holes in the Perspex lid. These were soldered to copper wire, which were in turn soldered to SMA connectors that were glued onto the sides of the lid.

3.1.4 Flow Cell Design 2: 3D-Printed

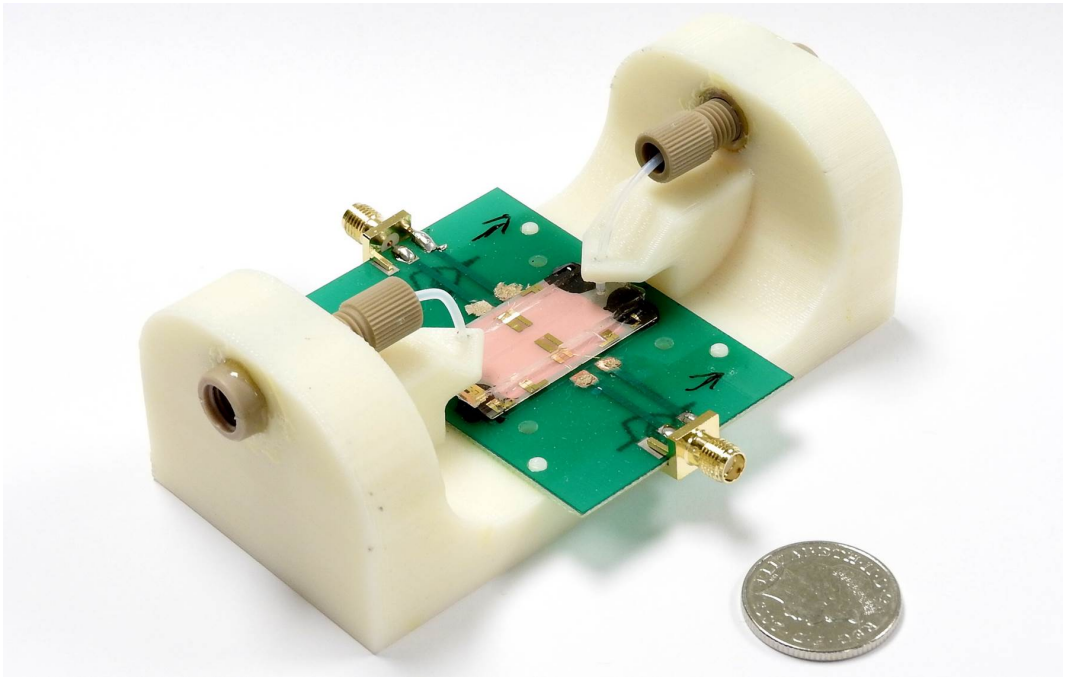

Figure 3.10: Photograph of a 3D-printed flow cell holding a SAW-DEP device. This consisted of an ABS-plastic flow cell (ivory colour) with glued-in fluidic connections (brown). Tubing was directed into a PDMS microchannel (transparent) plasma bonded onto the SAW chip (with pink underlay). Electrical contacts were made by wire-bonding the SAW chip to a PCB (green).

While the 'Perspex Lid' design was efficient at keeping fluid/particle suspensions away from the electrical transducers, it was inadequate for both retrieval of cells and maintaining a steady flow rate. This is mainly because of the poor fluidic seal between the tubing and the Perspex lid. When the design was adapted so tubing could be pushed directly into the PDMS (at a 45°-angle), it produced a torque on the underlying PDMS such that the microchannel was deformed and did not seal properly.

A new design was made to permanently seal PDMS microchannels onto the chip surface by plasma bonding. The chip length was extended from 18 to 36 mm

(note the two sets of alignment marks in Figure 3.2) to allow tubing to be pushed in at a 90°-angle (thus minimising torque) with room for a microscope objective to fit in between. New 3D printing facilities meant that the flow cell could be designed for additive manufacturing methods, allowing greater flexibility (see overhanging tube-holder protrusions in Figure 7.3).

A different 3D printer (for stereolithography) was also used to produce PDMS moulds for the microchannels. This allowed adequate resolution (50 µm in XYZ) at a cost of ~ 100 x less than a standard photolithography mask and could be rapidly made in-house.

Flow cell

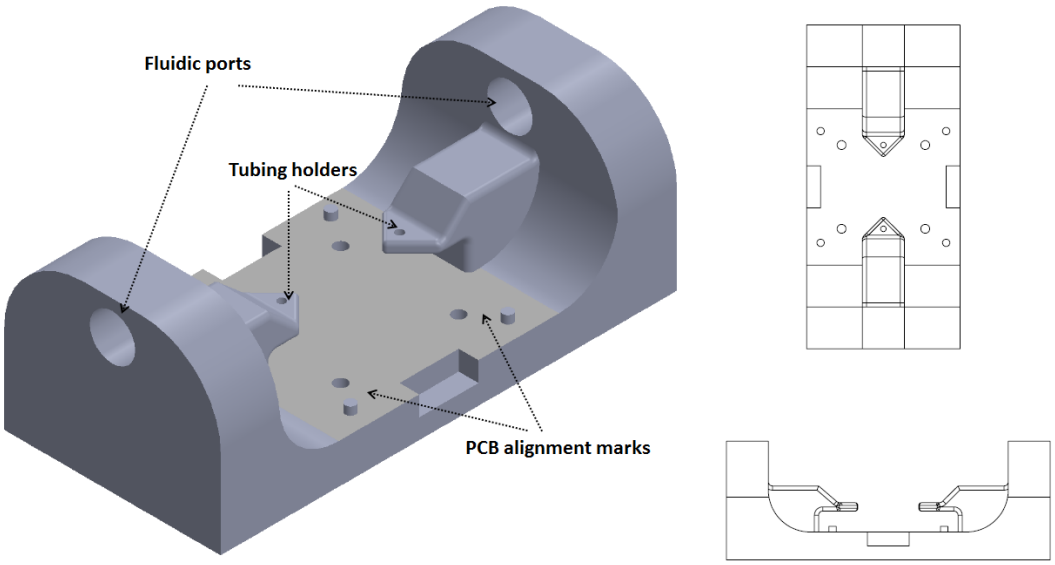

Figure 3.11: Flow cell design.

The flow cell was designed on SolidWorks 3D CAD software (Dassault Systémes, France) (see Figure 3.11). The key features were alignment studs for the PCB and tubing holders to direct tubing into the correct part of the PDMS, and hold it in place to minimise torque. PEEK fittings for 1/16th OD PTFE tubing were

ordered from Upchurch Scientific, UK.

3D-printed microfluidic moulds

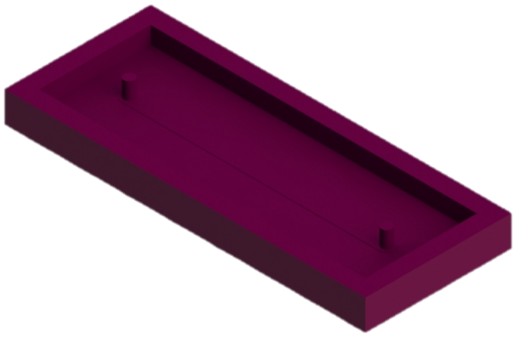

Figure 3.12: 3D-printed microfluidic mould design. PDMS is poured into the gasket. The two pillars either end define where inflow and outflow tubing is pushed into the PDMS. Between the two pillars is a slightly raised strip to define the microfluidic channel.

Miicraft 3D printers offer a very high resolution with a smooth finish, thus making excellent potential microfluidic moulds. However, the cured resin is reactive with uncured PDMS, and so the latter does not cure properly when in contact with Miicraft-resin mould (164). This can be fixed by passivating the surface with a silane layer, as was investigated for this work.

Moulds were designed on SolidWorks 3D CAD software (see Figure 3.12) and printed on a Miicraft 3D printer (Miicraft, Young Optics, Taiwan). To passivate the surface, moulds were cleaned in isopropanol for 5 minutes, dried under N_2 and cleaned further by UVO for 10 minutes, before transferring immediately into a solution of 5% chlorotrimethylsilane solution (isopropanol solvent), which was sealed with Parafilm® (Camlab, UK) and left for 30 minutes. Following this, moulds were removed and dried under N_2.

PDMS was made from a Sylgard-184 kit (Dow Corning, MI) with a 10:1 ratio of elastomer to cross-linker. This was poured into the moulds and degassed at ~ 5 mBar for 30 minutes, before being cured by baking on a hotplate at 70°C for 1 hour. The PDMS, with microfluidic channels, could now be removed from the mould with a scalpel.

PCBs

PCBs were designed on EAGLE software (Autodesk, CA) by Roberts Rimša and made on copper PCB by the Leeds School of Electrical and Electronic Engineering Workshop. The SAW chips were glued onto PCBs with black wax, and wire bonded as described previously (Section 3.1.2).

3.1.5 Device setup

Electrical connections

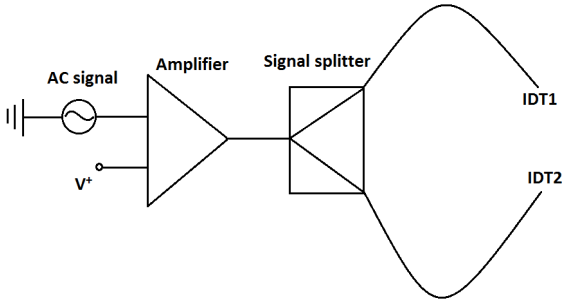

Figure 3.13: Schematic showing how the devices were connected to an AC power supply.

Figure 3.13 shows how the devices were connected to AC power supply. A signal generator (Marconi, UK, model 2022E) was connected to an amplifier (Mini-Circuits, NY, model ZHL-1-2W) with a 20V reference voltage (Agilent, CA, model E3620A). The signal was split in a signal splitter (Minicircuits, model 2APD-30-s) and sent to each IDT. The 20V power supply (top) and signal generator are shown in Figure 3.15**a**.

Imaging

For imaging during experiments, an Olympus BX60 fluorescence microscope was used (Figure 3.15**b**); the flow cell sat on the microscope stage as shown in Figure 3.15**c**). Figure 3.15**d** shows the syringe pump (Harvard PHD 2000) that was used to push fluid through the system. Finally Figure 3.15**e** shows the layout of all this equipment used in these experiments.

Fluidic connections

The sample was moved along the fluidics using Harvard PHD 2000 syringe pump (Harvard Apparatus, MA) with a fluid-filled 2.5 ml syringe, connected to 0.75

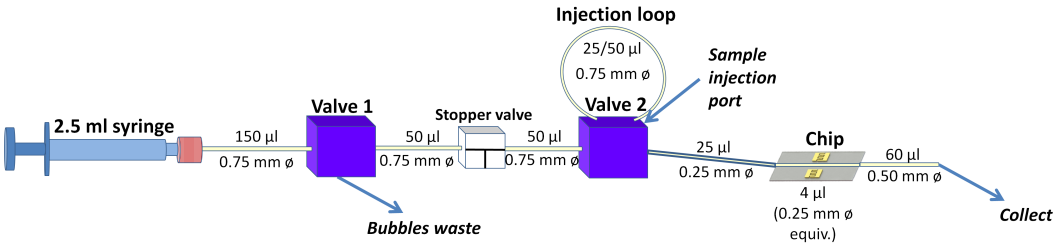

Figure 3.14: Schematic showing the fluidic connections used in most of this work. The samples were pushed through by liquid, coming from a 2.5 ml syringe. This was connected to PTFE tubing (0.75 mm ⌀) directed to Valve 1, which worked to re-direct any bubbles introduced when the syringe was changed. The sample (a cell or bead suspension) was injected into a sample loop held by Valve 2. A 'stopper' valve was placed between Valve 1 and 2 in order to stop flow when required for imaging. From Valve 2, the sample was led to the chip via a narrower (0.25 mm ⌀) tube at a gentle incline (allowing a slow flow rate with minimal cell sedimentation). From the chip, cells were directed into an outflow collection tube (a 15 ml Eppendorf tube).

mm ⌀ ID PTFE tubing (Figure 3.14). Two Rheodyne PEEK HPLC valves (model 9010, Sigma-Aldrich, UK) were inserted to the fluidic connection between the syringe and the device (Figure 3.14). The purpose of the first valve was to re-direct any air bubbles that got introduced when the syringe needed to be changed. The second valve was an injection valve, so that an exact quantity of liquid (25 µl) could be delivered per experiment (this was more important for the experiments shown in subsequent experimental chapters). A stopper valve (Upchurch Scientific, model V-101D, from Gilson Scientific, UK) was placed before Valve 2 to stop the flow on the chip for imaging.

When using a slow flow rate for cell alignment (typically 3µl/min) it was found that cells were sedimenting. By using narrower tubing (0.25 mm ⌀ tubing) the flow velocity increases from 0.1 to 1.0 mm/s, significantly reducing the effects of sedimentation, and thus enabling an even flow rate and particle concentration throughout the longer experiments.

The PDMS microchannel on the chip was 1.5 µl, with approximately 1 µl of dead space where the tubing comes in (the tubing - 1.5 mm OD - is cut at a 45 ° angle to allow space for cells to flow onto the chip - see Figures 5.4**b** and **c**). The outflow tube was angled downwards (after the flow cell) and into a 15 ml Eppendorf tube for collection. A tubing ID of 0.5 mm was chosen (between 0.25 and 0.75 mm to trade off between a fast flow velocity while minimising resistance). At the end of the experiment, 60 µl - the length of the outflow tube - would be collected at fast flow rate (200 µl), to dislodge any cells sedimented post-chip.

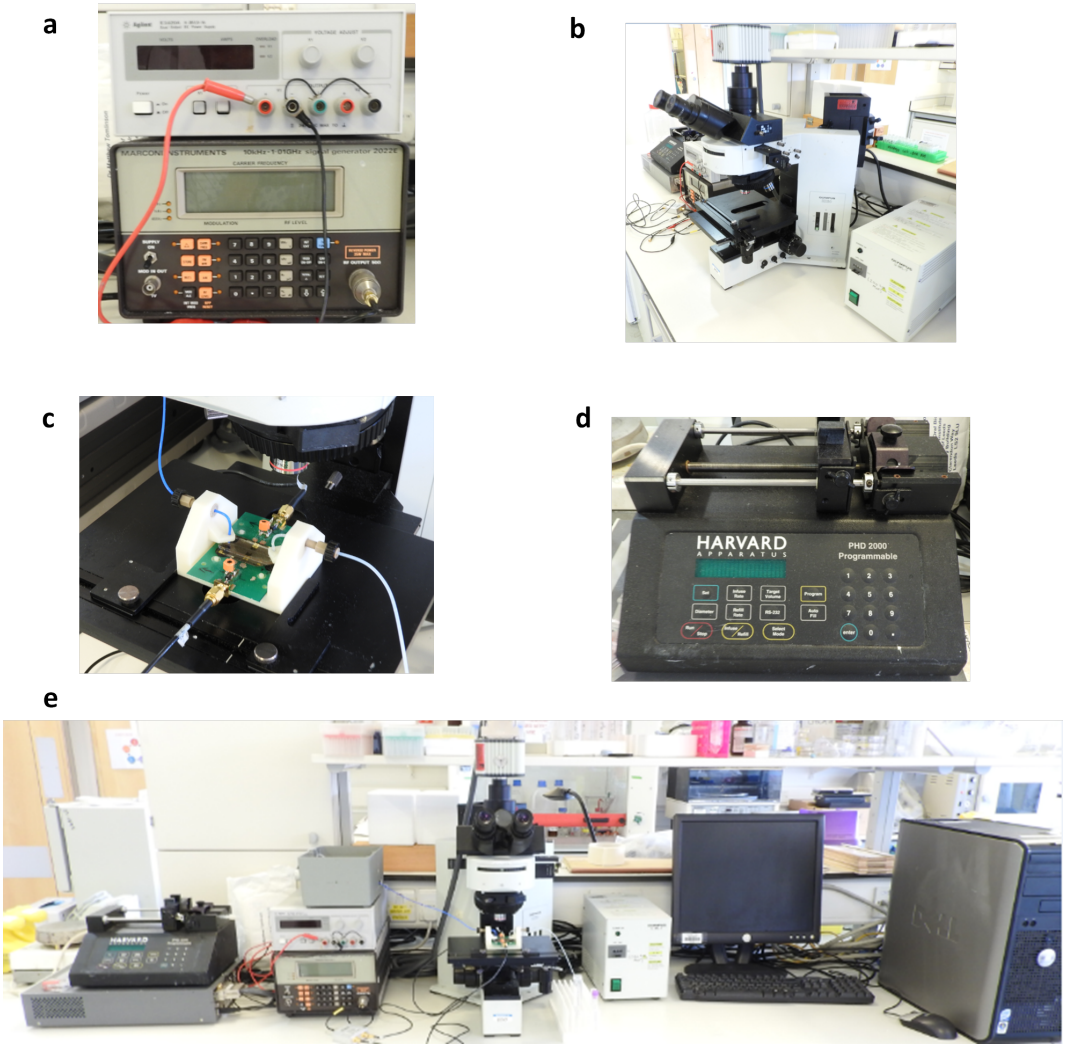

Figure 3.15: Photograph of equipment used in most SAW-DEP imaging experiments. **a** Signal generator (bottom) and DC power supply (top), **b** Olympus BX60 fluorescent microscope, **c** SAW-DEP device on microscope stage, **d** Harvard syringe pump, **e** equipment layout.

3.2 Chapter 4 procedures and protocols

This section should be complimentary to Chapter 4, where the methods to the experiments are described in the same order as in the experimental chapter.

3.2.1 Initial latex beads experiments

Theoretical calculation of DEP properties of latex beads

The DEP properties of latex beads was calculated by putting Equation 2.2.25 (157) into a NumPy (Numerical Python) script (see Appendix B.1). The value for particle permittivity of 2.56 was obtained from the bead manufacturer datasheet.

Latex beads preparation

1 µm diameter carboxylate-modified latex beads (1 ml aqueous suspension, 1% m/v) were purchased from Sigma, MO, and diluted 1:99 in DI water.

Conventional DEP experiments

The setup of equipment was the same as described in Section 3.1.5, but because the signal only went to one set of IDTs (not two), the signal splitter was not used. 79 mW power was applied to the transducers - less than for SAW-DEP experiments (typically 1,000 mW). This is because SAW-DEP requires more power because energy is lost coupling the current to the SAW, then into the evanescent field.

Beads were applied to the surface by pipetting 2 µl of bead suspension onto the IDTs, and this was overlaid with a coverslip before applying the signal. The images shown were taken under Brightfield with a Penguin Pixera 150CL camera.

Coverslip device experiments

The procedure was similar for SAW-DEP coverslip device experiments with latex beads, however, the signal was split and 1,000 mW was given to each set of IDTs. Different devices had slightly different resonant frequencies - these could be identified by examining in the network analyser (see Section 3.1.1: Matching Networks), but were ultimately fine-tuned by observing bead behaviour while stepping the frequency in 0.05 MHz intervals around the target frequency (10 and 20 MHz). For example, 10 MHz devices typically were operated at 9.90 MHz or 9.75 MHz, etc, depending on which frequency showed the strongest force exerted on particles.

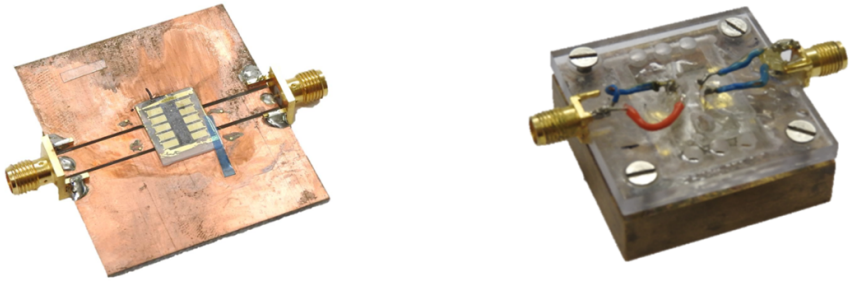

Figure 3.16: Photographs of the two devices used in Chapter 4: A cover-slip device (left), and Perspex-lid flow cell (right).

To observe bead behaviour, 2 µl of bead suspension was pipetted in between IDT pairs and this droplet was overlaid by a strip of glass coverslip, before applying the signal.

Images were taken using a Pixera Penguin camera, with blue filter excitation (SWB filter on the microscope). The droplet tended to evaporate after ~ 60 seconds. After this, latex beads were cleaned off the chips using cleanroom cotton swabs dipped in acetone, followed by cotton swabs dipped in isopropanol

Perspex lid flow cell experiments

Roughly 100 µl of latex bead suspension was taken up in a 1 ml syringe, and pushed (by air) through the tubing until it reached the chip. Images were taken with a Hamamatsu Orca camera (Japan), under blue excitation. Experiments typically lasted ~ 30 minutes before the surface became fouled or the device started leaking, after which the flow cell was disassembled and the chip was cleaned with acetone and a cleanroom cotton swab.

3.2.2 Effect of fluidic conductivity on insertion loss

To test the effect of fluid conductivity of the device insertion loss, the device was connected directly to an Agilent network analyzer (i.e. no additional signal input). Saline solutions of various concentrations had been made and their conductivities measured. The insertion loss at the resonant frequency (of a 20 MHz device) was noted; after this, 1 ml of DI water was flushed through the device and the insertion loss was noted again. The process was repeated for increasing concentrations of saline.

3.2.3 Latex beads force measurements

These experiments were conducted using the 3D-printed flow cell, with the equipment setup described in Section 3.1.5.

Latex beads of 3, 5, and 10 µm diameter were ordered (green fluorescent polystyrene, 1% m/v solutions) from Fisher Scientific, MA. These were suspended in 0.1% Triton solution to aid bead dispersion[1], at ratios of 50:1, 19:1, and 9:1 for 3, 5, and 10 µm beads, respectively.

[1]Triton is an anionic surfactant, however, it still increases the conductivity a little. The conductivity of 0.1% Triton solution was measured to be 0.00023 S/m.

Beads were delivered to the device via the fluidic setup shown in Section 3.1.5. The syringe was filled with 0.1% Triton solution to push the bead suspension through.

After delivery to the chip, a range of power settings were investigated, as detailed in the results[1]. Videos were recorded on a Hamamatsu Orca camera, generally at 16 fps (2x binning) and the quickest videos (i.e. 10 µm beads at 0.5 and 0.35 mW) were recorded at 30 fps (4x binning).

Post-analysis

The tracks of beads were recorded using the TrackMate plugin for ImageJ image analysis software (165). An overview of the particle tracking process is shown in Figure 4.13, and a basic guide to TrackMate can be found at (166). Beads were detected with the LoG detector setting, and tracks were made with the Simple LAP tracker. Tracks were exported to XML files.

A Javascript programme was made courtesy of Christoph Wälti (see Appendix, Section B.5). The programme measured the speed of beads (and therefore the DEP force) according to their spatial position. This finds not only the DEP force of beads, but also maps out the electric field in the channel. More detail of this process is given in Section 4.4.3.

3.2.4 Yeast cell separation experiments

Theoretical calculation CM factor for yeast cells

The DEP properties of yeast cells was calculated by putting Equations 2.2.30 and 2.2.31 ((103)), along with the biophysical values for yeast from (103) into a Python script (see Appendix B.2).

[1] the aim of these measurements was to compare the DEP force for different applied powers, as well as different bead sizes.

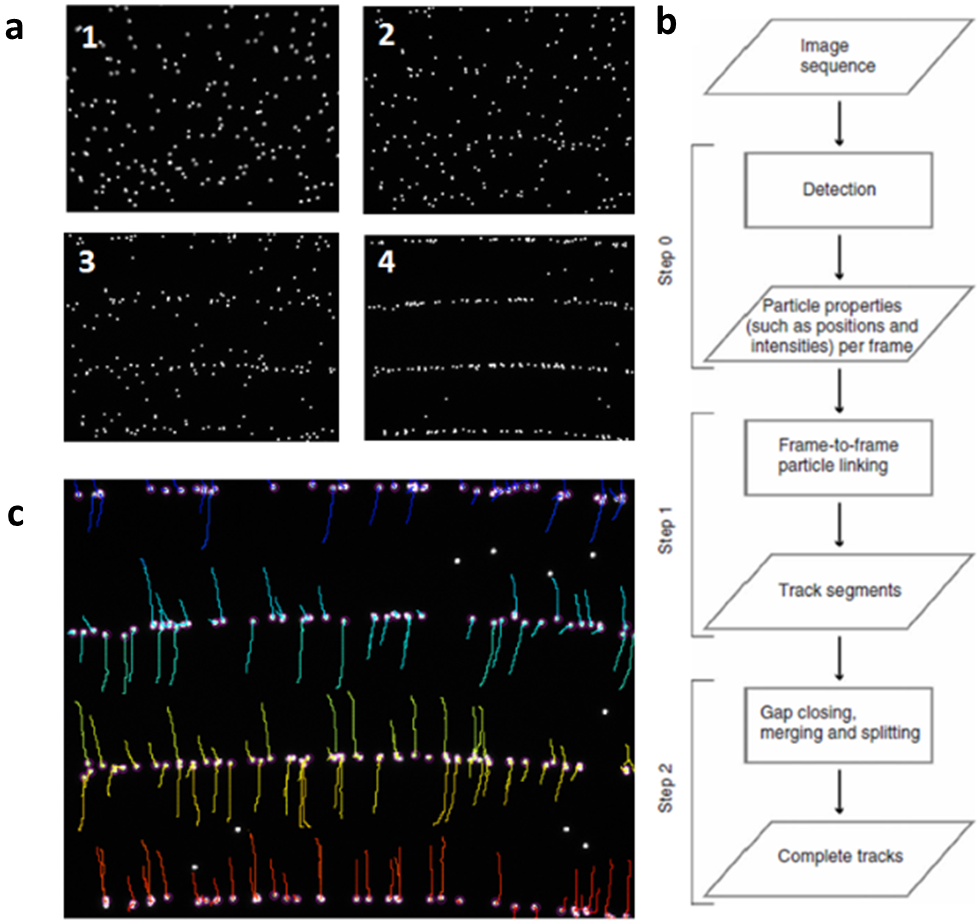

Figure 3.17: Overview of particle tracking in Trackmate. (a.) Sample of raw image sequence (NB full image sequences were 100-500 frames, depending on alignment time (taken at 16 or 30 fps) (b.) Processing sequence, from (165) (c.) Screenshot of particle (bead) tracks taken during processing of videos in TrackMate. Beads (white) are shown pictured at the end of the video sample; the coloured 'tails' show their path from the start of the video (typically a few seconds). Beads which do not have a pink ring or tail attached have been de-selected from analysis, normally because they were observed to not move throughout the video, presumably because they are stuck to the PDMS channel.

Culture of yeast cells

Dormant (yet to be activated) baker's yeast granules were bought from a supermarket. The culture medium was made by dissolving 3 g of Sabouraud dextrose

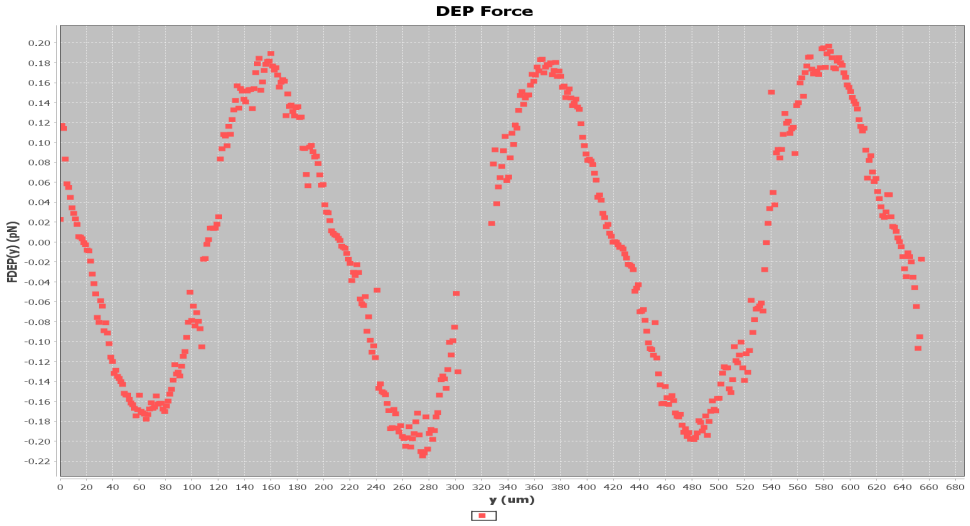

Figure 3.18: Sample raw output data from the Javascript, after processing the particle movement data for one video sample. The antinodes at which beads align by nDEP correspond to 20, 220, 420, and 620 µm on the x axis, which in turn correspond to the red, yellow, cyan, and blue final bead positions in Figure 4.13**c**, respectively.

broth (Sigma-Aldrich, UK) (as used in (103)) in 100 ml of DI water, with the aid of a magnetic stirrer. This was heated to 37°C (to ensure yeast activation) before adding 1 g of yeast. The activated yeast in sugar/nutrient solution was then transferred onto a magnetic stirrer at room temperature, and left to multiply.

After 24 hours, the 100 ml was separated into four separate 25 ml Falcon tubes and taken to a centrifuge, where they were pelletted at 10,000 g for ten minutes. The supernatant was discarded and replaced with 24 ml of 0.85 % NaCl into each of the four Falcon tubes, and the yeast were re-suspended by pipette mixing. They were left in NaCl solution for up to five days before experimenting (a simple 0.85% NaCl solution keeps yeast in an activated state, while not providing any nutrients to grow further). Fresh batches were made every five days to ensure high viability of yeast.

Figure 3.19: Bakers yeast used in these experiments (left), and Trypan blue (right), which selectively stains dead yeast.

Preparation and staining of yeast cell solutions

Separate populations of live and dead yeast

In order to generate separate populations of both live and dead cells, the yeast suspended in NaCl were concentrated by pelletting at 10,000 g for ten minutes and resuspending in 2 ml of 0.85 % NaCl. Of this, 1 ml was pipetted into 24 ml of isopropanol (IPA) (for dead cells), and 1 ml was pipetted into 24 ml of 0.85 % NaCl (live cells). The cells were incubated for an hour, then pelletted at 10,000 g for ten minutes, before each sample (live and dead) was resuspended in 2 ml 0.85 % NaCl. 1 ml of this suspension was added to 1.7 ml minicentrifuge tubes. The samples were then washed (mainly to remove any residual IPA) by minicentrifuging at 6,700 g for one minute, then re-suspending in 1 ml of 0.85 % NaCl. This was repeated twice.

Staining yeast cells

To stain the cells, 15 μl of live cell solution and 50 μl of dead cell solution[1] was added to the same 1.7 ml centrifuge tube, followed by 435 μl of 100 % PBS

[1]Because dead cells are lighter and fragment, a higher proportion are lost during centrifugation steps. Thus, a ratio of 15:50 live:dead suspensions resulted in an even concentration of live and dead cells

solution (of physiological conductivity), to make up 500 μl. 500 μl of 0.04 % Trypan blue cell stain in physiological saline solution was added to this (a 1:1 dilution), and this was incubated at room temperature for five minutes. Trypan blue selectively stains the cytoplasm of dead cells blue, but is excluded from live cells. This is because the dead cell membrane becomes permeable during the apoptotic and necrotic cell death pathways, a process of gradual disintegration (167).

The stain was washed out by centrifuging the solution, pouring out the supernatant, and re-suspending in 10% PBS solution (measured to 0.16 S/cm). This was repeated twice.

Device surface preparation and experiment
Devices were functionalised by flowing 1% BSA solution and incubating for >30 minutes before the experiment. This was in order to form a blocking layer on the surface (of nonspecifically-bound BSA protein), to prevent fouling by yeast cells. BSA solution was removed before flowing the stained yeast solutions. Pictures of yeast were taken in Brightfield (with the Pixera Penguin camera) for no longer than two hours after staining.

3.3 Chapter 5 procedures and protocols

This section will discuss the experimental procedures used in Chapter 5. In summary, human dental pulp stromal cells (DPS cells, a candidate cell type for cell therapies[1] were grown by standard tissue culture methods. A number of tests were carried out on the DPS cells to see if SAW-DEP and related procedures (DEP buffer, microfluidics) had any adverse effects on cells (which could limit the medical applications of the technology). The tests consisted of FACS to assess cell viability, and biochemical assays to assess the differentiation potential of cells following SAW-DEP.

3.3.1 Tissue culture

General Procedure

Growth conditions

Tissue culture is so called because studying animal cells *in vitro* normally involves growing them as a tissue or layer of cells. Mammalian cells are typically grown in a 37°C incubator with 5% CO_2, so as to mimic the conditions of the human body. Most 'adherent' cells (cells which are 'anchored' to tissue within the body) will readily adhere to the bottom of a polystyrene plastic culture flask (Figure 3.20a), by applying them into the flask within a suspension of liquid culture medium, containing food for the cells.

Cell density

Researchers typically add a sufficient concentration of cells to cover 10-30% of the surface (i.e. 10-30% 'confluency'), after which cells will continue to multiply and expand across the surface. The growth medium is changed typically 2-3 times per week to provide fresh food (Figure 3.20b). Typical doubling times are 1-4 days. When the surface is >80% covered (confluent), the growth phase of cells often changes through extra-cellular signaling, and cells may change phenotype or differentiate. For example, when dental pulp stromal (DPS) cells reach high

[1] Discussed in Section 1.1

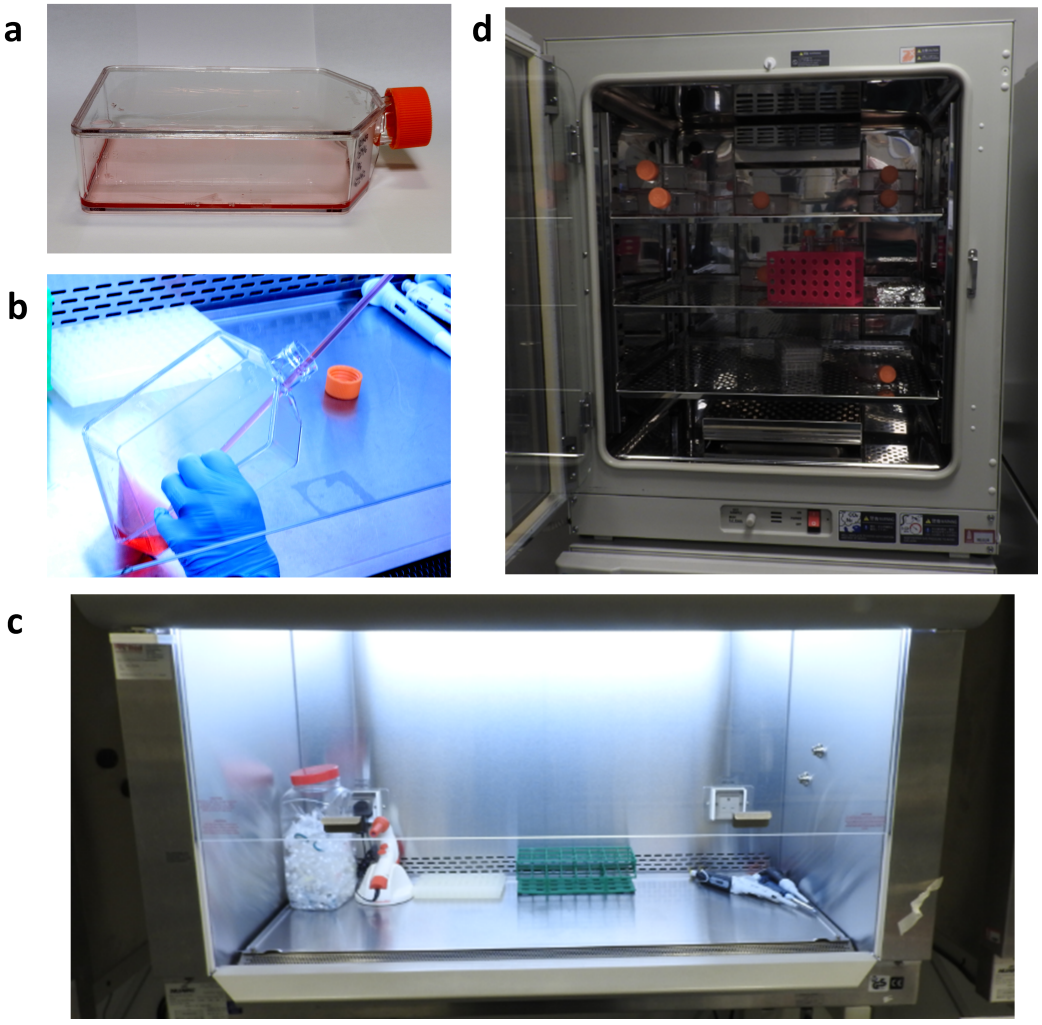

Figure 3.20: Photographs of tissue culture apparatus. **a** Tissue culture flask, 175 cm^2 **b** Aspirating medium out of flask (e.g. when changing medium to feed cells) **c** Positive pressure sterile hood for handling cells **d** 37°C, 5% CO_2 standard incubator.

confluency, they will increase alkaline phosphatase expression, an early marker for differentiation into bone tissue.

Passaging cells

Unless differentiation is the end goal, it is often desirable to reduce the density of cells before a change in phenotype occurs, for consistency between experiments.

The adherent cell layer is released from the surface by applying 'trypsin', an enzyme often found breaking down food in the stomach, which severs the cellular anchors to the surface. Researchers can then transfer a fraction of this cell suspension to a fresh flask and begin the expansion process again. This transfer of cells is known as 'passage' (168).

Because a cell's phenotype often changes during subsequent passages (either due to differentiation, or possible mutation in the case of cell lines) it is desirable to only keep cells up to a certain number of passages (generally ~ 5 for DPS cells from donors, more for engineered cell lines). Cells of an early passage are stored in liquid nitrogen (-196 °C) as a bank for future use.

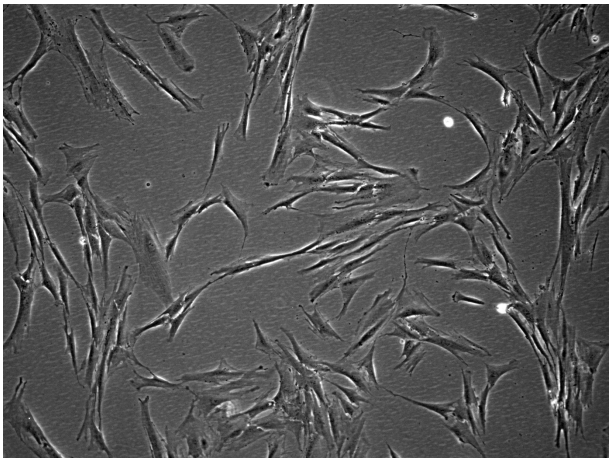

Figure 3.21: Microscope image of adherent DPS cells growing in a tissue culture flask (10x objective).

Maintaining sterility

One of the key concepts to tissue culture researchers is that of sterility - out of the body, cells do not have the benefit of the immune system and protective layers, so contamination with bacteria and yeast is a general concern which can result in loss of work and ruined experiments. For this reason, tissue culture flasks contain sterile pores (less than 0.2 µm, too small for bacteria etc) for gas exchange in the lids; whenever the lid is removed to transfer cells or media, this

must be carried out in a sterile hood (Figure 3.20d). Air flow in a sterile hood ensures positive pressure, such that microparticle (including microorganisms) cannot be blown in from outside. Anything that the researcher transfers into the hood (e.g. flasks, media bottles, their gloved hands and arms) must be sprayed in a mist of ethanol (typically 70% in water) to sterilise them.

Protocol - dental pulp stromal cells

Dental pulp stromal cells were harvested, courtesy of Matt Tomlinson, from extracted impacted third molars obtained with consent from three donors, both male and female aged between 21-46 years, through the Leeds School of Dentistry Skeletal Tissues Research Tissue Bank (07/H1306/93+5) and were cultured in basal medium. DPS cells were isolated using collagenase I (3 mg/ml) (Invitrogen, UK)/dispase (4 mg/ml) (Roche, Germany) digestion and selected using plastic adherence and colony formation (169).

Cultured cells were maintained in a basal medium comprised of -MEM, 10% foetal calf serum (FCS) (Sigma-Aldrich, UK), 100 units/ml penicillin, 100 g/ml streptomycin solution (Sigma-Aldrich, UK) and 1% of 200 mM L-glutamine (Sigma-Aldrich, UK). Cultures were incubated at 37°C, 5% CO2 until 70-80% confluency, after which they would be split 1 in 5. DPS cells at passage 3 to 5 were used in all experiments.

3.3.2 FACS experiments - effect of SAW-DEP on cell viability

Composition of DEP buffer

Considerations

DEP is typically performed in low conductivity buffer (<0.01 S/m). This rules out typical cell buffers such as culture media and PBS (phosphate buffered

saline, ~ 1.5 S/m). In order to ensure the solution is osmotically balanced[1] (~ 300 mOsm) researchers typically use a sugar-based solution (typically 8.5-9 % m/v) which is topped up with NaCl to fine tune the conductivity. To buffer the pH (to keep it in the suitable range for cells, pH 6.8-7.4) researchers often use the low-conductivity HEPES buffer. Lastly, because mammalian cells are notoriously sticky in microfluidics, researchers try to counter this with EDTA, typically 0.02% m/v and BSA 0.5 - 2%. EDTA chelates Ca^{2+} ions, which prevents cells attaching from each other (Ca^{2+} is necessary to form cell-cell junctions; BSA coats the surface of both the fluidics (as used in earlier yeast experiments) and cells, reducing non-specific binding of the cell to surfaces.

Because a relatively high conductivity of 0.15 S/m was chosen to perform experiments, the concentration of sugar was dropped slightly lower to 7.5% to ensure osmolarity of 300 mOsms. Osmolarity was calculated using a Python script (Appendix, Section B.4), which assumed 1 Osmol/mol for sucrose, dextrose, EDTA, BSA, HEPES, and 2 Osmol/mol for NaCl (because one mole of NaCl dissociates completely into 1 mol of Na^+ and 1 mol of Cl^-.

Composition and storage

The DEP buffer used was therefore 7.5% sucrose (all % are m/v), 0.3% dextrose, 2% BSA, 0.02% HEPES. After adding HEPES the pH was adjusted (from ~ 5.8 to 7.0-7.2) by adding 10-15 drops of 5 M KOH. Finally the conductivity would be adjusted to 0.15 S/m by adding NaCl (~ 0.05%).

To minimise risk of buffer contamination, buffers were filtered by passing them through a 0.2µm sterile filter (Merck Millipore, Germany) on the end of a syringe into sealed aliquots in 7ml Bijou tubes (Thermo Fisher, MA) in a sterile tissue

[1]The osmotic potential is determined by the concentration of solute molecules both inside and outside the cell. If there is a much lower concentration of solute outside the cell (for example, in a low-conductivity buffer that has not been osmotically boosted with sugars), then water will osmotically diffuse into the cell due to its higher potential, leading to swelling and rupture.

culture hood. These were frozen at -4 °C, and used within two months.

A further eight 'DEP' buffers, based on that used in the literature, were made to assess their effect on cell viability. The constituents, along with those of the previously mentioned media, are listed in Table 5.2.

SAW-DEP and FACS procedure

Device functionalisation
The fluidic setup (described in Section 3.1.5, Figure 3.15) was stored overnight in 5% (v/v) Decon90 surfactant solution (Camlab, UK) to dissolve cellular residues from the previous experiment. These, along with soap residues, were removed prior to the experiment by flowing ethanol and functionalised by flowing DEP buffer into the channel (at least 500 µl to remove residual ethanol). DEP buffer would be left for >30 minutes while cells were prepared, to ensure a monolayer of BSA formed on the surfaces.

Cell preparation
Culture medium would be aspirated from one 175 cm^2 flask of cells (containing ~ 4 x 10^6 cells), and adherent cells would be washed in PBS (add 10 ml of PBS, swirl, aspirate off) before incubating in 5 ml trypsin for 4 minutes. Any cells still adherent would be detached by gently tapping the side of the flask. Trypsin was inactivated by adding 5 ml of culture media (the FCS blocks trypsin's active site), and the suspension (10 ml total) was transferred to a 15 ml Falcon tube (Fisher Scientific, MA), whereupon it was pelleted by centrifugation (each centrifugation step was for 5 minutes at 200 g). The supernatant was discarded and the pellet resuspended in 1 ml DEP buffer, and passed through a 50 µm cell filter and into a fresh 15 ml Falcon tube (this removes any large cellular debris that can block microfluidics). The suspension was centrifuged and resuspended a further two times to remove residual culture medium. The final suspension was in 400 µl of DEP buffer for a concentration of ~ 1 x 10^6 cells per 100 µl.

Table 3.1: Buffer constituents

Buffer	**Constituents (in mass/volume)**, conductivity at 20 °C
Culture media	Significant components are 10% fetal bovine serum[1], 0.68% NaCl, ~ 0.08% other salts, 0.1% amino acids (170). 1.25 S/m (171).
PBS	Significant components are 0.8% NaCl, and 0.115% phosphate buffer (Na_2HPO_4) (172). 1.5 S/m.
Remote DEP buffer	0.02% EDTA, 2% BSA, 0.595% HEPES buffer (25 mMol), 7.5% sucrose, 0.3% dextrose, pH adjusted to 7.1-7.4 with 5 M KOH. 0.15 S/m.
1	8.5% sucrose, 0.3% glucose, 0.725% (v/v) RPMI media stock(143). 0.01 S/m.
2	8.5% sucrose, 0.3% glucose, 6mMol HEPES. 0.0096 S/m.
3	8.5% sucrose, 0.3% glucose, 0.02% EDTA, 2% BSA, 10 mMol HEPES, 0.044 S/m.
4	8.5% sucrose, 0.3% glucose, 27 mMol HEPES, 0.030 S/m.
5	9% sucrose, 0.3% glucose, 0.03% EDTA, 0.8% BSA, topped up with HEPES to 0.030 S/m.(56).
6	9.5% sucrose, 0.3% dextrose, 2.1% 1 x stock PBS solution, 0.03 S/m. (122)
7	8.5% sucrose, 0.3% dextrose, 2% BSA, 0.025 S/m.
8	8.5% sucrose, 0.3% dextrose, 2.1% stock saline solution

SAW-DEP procedure

A 25 µl sample of cell suspension (containing ~ 2.5 × 10^5 cells) was used to fill the injection loop. Cells were flown to the chip, and subjected to SAW-DEP at a flow rate of 3 µl/min at 3.2 mW of applied power (this was the maximum power output of this device - 3 µl/min was the fastest flow rate at which cells would properly align/become separated). To check that cells were properly undergoing SAW-DEP during the whole process, a picture was taken of cell alignment in the aperture every 30 seconds. Cells were collected via the flow cell outflow tube into a 15 ml Falcon tube.

For the "Fluidics control" cell sample: these underwent the same procedure as outlined above, the only difference being the SAW-DEP field was never turned on (n = 9 for both SAW-DEP and Fluidics Control samples).

SAW-DEP Controls

To gauge how much cell death was not attributable to either SAW-DEP (e.g. electric field intensity) or the Fluidics (shear forces), controls were carried out by leaving cells in basal medium, PBS, and DEP buffer in Eppendorf tubes at the lab bench while SAW-DEP was being carried out (30 minutes total). These were prepared in parallel to preparing cells for SAW-DEP (or Fluidics Control), but substituting basal medium/PBS for DEP buffer (n = 18 for each of these controls).

FACS preparation and procedure

All samples were prepared for FACS in parallel. 200 µl of each sample (2-5 × 10^4 cells) was topped up with 1 ml of PBS and centrifuged, whereupon the supernatant was discarded and the pellet was re-suspended in 100 µl of PBS. 5 µl of PI solution (BioLegend, CA) was added to stain cells. After 12 minutes, the concentration of cells was adjusted by adding 250 µl of PBS (giving a final volume of 355 µl), ready for the flow cytometer. A BD^{TM} LSRII instrument was used for flow cytometry. Samples were excited with a blue 488 nm laser, and fluorescence was collected via a 500 nm long pass dichroic mirror and a 575/26 nm band pass filter.

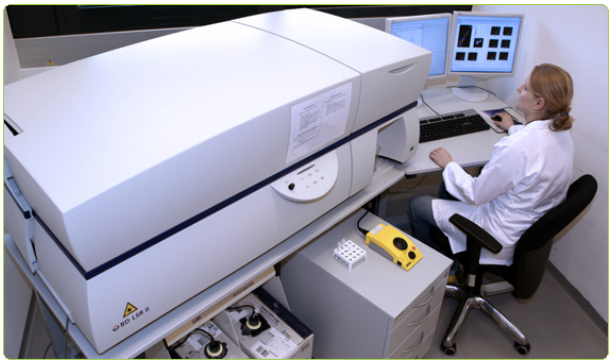

Figure 3.22: Photograph of the flow cytometer model used in these experiments (173).

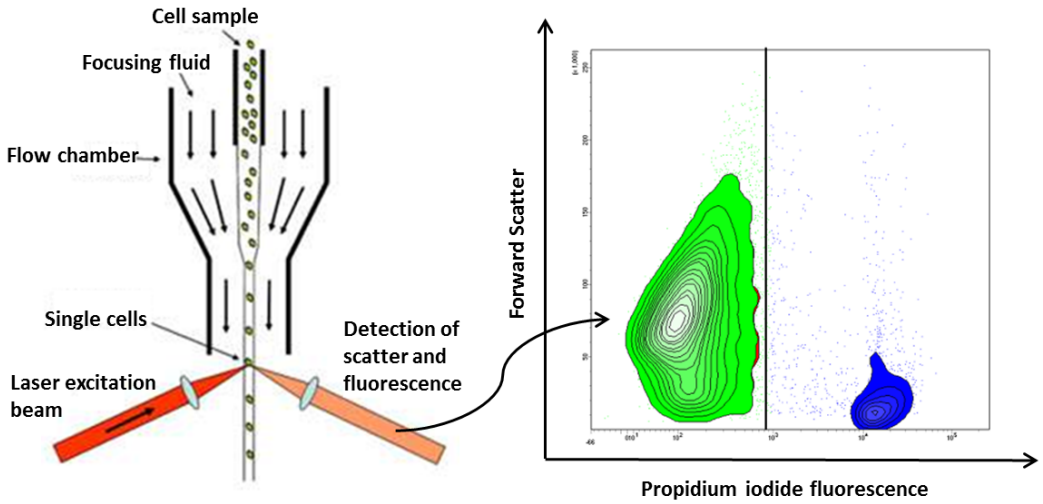

Figure 3.23: FACS overview. (Left) Schematic of flow cytometer flow cell (174). The cell sample is hydrodynamically focused such that cells can be probed one at a time. Each cell is interrogated with a laser beam, and data is collected for its fluorescence and light scatter. (Right) Sample contour plot of ~ 10,000 cells, exhibiting two populations off PI fluorescence - i.e. highly-fluorescent population has taken up more PI because they are dead cells.

Forward scatter (FSC) and side scatter (SSC) were measured simultaneously on a contour plot to define a population of intact cellular bodies. A gate was drawn around the first definable population above the background (caused by electrical noise and particulate matter, including cellular debris) such that only intact cel-

lular bodies were examined. This gate was used for all experiments, and 10,000 - 20,000 events were counted per experiment (generally 60-70% of which were intact cellular bodies). Forward scatter and PI fluorescence (logarithmic scale) were measured simultaneously on a contour plot to define viability. The positive control showed two separate populations, one of which was heavily fluorescent with PI and was assumed to be the dead fraction. The live/dead gate was drawn between these two populations, at a PI fluorescence intensity of 103, to give a realistic viability for the positive control, which was an average of 96.7% (n=18). This gate was kept the same for all experiments.

Verification of live/dead gate - incubator experiments
For these experiments (n = 3) (Section 5.3.4, Figure 5.11), the first part of the experiment consisted of cells undergoing SAW-DEP and FACS as described before. The second part of the experiment was conducted straight after (all in one day) with a flask of cells of the same donor and passage number - for these cells, an extra step was added: After SAW-DEP, the cells were centrifuged and resuspended in 1 ml of basal medium and left for 1 hour in the incubator, before being prepared for FACS as described before.

Assessing effect of DEP buffer composition experiments
For these experiments, no sample underwent SAW-DEP, and preparation and analysis was the same as for 'SAW-DEP controls', described earlier, with the only difference being the precise buffer they were suspended in. The buffer compositions are listed in Table 5.2.

Statistical analysis
To determine whether there was statistical difference in the viability between various samples (most important, SAW-DEP vs cells which had not undergone SAW-DEP), significance tests were carried out via IBM SPSS Statistics 21 software. Initial Kolmogorov-Smirnov and Shapiro-Wilk tests showed that the data was not normally distributed. Therefore, Mann-Whitney U (non-parametric) tests were performed between each of the five conditions (SAW-DEP, Fluidics,

DEP buffer, Basal Medium, PBS), with p-values >0.05 deemed as significant.

3.3.3 Effect of SAW-DEP on differentiation ability of stem cells

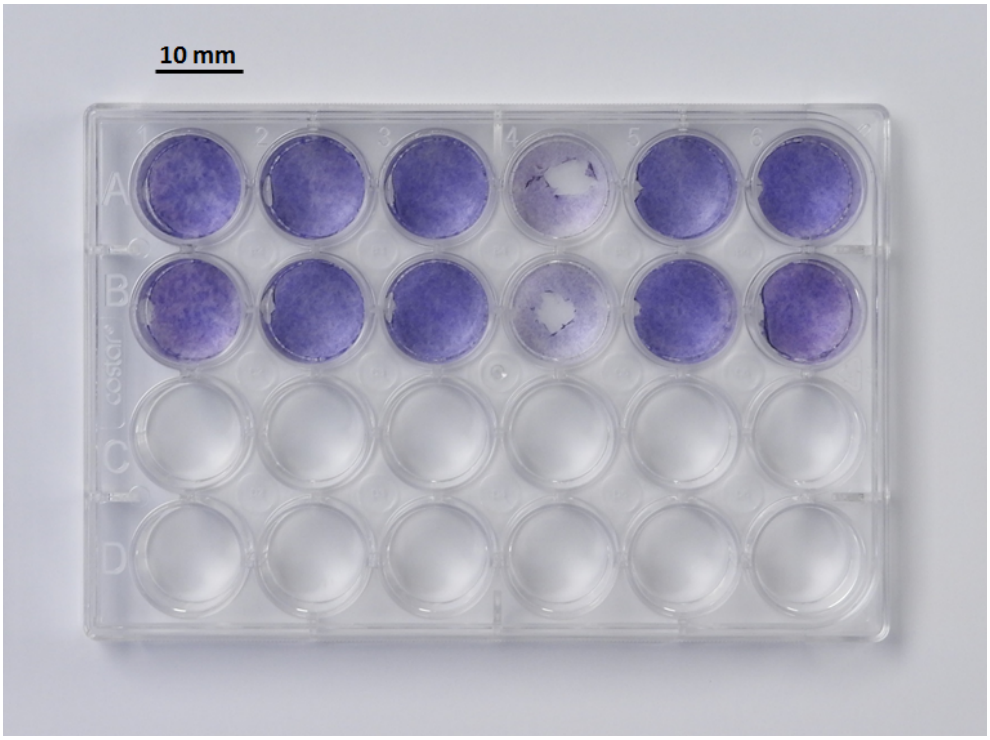

Figure 3.24: Picture of a 24 well tissue culture plate. The top two rows contain monolayers of cells, grown for 10 days (the bottom two rows are empty). The monolayers have been fixed in ethanol, and stained (blue) for alkaline phosphatase expression, an early marker in osteogenic differentiation of DPS cells. The fourth pair in is a negative control (not expected to be undergoing differentiation) which explains why it is far more weakly stained.

Overview

To test the effect SAW-DEP has on stem cells differentiation ability, DPS cells were subjected to SAW-DEP in a similar manner to the FACS experiments, after

which they were cultured in 12 or 24 well plates (see Figure 3.24). Growing cells in these removable-lid plates allows for easy access to cells for staining and biochemical assays. This consisted of (1) alkaline phosphatase (ALP) activity assay (ALP is a marker for osteogenic lineage differentiation), (2) ALP stain, and (3) a mineralisation stain (after 3-4 weeks, cells pushed down an osteogenic lineage should begin forming mineral deposits, the precursor of bone).

A more detailed introduction to the induction of differentiation of DPS cells can be found in Section 5.5.1.

SAW-DEP procedure

The device used for this experiment had a lower coupling coefficient (~ 1.6 mW at full power) so a lower flow rate of 1.5 µl/min was used to ensure full alignment. Cells were prepared for SAW-DEP as before, but using BSA buffer adjusted to 0.15 S/m (8.5% sucrose, 0.3% dextrose, 2% BSA, NaCl to 0.15 S/m) instead of the previous DEP buffer. A 50 µl injection loop was filled with cells concentrated to ~ 10^6 cells per 100 µl, and this was delivered to the chip at 1.5 µl/min before being collected (recovery was measured to be 75%).

Preparation of controls

The 'Fluidics' control was prepared the same as the SAW-DEP sample, but was delivered through the device with the SAW off. The DEP buffer and basal medium controls were prepared in the same manner (basal medium control suspended in basal medium, not DEP buffer) and left on the lab bench for the experiment time (45 minutes). Positive and negative controls were prepared from a fresh flask of cell from the incubator.

Seeding and growth in osteogenic media

Cells were re-suspended in basal medium by centrifugation, counted by haemocytometer, and seeded at a density of 4×10^4 cells/cm^2 (24 or 12 well plates for ALP/mineralisation tests, respectively) in basal medium. Cells were then left overnight (for full attachment to surface) before the basal medium was aspirated and replaced with osteogenic media (Complete StemPro® Osteogenesis Differentiation Medium by Gibco^{TM} from Thermo Fisher, MA, supplemented with 1% (v/v) Penicillin-Streptomycin antibiotic solution (100 units/ml penicillin, 100 g/ml streptomycin solution, from Sigma-Aldrich, UK)). The medium was changed every four days.

ALP stain

After 8 days in osteoinductive medium, cells were washed 3 times in Ca^{2+} PBS (Sigma Aldrich, UK), before being fixed in chilled 70% ethanol for 15 minutes. Cell monolayers were then washed three times with distilled water, before being immersed in stain solution: napthol AS-MX phosphate aqueous solution with fast blue RR salt (85L1) (Sigma-Aldrich, UK), passed through a .22 µm syringe filter. Monolayers were left in the dark for 30 minutes to stain. Following this, the samples were washed three times in distilled water, leaving for 5 minutes in a gentle shaker (60 rpm) with each washing step, before being photographed with a Nikon Coolpix P610 camera.

ALP activity assay

The ALP assay was also performed following 8 days in osteoinductive medium. Cells were washed twice in Ca^{2+}-free PBS and immersed in 0.1% Triton-X100 (Sigma-Aldrich, UK) solution to lyse cells. To fully break up cells and release DNA, the samples were frozen in a -80 °C freezer for 5 minutes, before each sample monolayer was scraped and mixed methodically by pipette for 1 minute, and this process was repeated twice.

The assay was carried out in 96 well plates. 10 µl of each cell sample was added into the appropriate well. Calibration standards were made of 4-nitro phenol solution (Sigma Aldrich, UK) in concentrations of 10, 50, 100, and 200 nmol/ml. To start the reaction, 90 µl of substrate solution was added (4-Nitrophenol Phosphate substrate liquid system - Sigma Aldrich, UK) to each well. This was incubated at 37 °C for 30 minutes, before the reaction was stopped by adding 100 µl of 1 M NaOH solution. Following this, plates were excited at 405 nm using a Varioskan Flash model microplate reader (Thermo Fisher, MA) to quantify fluorescence.

Figure 3.25: Photograph of a typical microplate reader (175). It is essentially a UV-vis spectrophotometer, containing a laser that probe cells at various wavelengths, measuring the absorption or excited emission of the sample, typically to detect for photolabels, similar to the flow cytometer discussed in Section 3.3.2.

To calculate the ALP activity per cell (thus discounting lower ALP activity in samples with less cells, or vice versa), DNA assays for standardisation were carried out in parallel to ALP activity assays (see below).

ALP assay - DNA assay for standardisation

10 µl of each cell sample was added into the appropriate well, as well as 10 µl of DNA standard solution. DNA standards were made from DNA Standard 1ug/ml solution (Cambio, UK) into concentrations of 1, 10, 100, and 500 ng/ml. Wells were topped up with 90 µl of 1 X TE buffer solution, and 100 µl of working Pico Green solution was added (working Pico Green solution was made by diluting Pico Green^{TM} DNA Assay solution (Cambio, UK) 1:199 in TE buffer). After dark incubation for 5 minutes, plates were read in a Varioskan Flash microplate reader (Thermo Fisher, MA), using 480 nm excitation and 520 nm emission wavelengths.

Data for ALP activity and DNA quantification was exported and analysed in Microsoft Excel 2010.

Mineralisation stain

For the mineralisation stain, cells were cultured in osteoinductive medium for 16-19 days (as specified in Results). Cells were washed 3 times in Ca^{2+}-free PBS (Sigma Aldrich, UK), before being fixed in chilled 70% ethanol for 15 minutes. Cell monolayers were then washed three times with distilled water, before being immersed in Alizarin red stain solution (Millipore, UK) in the dark for 15 minutes. Following this, the samples were washed three times in distilled water, leaving for 5 minutes in a gentle shaker (60 rpm) with each washing step, before being photographed with a Nikon Coolpix (model P610) camera.

3.4 Chapter 6 procedures and protocols

In summary of Chapter 6, the DEP properties of three cell types was examined under SAW-DEP. The cell types were DPS cells (described previously), 16HBE cells (a bronchial epithelial cell line), and MCF7 cells (a breast cancer cell line). Firstly, DPS cells were fluorescently stained to visually discriminate live and dead cells, and the optimal conductivity for separation was investigated.

Following this, the DEP properties of live DPS, 16HBE, and MCF7 cells were analysed by seeing whether they underwent nDEP or pDEP at various conductivities. There was also a preliminary experiment in separating 16HBE and DPS cells under SAW-DEP. Finally, the DEP properties of DPS cells as a function of age was examined, in a similar manner.

3.4.1 Live and dead DPS cell staining and separation

Staining mechanism background

Different dyes were used to discriminate dead and live cells (see Figure 3.26). Dead cells were stained with propidium iodide, which permeates the membrane of dead cells (but not live cells) to intercalate between DNA bases. When bound, it fluoresces in the 'red' range.

Live cell stains are generally more expensive, with more elaborate molecules manufactured to permeate the intact cell membrane. Calcein-AM consists of the fluorescent, charged molecule calcein 'capped' by acetoxymethyl which supresses both fluorescence and charge (the latter quality allowing the molecule to cross the membrane). Once inside, serum esterases (found in live, metabolically active cells, but not in dead cells) will cleave off the AM cap. This leaves a fluorescent (green), *charged* molecule which is now retained in the membrane.

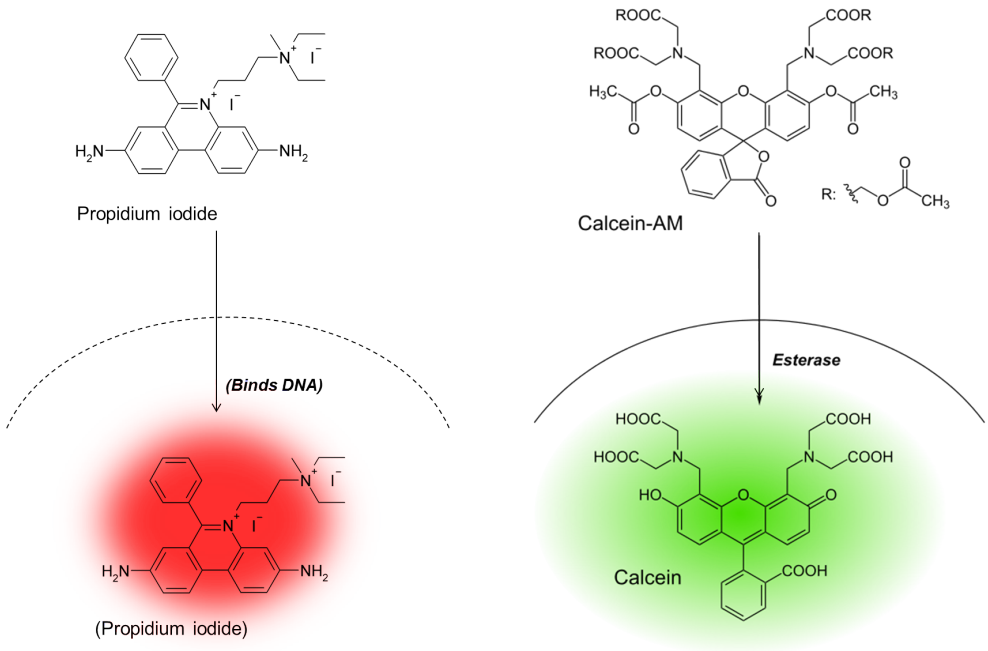

Figure 3.26: Schematic showing mechanism of selective dead/live cell staining by propidium iodide/calcein AM, respectively. (Left) Propidium iodide is permeable to the dead cell membrane, but not the live cell membrane (due to the former's diminished integrity and function). Once inside, it binds to DNA and fluoresces in the red spectrum. (Right) The fluorescent calcein molecule is 'capped' with acetoxymethyl (calcein-AM), which prevents fluorescence and neutralises the molecule, such that it can cross both live and dead cell membranes. When inside live cells, the -AM is cleaved off by the active esterase metabolic proteins within the cell; the resulting calcein molecule is strongly fluorescent (green), and moreover, cannot diffuse back across the membrane because it is now charged. Conversely, calcein-AM is not cleaved by dead cells (or cleaved far less) due to the lack of active enzymes, such that it will diffuse back out of the cell without fluorescing (176, 177).

Separation at 0.15 S/m

DPS cells were cultured as in the previous section. Two flasks of cells were used per experiment, with a flask for live and a flask for dead cell populations. Cells in both flasks were detached simultaneously by 5 ml trypsin, topped up with 5

ml of basal medium, and centrifuged at 200 g for 5 minutes in 15 ml Falcon tubes.

For live cells, one tube of cells was washed once in PBS by centrifugation, to remove residual serum that would occupy esterase activity. Cells were then re-suspended in a 10 µM working dilution of Calcein-AM (ThermoFisher, UK) and incubated in the dark to allow staining. After 30 minutes, the cell pellet was washed twice in low conductivity DEP buffer (8.5% sucrose, 0.3% dextrose, 2% BSA) and topped up with 10% v/v propidium iodide (PI) solution (Biolegend, UK). The final volume of cell suspension is ~ 400 µl, aiming for 10^6 cells per 100 µl. Adding 10% PI solution not only ensures any dead cells are accordingly stained, but also adjusts the final conductivity to 0.15 S/m. (PI solution is made up of 0.04% m/v PI diluted in PBS solution.)

While the live cells were incubated in the stain solution (for 30 minutes), the dead cells were prepared. For this, the other tube of cells was washed twice in low-conductivity DEP buffer and topped up with 10% v/v PI solution. To kill the cells, the final suspension of cells was left (in a 15 ml Falcon tube) in a 60 °C water bath for 12 minutes, a method described in an earlier DEP-based live/dead separation paper (143), following which they were cooled in a 4 °C fridge for >2 minutes.

Finally, dead cell and live cells fractions were mixed in a 1:2 ratio (live cells spread out more due to the pearl chaining effect, so a higher concentration was used for even distribution). They were injected into the same fluidic setup described in the previous section, pushed through with 0.15 S/m DEP buffer.

Imaging

To image, the flow was stopped with the stopper valve (to completely stop flow, the outflow tube was plugged with blue tack and taped upright to the side of the microscope). The SAW was excited at 5 mW per IDT (by applying 500 mW to each transducer) as in previous experiments, and alignment occurred in <1

second. An image was taken (with the Hamamatsu Orca camera) under the SWB filter (blue light, to excite calcein in live cells), and immediately after another was taken through the WIG filter (green light, to excite propidium iodide in dead cells). Cells were flown on and more pictures were taken, typically for up to 30 minutes, after which a large proportion of the cell population is dead and aligning in the nDEP region only.

Following the experiment, images were opened in ImageJ. For simplicity, images were thresholded (all pixels made either 1 or 0) and coloured artificially according to the excitation filter used. Adjacent SWB and WIG images were combined by the 'Merge Channels' function.

Separation at 0.0625 S/m

Because experiments at 0.15 S/m showed that many live-stained cells were aligning in the dead, nDEP regions (although pDEP regions were generally up to 100% live cells), further experiments were conducted to try get a binary split of live and dead cells within the channels. For this, the concentration of PI solution in the final suspension was lowered from 10% until 3.5% was found to show good binary separation.

To ensure that 3.5% PI solution was still a sufficient concentration to stain all dead cells, a control experiment was done with dead-only cells suspended in 3.5% PI solution. This, overlayed with a brightfield image to define cells, showed that all cells were stained.

3.4.2 Conductivity-stepping experiments

Cell culture

DPS cells: DPS cells were cultured as discussed earlier, and cells of passage 3-5 were used for experiments. (Cells of later passage were found to have altered

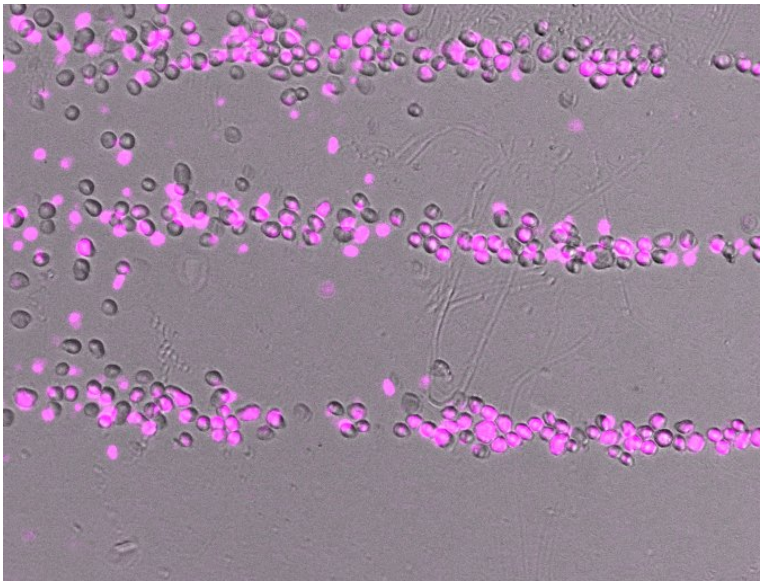

Figure 3.27: Microscope image from control experiment to show that 3.5% (v/v) PI solution still stained all the cells (the manufacturer's instructions are to use 10%). NB the overlay is imperfect because the fluorescent image was taken a few seconds after the brightfield, and there is some cell movement.

crossover characteristics, discussed later.)

MCF7 cells: MCF7 cell line was kindly donated by James Beattie (School of Dentistry, University of Leeds). Those used for these experiments were on passage 37-41. They were cultured in the same way as DPS cells, described earlier.

16HBE cells: 16HBE cell line was donated from Shane McGettrick (School of Dentistry, University of Leeds) and cultured in the same as DPS cells described earlier. Those used for experiments were on passage 15-21.

Composition of buffer solutions

The different conductivity buffers were made by diluting PBS with low conductivity DEP buffer (8.5% sucrose, 0.3% dextrose, 2% BSA (conductivity 0.025 S/m)). These were typically 3.5% PBS, 7.5%, 9%, 10%, 15%, 20%, 25%, 30%.

Conductivity was checked with a conductivity meter (ECTester 11+ multirange, Cole Parmer, UK) calibrated to 0.1413 S/m (Hi-7031L calibration solution, Hannah Instruments, UK), and was typically ~ 0.065 S/m for 3.5%, and ~ 0.37 S/m for 30%.

Cell preparation - DPS cells

Instead of checking all 8 conductivities in one run, each experiment was split into two parts, so that cells were not left for >30 minutes following preparation (after which the increased cell death complicates the results).The same flow cell setup was used as for the previous experiment; prior to the experiment, the fluidics and channel were filled with 7.5% PBS dilution DEP buffer (the first conductivity to be tested).

1. For the first part of the experiment, three T175 flasks of cells were trypsinised as described earlier, split into 5 labelled falcon tubes (3.5%, 7.5%, 9%, 10% and 15%) and washed twice in the appropriate buffer, resuspending to give a final concentration aiming for ~ 10^6 cells per 100 µl, typically ~ 200 µl of final cell suspension per conductivity buffer.

2. Following preparation, the 7.5% sample was injected into the (25 µl) injection loop and flown into the channel. A SAW power of 5 mW (as for previous experiments) was applied to each IDT and flow was halted using a stopper valve, with images taken under brightfield. For each conductivity, 3-5 images were taken, to give a statistically-relevent sample size of generally >1,000 cells, with a minimum of 500 (a note was made of samples with <1,000 cells). Only the first 5-10 µl fraction of the sample was used for experiments, for consistency.

3. After 7.5% had been imaged, the flow cell was flushed with 100 µl of the next conductivity, 9% PBS in DEP buffer, and the process was repeated with the 9% PBS conductivity cell suspension. If the channel became fouled midway through an experiment, the channel would be flushed with 10%

NaOH solution (to dissolve organic matter) and 70% ethanol (to remove any air bubbles), before running at least 150 µl of the next conductivity solution.

4. The order was 7.5%, 9%, 10%, 15%, and finally 3.5%. This is because 3.5% was previously shown to give a good indication of the % of cell death (by counting proportion of cells aligning in nDEP regions), and thus could indicate the maximum amount of cell death during an experiment. (This number was subtracted from cells aligning in nDEP regions in subsequent analysis, so that dead cells in the sample could be ignored.) Cell death, after <30 minutes of experiment time, was generally 3-5%, maximum 7%.

5. For the second part of the experiment, three flasks were trypsinised as before, and cells were suspended in 3.5%, 15%, 20%, 25%, and 30% conductivities. The experiment started on 15%. Because this 15% sample had been tested at the start of (the second part of) the experiment (0 minutes) and the 15% sample in the first part of the experiment was tested in the final 20-25 minutes, the difference between the crossover % of these two samples could be used as an indication for error attributable to cell death variation from the start to finish of the experiment; this was typically 2-10%.

Cell preparation - differences

Because 16HBE cells and MCF7 cells do not stretch out on the adherent plastic like DPS cells, they grow at a higher population density. Thus, to get a similar final concentration of cells (~ 10^6 per 100 µl), only 1 flask of MCF7 cells, and 2 flasks of 16HBE cells were used in their experiments.

Because MCF7 cells have a habit of clumping far worse than the other cell types, each conductivity sample was filtered through a 50 µm filter (Celltrics, Wolf Laboratories, UK) immediately prior to being injected into the microfluidics. Researchers should be warned that they foul the microchannel much more readily, and 10% NaOH solution is recommended as the best way found to dissolve

them quickly.

Chapter 4

Device characterisation with latex beads and yeast cells: Proof of concept experiments and DEP force measurements

4.1 Introduction and chapter summary

4.1.1 Aims of chapter

As discussed in Section 1.4.14, the goal of the experimental work in this thesis was to develop a SAW-DEP cell sorter that would allow high fidelity separation of different cell types, at high throughput and physiologically-relevant conductivities.

This chapter focuses on the use of SAW-DEP device (Figure 4.1**a**) to align latex spheres in the size range 1 µm 10 µm, followed by trial separations of live from dead yeast cells. The key questions addressed in this chapter, together with a summary of findings, are listed below:

1. Can the spacing of bead alignment (Figure 4.1**b**) be predicted according

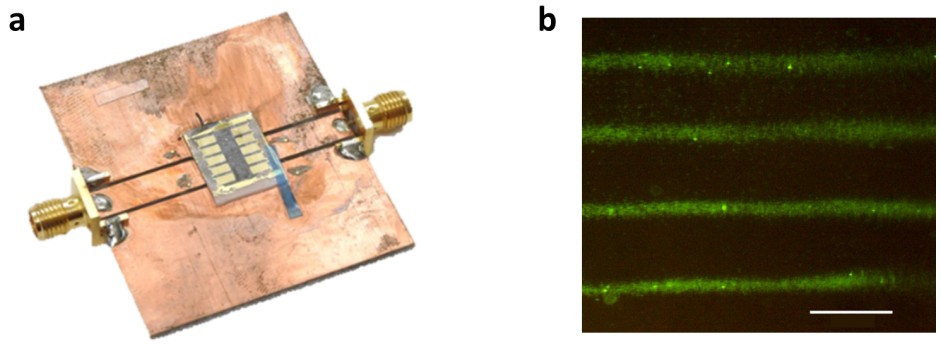

Figure 4.1: **a** Photograph of an early device iteration. **b** Fluorescent microscope image: Proof-of-concept image from the first device iteration, showing fluorescently-labelled 1 µm latex beads being aligned by forces exerted by the device. The scale bar is 100 µm.

to the applied frequency/wavelength, thereby allowing tunable control of particle manipulation?

- *Section 4.2*: Early experiments consisted of pipetting a droplet of latex beads solution onto the surface of a SAW-DEP chip between the transducers, and confining the beads to the surface by overlaying a coverslip. Beads were observed to align by nDEP at a periodicity that matched the SAW device wavelength; however, because the system was not well sealed, alignment was often disturbed due to evaporation. Furthermore, if conductive solutions were used (such as those more relevant to cell separation in clinical settings), alignment was far less uniform, presumably due to convection currents caused by Joule heating by the electrodes, which were (unintentionally) in contact with the fluid.

2. Is the SAW-DEP device still effective at higher, physiologically-relevant fluid conductivities?

- *Section 4.3*: To address this, a new flow cell was designed wherein the particle solution could be confined away from the electrodes within a

microfluidic channel defined in PDMS. With the electrodes now protected from the fluid, an experiment was carried out to test whether the device dissipated energy into the surrounding fluid, by measuring the device's insertion loss as a function of fluidic conductivity within the channel.

3. Can the electrical field gradient and associated force of the SAW-DEP system be mapped out analytically, and supported by experimental evidence? Is particle movement definitely caused by DEP forces and not by acoustic forces (as would be the case for Rayleigh SAW devices)?

    - *Section 4.4*: To show that the force exhibited on the beads was due to DEP and not acoustic forces, bead movement was measured and analysed using particle tracking software, to calculate the force as a function of applied power, bead size, and position in the SAW-DEP field. This was compared to a simple DEP system model, and they were shown to closely match. The low force exerted, while able to achieve alignment, also reinforced the method's potential as being used for a minimally-manipulative cell sorter.

4. Can the device exert both positive and negative DEP forces on particles (namely cells) to produce a binary separation?

    - *Section 4.5*: After characterising the system with beads, the device was used on yeast cells. The device was shown to effectively separate live from dead yeast cells based on differences in their conductive properties, with live cells being enriched into separate lines of 98.7% purity (from a 50:50 starting mix). In addition, modifications to the microfluidic channel were implemented to syphon off SAW-DEP separated cells into separate regions on the device.

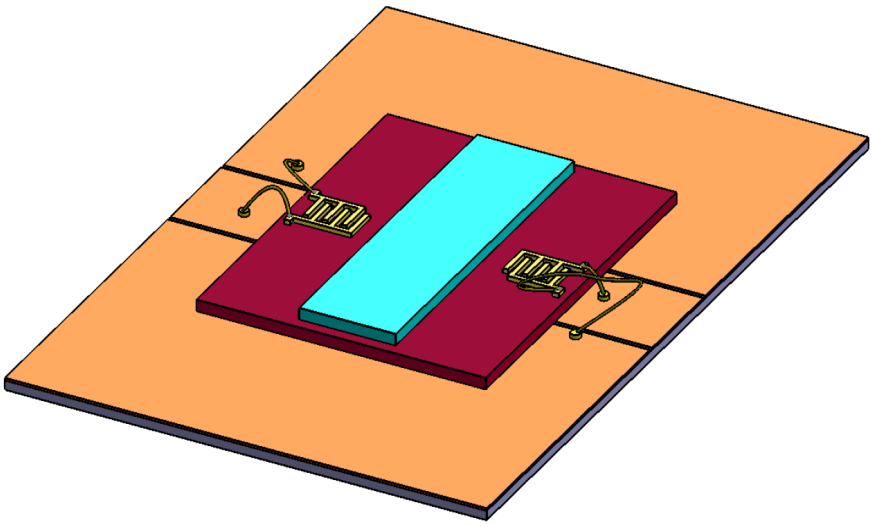

Figure 4.2: Schematic showing the first device iteration. The device consisted of a SAW chip (red) mounted on top of a PCB (orange), with IDTs wirebonded to the PCB. Particle solutions were pipetted onto the chip between the two sets of IDTs, and confined to the surface by overlaying with a glass coverslip (blue).

4.2 First device iteration

4.2.1 DEP properties of latex beads in DI water

Initial experiments consisted of observing latex bead behaviour in a 20 MHz SAW-DEP device (Figure 4.2, fabrication described in Section 3.1.2). To predict latex bead behaviour at the set frequency, a theoretical CM factor of 1 µm latex beads suspended in DI water (10^{-4} S/m) was calculated using Equation 2.2.25 (see Section 2.2.4) (assuming a relative permittivity of latex of 2.56), and this is plotted in Figure 4.3**a**. This graph shows that latex beads are expected to exhibit positive DEP (pDEP) at frequencies below 10 KHz, with crossover at 100 KHz, and negative DEP (nDEP) after 1 MHz. Because the initial device was designed to operate at 20 MHz, any observed alignment would presumably be due to nDEP.

To verify the theoretical calculation of latex bead CM factor at 20 MHz, a basic 'interdigitated transducer' DEP device (i.e. conventional DEP, not SAW-DEP) (see Literature Review 1.4.5) was fabricated using the same electrode design

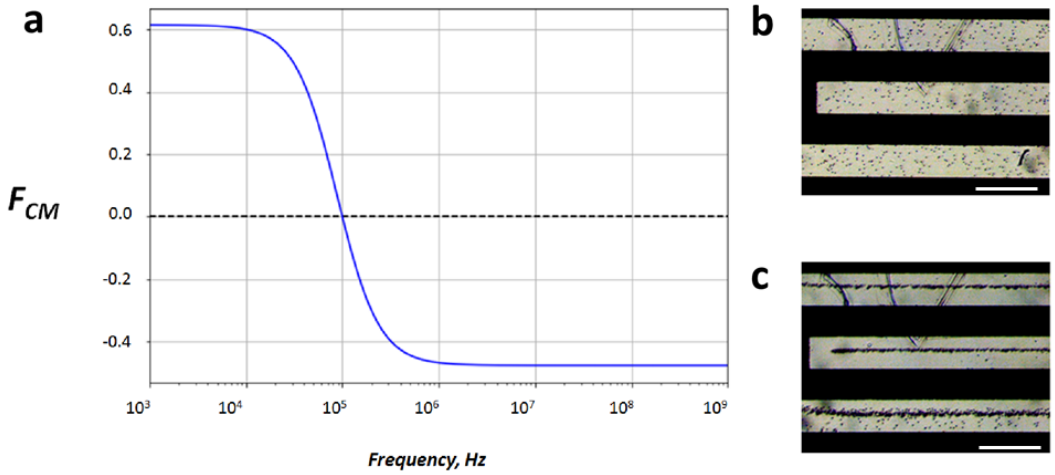

Figure 4.3: **a** Plot of latex bead CM factor against frequency, in DI water. The graph shows that below 100 KHz, particles will experience pDEP, because the CM factor is positive - the particles are more electrically polarisable than the surrounding liquid (DI water) at this frequency, and the electrical field prefers to pass through the particles instead of the liquid; at 100 KHz the CM factor is 0 and the particles will experience no DEP force (i.e. they are at 'crossover' - their polarisability matches that of the liquid at this frequency); and above 100 KHz, the particles are less polarisable by the electric field than the liquid, and experience nDEP. **b** Latex beads on an interdigitated transducer DEP device at 100 KHz (no DEP force). The light areas are the metal (Au) electrodes. **c** Latex beads on an 'interdigitated transducer' DEP device at 20 MHz, exhibiting nDEP (moving to the area of lowest field gradient).

as the 20 MHz SAW device, but patterned onto a glass substrate instead of $LiTaO_3$ (Methods 3.1.1). To test the behaviour of beads, a droplet of latex bead suspension (0.01% m/v) was pipetted onto a set of IDTs and overlaid with a glass coverslip to confine the beads/liquid to the substrate. Immediately after, a signal was applied (from 100 KHz - 100 MHz[1]) and the behaviour of beads was

[1]The signal generator used for this work did not go below 100 KHz frequency. Below this, one could expect to observe positive DEP behaviour, where particles align at the edges of the electrodes.

observed. In such a device, bead alignment by pDEP is expected to occur at the edges of the electrode (highest field gradient), and bead alignment by nDEP is at the top centre of the electrodes (lowest field gradient).

Using this device, as predicted at 100 KHz no DEP behaviour (i.e. no positive or negative alignment) was observed by the beads (i.e. CM factor of 0) (Figure 4.3**b**), and above 1 MHz the beads exhibited nDEP behaviour. This can be observed in Figure 4.3**c**, where beads align at the top centre of the electrodes.

For SAW-DEP experiments, a droplet of solution of 1 µm-diameter latex beads was pipetted between the two electrode pairs, and confined to near the surface using a coverslip (see schematic in Figure 4.2).[1] SAW-DEP behaviour was observed in the 1 mm^2 between the two sets of IDTs in the middle of the chip; Figure 4.4a shows some typical early results demonstrating alignment of beads in the device.

These results showed, firstly, that the pitch of the alignment was very close to the expected wavelength of the SAW, assuming the alignment represented two adjacent antinodes along the standing SAW (see Figure 4.5). At 20 MHz the observed pitch was 107 µm, suggesting a wavelength of 214 µm. At 20 MHz, at a speed of 4,022 m/s, the wavelength would theoretically be expected to be 201.1 µm (using $\nu = f \cdot \lambda$), so the experimental findings were 2.7% higher than our theoretical calculation. This is close enough to assume the alignment was due to the effects of a standing SAW, such a discrepency (i.e. a marginally longer experimental wavelength compared to the design wavelength) is found in almost all SAW devices, due to the mass loading effects of the transducers.

The SAW-DEP devices fabricated in this work tended to have a practical working

[1] A very rough calculation of the channel height was estimated to be ~ 20 µm. This was based on the observation that a 2 µl droplet (i.e. 2 mm^3) spreads out to ~ 10 mm^2, thus the height remaining would be 0.02 mm (0.02 mm x 10 mm x 10 mm = 2 mm^3).

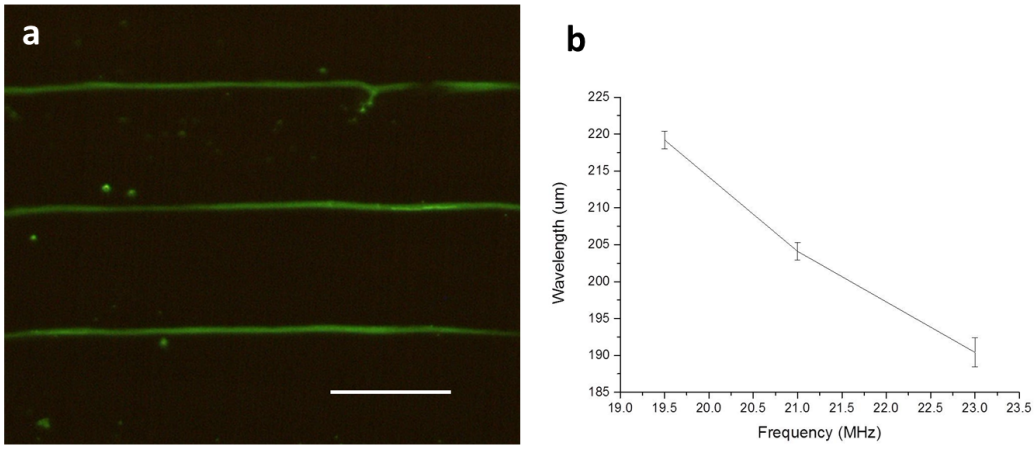

Figure 4.4: **a** Microscope image showing 1 µm beads aligning by nDEP in a SAW-DEP device. The scale bar is 100 µm. **b** Graph showing the measured wavelength of the alignment (i.e. across two antinodes, e.g. between the top and bottom green lines in **a**), at the three separate applied frequencies.

bandwidth of ~ ± 1 MHz around the target frequency[1]. That is, while the highest transmission peak for a 10 MHz-designed device would be found at 10 MHz (measured by S_{21} scattering parameters, typically ~ -20 dB, matched), several secondary peaks (e.g. of >-23 dB) could be found within the 9-11 MHz range. This allowed alignment of beads at different frequencies/wavelengths within this range, as measured in Figure 4.4b. It should be noted that the force on particles becomes much attenuated farther from the resonant frequency, because the insertion loss is larger and thus less power is being coupled into the SAW.

Discussion on observations from first device iteration

One initial observation of beads aligning in the device was that the alignment was very regular and uniform compared with acoustic alignment of microparticles (100, 101, 145), where various (acoustic) standing waves of different wavelengths ('overtones') form within the channel and fluidic streaming disrupts alignment.

[1]The size of the bandwidth in SAW devices is inversely proportional to the number of finger pairs, i.e. in this work 15 pairs for all devices.

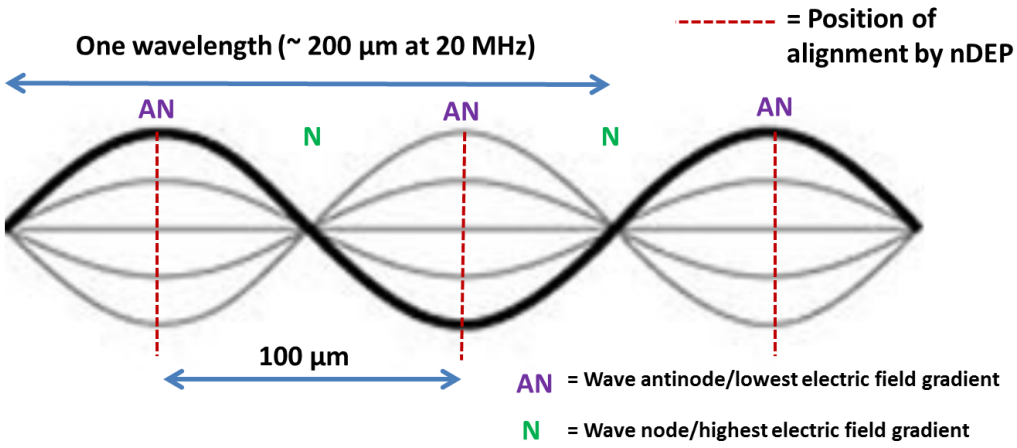

Figure 4.5: Schematic of standing SAW electric field (178), showing where particles align by nDEP. For example, within a SAW wavelength of 200 µm (such as that in a 20 MHz device on $LiTaO_3$), there would be two antinodes (**AN**) and two nodes (**N**) per period of the standing wave. The associated electric field is analogous in periodicity to the SAW (acoustic) field, with the regions of highest and lowest field gradient at the nodes and antinodes of the standing wave, respectively. The latex beads, in this case, would align by nDEP at the antinodes/regions of lowest field gradient (shown by red dotted line).

However, the lines were still noticably sinuous, particularly away from the centre of the droplet/coverslip, and this was thought to be mostly due to evaporation currents which were evident at the edges of the droplet.

With regards to conducting further experiments, the limitations of the early device were that (a.) it was not a closed system and so evaporation occurred continuously, disrupting flow in the channel, and (b.) the electrodes were not kept separate from the fluid. This latter issue is a primary problem with most conventional DEP devices. Indeed, the effect of higher conductivities was investigated using this device - while some alignment was observed at the higher, physiologically-relevant conductivities (i.e. up to 0.1 S/m), it became progressively poorer and unclear to see what was happening to the particles (see Figure 4.6).

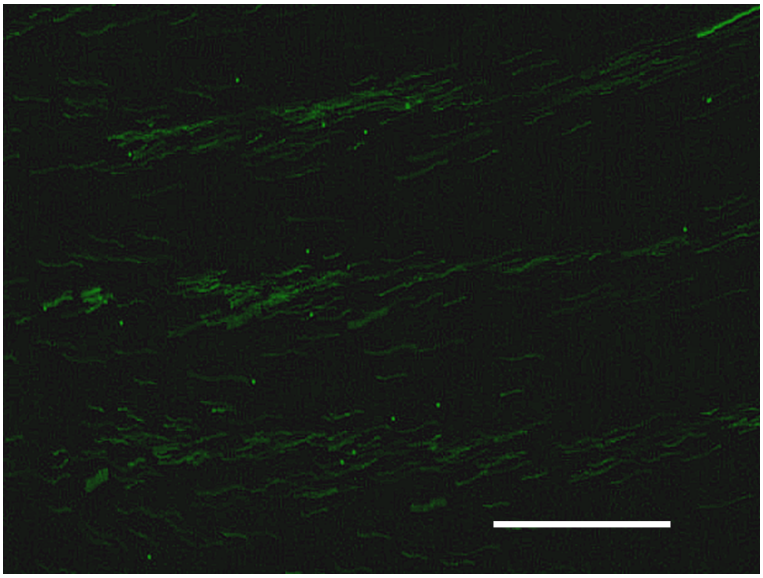

Figure 4.6: Fluorescent microscope image of bead alignment at 0.1 S/m (20 MHz device, scale bar is 100 µm. The uniformity of alignment is noticably poorer than at lower conductivities, and this is thought to be due to disruptive convection currents emanating from the SAW-IDT electrodes, which are not fully confined away from the fluid in this early device.

In summary, these experiments showed that the initial SAW-DEP device was sufficient to produce relatively neat alignment of latex beads in DI water. However, in order to align (and eventually separate) particles in more physiologically-relevant (i.e. higher conductivity) solutions, it was clear that a more sophisticated flow cell design was necessary, to control the flow of liquid, and confine the liquid away from the electrodes; this is discussed in the proceeding section.

4.3 Second device iteration: Flow cell and early findings

4.3.1 Improvements to the device: Acrylic lid design

A second device was designed to address the practical problems manifest in the initial device - namely that the liquid needed to be confined away from the electrodes (i.e. between the two sets of IDTs), and also to administer particle solutions in a more controlled manner. The design for the second device iteration can be seen in Figure 4.7a, and a photograph of the device is shown in Figure 4.7b.

The device consisted of a 2 mm-thick section of PDMS (polydimethylsiloxane, a transparent, rubbery polymer) placed on top of the SAW chip, with a microchannel defined in the PDMS running between the two sets of IDTs (Figure 4.7). A perspex lid was clamped onto a brass plate, sandwiching the PDMS channel in between, and thus applying pressure to seal the channel. While this conformal sealing technique for PDMS cannot withstand as high fluidic pressure as, for example, fabrication techniques like plasma bonding (~ 5 psi compared with ~ 30-50 psi for irreversible sealing like glue and plasma bonding (179)), the advantage was that different channels could be used without having to fabricate new devices; this made it favourable for the rapid prototyping that was being carried out at this stage.

The microchannel cross-section was 50 µm high and 1 mm wide. A height of 50 µm was chosen because it is small enough to confine particles to the surface of the chip (in contact with the electric field), but not too small that large particles like mammalian cells (typically 10-20 µm diameter) would get stuck or block up the channel. The channel was 10 mm in length (between the tubing inflow and outflow holes), although cells were only exposed to the SAW-DEP field for a 1 mm section within the SAW aperture defined by the IDT design (see Section 3.1.1).

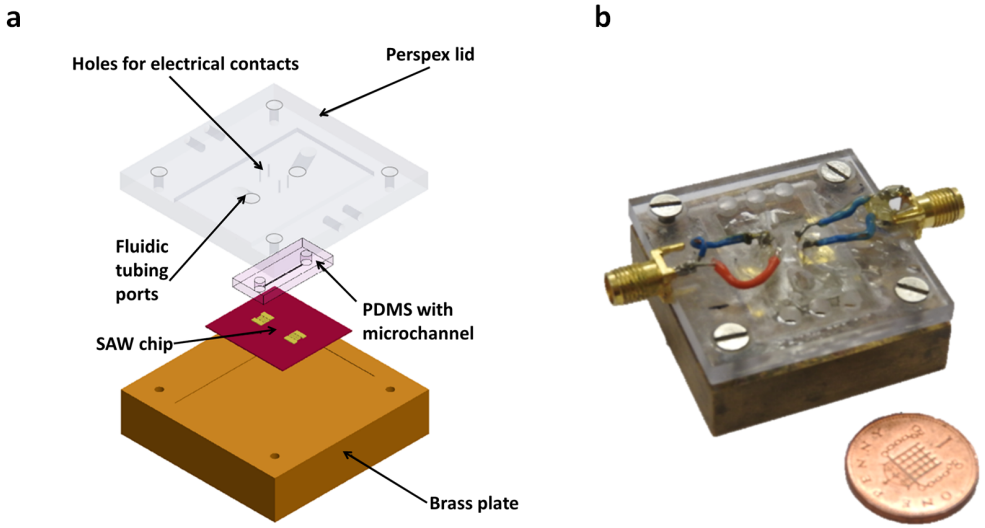

Figure 4.7: **a** Schematic showing the second device iteration. A microchannel defined in PDMS was placed to run between the two sets of IDTs. This is held in place/fluidically sealed by clamping the PDMS onto the chip between a transparent acrylic lid and a brass plate. The lid has holes for fluidic tubing to be pushed into. There are also holes in the lid for electrical contacts, made using pogo pins that pressed onto the IDTs, which were in turn soldered to SMA connectors glued into the side of the lid (shown in Figure 4.7b). **b** Photograph of the second device iteration, with a penny coin (1p) for scale. As well as that discussed in Figure 4.7a, the picture also shows SMA connectors glued into the lids, with wires (red and blue) soldered to pogo pins (inserted into 'Holes for electrical contacts' detailed in **a**) which made direct contact to the IDTs on the SAW chip.

4.3.2 Experimental observations from Perspex lid device: Improved bead alignment, and effect of fluid conductivity of insertion loss

As expected, early results from the device showed that it had successfully overcome the initial limitations of the previous device. Figure 4.8a shows significantly improved alignment of 1 µm beads in a device operating at 9.9 MHz (using a 10

MHz IDT design), unhindered by evaporation or convection currents[1].

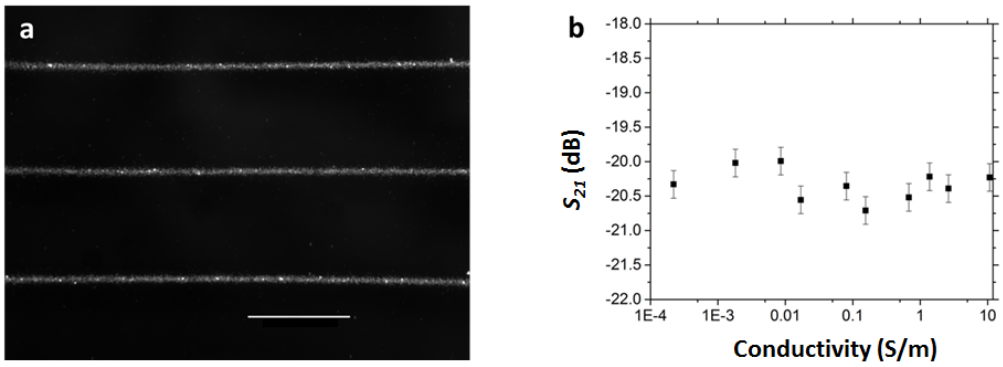

Figure 4.8: **a** Fluorescent microscope image of 1 µm latex beads aligning at 10 MHz, in the acrylic lid flow cell. The scale bar is 200 µm. **b** S_{21} values at 10 MHz as a function of liquid conductivity inside the channel. The graph shows that there is no decrease in SAW transmission (i.e. due to power loss to the liquid) as the liquid conductivity is increased. Note that S_{21} can be converted to insertion loss by simply switching "–" to "+", such that the graph would be mirrored above the x axis.

To verify that higher conductivities did not lead to fluid heating (which as well as generating disruptive convection currents, is also harmful to cells for clinical applications), the effect of fluid conductivity in the channel was measured against the insertion loss of the device in a network analyser (Figure 4.8b). If the device was heating up the surrounding liquid, there would be a corresponding increase decrease in SAW transmission, as measured by the S_{21} (or S_{12}) scattering parameter (as less power was transmitted between the two ports due to heat dissipation). Because Figure 4.8b shows that there is no significant change in insertion loss/S_{21} due to conductivity, this suggests that, as predicted, no electric current is passed from the SAW field into the surrounding substrate.

[1]The spacing of the lines was 207 µm giving the wavelength to be 414 µm. At 9.9 MHz, the expected wavelength is 406 µm, so the discrepancy is +2.0%.

The insertion loss data gave good evidence that no significant energy from the electric field resulting from the SAW is dissipated into the solution, for example, as a current. We note that the electric field is produced from static, bound charges in the substrate, in contrast to excess highly mobile charges in metal electrodes. However, there was not yet convincing evidence to show that the observed alignment of beads was due to an electric field/DEP force, and not in fact the mechanical/acoustic forces that researchers normally exploit in SAW devices. Because force on particles as a function of applied power scales differently for acoustic and DEP forces, this (and other parameters) were investigated in the next section, in order to characterise the force that was being exerted on the particles.

4.4 DEP force measurements on latex beads

4.4.1 Introduction to DEP force measurements

Aim of section

In this section, the movement of latex beads in a SAW-DEP device was tracked by camera in order to quantify the force that was acting on the particles. The purpose of this work was (1) to verify whether the force acting on particles was DEP or acoustic in nature, and (2) to quantify the strength of the force acting on the particles.

Differences between DEP and acoustic forces

DEP and acoustic radiation forces can be distinguished from each other by observing how the force scales to the input power. This can be inferred from the following key equations for DEP and acoustic radiation forces, respectively:

$$\vec{F}_{DEP} = 2\pi r^3 \epsilon_m Re[F_{CM}] \nabla E_{rms}^2 \tag{4.4.1}$$

where r is the particle radius, ϵ_m is the permittivity of the liquid, $Re[F_{CM}]$ is the real part of the Clausius-Mossotti factor, and ∇E_{rms}^2 is the gradient of the square of the electric field. This equation was given previously in Theory Section 2.2.2, Equation 2.2.19.

And:

$$F_x = \frac{4\pi r^3}{3} \frac{\delta P}{\delta x} \tag{4.4.2}$$

where F is the acoustic radiation force (ARF), x is the direction of SAW propagation, r is the particle radius, and P is the pressure as a function of wave

position.

In the case for DEP force (Equation 4.4.1), it can be seen that $\vec{F}_{DEP} \propto \nabla E^2$. Because $E = -\nabla\phi$ (where ϕ is the electrostatic potential - see Section 2.1.5, Equation 2.16), E scales to the applied voltage, u. Due to the fact that $\vec{F}_{DEP} \propto \nabla E^2$, then $\vec{F}_{DEP} \propto u^2$. Because the applied power (e.g. in watts), P, is $\propto u^2$, then it should then be observed that, in the case of DEP, $\vec{F}_{DEP}$ scales linearly with the applied power, P.

On the other hand, in acoustic-based trapping systems, the acoustic radiation force is proportional to the mechanical force, F of the fluid, where $\vec{F}_{ARF} = -|\nabla E|$ (180). Thus, $\vec{F}_{ARF} \propto u \propto \sqrt{P}$, and it should be observed that $\vec{F}_{ARF}$ scales to the square root of the applied power, P.

Typical DEP forces on particles

Cells and other particles (generally 1-15 µm latex beads) have been shown to be trapped by DEP at sub-piconewton (>0.1 pN) forces (181, 182), however, this force can be increased (generally by increasing the applied power) for systems designed to maximise output by increasing the speed or rate of cell trapping, with up to 430 pN reported (183). The amount of force used to trap cells by DEP can generally be tuned by adjusting the voltage applied to the system.

To put these force levels into context, the force on cells by centrifugation is ~ 1.96 nanonewtons (nN) (using F = mass of a cell [1 ng] × acceleration [200 g, where g = 9.8 m/s/s]), to which cells are subjected for >5 minutes. While this is considered a safe, non-harmful technique for enriching cells in tissue culture procedures, it far exceeds the natural forces cells experience in the body, typically in the order of piconewtons, pN. For example, the force exerted by myosin on actin (in the process of muscle contraction) averages ~ 8 pN, and the isometric force of a single kinesin molecule (a common motor protein) is ~ 1.9 pN (184).

Quantifying DEP forces - theoretical and experimental

The DEP force on cells can be calculated analytically using Equation 4.4.1 and assumed values for the DEP device in question (one for this particular system is discussed in Section 4.4.2). These show force maps for how the electric potential (and resulting DEP force) varies across the non-uniform electric field.

It is also desirable to quantify force experimentally by tracking the movement of particles in a DEP device. Major prior studies have tended to simply obtain the average velocity of cells or particles in a system (115, 185), rather than mapping velocity (and extrapolated DEP force) as a function of particle position across the non-uniform electric field.[1] However, the work described in Section 4.4.3 details how a relatively new (2016) particle tracking software (in this case, the Trackmate plugin in ImageJ (165)) was used to map out the movement of individual particles as function of position in the electric field, and subsequently fitted to an analytical model to quantify the DEP force.

The remainder of this section will discuss an analytical model of the DEP system used in this work, followed by experimental results from particle tracking to fully map out the force/electric field at different regions across the channel.

4.4.2 Theoretical modelling of DEP force

An analytical expression for the electric field gradient, and thus the electric field, was calculated by modelling the 'virtual electrodes' on the $LiTaO_3$ substrate as interdigitated electrodes. While this is clearly not an accurate description of the actual experimental situation, it is nevertheless useful as an initial approximation of the resulting DEP force, such that it can be compared with the empirically measured forces. An analytical expression for the electric field generated by interdigitated electrodes has already been described by Morgan *et al.* (115, 132, 186),

[1] The likely reason for this is that because the majority of these studies took place from 1987-1999 (115), computing power was not sufficient, given that today's commercial computers struggle with the particle tracking software.

and the equations used for this work were adapted from these sources.

Modelling the virtual electrodes

The experimental system was modelled using a 2D cross-section model along the channel, i.e. perpendicular to the direction of alignment. As mentioned, the virtual electrodes were modelled as interdigitated electrodes, where the pitch matched the wavelength of the standing SAW. The dimensions of the virtual electrodes were the same as the physical IDTs that generated a 10 MHz SAW on $LiTaO_3$ - i.e. a pitch of 100 µm with a 1:1 mark to space ratio (see Figure 4.9). Analogous to the physical IDTs, an AC potential of 10 MHz is applied to the driven electrodes, while alternative electrodes are grounded. The system was considered to be infinitely high, such that the electric field was not constrained in the positive z-direction. However, the channel height over the electrodes was set to 50 µm, which constrained the movement of the particles in the z-direction.

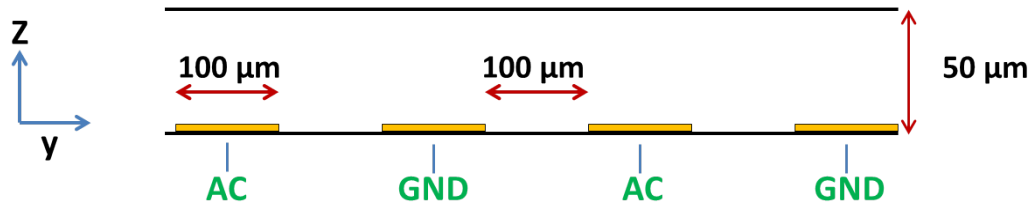

Figure 4.9: Schematic showing the 2D cross-section used to model this work, with the appropriate dimensions used in the calculations. The schematic shows a cross-section of interdigitated transducers (gold colour) in a 50 µm channel, which are alternatingly grounded and driven. Not to scale.

The electric potential along the y-axis was set as constant on the electrode surfaces, and assumed to vary linearly between neighbouring electrodes. If we assume the number of finger pairs to be large, then the potential becomes approximately periodic and can be written as a Fourier series:

$$\phi(y,z) = \sum_{n=0}^{\infty} A_n \cos(k_n y) e^{-k_n z} \tag{4.4.3}$$

where $\phi(y,z)$ is the potential in y (horizontal) and z (vertical) directions, $k_n = (2n+1)\pi/2d$ where $d = 50$ µm is the width of the electrodes, and A_n are the Fourier coefficients. The Fourier coefficients can be worked out and are:

$$A_n = \frac{8V_0}{\pi^2(2n+1)^2} \cos\left(\frac{(2n+1)\pi}{4}\right) \tag{4.4.4}$$

where V_0 is the amplitude of the applied voltage. The quantity of interest to calculate the DEP force resulting from the potential ϕ when it is oscillating with ω is the electric field, which is given by

$$\mathbf{E}(y,z,t) = -\nabla\phi(y,z)\cos(\omega t) \tag{4.4.5}$$

where t is time.

Morgan *et al.* (132) have derived a closed form for the electric field, which in component form is given by:

$$E_y(y,z) = \frac{V_0}{\pi d}\left(\tan^{-1}\left(\frac{\sin(\tilde{y})}{\sinh(\tilde{z})}\right) - \tan^{-1}\left(\frac{\cos(\tilde{y})}{\sinh(\tilde{z})}\right)\right) \tag{4.4.6}$$

$$E_z(y,z) = \frac{V_0}{2\pi d}\ln\left(\frac{(\cosh(\tilde{z})+\cos(\tilde{y}))(\cosh(\tilde{z})+\sin(\tilde{y}))}{(\cosh(\tilde{z})-\cos(\tilde{y}))(\cosh(\tilde{z})-\sin(\tilde{y}))}\right) \tag{4.4.7}$$

where $\tilde{y}$ and $\tilde{z}$ are the normalised coordinates given by

$$\tilde{y} = \frac{\pi y}{2d} + \frac{\pi}{4} \tag{4.4.8}$$

$$\tilde{z} = \frac{\pi z}{2d} \tag{4.4.9}$$

The derivatives of the electric field components can now be calculated and are given by:

$$\frac{\partial E_y}{\partial y} = -\frac{\partial E_y}{\partial y} = \frac{V_0}{d^2}\left(\frac{\sinh(\tilde{z})\cos(\tilde{y})}{\cosh(2\tilde{z}) - \cos(2\tilde{y})} + \frac{\sinh(\tilde{z})\sin(\tilde{y})}{\cosh(2\tilde{z}) + \cos(2\tilde{y})}\right) \quad (4.4.10)$$

$$\frac{\partial E_y}{\partial z} = \frac{\partial E_z}{\partial y} = \frac{V_0}{d^2}\left(\frac{\cosh(\tilde{z})\cos(\tilde{y})}{\cosh(2\tilde{z}) + \cos(2\tilde{y})} - \frac{\cosh(\tilde{z})\sin(\tilde{y})}{\cosh(2\tilde{z}) - \cos(2\tilde{y})}\right) \quad (4.4.11)$$

As discussed in Section 4.4.1, the DEP force is proportional to $\nabla|E^2|$ which can now be expressed by

$$\nabla|E^2| = \nabla(E_y^2 + E_z^2) = 2\hat{\mathbf{y}}\left(E_y\frac{\partial E_y}{\partial y} + E_z\frac{\partial E_z}{\partial y}\right) + 2\hat{\mathbf{z}}\left(E_y\frac{\partial E_z}{\partial y} + E_z\frac{\partial E_z}{\partial z}\right) \quad (4.4.12)$$

where $\hat{\mathbf{y}}$ and $\hat{\mathbf{z}}$ are the unit vectors in the y and z direction, respectively.

Results from analytical approximation

The DEP force resulting from the virtual electrodes when modelled as interdigitated finger electrodes can now be calculated using Equation 4.4.12. The amplitudes of the horizontal (y) and the vertical (z) components of the expected DEP force experienced by a 5 µm diameter latex bead at different positions along the SAW path and at different heights above the surface of the electrodes are shown in Figure 4.10. The applied voltage on the interdigitated finger electrodes was 1 V, the DEP frequency set to 10 MHz, and the surrounding liquid was water, which led to a CM factor for the latex beads of −0.45. The positions of the electrodes are indicated by black bars underneath the figure. It can be seen from the figure that both components of the DEP force decrease with increasing height above the surface of the electrodes.

The component of the DEP force in the y direction has distinct minima at the position where the standing SAW wave features nodes, i.e. at the centre between two electrodes at $\pm 100\mu m$, and, at least above a height of 40 µm, is strongest at positions above the edges of the electrodes (± 50 µm and ± 150 µm, see Figure 4.10).

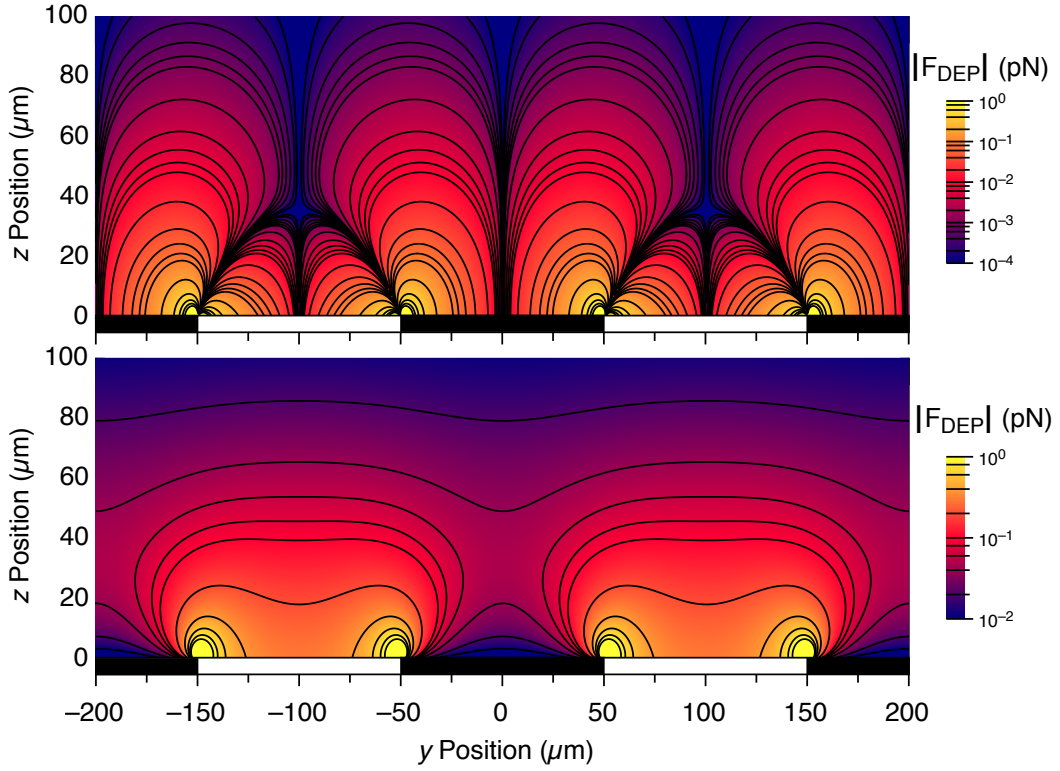

Figure 4.10: Force plot showing the amplitudes of the horizontal (y, top) and vertical (z, bottom) components of the expected DEP force experienced by a 5 µm diameter latex bead at various heights (z position) and horizontal (y position) locations along the SAW path.

In addition, two other types of minima can be observed, the first above the centre of the electrodes, i.e. the positions of the antinodes of the standing SAW. A third type of minima can be observed from the edge of the electrode towards the nodal position. Interestingly, this minima only exists up to a certain height above the channel of just under 40 µm, which corresponds to half the pitch d. As will be discussed below, the third minima can in fact be observed experimentally and leads to distinct shoulders in the measured force profile.

The situation for the vertical component of the DEP force is significantly simpler. It can be seen that the vertical component of the force is, in general, significantly stronger than the horizontal component. This can be seen clearly from Figure

4.11 which shows the vertical and the horizontal component of the DEP force as a function of height above the channel, and at the position y = 50 µm across the channel.

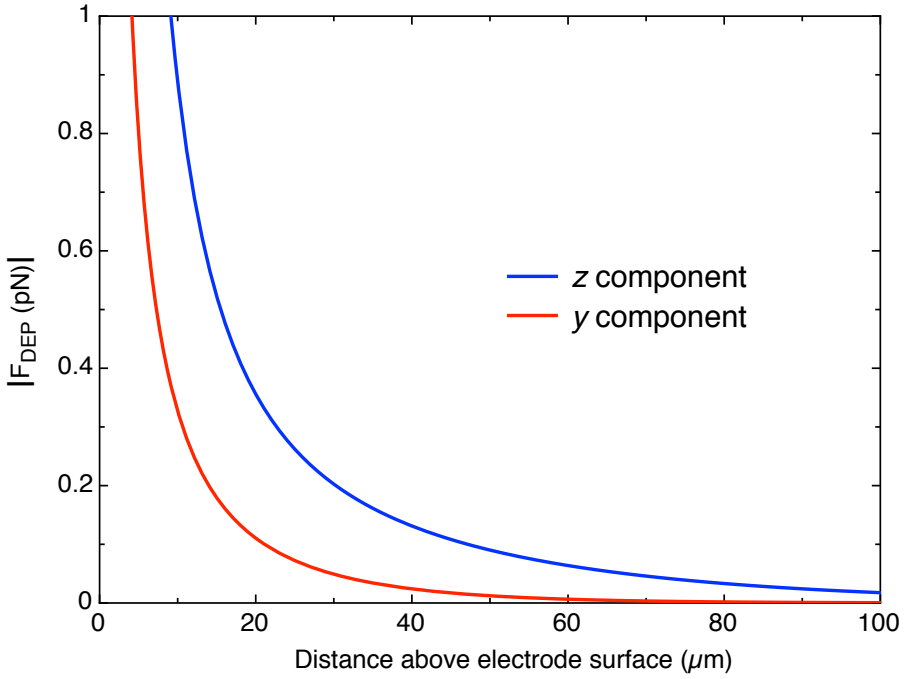

Figure 4.11: Vertical (z) and horizontal (y) components of the DEP force as a function of height above the channel and at $y = 50$ µm, i.e. where the horizontal DEP force is strongest.

Given that the vertical component is significantly bigger than the horizontal component, it can be expected that the latex beads would be pushed up to the top of the channel where they then subsequently align. This fact could be exploited experimentally by using fluidic channels of different height where the beads would then experience a different force profile during alignment. This is illustrated in Figure 4.12 which shows the horizontal component of the DEP force, i.e. the component which leads to bead trapping or alignment, at different heights above the surface of the electrodes. Here, the effect of the third minima becomes apparent. The inset of Figure 4.12 shows a magnification of the area between 50 µm and 150 µm, and for the lowest height, 20 µm (red curve), three

distinct roots exists, but they gradually merge into one as the height is increased, and at a height of 50 µm, only a slight shoulder-like feature is left.

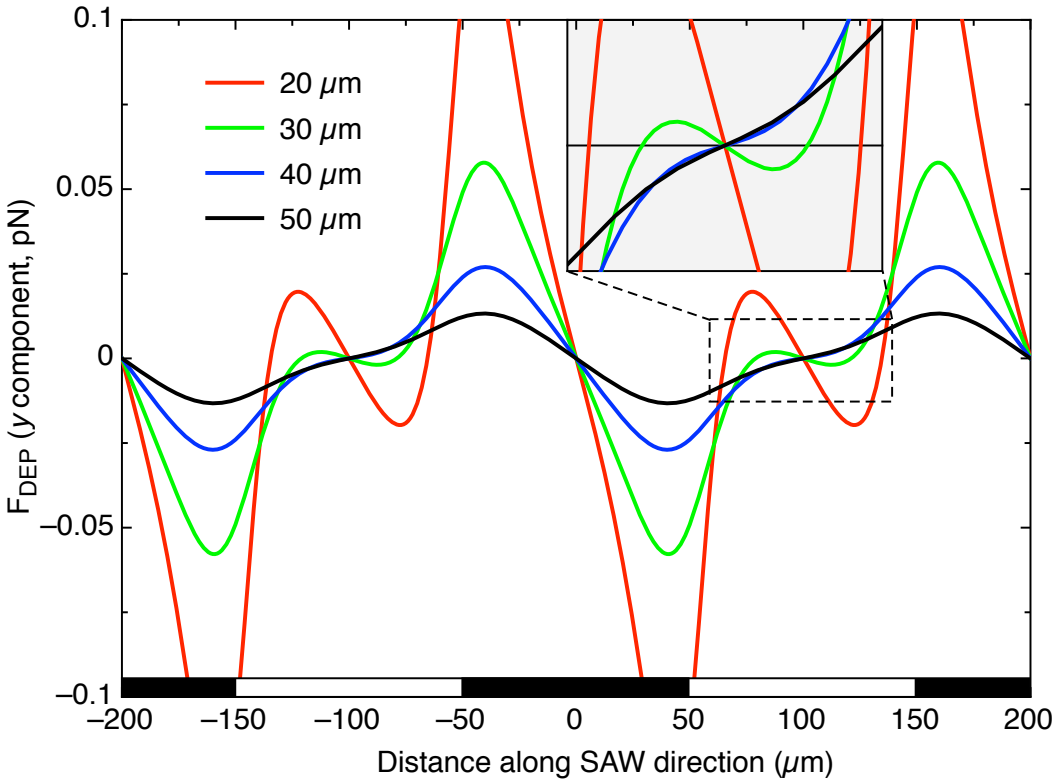

Figure 4.12: Horizontal component of the DEP force at different heights (20, 30, 40, and 50 µm) above the surface of the electrodes. The inset shows a magnification of the area between 50 µm and 150 µm.

This work focused on a height of 50 µm, where only a single nDEP trapping position is expected, while at the same time still reasonably large DEP forces exist.

4.4.3 Experimental determination of DEP force on latex beads

How the data was gathered

The full methodology for this section is given in the Theory Chapter 3.2.3. The DEP force acting on latex beads of various sizes — 3, 5, and 10 µm — was determined at a range of input powers (0.03 to 1 mW), in order to characterise the SAW-DEP device. To do this, videos were recorded of latex beads aligning in a device featuring a 50 µm-high channel and at an applied ac voltage of 10 MHz. Particle tracking software (Trackmate, together with ImageJ) was then used to track the position of several hundred beads per condition frame-by-frame to establish the position of the beads as a function of time.

Four separate snapshots from a raw video of bead alignment before the Trackmate analysis are shown in Figure 4.13**a** - *n.b.* the full videos contained 100 – 500 frames, at 16 or 30 frames per second (fps). The steps by which Trackmate tracks particles' positions is shown in Figure 4.13**b**. Figure 4.13**c** is a snapshot from the Trackmate process, which shows how the software has drawn the path that each individual bead has taken over the course of the video. From here, a datasheet can be exported (e.g. in the form of a .xml file) which has information on each bead's position in x and y over every frame of the video.

How the data was analysed

The tracks of each bead's position over time were analysed to extract the force acting on the beads, using a custom-developed software. The steps to finding the DEP force were as follows:

1. For an individual bead, its y-position as a function of time, obtained via the constant frame-rate of the recorded video, was fitted locally at each time point with a quadratic polynomial. Ten points either side of the considered time point were used for the local fit, and from the fitted quadratic

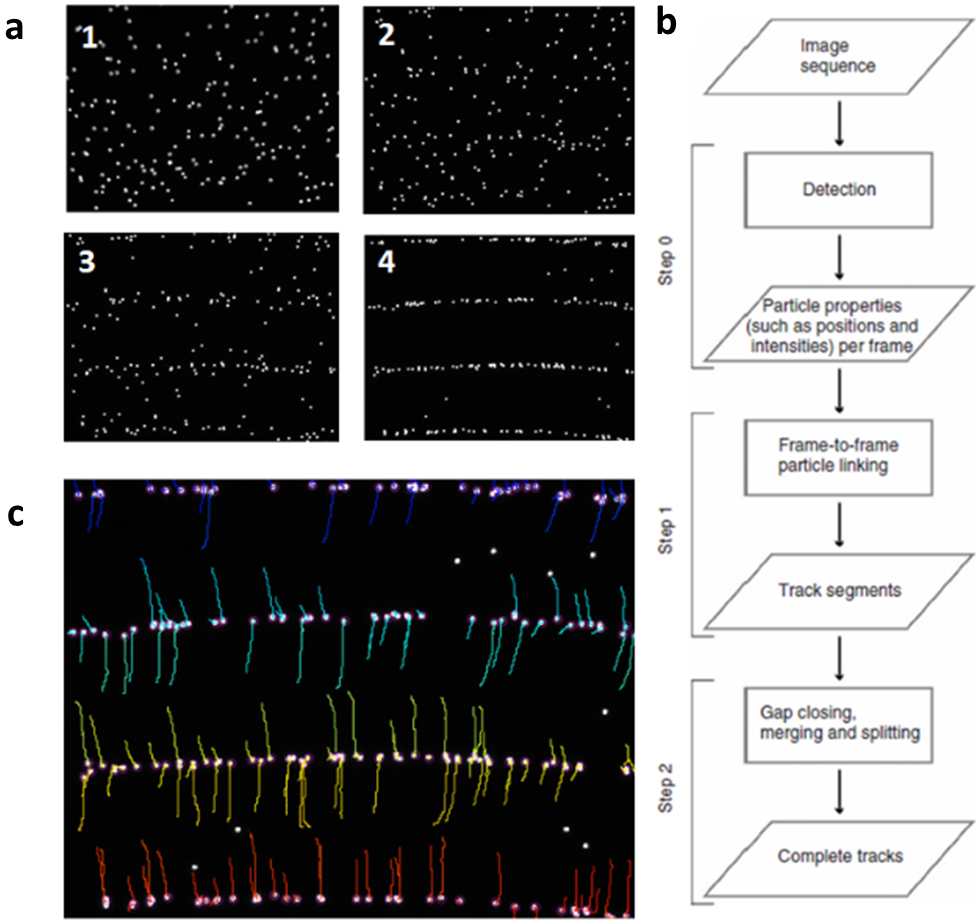

Figure 4.13: Overview of particle tracking in Trackmate. (a.) Sample of raw image sequence (NB full image sequences were 100-500 frames, depending on alignment time (taken at 16 or 30 fps). The frame size is 650 x 850 µm. (b.) Processing sequence, from (165) (c.) Screenshot of particle (bead) tracks taken during processing of videos in TrackMate. Beads (white) are shown pictured at the end of the video sample; the coloured 'tails' show their path from the start of the video (typically a few seconds). Beads which do not have a pink ring or tail attached have been de-selected from analysis, normally because they were observed to not move throughout the video, presumably because they are stuck to the PDMS channel. The frame size is 650 x 850 µm.

polynomial the velocity at each time-point was obtained via the derivate of

the local fit. This yielded the velocity in y as a function of time, i.e. $v(t)$. We note that the x-component of the particle movement was a result of the fluid-flow with which the beads were injected into the fluidic channel and hence assumed to be irrelevant for extracting the DEP force.

2. The same process as for the y-position as a function of time was repeated for the velocity in y as a function of time to obtain the acceleration of the bead first as a function of time, and then, via $t(y)$, i.e. the inverse of $y(t)$, as a function of y.

3. To calculate the DEP force (F_{DEP}), it was assumed that the only forces acting on the particle in the y direction are the DEP force and the drag force (which act in opposite direction), and hence:

$$F_{\text{total}} = ma(y) = F_{DEP} - F_{drag} \tag{4.4.13}$$

where m is the mass of the bead, and $a(y)$ the acceleration at each position. The drag force is given by the Stokes drag, $F_{drag}(y) = 6\pi r\eta v(y)$, where η is the fluid viscosity and r the Stokes radius of the particle (which we assume to be the bead radius). Both the mass and the acceleration were found to be very small, and ma was several orders of magnitude lower than the drag force, and hence

$$F_{DEP} = F_{drag} = 6\pi r\eta v(y) \tag{4.4.14}$$

Therefore, $F_{DEP_i}(y)$, where i refers to the i^{th} particle analysed, could be calculated for each tracked particles.

4. Typically 200 – 1,000 particles were tracked per parameter set (i.e. ~ 50 particles for larger (10 µm) beads, ~ 1000 particles for smaller (3 µm) beads per video, and typically 3–4 videos were per bead size and power level, to get a large sample size), and all $F_{DEP_i}(y)$ functions for each condition were then averaged to yield $F_{DEP}(y)$.

Results from particle tracking analysis

Figure 4.14**a** depicts a representative image of 5 µm diameter latex beads in water aligned into several lines using SAW-DEP at an applied power of 4 dBm. The coloured 'tails' show the motion paths of the beads, as tracked by the software. Figure 4.14**b** shows the DEP force experienced by the latex beads measured by analysing the tracks of 286 beads (red solid circles). The positions where the beads aligned taken from **a** are indicated by blue arrows, and correspond to positions in the force profile where the force is zero as expected.

The maximum force experienced by the particles is approximately 5 pN. Interestingly, at the positions where the beads align, the force profile exhibits a distinct shoulder, reminiscent of the shoulder that is predicted by the analytical model presented above. Indeed, a fit of the model to the experimentally determined DEP force data, shown as a dotted line in the figure, represents the data surprisingly well, including the shoulder in the force profile. This is remarkable, given that the employed model is very basic. For example, the model assumes the virtual electrodes generated by the standing SAW to be analogous to physical electrodes with constant potentials (and thus zero electric field) across the entire electrode. In addition, the model is assumed to be semi-infinite, i.e. the acoustic aperture is infinitely wide, and the dielectric layer above (water) is infinitely thick. Both assumptions are not an accurate representation of the actual experimental situation, but nevertheless, the model is capable of representing the data sufficiently.

To characterise the system in more detail, the DEP force experienced by particle of different size (3, 5, and 10 µm diameter) were investigated under different applied powers (-11 dBm – 4 dBm; not all powers were used for all beads as for example for the 3 µm the lowest power settings did not produce enough force to lead to any meaningful alignment, and for the 10 µm the highest powers led to very fast alignment which could not be temporally resolved with the equipment used).

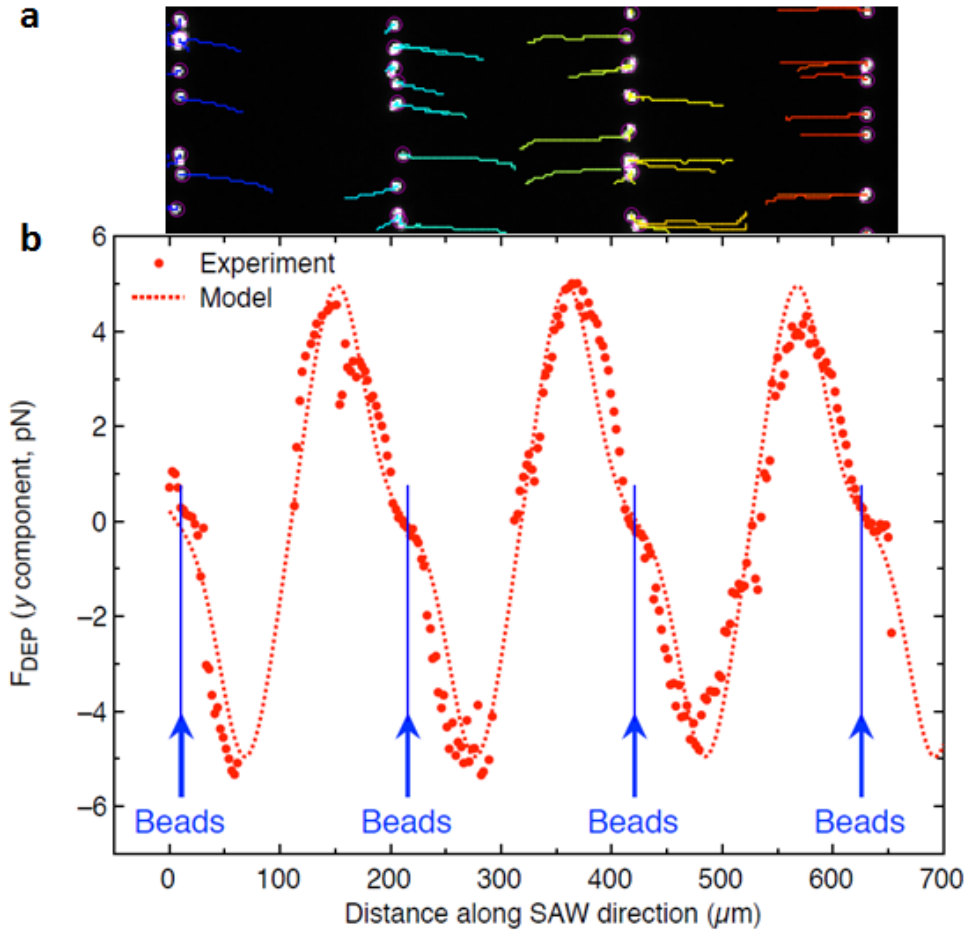

Figure 4.14: **a** Representative image of 5 µm latex beads in water aligned into several lines using SAW-DEP at an applied power of 4 dBm. The coloured 'tails' show the motion paths of the beads, as tracked by the software. **b** Force measurements from tracking bead movement at various positions along the SAW standing wave. Blue lines mark where beads finally aligned, corresponding to the alignment seen in **a**.

The results for 5 µm beads at various power levels are shown in Figure 4.15**a** (similar results for 3 µm and 10 µm beads can be found in the Appendix C.1, Figure C.1). Note that the force profiles for the different applied powers are all vertically centred around zero force, but are offset vertically for clarity of presentation. The analytical model was fitted to each experimentally measured

force profile with V_0 as the only free parameter, and all fits are shown as solid lines in the respective graphs. It can be seen that the model fits the behaviour of all beads at all employed powers reasonably well, in particular when taking into account the limitations of the model.

Figure 4.15**b** shows the voltages obtained from the fitting for the three different bead-sizes as a function of the applied power to the SAW transducers. As can be seen, the correlation of the obtained voltages between the different bead sizes is very high.

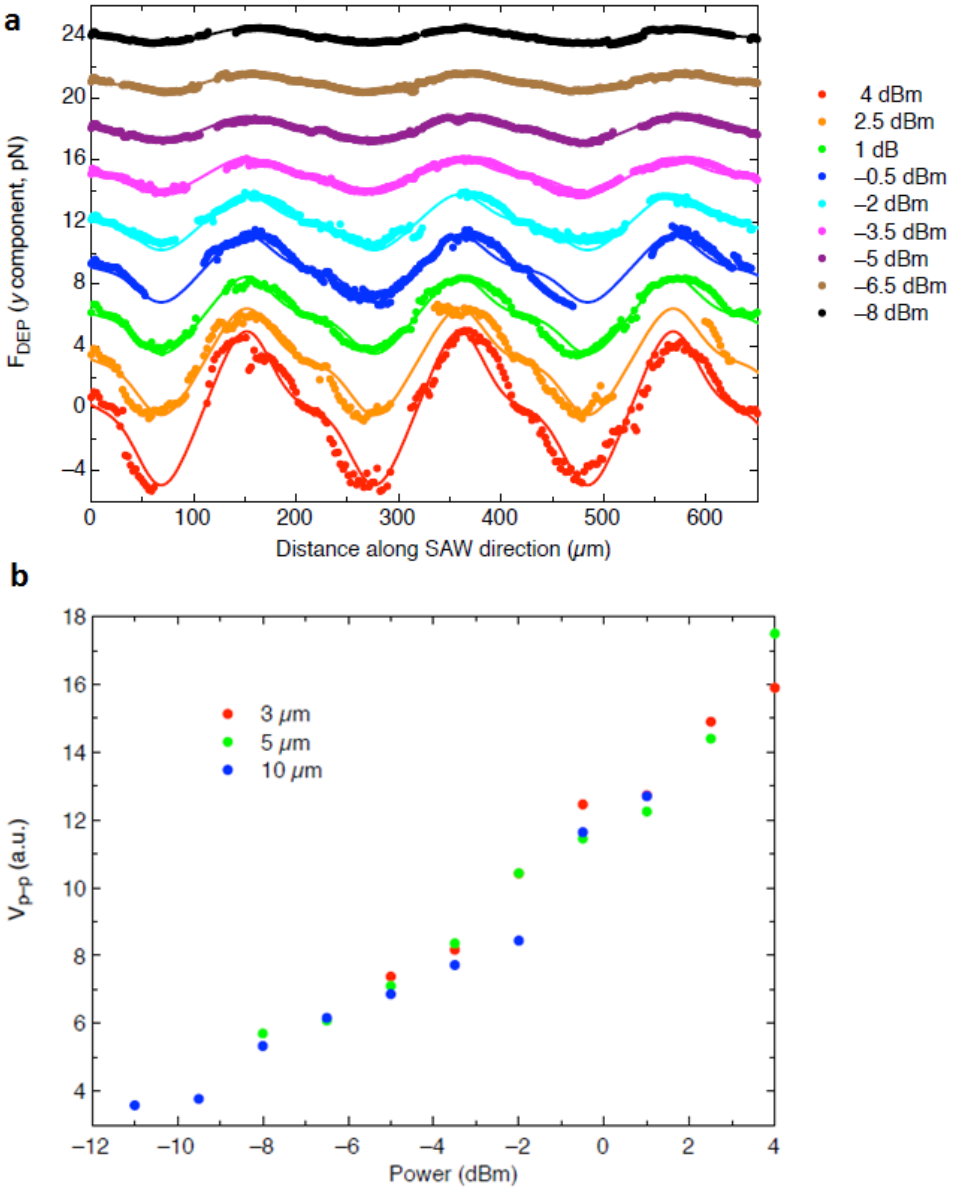

Figure 4.15: **a** Force measurements from tracking movement of 5 µm beads at various positions along the SAW standing wave, for various power input levels (different colours). **b** Voltages obtained from the fitting for the 3, 5, and 10 µm beads as a function of the applied power to the SAW transducers.

4.4.4 Section summary

The results provided in Figure 4.15 show that SAW-DEP can align latex beads in a consistent and predictable manner, such that the analytical expression can now be used to reliably predict DEP force for a range of bead sizes (3-10 µm) and applied voltages.

Figure 4.16 shows the peak DEP force (in the y direction) experienced by 5 µm beads at a range of power levels. The data was fitted to a square root equation and a linear equation, to verify whether the force is acoustic or DEP in nature, respectively.

It can be seen that in the case of the square root equation, the line is not within the error margin of a single point ($1/\chi^2 = 0.0003$), while the linear fit equation is within the error margin of seven out of the nine datapoints ($1/\chi^2 = 0.545$). This shows that there is a far better fit to a linear equation rather than a square root equation and therefore, *a propos* the discussion in Section 4.4.1, the experimental data strongly indicitates that particles are subjected to a DEP force and not an acoustic force.

While the forces in the y direction measured by particle tracking were all <10 pN (and therefore likely to be suitable for cell manipulation), the analytical expression did imply that the force experienced by particles in the z direction was approximately an order of magnitude higher (i.e. up to 100 pN), and so particles are rapidly pushed upwards in z before aligning in the y axis. To track this movement in z empirically would have required a radically different experimental setup, and so this was not investigated in this work due to time constraints.

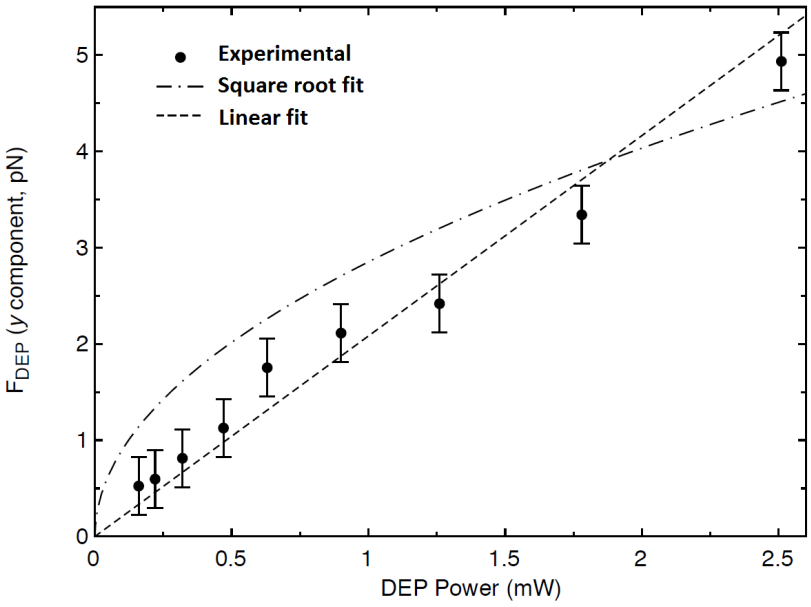

Figure 4.16: Line graph showing the peak DEP force in the y direction experienced by 5 µm latex beads as a function of applied power, with a linear fit line.

4.5 Positive and negative DEP separation of live and dead yeast cells

4.5.1 Overview

Following on from characterising the device by manipulation of latex beads, separation of live from dead yeast cells was investigated to demonstrate that the technology could be used on living cells. This also afforded the opportunity to show positive DEP in the device, because latex beads will only experience negative DEP in the 10 and 20 MHz devices used in this work.[1]

The separation of live from dead yeast cells is a classic demonstration of separating two cell types by positive and negative dielectrophoresis (103, 114, 124, 185, 187), having been done first by Pohl and Hawk in 1966 (114). Live and dead cells are dielectrophoretically distinct due to differences in cytoplasm conductivity - in dead or dying cells, the cell membrane starts structurally disintegrating, such that the electrolytes it normally holds in the cell cytoplasm start to diffuse out into the surrounding fluid.

The advantages of using yeast cells (generally *Saccharomyces cerevisiae*, otherwise known as baker's yeast) are that they are ~ 5 µm in diameter and easily imaged using a reflection light microscope (unlike bacterial cells, which are typically ~ 1 µm diameter). Secondly, they can be flowed into microfluidics in simple salt solutions without badly fouling the microchannel or apoptosing, which are issues when using mammalian cells. Thirdly, they are very easy to culture (after which they can be stored for several days before use), and lastly they are incredibly cheap, with one tub of Allinson's Yeast from Morrisons (£2.80) (Figure 4.17a) lasting the entirety of this research.

[1] Latex beads will demonstrate pDEP below 10 KHz; however, a SAW device chip on $LiTaO_3$ at this frequency would have to be 1,000 times longer than the current 10 MHz devices, assuming the same number of finger pairs was used.

The CM factor as a response to frequency for live and dead yeast cells is shown in Figure 4.17b (188). This is calculated using the Dual Shell Model described in Section 2.2.4. By plotting the CM factor as a function of frequency, researchers can use this to find the optimum frequency at which the separation of two cell types (into pDEP and nDEP) can be achieved (for example in the beige-shaded regions in Figure 4.17b).

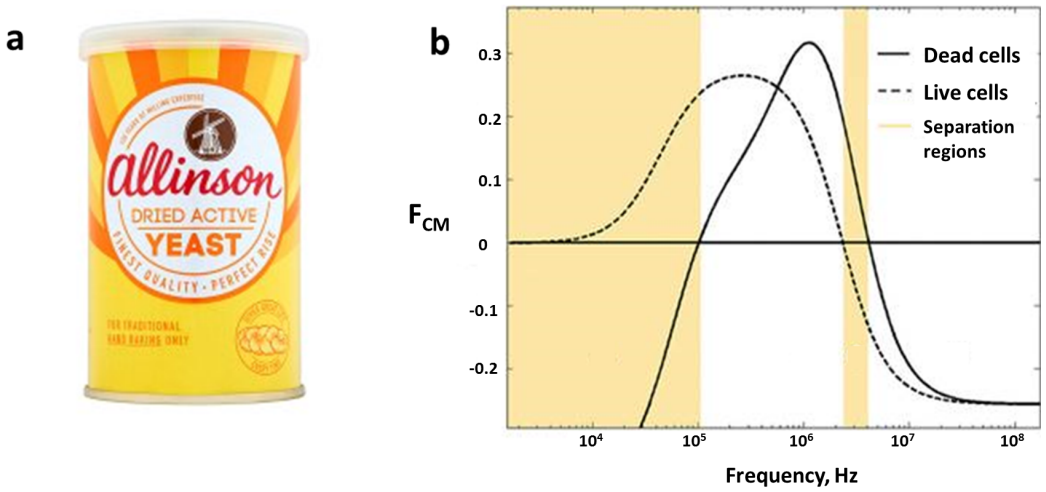

Figure 4.17: **a** Tub of commerical baker's yeast used for the research **b** Example DEP response of live and dead yeast cells, as a function of frequency (188).

In SAW-DEP, the frequency is fixed to that at which the device was designed to operate (i.e. the devices used in this work could only be operated at close to 10 or 20 MHz). Although this restriction could be considered to be a disadvantage compared to conventional DEP, a key advantage of SAW-DEP is that it can be performed at much higher fluid conductivities; therefore, variation of the fluid conductivity can be used to tune DEP behaviour, much as altering the operating frequency is used in conventional DEP. Figure 4.18 shows the DEP response of live and dead yeast (*S. cerevisiae*) cells as a function of conductivity. Calculations were made using a Dual Shell Model (see Section 2.2.4) and biophysical values for yeast from (103), with altered cytoplasm conductivity (0.515 S/m for live yeast, 0.075 S/m for dead yeast) to match experimental findings.

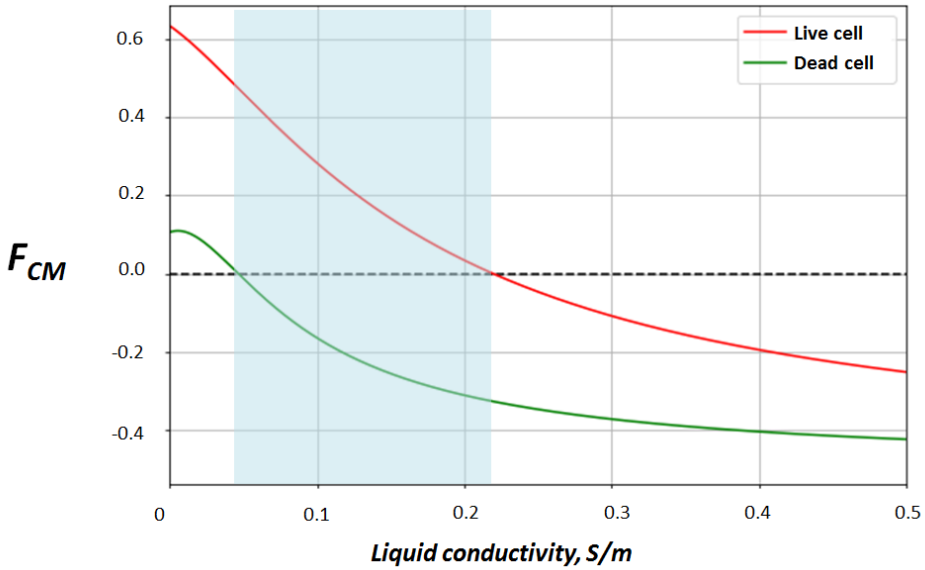

Figure 4.18: DEP response of live and dead yeast cells, as a function of conductivity. From 0 to 0.05 S/m liquid conductivity, both live and dead cells (red and green lines, respectively) will experience pDEP. From 0.05 to 0.21 S/m (light blue highlighted region) live yeast cells will experience pDEP, while dead yeast cells will experience nDEP; thus, between these conductivities, the two cell types can become physically separated in a 10 MHz DEP system. Above 0.21 S/m, both cell types will experience nDEP.

4.5.2 Separating live and dead yeast cells at 10 MHz and 20 MHz

A liquid conductivity of 0.15 S/m was chosen to separate live and dead cells in 10 and 20 MHz devices. This was made by diluting PBS solution in DI water to a 0.1x PBS solution. Live and dead yeast cells were prepared as described in Section 3.2.4, with dead yeast cells finally being stained (blue) using Trypan blue solution. Separation was achieved, as shown in Figure 4.19. Figures 4.19a and 4.19b show separation of live and dead yeast cells at 10 and 20 MHz, respectively. As a demonstration, a multi-channel separator channel was also designed for 10 MHz devices (design and fabrication described in Section 3.2.4), which enabled live and dead cells to be directed into physically separated sub-channels following

SAW-DEP separation.

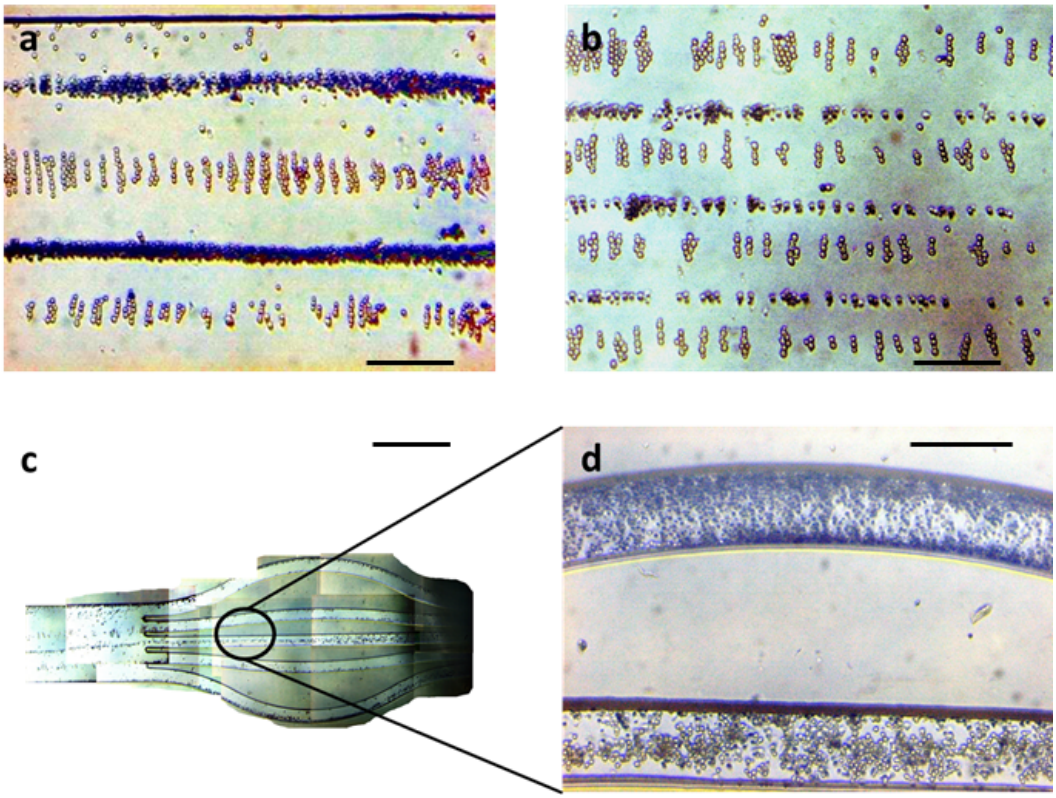

Figure 4.19: **a** and **b** Separation of live from dead yeast cells at 10 and 20 MHz, respectively. Scale bars 100 µm. **c** overview (scale bar 500 µm) and **d** close up (scale bar 100 µm) - directing live and dead cells into separate channels via SAW-DEP (10 MHz).

By analysing pictures of separation occuring within the channel (examples of which are provided in Figures 4.19a and b), 9,209 cells were counted (credit to Roberts Rimša) to verify what proportion of live and dead cells aligned in either the pDEP or nDEP regions. Enrichment was found to be 97% and ~ 99% for live and dead cells, respectively.

To show that raising or lowering the fluid conductivity could cause both cell types to experience negative or positive DEP, respectively, the effect of the SAW-DEP

electric field was examined when cells were suspended in 0.75 S/m (0.5x PBS) and 0.015 S/m (0.01x PBS) solutions. This is shown in Figures 4.20**a** and **b**, where both cell types (live, white and dead, blue) are seen to align together and are not spatially separated. The presence of pearl chaining in the 0.015 S/m experiment (**b**) indicates that the cells are undergoing pDEP, while the lack thereof in the 0.75 S/m experiment (**a**) is indicative of nDEP.

Tests were also carried out to make sure that the Trypan blue stain was not in any way influencing the DEP behaviour of the cells. Unstained live and dead cells were flowed in separately, and the images were spliced together, as shown in Figure 4.20**c**, to show that they still aligned in separate regions of the channel.

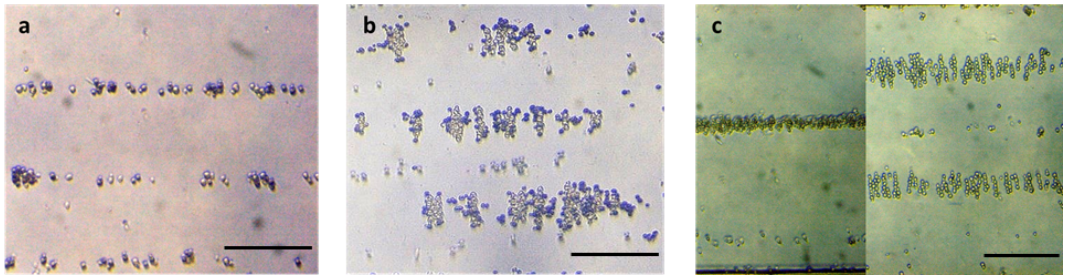

Figure 4.20: **a** Live and dead yeast cells (white and blue, respectively) experiencing nDEP at a conductivity of 0.75 S/m (10 MHz, scale bar is 200 µm). **b** Live and dead yeast cells experiencing predominantly pDEP (regions of pearl chaining) at 0.015 S/m (20 MHz, scale bar is 100 µm). Some dead cells (blue) also experience nDEP - there also appear to be some white (live) cells in these regions, however, these are actually reflections of the dead cells. **c** Unstained dead cells (left) and live cells (right) undergoing nDEP and pDEP, respectively, at 0.15 S/m, to show that the Trypan blue stain had no effect on the DEP behaviour of the cells (10 MHz, scale bar is 100 µm).

4.5.3 Section summary and end of chapter conclusions

In summary, the work separating live and dead yeast cells provided further proof that the force exerted on particles was in fact a DEP force. This is demonstrated

by the observation of both positive and negative DEP, where cells of different polarisabilities aligned in different regions, thus confirming that it was DEP, and not acoustic forces that were responsible for alignment. This notion can also be reinforced by considering that acoustic forces would never result in pearl chaining; simarly, using the CM factor calculations to predict where cells would align when the conductivity was modulated can only be achieved through DEP, not acoustic forces.

The nature of the cell separation shown in Figure 4.19 provided proof that SAW-DEP can be used to sort cells in a precise, efficient manner. The potential of SAW-DEP in the field of cell sorting was further emphasised by the statistical evidence of 97-99% separation efficiency. The next logical step was to investigate separation of a more clinically-relevant cell type, and this is addressed in the following two experimental chapters.

One major limitation of the Perspex-lid flow cell setup was that it performed poorly when attempting to achieve continuous throughput of cells. This was mainly because the tubing was too large (1/16") such that cells tended to sediment when flowed through at a rate slow enough to allow cell alignment, and also because the Perspex lid formed a poor seal with both the tubing on top, and the PDMS, meaning that leaking often occurred in these regions during experiments.

As a continuation from this work, the next chapter will primarily address the following two questions: 1.) Is the throughput that can be achieved with this device sufficient for that required in clinical applications? 2.) Is the electric field associated with SAW-DEP likely to cause harm to cells during sorting procedures?

Chapter 5

Cell viability and differentiation potential of dental pulp stromal cells following SAW-DEP: Assessing for detrimental effects

5.1 Introduction and chapter summary

Following the device characterisation and the separation of live and dead yeast cells as described in the last section, the next steps were to use the technology to separate clinically-relevant cells, and determine if this had any detrimental effects on cell viability and differentation ability. Before this could be addressed, however, it was necessary to adapt the device flow cell to provide a better fluidic seal for continuous throughput and post-SAW-DEP cell collection.

The questions to be answered in this Chapter included:

1. Can the device flow cell be adapted to efficiently sort live and dead mammalian cells at a clinically-relevant rate, for subsequent extraction and testing of the cells following exposure to SAW-DEP?

- *Section 5.2*: Improvements were made to the flow cell design to allow for better fluidic sealing. The main adjustment was to plasma-bond the PDMS microchannel onto the chip, and push PTFE tubing directly into the PDMS for delivery of cells. A stable assembly was made by 3D-printing an ABS-plastic flow cell. At the maximum power setting (1 mW applied power to the IDTs), live and dead cells could be separated at a flow rate of 3 µl/min, ~ 500 cells/second. The recovery rate (extraction of inflowed cells) was 75%, with 25% of cells lost due to fouling or sedimentation within the fluidics.

2. Does exposure to SAW-DEP adversely affect cell viability?

   - *Section 5.3*: Dental pulp stromal cells were chosen as a clinically-relevant cell type to model the technology; these cells are from the mesenchymal lineage, are similar to bone marrow stromal cells and contain cells that are capable of differentiating along the ostogenic lineage. Cells were separated by SAW-DEP under settings that enrich for live cells, and afterwards assessed for viability by flow cytometry. The effect of the SAW-DEP electric field was found to have no statistical significance on the viability of the cells.

3. Is cell viability affected by any factors other than the electric field in the SAW-DEP procedure?

   - *Section 5.4*: Other factors were found to have a significant effect on cell viability, namely the microfluidic procedure (subjecting cells to shear forces), time spent out of the incubator/appropriate tissue culture medium, and the constituents of the DEP buffer medium. The latter factor was investigated more thoroughly, to find that adding bovine serum albumin (BSA) to the DEP buffer led to greatly improved cell viability.

4. Are dental pulp stromal cells that are separated by SAW-DEP still capable of undergoing normal osteogenic differentiation?

- *Section 5.5*: As well as remaining viable, it was important that the differentiation ability of stem cells was not adversely affected by SAW-DEP. Dental pulp stromal cells were separated by SAW-DEP and then cultured in an osteogenic medium. Various tests were carried out during culture, namely for alkaline phosphatise expression and mineralisation (Figure 5.1). These tests showed no change in differentiation ability of cells that had undergone SAW-DEP separation.

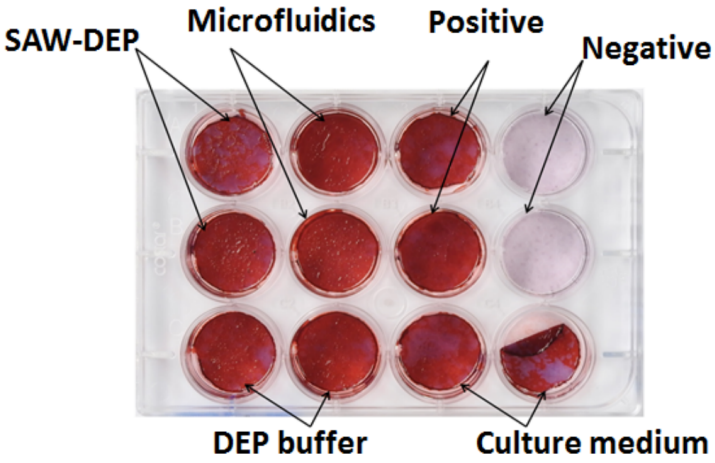

Figure 5.1: Photograph of mineralisation stain (red colour), for illustrative purposes (full description in Section 5.5.3).

5.2 Third device iteration: Adaptions for continuous throughput and extraction

A full description of the fabrication methods to produce the third device iteration are provided in Section 3.1.4. This subsection aims to summarise the key improvements made to this device (Figure 7.3) compared with the previous 'Perspex lid' design (Figure 5.3), in order to permit more advanced SAW-DEP experiments to be carried out in this chapter.

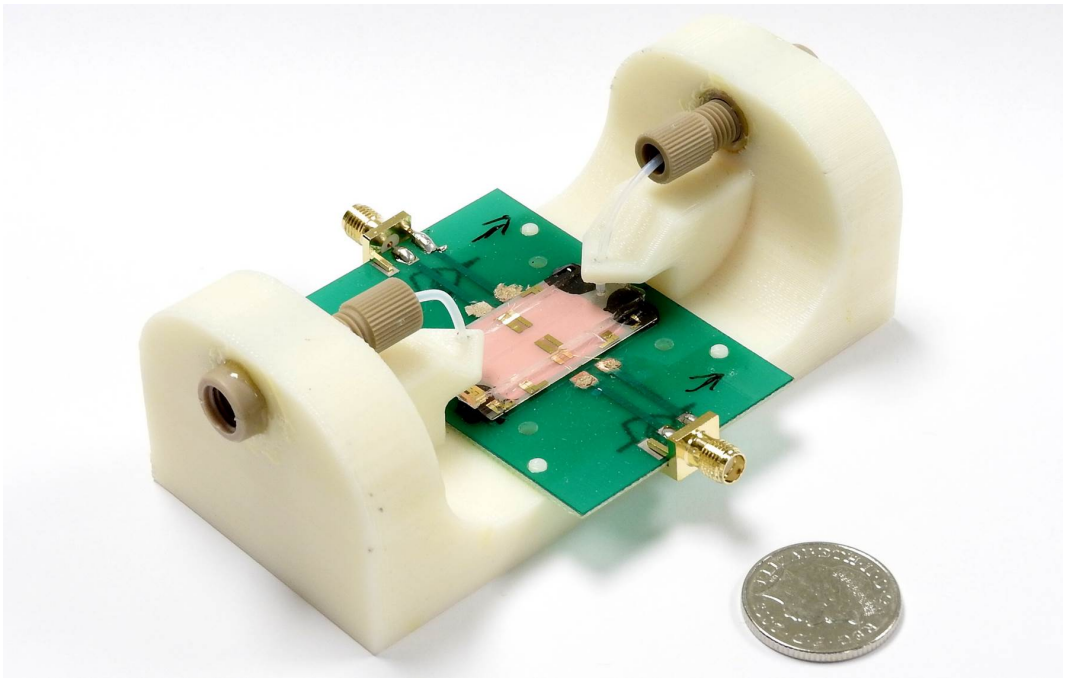

Figure 5.2: Photograph of the device used for this chapter. A PDMS microchannel was plasma-bonded onto the $LiTaO_3$ chip, which was mounted onto a PCB. Fluidic tubing was held in place via a 3D printed flow cell.

5.2.1 PDMS to chip: Improvements to fluidic sealing

The flow cell design used in the previous chapter, seen in Figure 5.3, was suitable for flowing cells onto a SAW-DEP chip where they could be separated and pho-

tographed. However, when trying to perform SAW-DEP while cells were flowed through at a continuous rate, and attempting to extract the cells afterwards, issues with poor fluidic sealing led to inconsistent flow rates and inadequate recovery of cells. The main points of leakage came from the interfaces where the (silicone) tubing was pushed into the fluidic tubing ports in the Perspex lid, and the interface of the underside of the fluidic tubing ports met the PDMS. Even if these interfaces are eliminated (for example, by pushing tubing directly into PDMS), the fluidic seal of a PDMS microchannel that has been 'conformally sealed' to the chip in this way (i.e. pressure-sealed, not chemically bonded) is far inferior to that of PDMS that has been chemically bonded (e.g. by glue or plasma-bonding). While chemically-bonded interfaces can withstand pressures of 2 - 3.5 Bar, those which have been conformally sealed can only withstand about 0.35 Bar (179).

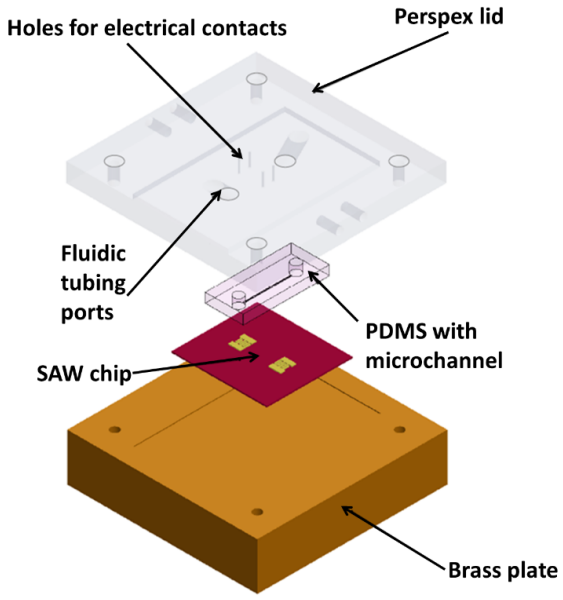

Figure 5.3: Schematic of the flow cell design described in the previous chapter. The major problem with the design was that leaking occured on top of the Perspex lid, at the interface between the silicone tubing and the tubing ports, and underneath the lid where the tubing ports mated with the PDMS.

The main adaption decided upon was to irreversibly seal PDMS microchannels by plasma-bonding to the chip, and to push tubing directly into the PDMS. This can be seen in Figure 5.4**a**. It should be noted that by irreversibly sealing the PDMS, the chip could not be disassembled to wipe clean the surface of devices after the experiment, as was the procedure for earlier devices. However, the ability to withstand far greater fluid pressures without leaking meant that the microchannel could be cleaned instead by flushing the channel with various cleaning solutions (typically 70% ethanol solution or 5% Decon90 solution (a surfactant)).

To accomodate these adaptions, the width of SAW devices (the fluidic channel axis) was increased from 18 mm to 38 mm. This was to allow room for a microscope objective to fit above the device whilst being able to focus on the channel (Figure 5.4**b**).[1] To avoid tubing being pushed flat onto the SAW-DEP surface (and blocking flow), the tubing was cut at a 45° angle (Figure 5.4**c**).

5.2.2 Device assembly: Practical considerations

The chip and plasma-bonded PDMS were mounted on top of a PCB to which the IDTs were wire-bonded, similar to that used for the first device iteration (Section 4.2). In order to hold tubing in place (which was important for minimising the pressure and subsequent deforming that the tubing might exert on the channel) a flow cell was manufactured out of ABS plastic by 3D printing (Figure 5.5). In terms of practical considerations, this additive manufacturing process was also far cheaper than the subtractive manufacturing process used to machine the Perspex lid flow cell, bringing the price down from ~ £500 to £5.[2] (A similar saving in cost and processing time was made by 3D-printing the moulds for

[1] The fluidic ports in the Perspex lid design (Figure 5.3) allowed tubing to be pushed in at a 45° angle, such that the chips could be smaller (to save costs) while still allowing space for a microscope objective. However, creating 45° inlet holes directly in PDMS is difficult to do in a consistent manner, and stress from the tubing can deform the channel, compromising the fluidic seal.

[2] Later flow cells were manufactured on a 3D printer that was built in-house, where the cost of manufacture reflected mainly just the raw material value, of around £0.50 per device.

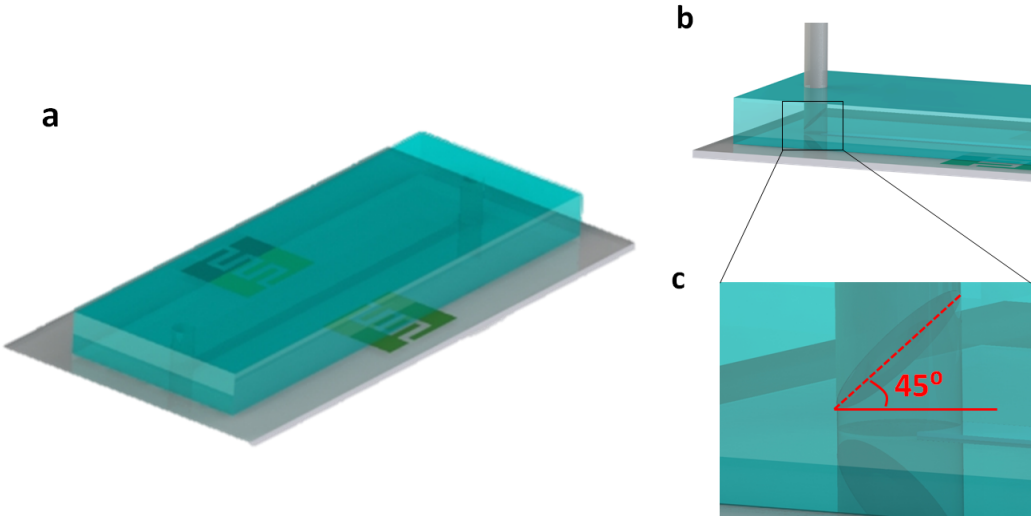

Figure 5.4: **a** Schematic of a PDMS channel bonded onto a SAW $LiTaO_3$ microchip. **b** Schematic of PTFE tubing going into a fluidic inlet/outlet in the PDMS. **c** Close up to show how tubing was cut at a 45 ° angle; cutting the tubing flat would have risked blocking the flow if the tubing was pushed against the substrate.

the PDMS microfluidic channel, as opposed to using cleanroom techniques - see Section 3.1.4.)

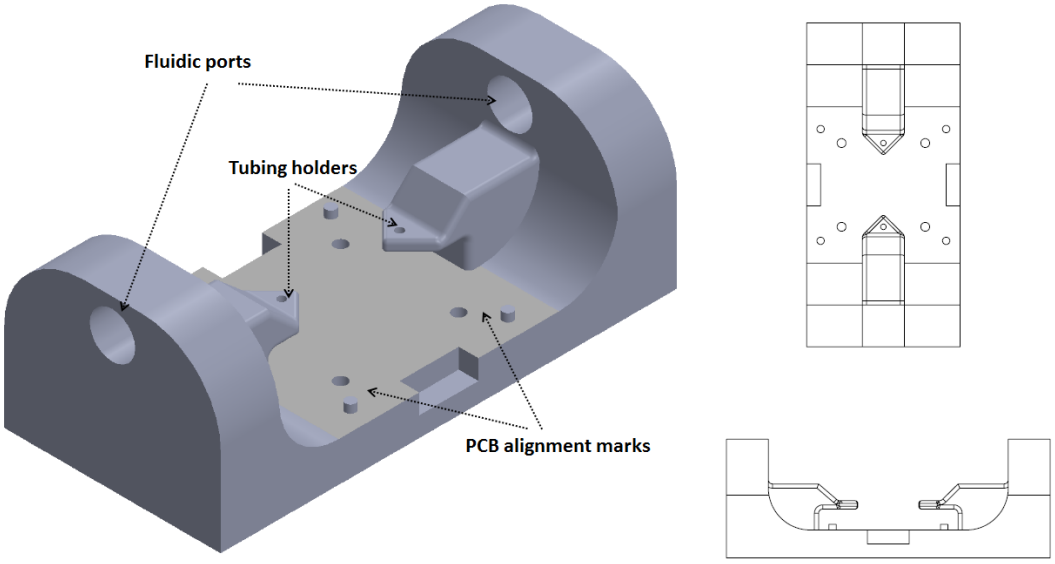

Figure 5.5: Snapshots from the design file for the 3D-printed flow cell. The file was converted into a .stl file and sent directly to a 3D printer.

5.2.3 Fluidic setup: Continuous throughput and minimising sedimentation

A fluidic setup was used that allowed for continuous throughput and collection of cells, shown in Figure 5.6. A full description, together with photographs of the setup can be found in Section 3.1.5. In brief, care was taken to minimise the tubing inner diameter (ID) so as to increase the flow velocity of cells and minimise the effects of sedimentation. For example, the sedimentation velocity for mammalian cells in aqueous buffers is typically 0.020-0.040 mm/s (34), while the flow velocity in the 1/16″ ID silicone tubing used for the 'Perspex lid' experiments was only 0.025 mm/s, at the 3 µl/min flow rate used in this chapter to separate cells; this is not sufficient to overcome the sedimentation velocity of the cells.

Cells were delivered to the chip via an injection port on Valve 2 (see Figure 3.1.5), thus minimising the amount of tubing that they had to be flowed through before reaching the chip. The tubing had an ID of 0.25 mm, such that the flow velocity at 3 µl/min was 1 mm/s. This was sufficient to overcome the sedimentation velocity of cells, and also matched the ID of the PDMS microchannel. The chip was positioned at a gentle incline ($\sim 5°$) from the injection port (in Valve 2), which further minimised the the chance of cells sedimenting and getting stuck in the tubing before reaching the chip.

5.2.4 DEP buffer solutions: Adaptions for mammalian cells

A summary of the buffer solution constituents and their role in the solution is given in Table 5.1. The solution in which cells are suspended has a considerable impact on how much fouling occurs within the fluidics, as well as the viability of cells during and after the experiment. The adaptions made to the DEP buffer solution are outlined below.

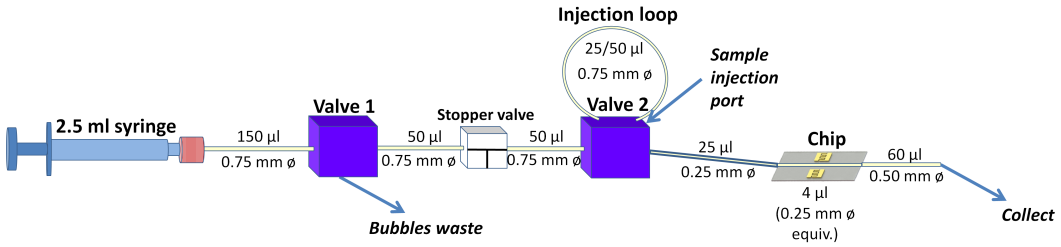

Figure 5.6: Schematic showing the fluidic connections used in this chapter. The cell suspension was injected into a sample loop held by Valve 2. From Valve 2, the sample was led to the chip via 0.25 mm ⌀ tubing at a gentle incline. From the chip, cells were directed into an outflow collection tube (a 15 ml Eppendorf tube). A full description of the fluidic setup shown here is given in Section 3.1.5.

The first consideration was to adjust the osmotic potential of the solution to match that inside the cells, ~ 300 mOsm/l. This is not an issue for yeast cells, which are surrounded by a mechanically robust cell wall that can withstand high osmotic pressures. For example, the 0.1X PBS solution (~ 30 mOsm/l) used in the yeast cell experiments (Section 4.5) would have been strongly hypotonic to the yeast cell, causing water to diffuse into it. If this occured in a mammalian cell, which lacks the strong cell wall support structure, the cell would swell and burst.

For DEP buffer solutions, researchers typically add the sugar, sucrose, to the solution (8-10% m/v), which has the effect of isotonically balancing the solution to ~ 300 mOsm/l without significantly raising the conductivity of the solution, which needs to be kept low to maximise DEP efficiency (56, 107, 143, 189).

To minimise cells sticking together, many groups add the chelating agent EDTA (ethylenediaminetetraacetic acid) (0.02-0.03% m/v) to the solution (e.g. (56)), which acts to chelate Ca^{2+} ions, which otherwise facilitate the forming of cell-cell junctions, causing cells to clump together. Similarly, adding the serum protein, bovine serum albumin (BSA) (0.05-2% m/v) to solutions coats the surface of the microfluidics and the cells themselves, therefore blocking non-specific binding

sites, and further minimising clumping and fouling.

HEPES (4-[2-hydroxyethyl]-1-piperazineethanesulfonic acid) buffer is often added (0.25-0.6% m/v) (56) to keep the pH stable (ideally 6.8-7.4) and minimise stress on cells. HEPES is used over, for example, TRIS or phosphate buffers because it is zwitterionic and therefore only minimally raises the net conductivity of the solution.

Finally, NaCl is added (typically <0.01% m/v) to adjust the conductivity to the desired value. The precise proportions of EDTA, BSA, and HEPES were picked based on various influential papers (56, 107, 143, 189); NaCl was then added to adjust the conductivity to 0.15 S/m (chosen to enrich live cells from a heterogenous mixture of live and dead), and sucrose was added to adjust the osmolarity to 300 mOsm/l (the osmolarity of the solution was calculated used a Numerical Python (NumPy) script - see Appendix B.4).

Table 5.1: SAW-DEP buffer solution constituents

Constituent	**Proportion, m/v (molarity)**	**Role**
EDTA	0.02% (0.68 mM)	Chelating agent, binds Ca^{2+} to prevent cell-cell junction formation and subsequent clumping
BSA	2% (0.3 mM)	Serum protein, blocks non-specific binding sites on device surfaces
HEPES buffer	0.59% (25 mM)	Keep pH stable, without significantly raising solution conductivity
KOH	(~ 100 µM)	Potassium hydroxide (strongly alkaline). To adjust the pH to 7.2-7.4 after addition of HEPES (which is typically ~ pH 5.8)
NaCl	~ 0.05%	To adjust the conductivity to modulate DEP-behaviour of cells
Sucrose	7.5% (219 mM)	To adjust the osmotic potential, without significantly raising the conductivity of the solution
Dextrose (D-glucose)	0.03% (1.7 mM)	Food source for cells. (*N.b.* sucrose itself cannot be taken up by cells unless it is digested into glucose and fructose, typically by stomach enzymes.)

5.3 Investigating mammalian cell viability following SAW-DEP separation

5.3.1 Section overview

In this section, the viability of cells after having undergone SAW-DEP separation was assessed to determine whether the procedure had a harmful effect on cells. Because the proposed application of this technology is for separated cells to be re-introduced back into a patient during surgery, maintaining high levels of viability is paramount to its efficacy (for reasons discussed in Literature Review 1.1.2).

5.3.2 Previous work examing the effects of DEP on cell viability

Two major studies have previously examined the effects on DEP separation/exposure on the subsequent health characteristics of cells (110, 190). The study by Archer *et al.* (190) studied cells (a fibroblast - i.e. connective tissue/skin - cell line) which had been trapped by positive DEP (pDEP) at 5 MHz for 15 minutes. Compared to a positive control (same conditions, except with no electric field/DEP-trapping), the authors found that trapping the cells had no effect on cell metabolism, as measured by an MTT (3-[4,5-dimethylthiazol-2-yl]-2,5-diphenyltetrazolium bromide) assay.

As well as the electric field/DEP-trapping itself, Puttaswarmy *et al.* (2010) (110) noted three key factors likely to cause damage to cells during DEP separation, summarised as:

1. The effect of charging the cell via the electric field
2. Suspending the cells in a non-physiological medium
3. Shear stresses on cells induced by the microfluidic flow

Specifically, Puttaswarmy *et al.* (2010) (110) examined the effect of buffer composition (i.e. point 2) on an hepatocyte (liver cell) cell line. Cells were trapped by negative DEP (nDEP) for 15-120 minutes, following which the viability was assessed by fluorescent staining (live/dead) and subsequent image analysis. The authors found that cells held in the optimised buffer (containing DMEM culture medium) for 120 minutes had 80% viability compared with 0% viability for cells held in a standard DEP buffer (HEPES and sucrose).

Further questions addressed in this work

One of the key differences in the work presented here is that primary human cells were used, as opposed to cell lines. Cell lines are genetically engineered to produce 'immortal' cells that can be expanded almost indefinitely, and are regarded to be more robust than actual primary donor/patient cells; therefore, using primary cells gives a more definitive answer to the likely effects of DEP separation in a clinical setting.

Another difference is that the work presented here used flow cytometry to count viable to non-viable cells, processing roughly ~ 1 million cells to give a statistically significant dataset. Finally, the effect of all three factors listed by Puttaswarmy *et al.* (2010) (110) (electric field, microfluidic shear forces, and buffer composition) were addressed in one experiment.

5.3.3 Experimental design

Choice of cells

Dental pulp stromal cells (DPS cells) were chosen as a clinically-relevant primary cell type to investigate viability (see Figure 5.7). These are mesenchymal cells which are found in the tooth stroma, and, due to the presence of a significant proportion of stem cells, are capable of differentiating into a number of tissue types, with the capability of differentiating into bone tissue the most important for this research. As a practical consideration, it is easy to obtain primary DPS

cells from donors (compared with bone marrow stem cells, for example), because of the large numbers of patients who get teeth extracted.

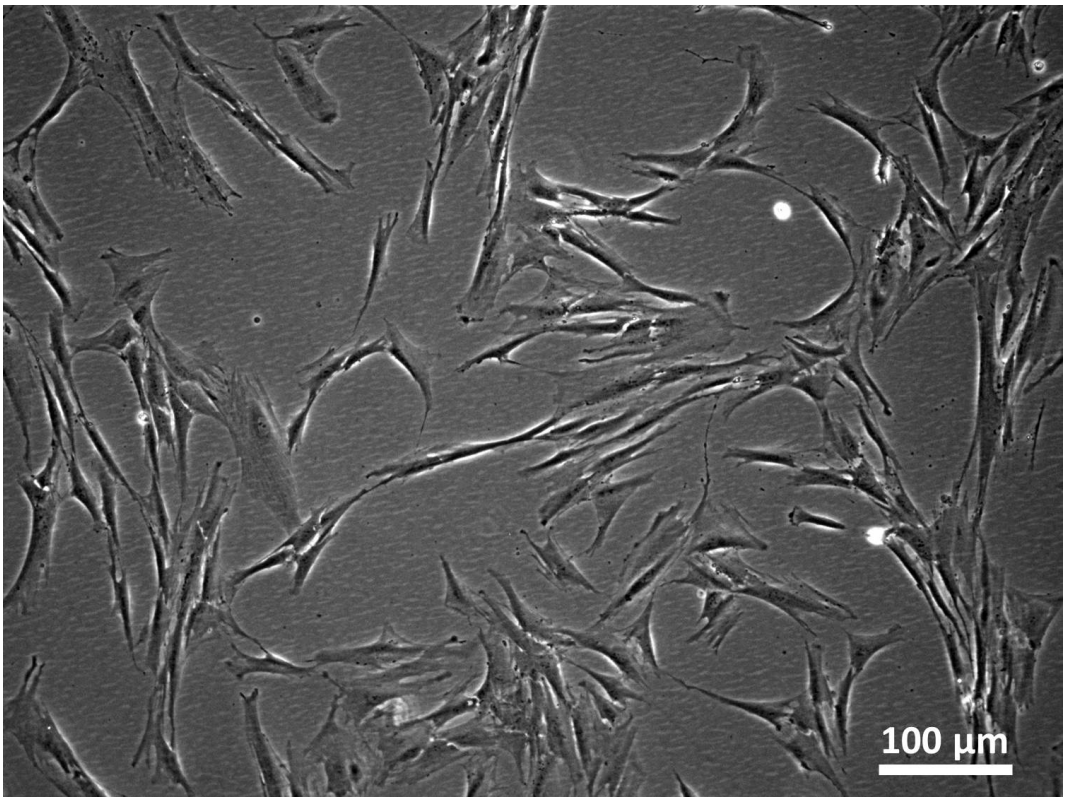

Figure 5.7: Phase contrast microscope image of adherent primary DPS cells growing in a culture flask.

Experimental Procedure

Before assessing viability, cells were subjected to SAW-DEP just long enough for clear alignment into pDEP and nDEP lines. At 0.15 S/m, this was shown to enrich live cells in the pDEP lines to >98% purity (see Figure 5.8), thus, a similar procedure could be used in a clinical setting. For simplification, however, pDEP and nDEP lines were not extracted as seperate populations downstream, and the overall viability of the cell sample was assessed relative to various controls

(detailed below).

Samples of DPS cells were suspended in DEP buffer (Section 5.2.4) and flowed through the SAW-DEP apparatus (Section 5.2.3) at 3 µl/min, the fastest flow rate at which clear separation could be observed. To obtain statistically-relevant sample numbers, cells were flowed through the apparatus for 15 minutes. Several controls were prepared:

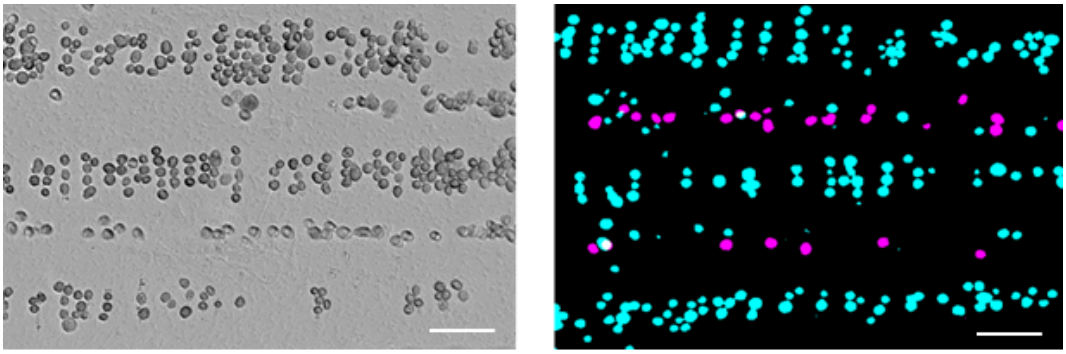

Figure 5.8: Microscope images of dental pulp stromal cells undergoing SAW-DEP at 0.15 S/m. Brightfield image (left) and fluorescent image (right), with viable (cyan) and non-viable (magenta) staining. The fluorescent image shows how live cells could be purified from dead cells (by aligning into separate lines), although some live cells remained in the 'dead cell' line regions. Scale bar 100 µm.

- Microfluidics: Cells flowed through the microfluidics but with the SAW-DEP electric field turned off - to assess the effect of the electric field
- DEP buffer: Cells kept in DEP buffer at room temperature for the same amount of time as the separation procedure - to assess the effect of the microfluidic shear forces
- Culture medium: Cells kept in culture medium at room temperature for the same amount of time as the separation procedure - to assess the effect of DEP buffer

- PBS: Cells kept in PBS at room temperature for the same amount of time as the separation procedure - to compare the effect of DEP buffer with another common experimental (i.e. non-culture) medium

Determining cell viability

A complete description of the experimental procedure can be found in Methods Chapter 3.3. Flow cytometry (Figure 5.9) was chosen to measure cell viability because of its ability to analyse large numbers of cells (in this work, samples of ~ 10,000 cells were processed in five minutes). Cells were incubated in propidium iodide to stain the nuclei of dead cells (similar to the use of Trypan blue in yeast cell experiments, Chapter 4.5), following which the number of stained (non-viable) vs non-stained (viable) cells was counted by the flow cytometer.

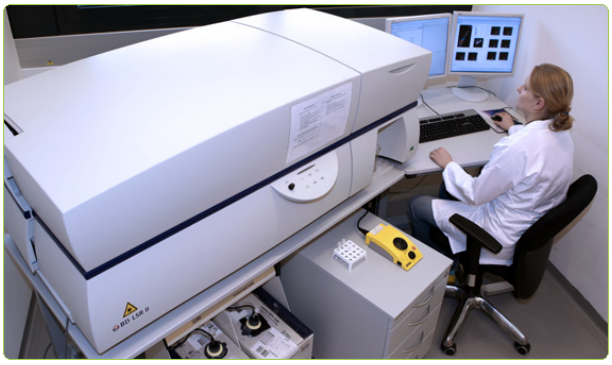

Figure 5.9: Photograph of the flow cytometer model used in this chapter (173), for illustrative purposes.

5.3.4 Experimental results

Qualitative analysis of contour plots

Figure 5.10 shows the flow cytometry contour plots for the five experimental conditions. A contour plot visualises the spread of data in two dimensions - in this case, this is propidium iodide (the stain for non-viable cells, x axis) and

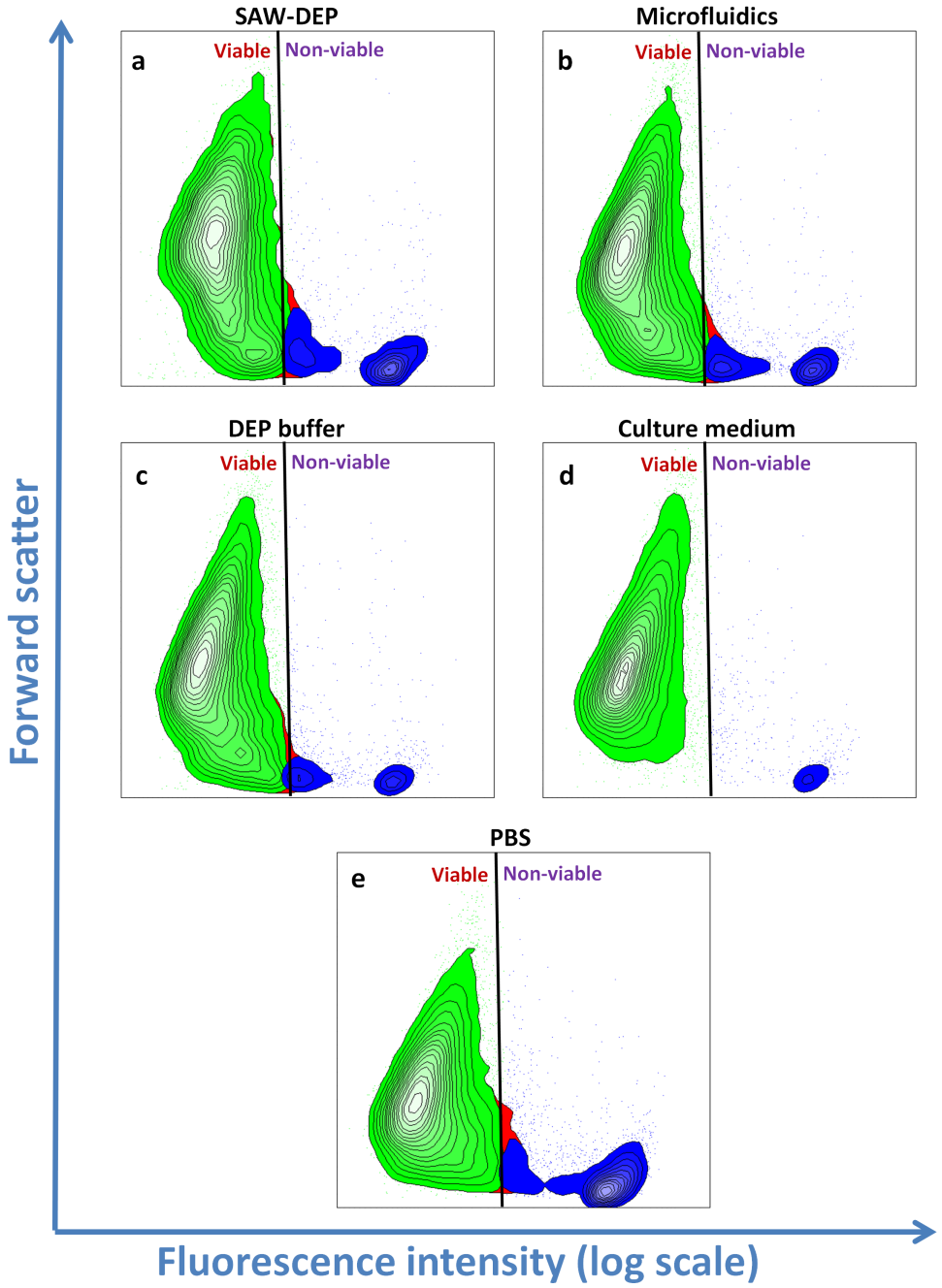

Figure 5.10: Scatter plots from one experiment (out of n=9) investigating the effects of SAW-DEP on cell viability. Samples are cells which: **a** Underwent the full SAW-DEP procedure; **b** Underwent the full procedure except without the SAW/electric field on; **c** Held in DEP buffer for the experiment time; **d** Held in culture medium for the experiment time; **e** Held in PBS solution for the experiment time. A viable/non-viable gate (vertical black line) is drawn to distinguish viable and non-viable cells, based on their fluorescence intensity (x axis). Forward scatter is plotted on the y axis; cells exhibiting greater forward scatter can be assumed to be larger in size. Both scales (forward scatter and fluorescence intensity) are arbitrary.

forward scatter (a rough indicator of cell size[1], y axis). A gate was drawn at a certain fluorescence intensity (*n.b.* arbitrary scale) to determine whether cells were viable or non-viable, and this gate was kept at the same fluorescence intensity for all experiments; cells which had taken up a sufficient amount of PI stain to fall to the right of the line were deemed non-viable, while those that fell left of the line were deemed viable.

The data is plotted in this way in order to see distinct populations within the data, that is, apices where the density of cells is highest, indicated by the smallest of a series of concentric irregular circles. For example, looking at 5.10**a** (the key sample, which underwent SAW-DEP), there are two distinct populations, with one population apex in the middle-left of the data set (live cells, green contour colour), and one to the bottom right (dead cells, blue contour colour). From the forward scatter measurements, it can be observed that cells which take up more PI (due to reduced membrane integrity) tend to shrink somewhat in size, as can be assumed from the reduced forward scatter values. This is in keeping with many observations of mammalian cells shrinking during the process of apoptosis (191).

Verification of the viable/non-viable gate

For the 'Culture medium' control (Figure 5.10**d**), the two populations are fully separated by the viable/non-viable gate; however, for all other samples the line falls within the distinct 'live population', making the viable/non-viable gate appear somewhat arbitrary. A smaller, third population (less distinct than the other two) can be seen in these samples, with an apex just to the bottom right of the viable/non-viable gate. These were presumed to be in a 'pre-apoptotic' state, where those to the left of the gate were assumed to remain alive if moved back into stress-free culture conditions (i.e. in an incubator in culture medium),

[1]Forward scatter measures the extent of low-angle scattered light resultant from the incident laser beam probing the cell. In general, larger cells will produce more forward scatter, although it is affected by other factors such as cell orientation and granularity.

while those to the right would die, joining the far-right cell population.

To verify that the viable/non-viable gate had been placed in the correct place, the experiment was repeated (n = 3), and half of samples were measured for viability (using the same gate settings) following re-introduction into normal tissue culture conditions (i.e. incubated in culture medium) for 60 minutes following the SAW-DEP procedure. This was shown to eliminate the 'pre-apoptotic' cell popuation, as shown in Figure 5.11**b**, where incubated cells exhibit two fully-distinct populations either side of the viable/non-viable gate. Figure 5.11**c** is a bar graph that shows there is no significant change in cell viability (according to the viable/non-viable gate) before and after the incubation period, hence, from this we can assume that the gate is set accurately.

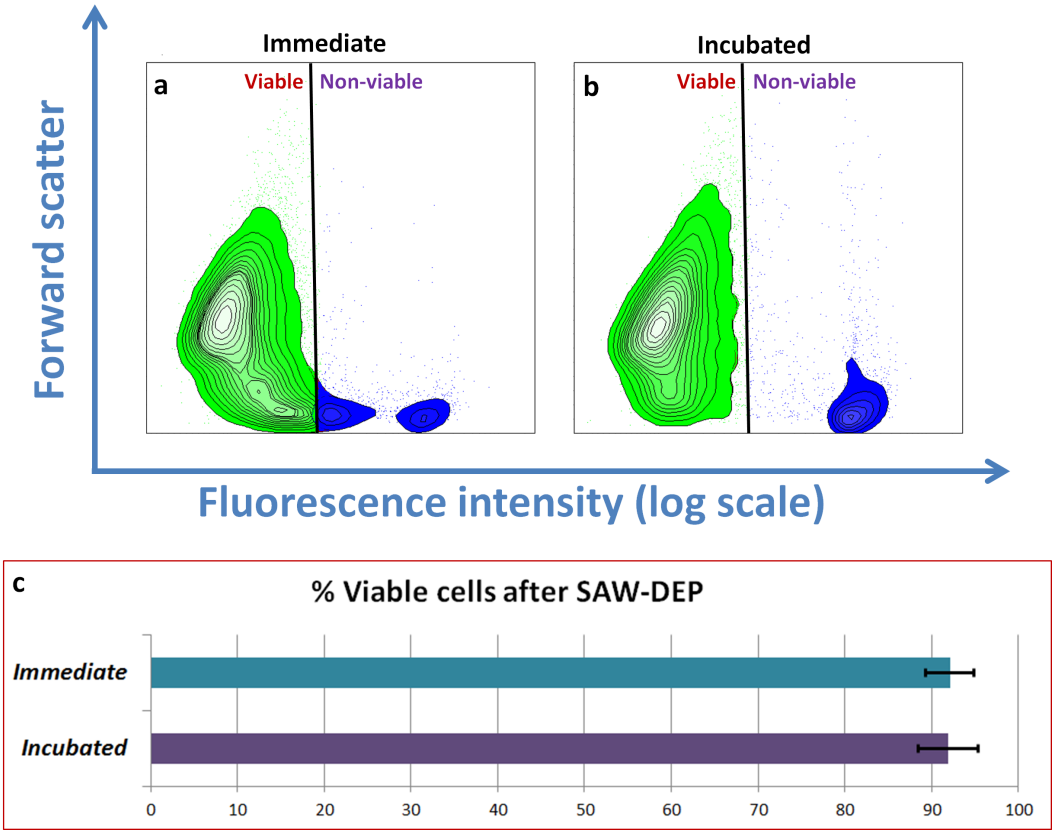

Figure 5.11: Contour plots showing viable/non-viable cell ratios measured by flow cytometry immediately after SAW-DEP (**a**) and after being re-introduced to normal tissue culture conditions ('Incubated') for 60 minutes following SAW-DEP (**b**); **c** A bar graph, with standard deviation bars, showing that the proportion of viable cells immediately following SAW-DEP, and after the 60 minute incubation, are not significantly different.

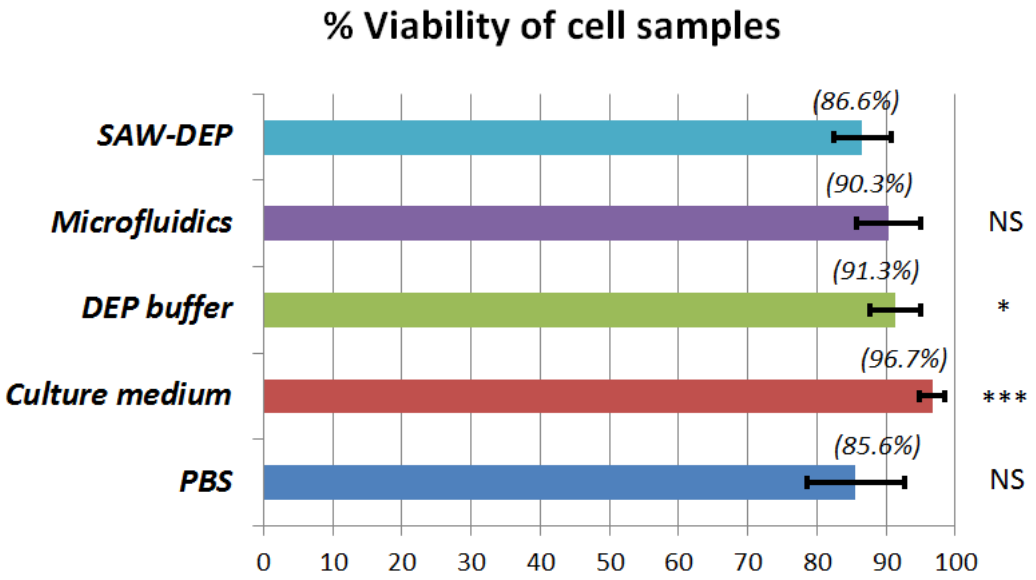

Figure 5.12: Bar graph comparing the viability of cells following SAW-DEP with various controls, with standard deviation bars. Statistical analysis was carried out to determine whether the viability of cells exposed to SAW-DEP was significantly different to the control sample: NS - no significant difference, * - Significant difference ($p < 0.05$), *** - Significant difference ($p < 0.001$).

Statistical analysis of the effect of SAW-DEP on cell viability

After verifying that the position of the viable/non-viable gate was placed effectively, data was pooled for nine experimental samples (three repeats for cells from three different donors) and statistical analysis was carried out to determine whether there was a significant difference between the viability of cells following SAW-DEP compared with that of the controls. The results are shown in Figure 5.12.

Figure 5.12 shows that the viability of cells after SAW-DEP was 86.6%. Compared with the 'Microfluidics' control (90.3% viability), where cells were not subjected to an electric field, this showed a 4.1% decrease in viability due to the electric field. However, this decrease was deemed as 'not significant' ($p > 0.05$)

by the statistical analysis, a Mann-Whitney U test.

There is a significant difference ($p < 0.05$), however, between the SAW-DEP sample and the 'DEP buffer' control - where cells had not undergone the microfluidic procedure or the electric field. It can therefore be concluded that the DEP electric field and microfluidic procedure of the technique combined lead to a significant decrease in viability. While there was also a significant difference ($p < 0.001$) between the 'Culture medium' sample (i.e. cells left in culture medium, not having undergone the electric field or microfluidic procedure) and the SAW-DEP sample, the latter did not show a significant difference between cells which had been left in PBS buffer ('PBS' sample) for the same time as the SAW-DEP experiment.

The data suggests that the key novel aspect of this work, the SAW-DEP electric field, on its own does not cause a significant decrease in viability of cells as used in this experiment; however, combined aspects of the electric field, microfluidic shear forces, and the DEP buffer composition (compared to culture medium) can combine to produce a significant decrease in cell viability which needs to be addressed and optimised before it can be further considered for use in its proposed clinical setting. A promising aspect, however, is that the full SAW-DEP procedure (electric field, microfluidic procedure and DEP buffer combined) did not show significantly lower viability than for cells which were held in PBS, a commonly-used experimental buffer, for the same amount of time.

It is worth noting that the statistical analysis also showed that cells held in DEP buffer (but did not undergo the DEP electric field or microfluidic procedure) showed a significant decrease in viability compared with cells held in culture medium ($p < 0.05$). A preliminary study was therefore conducted to address which constituents can be added to DEP buffers to increase cell viability, and this is discussed in the proceeding section.

5.4 Assessing the effect of DEP buffer composition on cell viability

5.4.1 Aims and experimental design

Having found that the electric field associated with the SAW-DEP separation procedure did not significantly affect cell viability, a preliminary study was carried out to find how the DEP buffer solution could be modified to improve cell viability. The experimental procedure was the same as that described in the previous section (5.3.3), but without running cells through the SAW-DEP or microfluidics.

Cells were incubated in eleven different solutions for 30 minutes, and the viability of cells afterwards was tested by flow cytometry as in Section 5.3. The experiments were repeated for $n = 5$, and the statistical significance between key samples was found by Mann-Whitney U test, as described in Section 3.3.2.

The different DEP buffer solutions were modified to compare the effects of solution conductivity, pH buffer, and BSA, as well as three DEP buffer formulations picked from the literature. The effects of sugar concentration and osmotic potential were not investigated in this work - the concentration of sucrose was varied slightly between solutions (7.5%-9.5%) to ensure the osmotic potential remained between 290-310 mOsm/l. Similarly, the effect of EDTA, another key constituent of the SAW-DEP buffer, was not investigated due to time constraints.

A tabular key of the components of the various buffers is given in Table 5.2. All solutions were of pH 7.1-7.4 (adjusted using 5 M KOH when HEPES buffer (pH ~ 5.8) was used).

5.4.2 Results

Effect of solution conductivity

The key difference between typical cell buffers and those used in DEP is that the latter must be tailored to far lower conductivities (<0.03 S/m compared with

Table 5.2: Buffer constituents

Buffer: Key feature	**Constituents** (% mass/volume), **conductivity** at 20 °C
PBS	Significant components are 0.8% NaCl, and 0.115% phosphate buffer (Na_2HPO_4) (172). 1.5 S/m.
Low PB-S/Vykoukal *et al.* (2008) (122)	9.5% sucrose, 0.3% dextrose, 2.1% 1 x stock PBS solution, 0.03 S/m.
Culture medium	Significant components are 10% fetal bovine serum[1], 0.68% NaCl, ~ 0.08% other salts, 0.1% amino acids (170). 1.25 S/m (171).
27mMol HEPES buffer	8.5% sucrose, 0.3% glucose, 27 mMol HEPES, 0.030 S/m.
2% BSA	8.5% sucrose, 0.3% dextrose, 2% BSA, 0.025 S/m.
SAW-DEP buffer	0.02% EDTA, 2% BSA, 0.595% HEPES buffer (25 mMol), 7.5% sucrose, 0.3% dextrose. 0.15 S/m.
Shafiee *et al.* (2010)(143)	8.5% sucrose, 0.3% glucose, 0.725% (v/v) RPMI media stock (192). 0.01 S/m.
Holmes *et al.* (2003) (56)	9% sucrose, 0.3% glucose, 0.03% EDTA, 0.8% BSA, topped up with HEPES to 0.030 S/m.

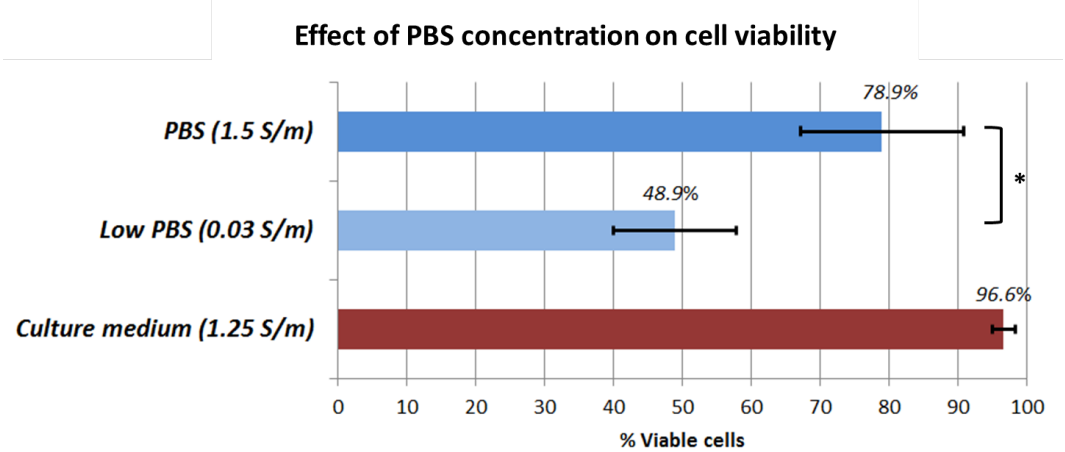

Figure 5.13: Bar graph showing mean values with standard deviation bars, comparing the effect of solution conductivity on cell viability. * - Significant difference ($p < 0.05$).

1.25 - 1.5 S/m for typical cell buffers) to avoid joule-heating in the solution; the lack of ions available to cells may therefore pose a detriment to cell viability.

To investigate, the viability of cells incubated in PBS buffer (1.5 S/m) was compared to cells held in 'Low PBS' buffer (containing 2.1% v/v PBS in osmotically-balanced sucrose solution, 0.03 S/m), a buffer used in a relatively recent article by a major DEP research group (122). As shown in Figure 5.13, cells held in 'Low PBS' buffer showed a considerably low viability (48.9%) compared with cells held in normal PBS (78.9%).

Figure 5.13 also shows that cells held in PBS exhibited significantly lower viability compared with cells held in culture medium (96.6%, 1.25 S/m), and this extra cell death cannot be attributed to low conductivity (PBS is higher conductivity, at 1.5 S/m).

The high conductivity/ionic concentration of PBS is largely attributable to it being 0.68% (m/v) NaCl (137 mM). However, the 'phosphate' (PO^{3-} component is also significant (0.115%, 10 mM) because it is responsible for keeping the pH

stable ('buffering' the pH) between 7.2-7.4. This is therefore a limitation of this particular experiment, because the decrease in cell viability could also have been attributed to the lack of effective pH buffer molarity. The effect of pH buffer on cell viability was examined further for the next experiment.

Effect of pH buffer

To buffer the pH in DEP experiments, HEPES (4-(2-hydroxyethyl)-1-piperazine-ethanesulfonic acid) tends to be used, because it dissolves as a zwitterion and therefore does not raise the conductivity of the solution as significantly as other common pH buffers like phosphate or TRIS. In tissue culture, the optimum concentration of HEPES buffer is 25 mM, for example, as found in the GIBCO® DMEM medium (193). For this experiment, a buffer was made composed of osmotically-balanced sucrose and 27 mMol HEPES, to give a final conductivity of 0.03 S/m (27 mMol HEPES); this was compared to the 'Low PBS' buffer (also 0.03 S/m) described in the prior experiment, where the pH (phosphate) buffer component was 0.21 mMol, ~ 50 times lower than its optimum concentration of 10 mMol.

Figure 5.14 shows that cells incubated in the solution with low pH buffer osmolarity (Low PBS) actually showed no significant difference in viability compared with those held in the solution with the optimal concentration of pH buffer (27 mMol HEPES buffer) (48.9% and 42.0%, respectively). This indicates that the contribution of pH buffer is insignificant. However, because both solutions showed very poor cell viability compared to the positive control (Culture medium, 96.6%), it cannot be ruled out that the addition of pH buffer may still have a role in maintaining viability when used with other 'viability-optimising' constituents.

Effect of BSA

BSA (bovine serum albumin) was a key component of the initial SAW-DEP buffer (2% m/v). A buffer was made of osmotically-balanced sucrose solution

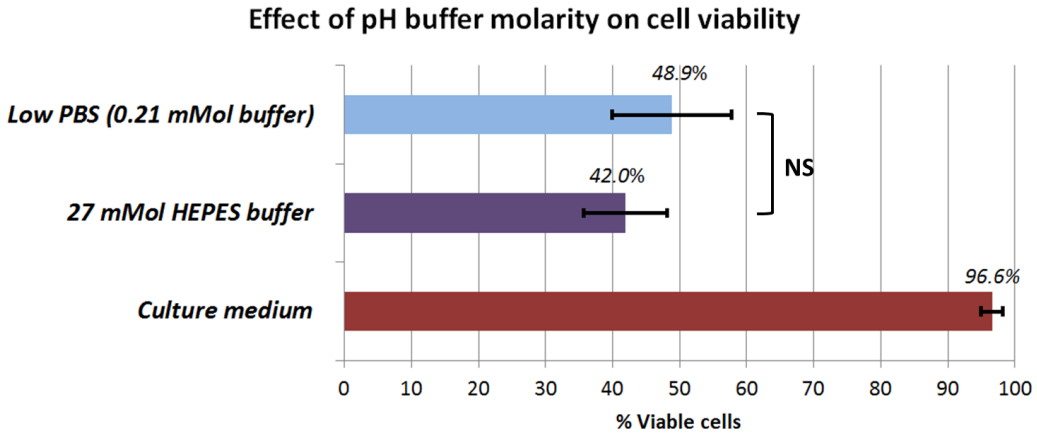

Figure 5.14: Bar graph, with standard deviation bars, comparing the effect of pH buffer molarity conductivity on cell viability. **NS** - No significant difference ($p > 0.05$).

with 2% BSA (final conductivity of 0.025 S/m), and this was compared to the 'Low PBS' buffer (which had a similar conductivity of 0.03 S/m).

Figure 5.15 shows that the buffer containing 2% BSA had significantly higher cell viability than the comparable buffer without BSA ('Low PBS'), showing that adding BSA to a DEP buffer consirably improves cell viability (93.7% compared with 48.9% viability). This was not an anticipated result, because BSA was only added to the initial SAW-DEP buffer in order to ensure cells travelled smoothly through the microfluidics, and this set of experiments was not performed using the microfluidic apparatus. The cell viability-effects of BSA appear to be often overlooked when formulating DEP buffers, however, its role in maintaining healthy cell cultures has been well-documented in the scientific literature concerning general tissue culture (194); its key function appears to be as carrier molecule for transporting ligands within the cell, although it also plays a role in maintaining pH and osmotic pressure in the surrounding liquid (194).

It can also be observed that the viability of the 2% BSA buffer was similar to that of Culture medium, and stronger than that of cells held in SAW-DEP buffer

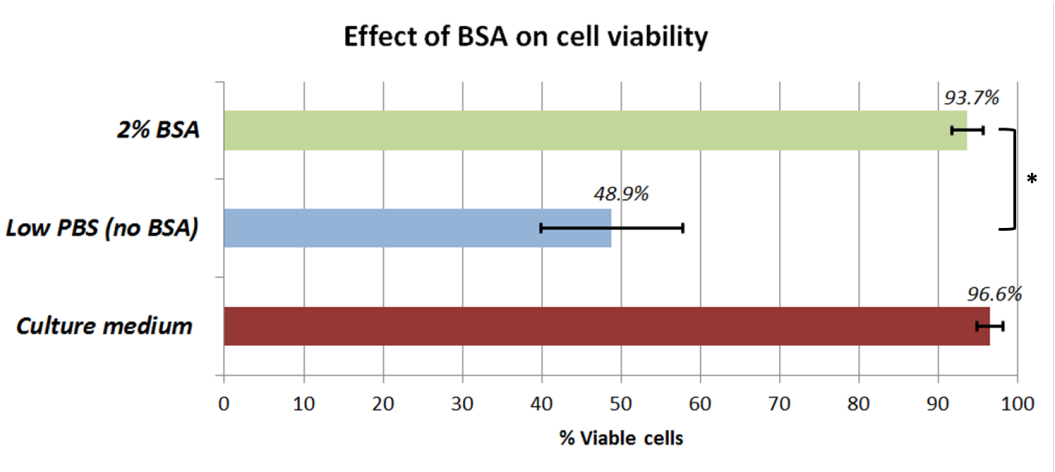

Figure 5.15: Bar graph, with standard deviation bars, examining the effect of BSA on cell viability. * - Significant difference ($p < 0.05$).

(86.7% for these experiments, see Figure 5.16). It is worth noting that Culture media is typically supplemented with 10% 'Bovine Calf Serum', which contains roughly 2% m/v BSA (194, 195). The final concentration of BSA in Culture medium is therefore ~ 0.2%, and total serum proteins are 0.35%.

Comparison of SAW-DEP buffer with DEP buffers in the literature

Within this experiment, the viability of cells in the initial SAW-DEP buffer was compared with that of several DEP buffers mentioned in the literature. These included two of the more recent DEP papers by influential DEP research groups, the Morgan group at the University of Glascow, UK (56), and the Gascoyne group at the University of Texas, USA (122) ('Low PBS'), as well as that used by the Davalos group at Virginia Tech, USA (111), a paper which was influential to this thesis.

Figure 5.16 shows that SAW-DEP buffer was the most effective DEP buffer at maintaining cell viability (86.7%), which was found to be significantly higher than for all other DEP buffers investigated (though still significantly lower than Culture medium). While cells incubated in the Morgan group buffer ((56), 78.8%

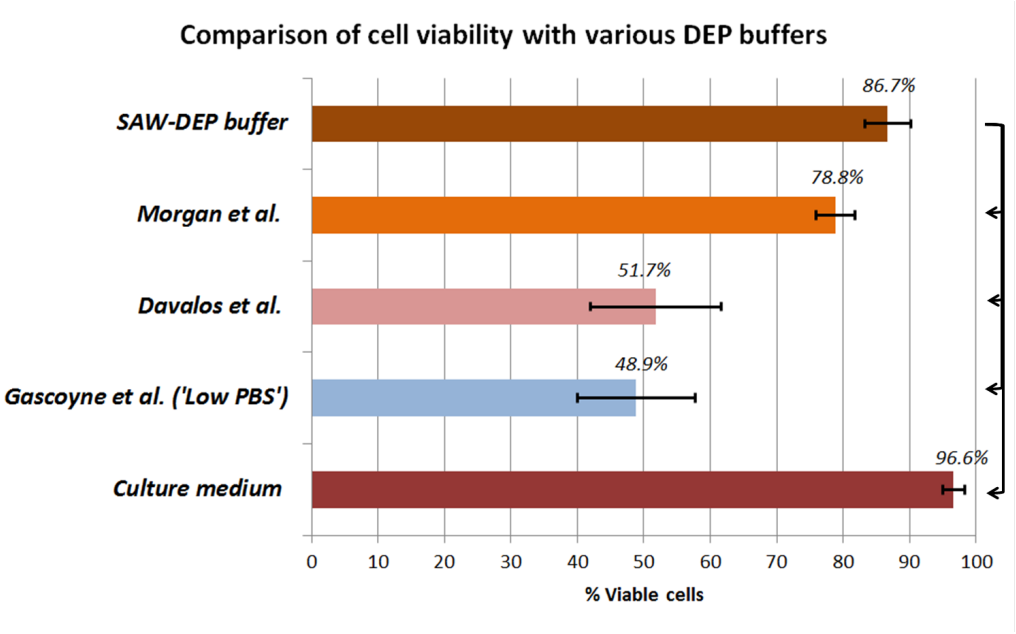

Figure 5.16: Bar graph, with standard deviation bars, comparing the viability of cells held in various DEP buffers, including three from the literature: Morgan *et al.* (56), Davalos *et al.* (111), Gascoyne *et al.* (122). * - Significant difference ($p < 0.05$).

viability) showed significantly lower viability than cells held in SAW-DEP buffer, this was still found to be significantly ($p < 0.05$) higher than for cells incubated in buffers of the Davalos and Gascoyne groups (51.7% and 48.9%, respectively). It should be noted that both the SAW-DEP and Morgan group buffers contain a significant amount of BSA, as well as EDTA, and HEPES, all of which could contribute to the improved cell viability.

5.4.3 Conclusions

The most significant finding of these experiments was that BSA can be used to dramatically increase the viability of cells held in a typical DEP buffer (consisting merely of an osmotically-balanced sucrose solution). While the viability of cells incubated in the '2% BSA' buffer did still not quite match that of those incubated in 'Culture medium' (93.7% compared to 96.6%), the simplicity of its composition and low conductivity make it a promising choice for future DEP experiments. While the initial 'SAW-DEP' buffer was continued to be used for the rest of this chapter for consistency, work in the next chapter (6) utilised the '2% BSA buffer', to limit the effects of cell death during experiments.

5.5 Assessing the effect of SAW-DEP on the differentiation ability of dental pulp stromal cells

5.5.1 Introduction to osteogenic differentiation

After examining the effects of the SAW-DEP procedure on the viability of cells, an investigation was carried out to find out if exposure to SAW-DEP adversely affected the differentiation ability of dental pulp stromal cells cells. Because the technology in this thesis is being proposed as a tool for autologous cell therapies, the focus of this particular investigation was the ability of dental pulp stromal cells (DPS cells) to differentiate into osteogenic tissue following the SAW-DEP procedure.

DPS cells contain cells that have a mesenchymal stem cell (MSC) phenotype, and are therefore capable of differentiating into a range of different cell types (see Figure 5.17), including bone, neuronal, cardiac, and liver cells, making them a strong candidate for autologous cell therapies and other forms of regenerative medicine (11). By culturing DPS cells in the right balance of growth and transcription factors, for example, it is possible to differentiate them along a number of lineages (11). This work will focus on osteogenic lineage differentiation, and subsequent mineral deposition, which are key to the bone forming process.

To differentiate DPS cells (and similar mesenchymal stem cells) into cells of an osteogenic lineage, the general method is to grow cells in an osteoinductive medium at high density - this involves simply allowing cells to become fully confluent in a tissue culture flask or well plate, before adding osteoinductive media. Osteogenic differentiation can be tested for by determining ALP expression at 1-2 weeks, which is a marker that signals the start of the differentiation process (11). At 3-4 weeks the cells can be tested for mineral deposition, generally with Alizarin red or von Kossa staining (205) and imaged under a microscope to show the presence of the formation of mineral nodules (see Figure 5.18).

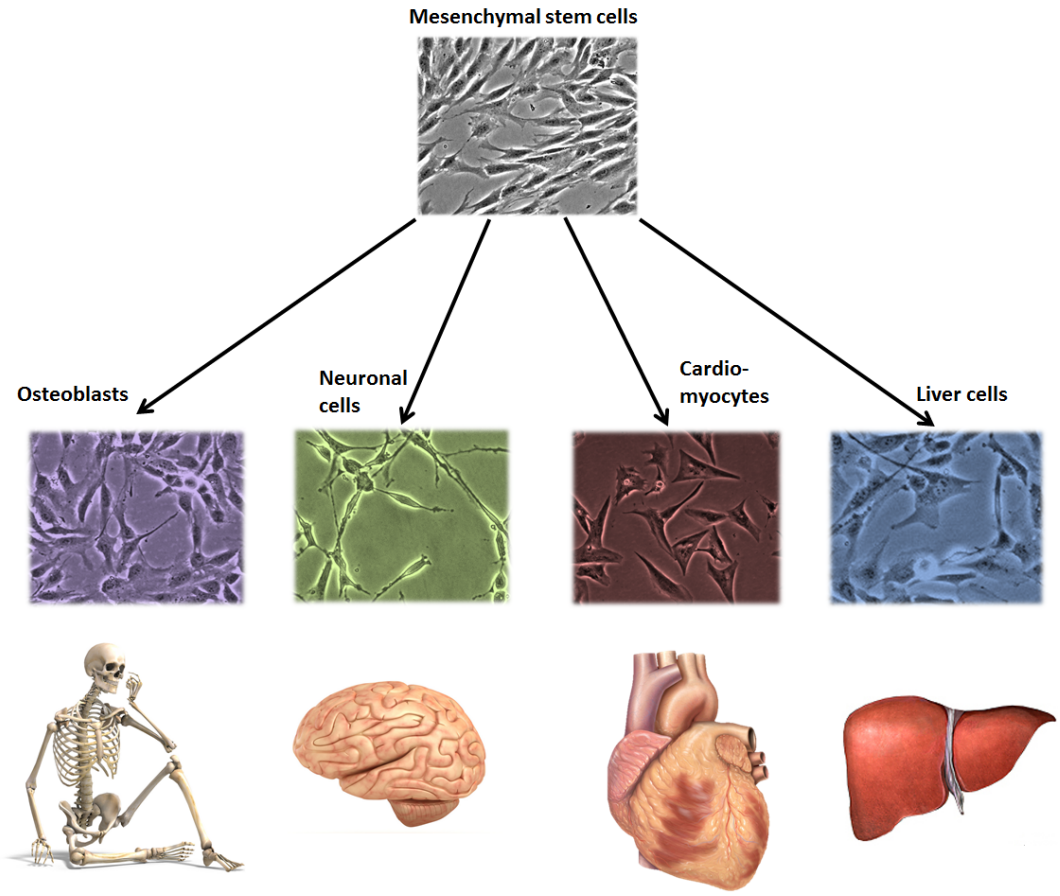

Figure 5.17: Potential differentiation routes for mesenchymal stem cells (196, 197, 198, 199, 200, 201, 202, 203, 204).

5.5.2 Experimental design

To see whether SAW-DEP and/or associated factors (microfluidics and DEP buffer) affected DPS cell osteo-differentiation, an experiment was designed using similar controls to those used in the viability studies. A full description of the materials and methods used for these experiments can be found in Methods 3.3.3.

Because the device used for this experiment had a slightly lower coupling coefficient than the device used before, a lower flow rate of 1.5 µl/min was used instead to ensure cells were experiencing sufficient DEP force. Because an even greater number of cells was needed for this experiment (2-4 $\times 10^5$ cells), to get a sufficient

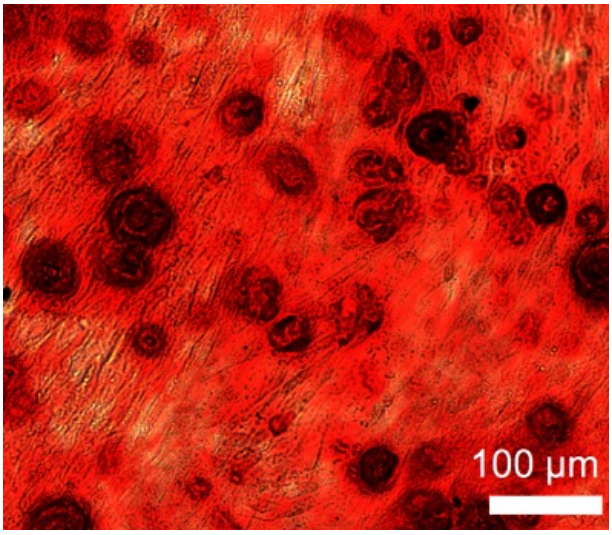

Figure 5.18: Nodule formation (dark rosette shapes) from DPS cells differentiated into osteoblasts (205).

seeding density, the cells were flowed through the fluidics for 45 minutes, such that the total time on the lab bench was 60 minutes as opposed to 30 minutes for the previous viability studies.

Samples of cells were exposed to SAW-DEP as described in Section 5.3.3, along with the same control procedures as for 'Microfluidics' (cells which went through the microfluidics without exposure to SAW-DEP), 'DEP buffer' (cells held in DEP buffer in lab bench conditions for the experiment time) and 'Culture medium (cells held in culture medium on the lab bench for the experiment time). Two additional controls were made: a 'Positive' control, which was osteoinducted straight from a fresh tissue culture, and a 'Negative' control, also straight from a fresh tissue culture, which was grown in the same conditions as the other samples, but in normal αMEM culture medium with no osteoinductive supplements.

In an initial experiment, an osteoinduction medium was made in-house by supplementing αMEM with 100 nM dexamethasone, 2 mM β-glycerophosphate, and 280 µM ascorbic acid. However, not even the positive controls showed evidence of osteoinduction in this experiment, and so it was decided thereafter to use

StemPro®, a proprietary medium by Gibco^{TM} (206) containing a formulation of various different osteoinductive supplements, and can be thought to give more reliable and repeatable results.

Cells were tested for ALP expression by biochemical assay and staining after eight days of culture on 24-well plates. The surface area of these plates (1.9 cm^2) is thought to be too small to grow osteoinductive cultures for more than 2 weeks because the cell monolayer has a tendency to peel off for want of attachment space; accordingly, cells stained for mineral deposition (after 18-21 days) were cultured in 12-well plates (surface area 3.8 cm^2).

5.5.3 Results

Alkaline phosphatase expression

Alkaline phosphatase (ALP) is a metalloenzyme present in tissues throughout the human body, but is particularly concentrated in the liver, bone, and kidneys. It is covalently attached to the outer face of the plasma membrane where, in the case of bone formation, it is hypothesised to be responsible for initiating the mineralisation process by hydrolysing inorganic pyrophosphate (PPi) to give phosphate molecules, which are incorporated into hydoxyapatite, that forms bone and dental enamal (207).

While mineralisation does not typically occur in cell culture for differentiating osteoblasts until 3-4 weeks, elevated levels of alkaline phosphatase expression appear much earlier, after 1-2 weeks of osteoinductive culture. In fact, when dental pulp stromal cells are cultured at high density, they are known to express alkaline phosphatase without the need for a special osteoinductive medium (205). The presence of elevated alkaline phosphatase expression after 1-2 weeks would therefore not necessarily confirm cells are fully capable of producing a mineralised matrix; however, a lack of alkaline phosphatase expression compared to controls would confirm that cells have been affected by the SAW-DEP procedure.

Staining for alkaline phosphatase expression

To detect alkaline phosphatase expression by staining, cell monolayers can be 'fixed' in ethanol and incubated in a solution containing naphthol AS-MX phosphate (208); if ALP is present, the phosphatase activity cleaves the phosphate, liberating naphthol AS-MX, which reacts with another molecule in the staining solution[1] to form a coloured precipitate. The staining results, after eight days of culture, are shown in Figure 5.19.[2]

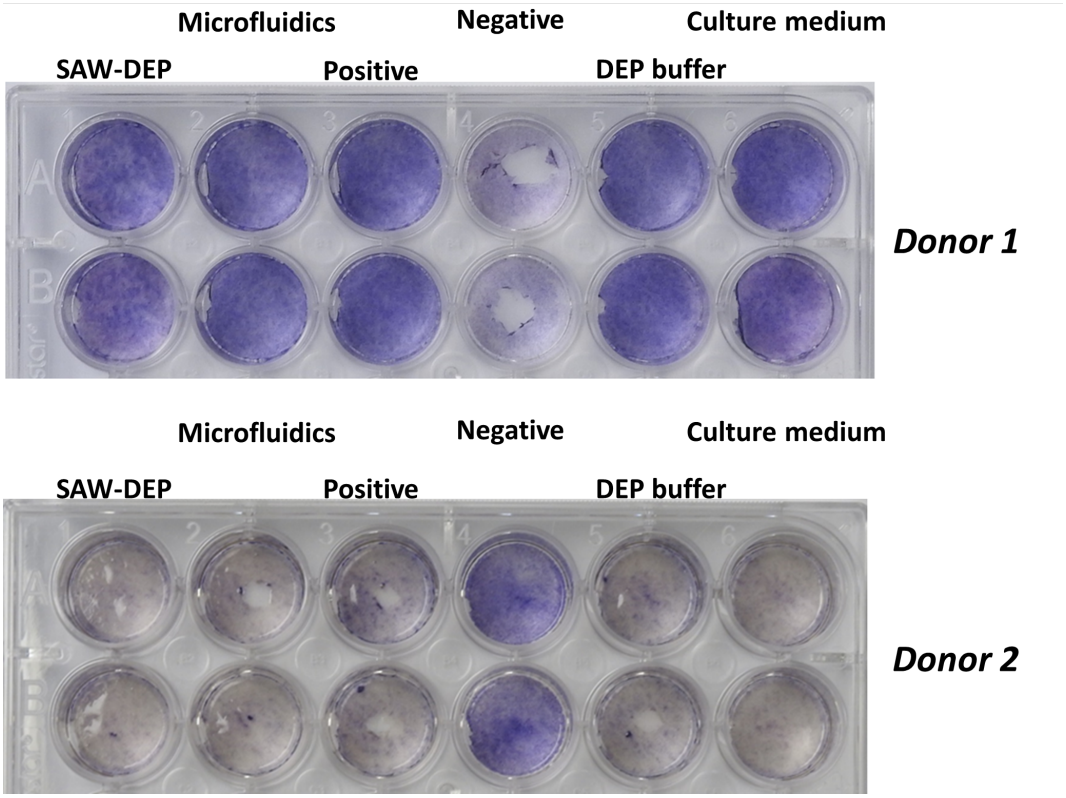

Figure 5.19: ALP staining following eight days of osteoinduction for two donors. Cells are positively stained by a blue precipitate that forms in the presence of alkaline phosphatase.

There were no qualitative observable difference between all samples that were

[1] 'Fast Blue RR', a diazonium salt

[2] Results for a third donor sample, 'Donor 3', were lost due to experimental error.

kept in the osteoinductive medium (i.e., all except 'Negative'). There is, however, a striking difference between the two donors; while the osteoinducted samples for Donor 1 all show high levels of ALP expression when compared to the negative control, the opposite is true for Donor 2.

The results for Donor 1 are what could have been expected; the cells in osteoinductive media all strongly express ALP and so appear to be on the lineage pathway to osteogenic differentiation. This contrasts with a lack of ALP expression in the Negative control, indicating the cells are not differentiating (yet, at least).

To explain the results for Donor 2, however, it must be considered that ALP expression tends to peak early on in differentiation, before tailing off; for example Choi *et al.* (2011) (209) observed peak expression at 7 days, followed by a 4-fold reduction in ALP levels by 14 days. It could be the case, therefore, that the cells began the differentiation pathway faster than those of Donor 1, such that the cells in osteoinductive media had already peaked and tailed off after eight days. The negative control cells, which we expect to express ALP without osteoinductive media when grown at high density, reached the high ALP expression-stage at 8 days (while the Negative control cells in Donor 1 had not reached this stage yet).

It is possible to quantify ALP activity via a spectrophotometric assay. This involves lysing cell membranes such that the constituent chemicals and enzymes inside the cells can be added into a solution. An ALP substrate is added to the solution (similar to that used for the stain) which becomes fluorescent after it is cleaved by ALP. The fluorescence can then be quantified by a 'plate reader', a type of UV-vis spectrophotometer.

As well as measuring the ALP activity of the different samples, the DNA content of the samples is also quantified, by intercalating DNA with a molecule that can also be quantified by fluorescence. This ensures that ALP activity can be standardised according to the amount of DNA present in each sample, to permit

comparisons of samples containing different cell numbers.

Quantitative assay

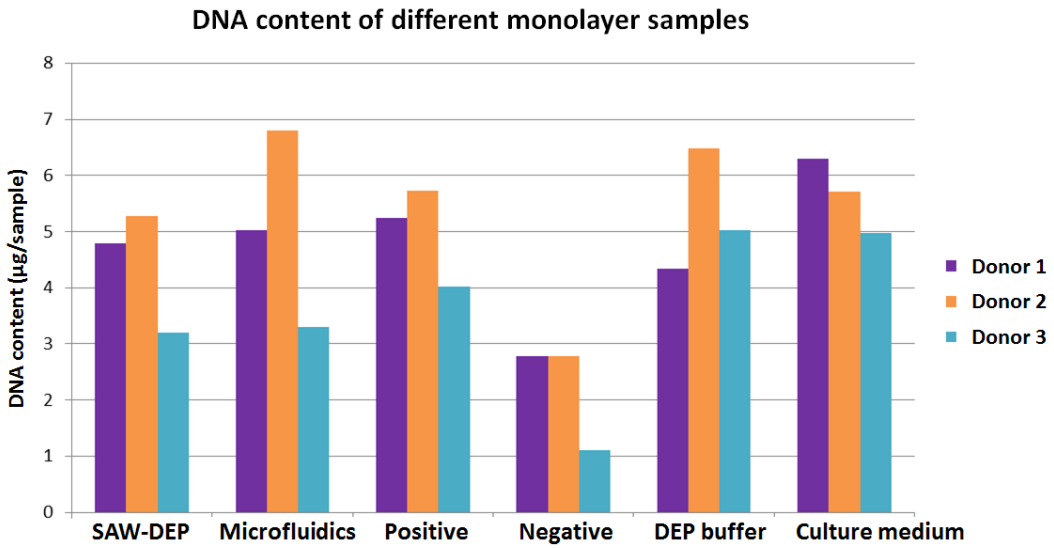

Figure 5.20: Bar chart showing the DNA content (an indicator of cell numbers/volume) in the wells used for the quantitative ALP assay (n = 2 wells, x 3 repeats, for three different donors). The samples were as follows: **SAW-DEP** Cells which underwent the full SAW-DEP procedure, **Microfluidics** Cells which underwent the full procedure except the SAW/electric field was not turned on, **Positive** Positive control: Cells which were cultured in the osteoinductive directly from normal tissue culture conditions, **Negative** Negative control: Cells which were cultured in a normal, non-osteoinductive culture medium (αMEM), **DEP buffer** Cells which were held in DEP buffer for the time taken to perform the SAW-DEP experiment (45 minutes), **Culture medium** Cells which were held in a normal culture medium (αMEM) for the time taken to perform the SAW-DEP experiment.

Figure 5.20 shows how DNA content varied between donors and experimental samples. Two consistant observations are that (1) DNA content was always lower in Donor 3 compared to the other two donors, and (2) DNA content was always

lower for the Negative control sample. With regards to (1), this is likely to be due simply because of donor variation, with Donor 3's cells growing more slowly than those of other two donors.[1]

A slower growth rate of cells in the Negative control would also explain (2); this indicates that cells were growing much faster in the StemPro® medium when compared with the normal Culture medium. This is likely to be because StemPro® is manufactured with various supplements and growth factors designed to enhance growth and speed up the differentiation process. Other studies have had similar results comparing cell growth in StemPro® and 'MEM' media (210).

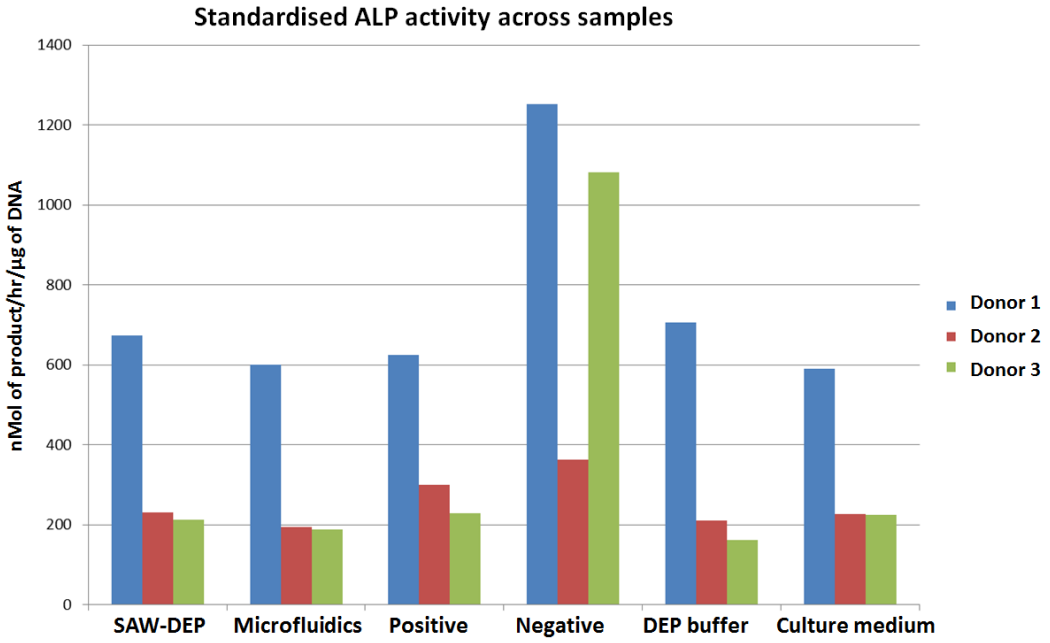

Figure 5.21: ALP activity in various samples for three donors (n = 2 wells, x 3 repeats).

[1]Because cells were seeded at the same density (see Methods 3.3.3), it can be assumed that any significant difference in DNA content was due to faster or slower cell growth between samples.

The results from the ALP assay are shown in Figure 5.21. Donors 1 and 2 in these results are the same as Donors 1 and 2 in the staining results (Figure 5.19); however, the cell samples the data is derived from were cultured separately on different days, so the two datasets are not directly comparable to each other.

The most obvious observation is that, intra-donor, ALP activity was always highest in the negative control. Again, this is thought to be because the ALP activity of the osteoinducted (StemPro®-cultured) samples had already peaked and tailed off by Day 8, at which point the Negative control sample has just reached peak ALP activity. The ALP activity in the SAW-DEP sample (intra-doner) is similar to all other controls, with no discernable differences or trends.

Mineralisation stain

A key test for osteogenic differentiation is a stain to determine whether the cell monolayer has begun depositing a mineralisable matrix, which in an *in vivo* system would be the beginning of the bone-forming or repairing process. Alizarin red staining is a common qualitative test for mineral deposition by putative osteoblasts, where alizarin is a simple organic compound which stains red when it chelates with calcium, a principal component of the mineral matrix.

It was planned to perform an alizarin red stain following 21 days of culture. However, while refreshing the medium of one of the three samples (which was just 18 days old), it was noticed that some of the cell monolayers had started detaching from the well plate,[1] meaning that they were now unsuitable for accurate staining. For fear of losing more experimental samples, all the samples (between 16-19 days old) were stained on that day, and the results are shown in Figure 5.22.

[1]Detachment of cell monolayers in a common problem in osteogenic differentiation experiments, and is generally attributed to cells becoming over-confluent (i.e. too dense) with limited surface area, such as that in a well-plate (211). Thus, the longer they are cultured, the greater the risk of this occuring.

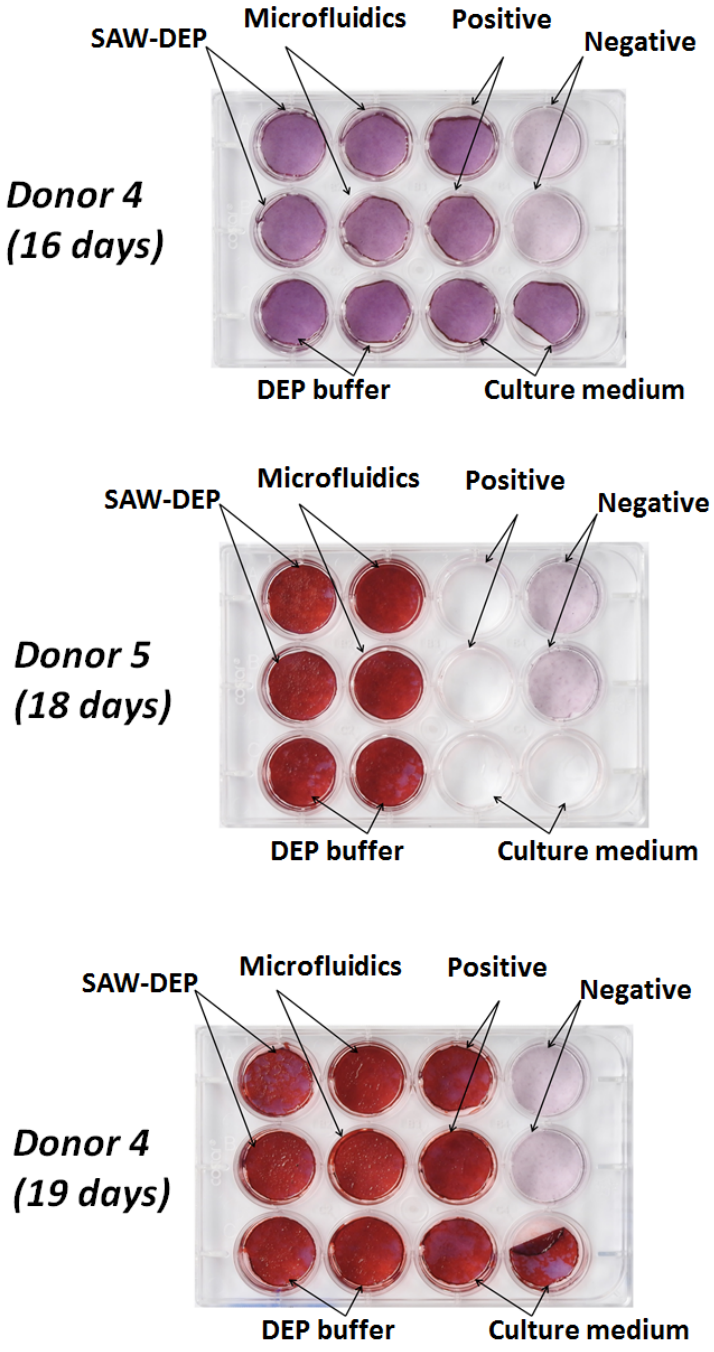

Figure 5.22: Alizarin red staining for various donors and samples at different timepoints. The '16 days' sample merely shows counter staining (purple) of the cells, to provide a contrast to show that there is no (red) staining of calcium deposits. Strong, deep red staining is shown for the 18 and 19 days samples, however, in all but the Negative controls. (The cell monolayers in Positive and Culture medium samples for '18 days' have peeled up, so the wells are empty.)

After 16 days, Donor 4 showed no evidence of calcification (i.e. red staining) in any of the samples, as could be expected after only 16 days of osteoinduction. (The Negative control shows far weaker colouration by the purple counterstain - this is likely to be indicative of a far lower cell density due to the lower growth rate for that culture medium.)

The change for the samples at 18 and 19 days is dramatic, with definitive red staining across all the samples that were grown in the osteoinductive medium. The extent of staining cannot be distinguished as being less or greater across the osteoinduced samples. The cell monolayer of the 19 days 'Culture medium' sample started peeling off during the staining process, as can be seen in the Figure.

Another test to verify that the osteoinduction process has begun in osteoinduced cell cultures is to examine samples under a microscope to check for nodule formation. This was performed on the samples following alizarin red staining, and can be seen in Figure 5.23.

The microscope images showed that rosette-like mineralised nodules had begun forming over the surface of all the osteoinducted samples, but not the negative control.

5.5.4 Section summary and end of chapter conclusions

Throughout all the ALP and mineralisation tests, the differentiation profiles of samples exposed to SAW-DEP showed no significant difference to the other positive controls, showing that none of the key factors (DEP buffer, microfluidics, and SAW-DEP electric field) produced a noticable impediment to DPS cells' abilities to undergo osteogenic differentiation. This was consistent with the findings in Section 5.3, where the SAW-DEP electric field did not cause cell viability to decrease significantly.

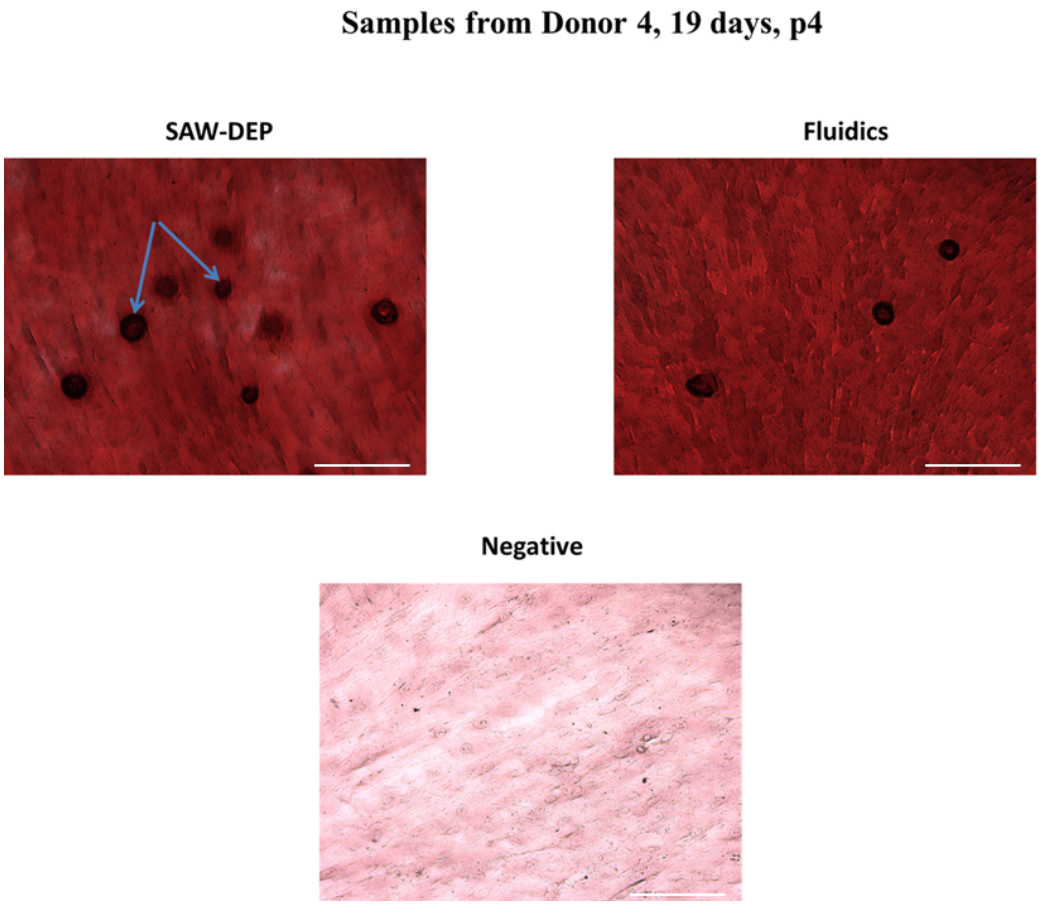

Figure 5.23: Microscope images of osteoinduced samples stained for alizarin red, with two of the mineralised nodules indicated by blue arrows. Note that the key evidence here (when comparing positive and negative controls) is the presence of rosette-like nodules, not the overall colour difference (although the latter is attributable to the presence of calcium). Scale bar 100 µm.

The negative control used for the differentation experiments, however, was evidently inappropriate. This was because the basal medium of the negative control was different from the positive controls (StemPro vs MEM), not just the osteo-inducing supplements. As was shown in the DNA content assay (Figure 5.20), the negative controls had roughly half as many cells as the positive controls. Due to the critical effects of cell density on differentiation this meant it was therefore not a fair test to compare these with the promising controls.

Together, these results indicate that SAW-DEP may be used to isolate clinically-relevant cells while retaining their key physiological and therapeutic capabilities. This chapter also addressed some practical considerations for SAW-DEP devices, resulting in a device design capable of outputting ~ 20,000 cells per minute, and highlighting the importance of BSA in maintaining high cell viability in low conductivity buffer solutions.

Chapter 6

Discerning different cell types using SAW-DEP

6.1 Introduction and chapter summary

The research described in the previous chapters has detailed how the electrical effect of SAW-DEP was characterised, how it could be used to enrich live from dead cells, and whether exposure caused harm to clinically-relevant human cells. This final experimental chapter of the thesis will discuss later work which aimed to look in greater detail at the fidelity with which SAW-DEP can separate live and dead mammalian cells, and whether SAW-DEP can be used to seperate different cell lineages.

The key questions addressed in this chapter, together with a summary of findings, are listed below:

1. Can SAW-DEP produce high-fidelity separation of live and dead mammalian cells?

    - *Section 6.2*: The separation of DPS cells at 0.15 S/m that was used for the experiments in Chapter 5 was shown to produce pDEP lines of 98% live cells. However, due to some live cell alignment into nDEP

regions, 14% of the total viable cell population was aligning in the nDEP regions, meaning this significant portion would be wasted in a real setting (being in the 'waste' stream). To increase the selectivity (i.e. fidelity) of the separation, the conductivity was adjusted from 0.15 S/m to 0.065 S/m, which was shown to give pDEP and nDEP alignment of 97% live cells and 99% dead cells, respectively (Figure 6.1).

2. How can SAW-DEP be used to examine the dielectric signatures of different mammalian cell types?

    - *Section 6.3*: SAW-DEP was used to discern the differences between the DEP behaviour characteristics of three mammalian cell types - primary DPS cells, 16HBE cells, and MCF7 cells. This was achieved by counting the proportion of cells that experience pDEP vs nDEP, as the conductivity of the solution was progressively increased - a technique named 'conductivity stepping'.

3. Can SAW-DEP be used to separate different lineages of cells?

    - *Section 6.4*: The aforementioned conductivity stepping method was used to find the best conductivity to separate two cell types. A preliminary study implied that a 1:1 mixture of DPS cells and 16HBE cells could be separated at a conductivity of 0.34 S/m to give seperate populations of 83% (16HBEs cells, pDEP) and 80% purity (DPS cells, nDEP).

4. Does the dielectric signature of DPS cells change as a function of passage number/age?

    - *Section 6.5*: The final experiment of this thesis utilised the conductivity stepping method to compare the DEP characteristics of DPS cells as a function of age/passage number. The results of this preliminary study suggested that the DEP characteristics changed as a function of passage number, indicating that it may be possible to separate older, differentiated cells from younger undifferentiated cells.

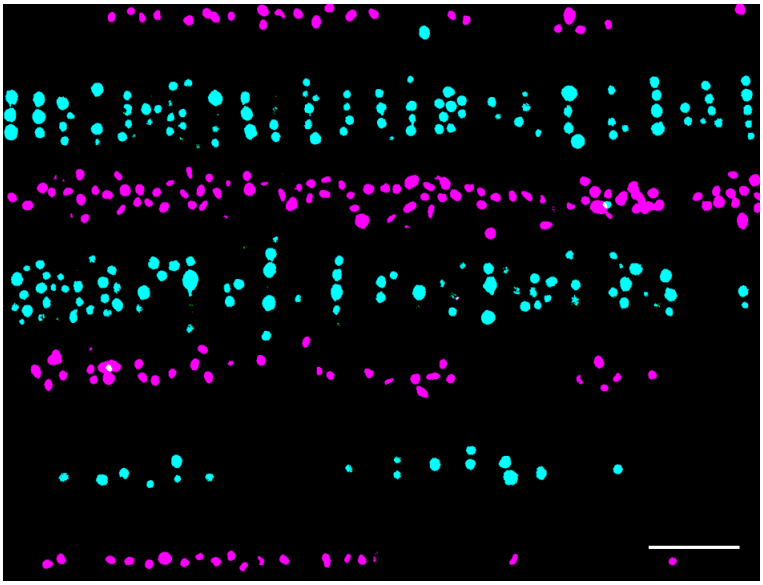

Figure 6.1: Dental pulp stromal cells undergoing SAW-DEP at 0.065 S/m, with live/dead stain, showing complete binary separation between live (cyan) and dead (magenta) cells. Scale bar is 100 µm.

6.2 High fidelity mammalian live/dead cell separation by SAW-DEP

6.2.1 Fidelity of live/dead cell separation at 0.15 S/m

Discrepency between cell viability and observed pDEP cell separation at 0.15 S/m

As discussed fully in Section 5.3, the focus of this experiment was to compare the viability[1] of cells after undergoing SAW-DEP separation with control samples. A conductivity of 0.15 S/m was chosen to ensure enrichment of live cells into pDEP regions. While the viability of the cell samples (n = 9) was found by FACS to be 87%, analysis of microscope images taken during the experiment showed that only 75% of cells aligned in the pDEP regions; this suggested that a significant portion of viable cells were aligning in the nDEP region. A comparison of % viability and % pDEP alignment for each of the three donors (n = 3 per donor) is shown in Figure 6.2.

As shown in Figure 6.2, the data for Donors 1 and 3 suggests the pDEP alignment is ~ 8% lower than the number of viable cells as counted by FACS, suggesting that ~ 8% of live cells are aligning in the nDEP regions. Because the proportion of viable cells is likely to be higher during the SAW-DEP separation than for the subsequent flow cytometry assessment (by which time a greater number of cells will have become non-viable due to stress in the experimental conditions), it is likely that more than 8% of live cells are aligning in the nDEP regions.

Donor 2 shows a larger discrepancy of 21% between viability and pDEP alignment. This is possibly indicative of the age of the cells (passage 9, compared with passage 3-5 for the other two donors) (149), a concept which is investigated further in Section 6.5.

[1] A note on terminology: 'Viable' and 'live' are taken to mean the same thing, as are 'non-viable' and 'dead'. However, the different synonyms are used to distinguish cells deemed 'viable' by FACS (a traditional method) and those deemed 'live' by SAW-DEP.

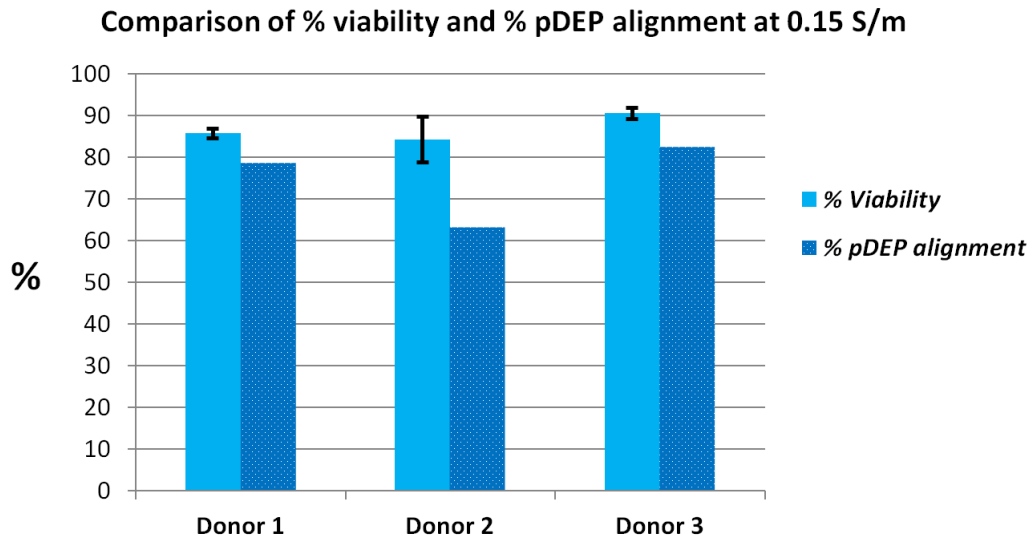

Figure 6.2: Column chart comparing cell viability (with standard deviation bars, n = 3), as measured by flow cytometry in Section 5.3, with the % cells aligning by pDEP, counted using pictures from the corresponding experiments.

It must also be noted that these interpretations of the data are based on the assumption that all of the remaining cells aligning in the pDEP were 'live' (based on previous results with yeast cells in Section 4.5). However, a far more certain way to investigate this would be differentially stain live and dead cells before analysing the alignment images, and this was carried out next.

Proportion of live and dead cells aligned by positive and negative DEP

Live and dead cells were stained different colours (the full protocol is given in Section 3.4.1) and imaged as they underwent SAW-DEP separation in a fluid conductivity of 0.15 S/m. Microscope images to illustrate typical cell separation, and to compare brightfield with fluorescent images, are shown in Figure 6.4.

Having counted >1,000 live cells and >1,000 dead cells, 86% of live cells were found to align in pDEP regions, with 14% in nDEP regions, while 98% of dead cells aligned in nDEP regions, with 2% in pDEP regions. The concentration of

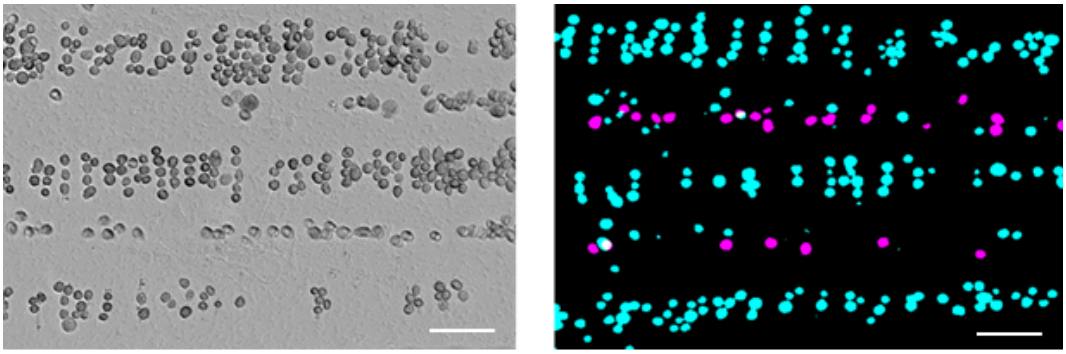

Figure 6.3: Microscope images of dental pulp stromal cells undergoing SAW-DEP separation in a fluid conductivity of 0.15 S/m. Brightfield image (left) and fluorescent image (right), with viable (cyan) and non-viable (magenta) staining. The fluorescent image shows how live cells could be purified from dead cells (by aligning into separate lines), although some live cells remained in the 'dead cell' line regions. Scale bar is 100 µm.

live cells in pDEP regions and dead cells in nDEP regions was therefore 98% and 88%, respectively. To avoid confusion, the concentration of target cells in pDEP or nDEP lines (e.g. live cells in pDEP regions) will be described described as the 'line purity', and will be expressed as a ratio; thus the line purity for live cells in the pDEP line was 49:1, and the line purity for dead cells in the nDEP regions was 44:6. This is shown graphically in Figure 6.4.

The 2% of dead cells found to align in the pDEP regions was thought to be due to some dead cells becoming stuck to live cells, as was observed during experiments. The 14% of live cells aligning by pDEP is presumably because at 0.15 S/m, their polarisability is less than that of the liquid. This could be due to, for example, heterogeneity within the population, or due to cells becoming stressed/pre-apoptotic. The next experiments aimed to enrich live cell alignment in pDEP regions by lowering the liquid conductivity such that all live cells exhibited greater polarisability than the liquid.

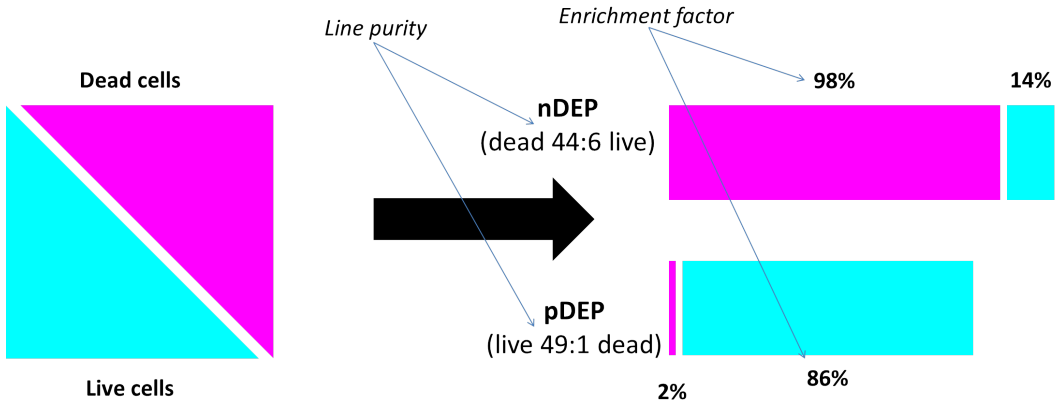

Figure 6.4: Schematic showing the fidelity of live/dead DPS cell separation at 0.15 S/m. If a 50:50 mixture of live:dead cells undergoes SAW-DEP at 0.15 S/m, 98% of dead cells align by nDEP, and 2% by pDEP. As for live cells, 86% experience pDEP, while 14% experience nDEP. Thus the enrichment factors for live and dead cells are 86% and 98%, respectively, and the purity of the nDEP and pDEP lines is expressed as a ratio.

6.2.2 Finding the optimal conductivity for high fidelity live/dead separation

In the previous experiment, the final buffer for suspension of cells consisted of DEP buffer (0.025 S/m) supplemented with 9% (v/v) propridium iodide stain solution (1.5 S/m), to give a final fluid conductivity of 0.15 S/m. In this experiment, the proportion of PI was reduced from 9% to 3.5% (conductivity 0.065 S/m), which was found to give near-perfect separation of live and dead cells, as shown in Figure 6.5.

This time, cell counting (1,000 live cells, 1,000 dead cells) showed 99.7% and 0.3% of live cells aligned in pDEP and nDEP regions respectively, a massive improvement (Figure 6.6). The 0.3% of misaligned live cells is possibly also due to cells sticking. Dead cells showed a similar distribution to 0.15 S/m, where 97% aligned in nDEP regions, and 3% aligning in pDEP regions. Again, misalignment of dead cells was presumed to be due to some dead cells being stuck to live cells.

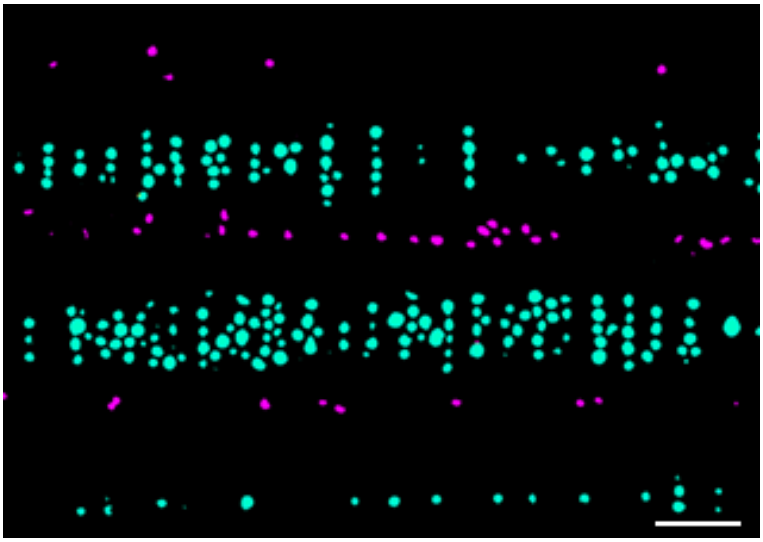

Figure 6.5: Dental pulp stromal cells undergoing SAW-DEP at 0.065 S/m, with live/dead stain, showing complete binary separation between live (cyan) and dead (magenta) cells. Scale bar is 100 µm.

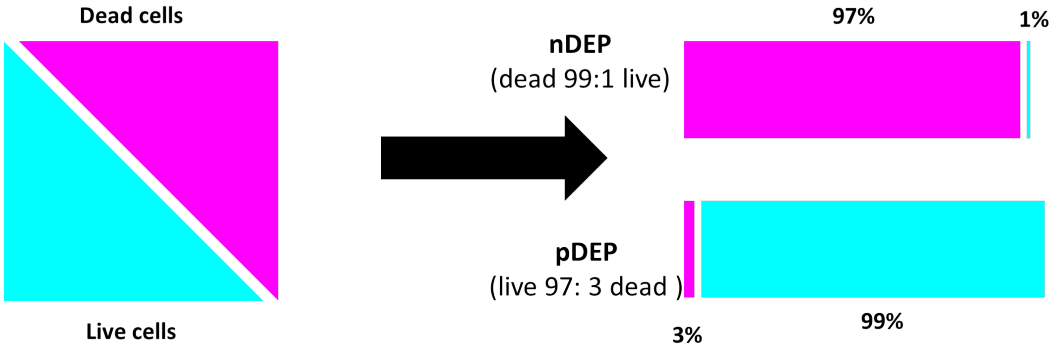

Figure 6.6: Schematic showing the fidelity of live/dead DPS cell separation at 0.065 S/m. If a 50:50 mixture of live:dead cells undergoes SAW-DEP at 0.065 S/m, misalignment of live and dead cells was shown to be 0.3% and 3%, respectively.

This level of enrichment showed that SAW-DEP is capable of separating live and dead mammalian cell types with great accuracy. It is postulated that greater accuracy, perhaps up to 100%, may be possible by flowing in a lower concentration of cells such that they are more sparsely distributed in the microchannel, and

therefore less likely to stick together.

After showing that SAW-DEP could separate live and dead mammalian cells with high efficiency, the remainder of this chapter was dedicated to investigating the ability of SAW-DEP to discern different cell lineages.

6.3 Determining DEP characteristics of cells by SAW-DEP: Conductivity stepping

6.3.1 Introduction to finding DEP characteristics of cells: Electrorotation method

After characterising and optimising the separation of live and dead cells, a logical next step was to use SAW-DEP to separate different cell types from each other. Other DEP methods, which should have similar selective capability to SAW-DEP, have been shown to separate a range of mammalian cell types, including different types of cancer cells (212), blood cell types (108), and stem cells from differentiated cells (106). Before attempting to separate two cell types, it is often necessary to perform some DEP characterisation of the cell types in question, typically by electrorotation.

Electrorotation, described in greater detail in Literature Review 1.4.3 is a method of observing the DEP behaviour of cells as they are trapped in a polynomial electrode design (see Figure 6.7). Whether a cell experiences positive or negative DEP can be determined by the direction in which the cell is spinning (clockwise or anti-clockwise). By gradually increasing the frequency throughout the experiment and noting both the speed and direction of the rotation, an electrorotation spectrum can be obtained for each cell (108) (Figure 6.8**a**). The information from this spectrum can then be used to extrapolate various dielectric parameters of the cells, namely the specific membrane capacitance, cytoplasm conductivity, and cytoplasm permittivity (108), and generate a graph of normalised DEP response (i.e. the Clausius Mossotti factor) as a function of frequency (Figure 6.8**b**) (108).

The method of using electrorotation to determine the DEP characteristics of cells is useful as a sensitive method for determining the DEP force, and extrapolating biophysical characteristics from that based on the applied frequency. This is because different biophysical aspects (generally simplified to membrane capacitance, cytoplasm conductivity, and cytoplasm permittivity (108)) dominate the DEP response according to what frequency is applied to the field (213). For

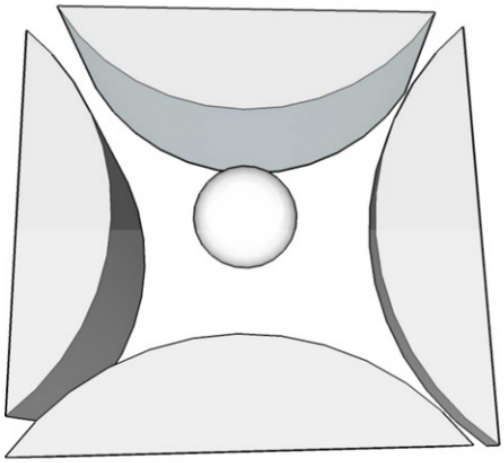

Figure 6.7: Schematic showing a cell trapped in a typical quadrupole electrode design (a type of polynomial electrode) (102). The phase the four electrodes are set to 0°, 90°, 180°, and 270°, such that the dielectric force the cell experiences causes it to rotate.

example, at 10 MHz (the frequency used in most of this work) differences in dielectric response are due almost entirely to cytoplasmic conductivity (214).

A potential drawback of this method, however, is the inability to process large numbers of cells at once; the typical data given in research papers are drawn from spectra of only ~ 20 cells, giving standard deviations of ~ 10% (108). Depending on cell type, we can expect significant heterogeneity within a cell population, with differentiation (106), cell death (215), and stage of cell-cycle (216) all factors which can effect dielectric parameters and cause this heterogeneity.

The issue of measurement throughput was addressed in the next section, which describes developing a SAW-DEP-based method to gauge the DEP characteristics of different cell types.

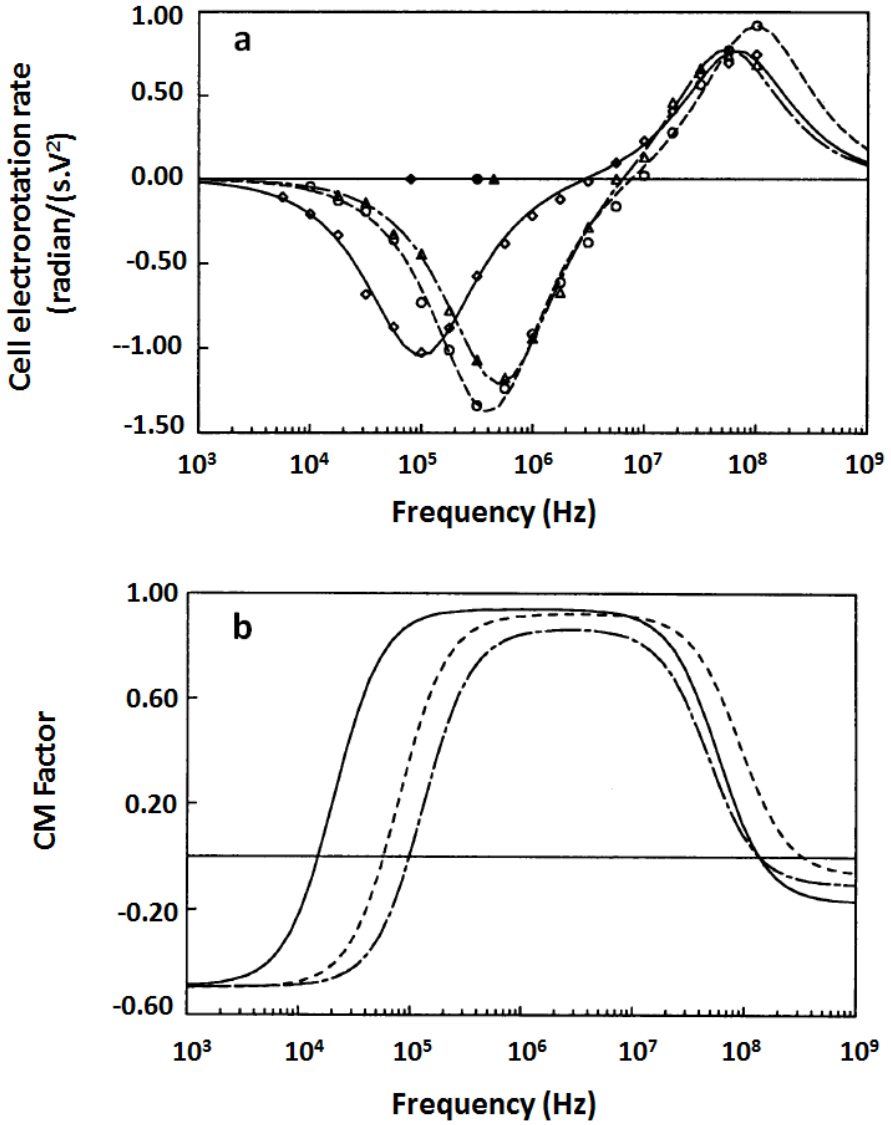

Figure 6.8: Example data from electrorotation measurements (108). **a** Electrorotation spectra for MDA231 breast cancer cells (⋄), T lymphocytes (type of blood/immune cells) (∘), and erythrocytes (red blood cells) (△). **b** The CM response as a function of frequency (at 0.01 S/m liquid conductivity) of MDA231 cells (—), T lymphocytes (---), and erythrocytes (—-—).

6.3.2 SAW-DEP for finding DEP characteristics of cells: Conductivity stepping method

The primary aim of investigating the DEP characteristics of different cell types in this thesis was to find the best conductivity at which to separate two cell types at 10 MHz. Instead of building an electrorotation device, which measures DEP response at a range of frequencies, a more direct method of probing was developed, which simply observed whether cells underwent positive or negative DEP at a range of conductivities.[1]

The procedure for the method (known as 'conductivity stepping') is outlined below; a full description of the protocol can be found in Methods 3.4.2.

- Aliquots of cells (initially dental pulp stem cells, DPS cells) were suspended in fluids of various (lower) conductivities (0.01-0.225 S/m) and stored temporarily in a 4°C refrigerator (<30 minutes).
- Starting at low conductivity, the different aliquots were flowed into the SAW-DEP apparatus and pictures were taken as they were separated. The number of dead cells were estimated in the experiment by flowing a cell aliquot at 0.065 S/m, which was found previously to separate live and dead cells (Section 6.2.2.
- More aliquots of cells were made, this time in (higher) conductivities from 0.225-0.4 S/m, and the experiment was repeated. (The experiment was carried out in two 'halves' like this to ensure that cells were not kept out of the incubator for >30 minutes at a time, thus minimising cell death which convolutes the results.)
- After the experiment, microscope images were analysed to determine the number of cells undergoing positive and negative DEP. Figure 6.9 shows sample images, together with a reference digital mask (blue and green bars)

[1] Building an electrorotation device would still have been useful to this work, not least because the results of one method could be verified against the other.

applied to indicate areas of positive and negative DEP. The percentage of cells recieving nDEP and pDEP was counted, at >1,000 cells per conductivity. Using the pictures of 0.065 S/m, the proportion of dead cells was estimated, and this proportion was subtracted from the 'nDEP' regions of the other conductivities, to give a more accurate representation of the alignment of live cells (the cells of interest).

6.4 DEP characteristics of DPS cells, 16HBE cells, and MCF7 cells

6.4.1 Measuring DEP characteristics of DPS cells, 16HBE cells, and MCF7 cells

Using the conductivity-stepping method, the DEP characteristics of DPS cells were compared with those of 16HBE cells and MCF7 cells. 16HBE cells are a cell line derived from human bronchial epithelial cells (the '16' comes from the fact that they were the 16th human bronchial epithelial cell line to become commercially available). They were chosen for this work because epithelial cells come from a distinct embrological origin (endodermal), compared to dental pulp stem cells (mesodermal origin) (see Figure 6.10).

The DEP characteristics of MCF7 cells were also investigated. MCF7 cells are a cell line derived from a breast ductal cell carcinoma (218), and are ectodermal in origin (219) (see Figure 6.10). Furthermore, these cells have previously been characterised by DEP electrorotation measurements, with Coley *et al.* (2007) (160) finding them to have a significantly lower cytoplasm conductivity than typical mammalian cells, (0.2 S/m, compared with 0.5 S/m for typical mammalian cells (159)), the dominant characteristic at 10 MHz (214).

Figure 6.11 shows the results for a typical conductivity sweep experiment with DPS cells. At the first two conductivities (0.060 and 0.115 S/m) no live cells experience nDEP, however, this increases to 70% by the final reading, 0.375 S/m.

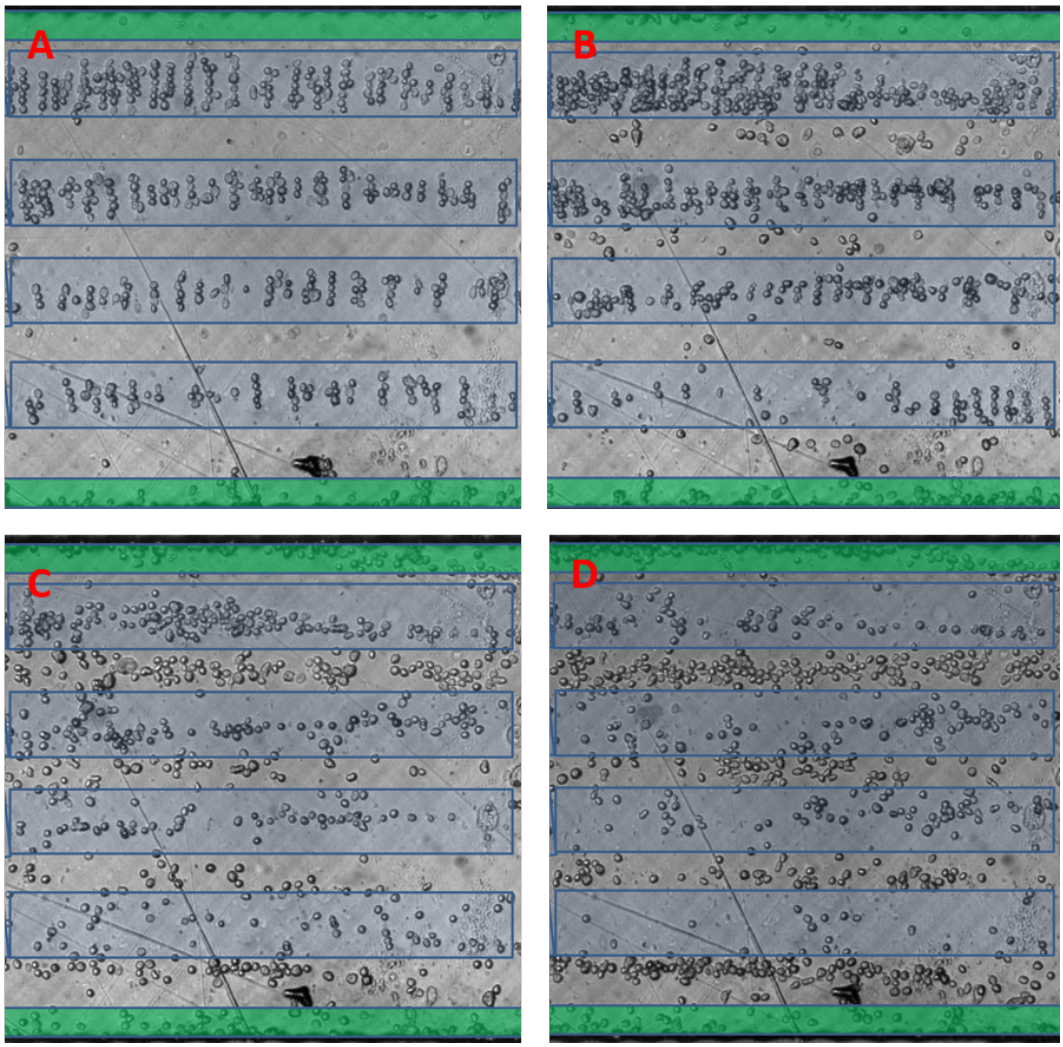

Figure 6.9: Example pictures used for analysis in conductivity-stepping experiments. Images are cropped to show only the channel and the acoustic aperture. Green bars are put at the edge of the channel (nothing is counted here due to inconsistency because of channel edge effects), and blue bars serve as a reference for pDEP. Conductivities are **A** - 0.065 S/m; **B** - 0.135 S/m; **C** - 0.27 S/m; **D** - 0.33 S/m. Frame sizes are 1.1 ×1.0 mm.

Readings were not carried out above ~ 0.4 S/m because such high conductivities were found to have a considerably weaker DEP force on cells, such that the alignment was slower and cell alignment was less uniform and therefore more

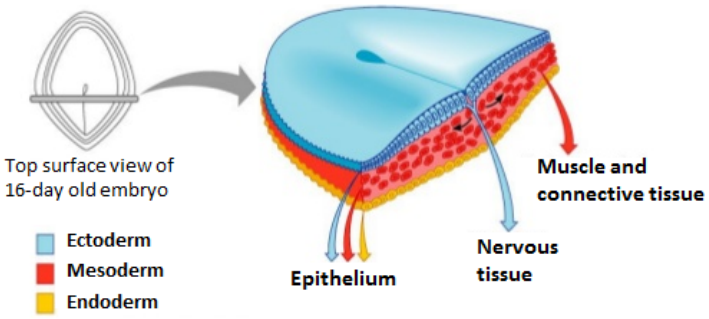

Figure 6.10: Schematic showing the three primary germ layers (ectoderm, mesoderm, and endoderm) in the developing embryo (217). DPS cells are derived from mesoderm, which forms the connective tissue of the body. In contrast, bronchial epithelium is derived from endoderm, a separate germ layer.

difficult to interpret.[1]

Figure 6.11 also shows that two readings were taken at 0.220 S/m - that is, one at the end of the first 'run' of samples (the higher % nDEP), and one at the start of the second run. The former sample of cells would have been stored in a refrigerator for ~ 20-25 minutes during the course of the experiment, while the latter sample will be 'fresh' (0-5 minutes), such that the sample contains less non-viable cells, leading to a greater proportion of pDEP-to-nDEP. As mentioned in Section 6.3.2, the proportion of dead cells (at 25-30 minutes) is substracted from all previous measurements; therefore, the first measurement (with higher % nDEP) is likely to be more accurate because it was measured just before the viability-determining sample. The gap between the two readings at 0.220 S/m (10% in this case) gives an indication of the margin of error from the start of a

[1]While SAW-DEP was still shown in this work to work well at much higher conductivities than conventional DEP methods, low performance at higher conductivities was a limiting factor of the device's capabilities. However, even at high conductivities, it is not anticipated that SAW-DEP produces joule heating, which is one of the main drawbacks for conventional DEP at high conductivity. The decrease in performance is thought to occur because ions in the solution 'screen' the static charges of the SAW-DEP substrate, leading to a lower force on cells. By making devices capable of coupling more power into the substrate from the IDTs (currently at 1 mW for the devices used in this work) it may be possible to use SAW-DEP at even higher conductivities.

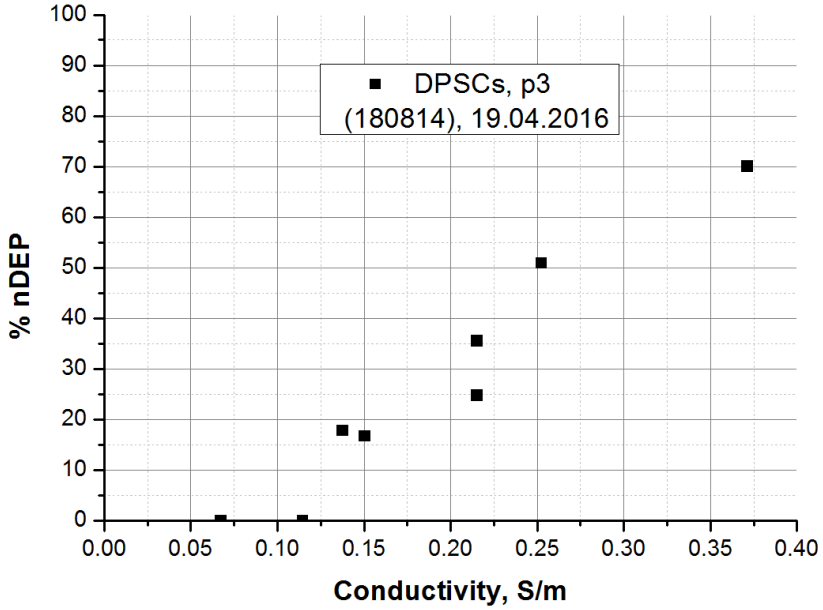

Figure 6.11: Results graph for a typical conductivity sweep experiment. As indicated by the legend, this sample comprised DPS cells at passage 3. The number 180814 is a reference number for the specific donor of the cells, followed by the date the experiment took place. The graph shows that the % of cells experiencing nDEP increases from 0% to 70% between 0.060 and 0.375 S/m. There are two readings at 0.220 S/m - one is from the end of the first 'half' of the experiment (where cells had been stored in a refridgerator for ~ 20-25 minutes), and one is from the start of the second 'half', where cells are freshly prepared (~ 0-5 minutes). This latter reading is the lower of the two in terms of % nDEP, because there is a lower proportion of non-viable cells, which all receive nDEP.

run to the end.

Figure 6.12 shows the data from several experiments (n = 3 or 4) plotted onto a single graph for each cell type, with fitted curves. The data was fitted to a simple sigmoidal curve equation, which was found to provide a statistically significant fit for the DPS cell crossover data, with an R-squared value of 0.952 (with >0.950 deemed to be statistically significant). For consistency, the same curve was fitted to MCF7 and 16HBE cells, although the significance test failed

for both of these due to the wide spread of the data (R-squared values of 0.651 and 0.602, respectively). The curves for MCF7 and 16HBE cells therefore can only be viewed as an indication for how the curves may look if more data is gathered.

The strong variance within the datasets does not necessarily mean the results gleaned from conductivity stepping are inaccurate - they come from a strong sample size of ~ 1,000 cells counted per datapoint, and care was also taken to ensure factors like confluency of cells (7-80%), passage number (within two passages for DPS cells [i.e. p4-p5], four passages for cell lines), and time spent out of the incubator (25-30 minutes), were kept relatively constant. Massive variance, for example, in MCF7 cells at a conductivity of 0.270 S/m is likely to be because cells are around a delicate tipping point in polarisability relative to the liquid (i.e. close to the crossover), such that small changes in the factors mentioned may tip a significant portion of the population from positive to negative DEP (or vice versa). Rather than suggesting that conductivity stepping is inaccurate as a technique, it more suggests that heterogeneity of DEP characteristics (e.g. cytoplasm conductivity) between cell sample preparations - at least of MCF7 and 16HBE cells - may make it instrinsically difficult to consistently separate them via DEP. Despite this variance, the data suggested it would at least be possible to significantly enrich different cell lineages with SAW-DEP (if not separate with high fidelity), and this was investigated next.

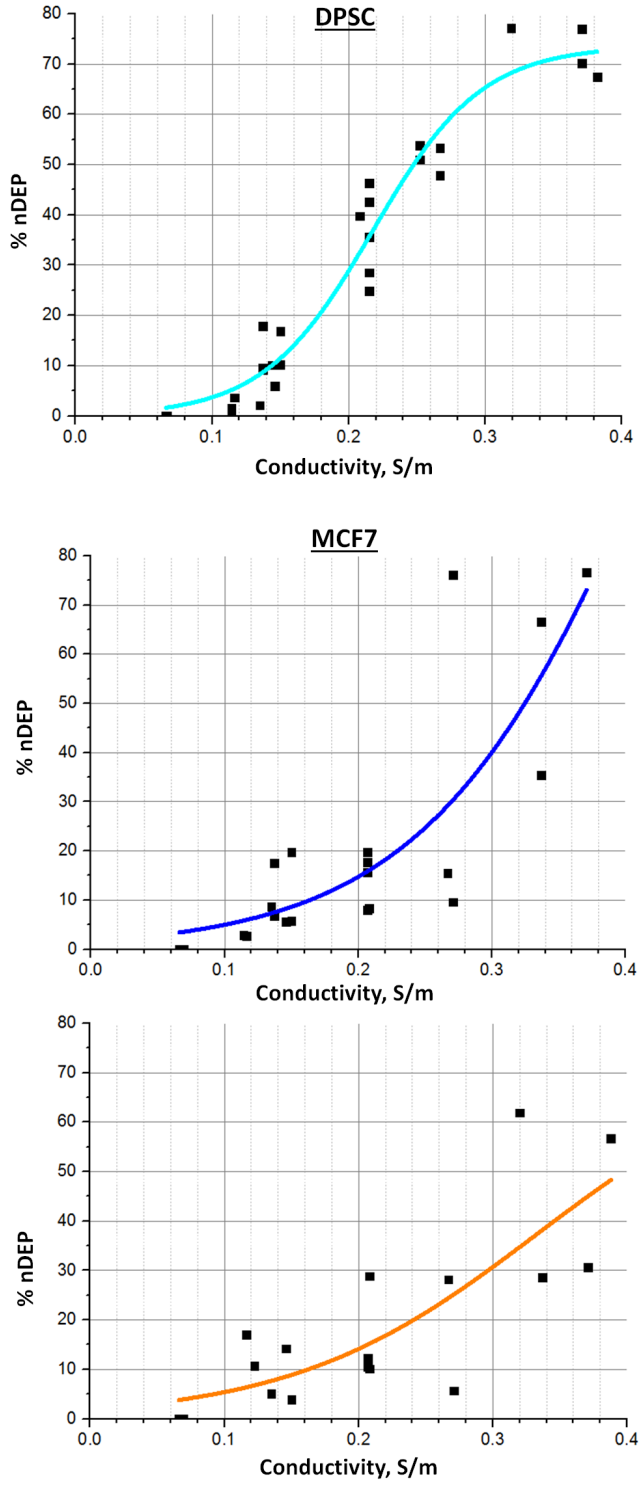

Figure 6.12: Fitted curves with raw datapoints for conductivity sweeps of DPS cells (n = 4 experiments), MCF7 cells (n = 3) and 16HBE cells (n = 3).

6.4.2 Separation of DPS cells and 16HBE cells by SAW-DEP

Figure 6.13 shows the fitted curves of all three cell types plotted onto one graph for comparison. A key reason for representing the data in this way is to indicate the possible degree of fidelity of separation between two cell types at a given liquid conductivity. The graph implies that a significant separation between DPS cells and 16HBE cells should occur where the curves of these cell types diverge, namely between 0.25 S/m and 0.35 S/m (pink shaded region). At 0.3 S/m, for example, the graph suggests that if a 1:1 mixture of DPS cells and 16HBE cells were were flowed in, 65% of DPS cells would align in the nDEP regions, and therefore 35% would align in the pDEP regions; as for 16HBE cells, 30% would align in nDEP regions, and 70% in the pDEP regions, such that a significant enrichment of either cell type can be made at this conductivity.

Based on this observation, a preliminary experiment was carried out to attempt to separate a mixture of DPS cells (at passage 4) and 16HBE cells; a sample microscope image from this experiment is shown in Figure 6.14. The figure shows significant separation of DPS cells and 16HBE cells (cyan and orange, respectively). The fidelity of this separation was estimated by counting the alignment of cells in pictures from this experiment, showing that 85% of DPS cells aligned in the nDEP region (726 total DPS cells counted), while 76% of 16HBEs aligned in the pDEP region (563 total 16HBE cells counted). Supposing even numbers of cells were flowed in, pDEP lines would be 83% 16HBEs, with nDEP lines containing 78% DPS cells. This is represented graphically in Figure 6.15.

It must be noted that two previous experiments (data not shown) had shown no significant separation, but this was presumed to be due to initial inconsistencies with the developing technique.[1] Even so, the results presented here require further verification to reliably conclude that SAW-DEP can be used to separate the

[1] A new staining procedure was developed using another dye, Resazarin (ThermoFisher, UK), to stain DPS cells a different colour to live 16HBEs (the latter stained by Calcein, as described previously).

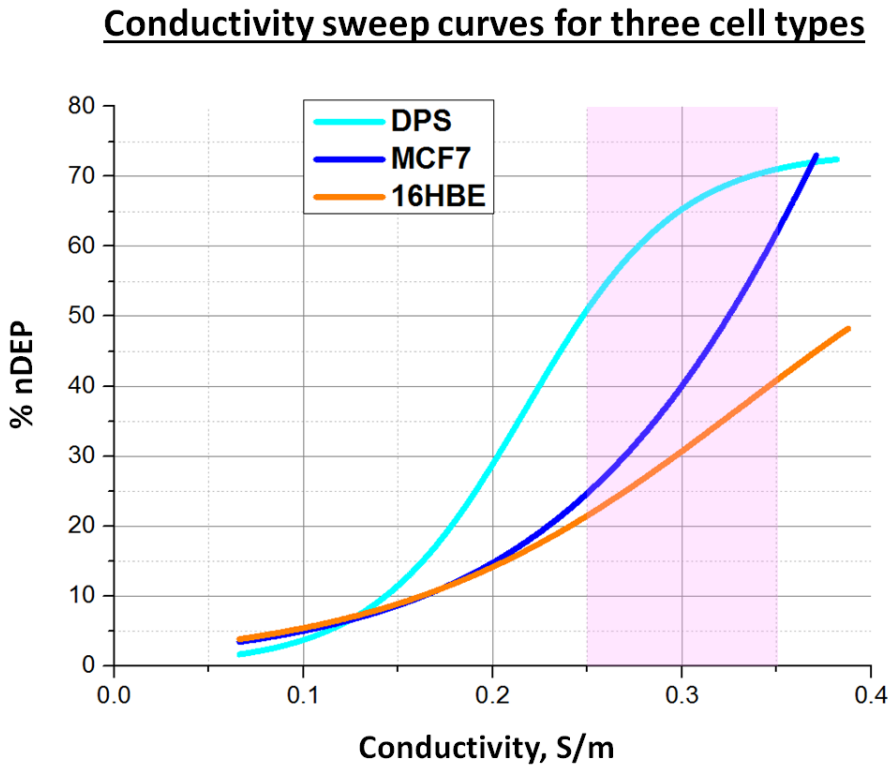

Figure 6.13: Fitted curves with raw datapoints for conductivity sweeps of DPS cells (n = 4 experiments) (p3-p5, different donors), MCF7 cells (n = 3) and 16HBE cells (n = 3).

two cell types at the stated fidelity. However, this was an experiment undertaken in the last few weeks of the experimental research conducted for this thesis, and time constraints limited the possibility of further consolidation. The results presented here, therefore, merely indicate that it may be possible to achieve significant separation of DPS cells and 16HBE cells.

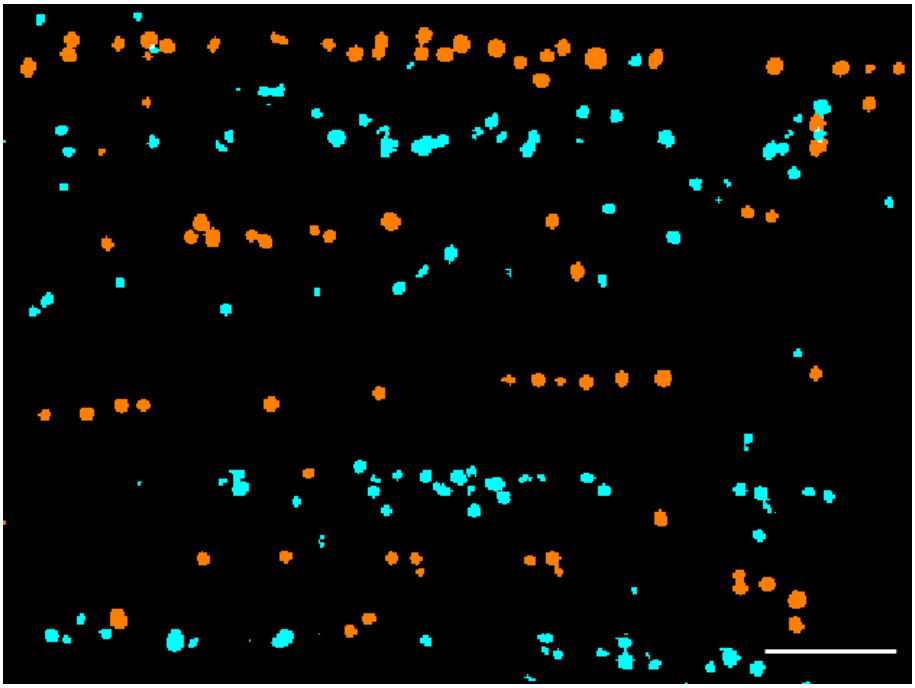

Figure 6.14: Fluorescent microscope image of 16HBE cells and DPS cells undergoing DEP at 0.34 S/m. The 16HBE cells (orange) are shown to exhibit predominantly pDEP while the DPS cells (cyan) exhibit predominantly nDEP. Scale bar is 150 µm.

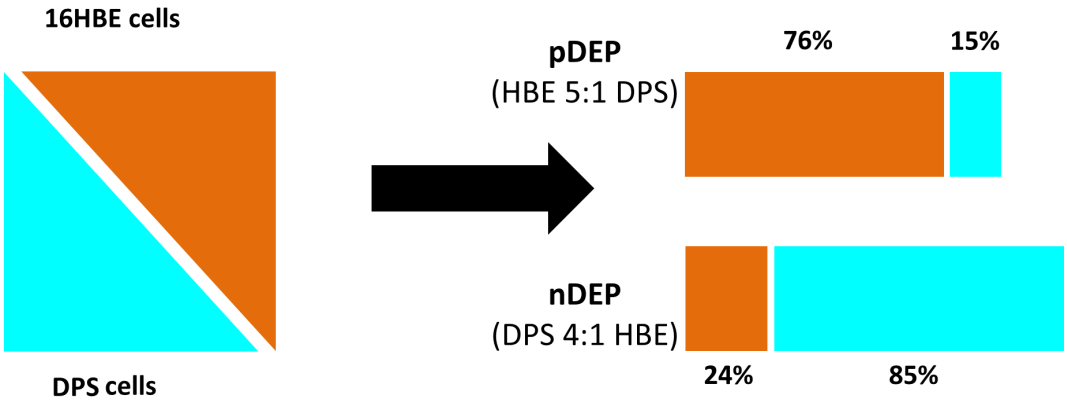

Figure 6.15: Schematic showing the fidelity of separation of DPS cells and 16HBE cells at 0.34 S/m. If a 50:50 mixture of DPS cells:16HBE cells undergo SAW-DEP, 'correct' alignment of DPS cells and 16HBE cells was shown to be 85% and 76%, respectively.

6.5 DEP characteristics of DPS cells as a function of passage number

The final experiment conducted during this research was another preliminary study, examining whether the DEP characteristics of DPS cells changed as they grew older. This was investigated partly due to an observation made in Section 6.2.1 that cells of a high passage number (P9) aligned with a significantly greater proportion in nDEP regions (38%) at 0.15 S/m, compared with those at passage 3-5 (~ 20%) (see Figure 6.2).

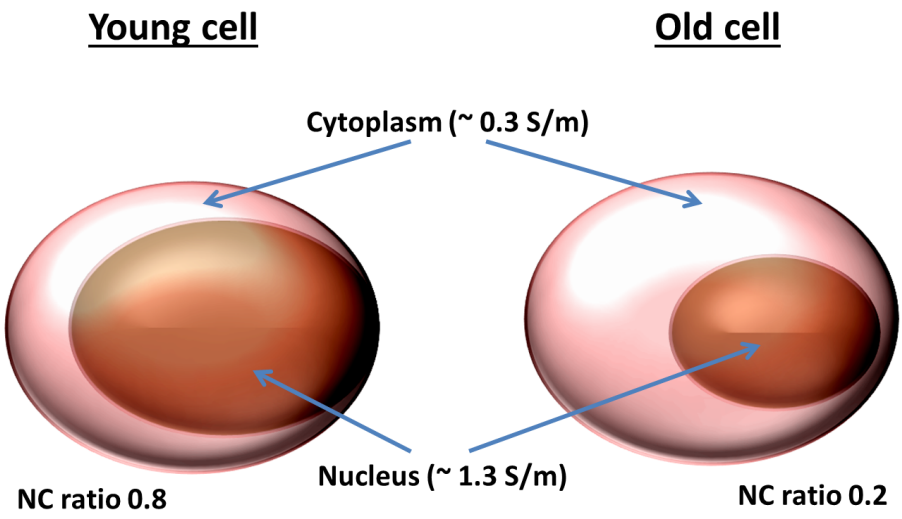

Figure 6.16: Schematic illustrating how the change in nucleus-to-cytoplasm (NC) ratio typically changes as cells mature, and how this effects overall 'cytoplasm conductivity' (which for DEP single-shell model calculations encompasses the nucleus within the cytoplasm). Typical values for cytoplasm and nucleus conductivity and NC ratios are from Pethig *et al.* 2010 (220).

Decreasing polarisability as a cell population ages has already been experimentally observed (220, 221). A key marker of ageing cells is their nucleus-to-cytoplasm (NC) ratio, which shrinks typically from 0.8 to 0.2 as cells mature and differentiate (220, 221). This reduction leads to a significant decrease in

cell polarisability, due to the fact that the cytoplasm has a significantly lower conductivity (typically modelled as 0.32 S/m) compared to the nucleus (modelled as 1.35 S/m) of the cell (220). This is represented visually in Figure 6.16. It must be stressed that the precise NC ratio of DPS cells (or similar cells like bone marrow stem cells) is not present in the literature, so 0.2-0.8 should only be considered as a rough guide.

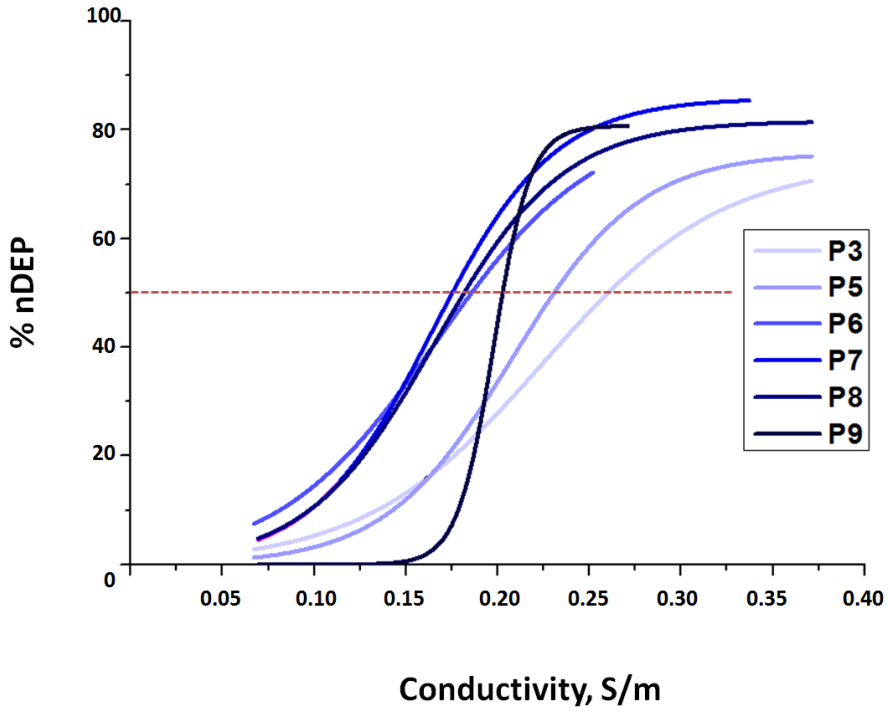

Figure 6.17: Fitted curves from conductivity sweep experiments to show change in % nDEP (at a given conductivity) as a function of passage number (P3,5-9). From P3, the 'crossover conductivity (at which 50% of cells have crossed over/experience nDEP - see red line) decreases from ~ 0.27 to ~ 0.18 at P7. However, this trend then reverses, with increasing crossover conductivities for P8 and P9 (~ 0.20).

The results from Section 6.2.1, however, are from different donors, so it was important to conduct a systematic study using the same donor to verify if polarisability of the cells did indeed decrease with passage number. Conductivity

sweeps were therefore performed with cells from passage 3-9[1] (except passage 4 which was lost due to user error), and the results are shown in Figure 6.17. Similar to Section 6.4.1, simple sigmoidal curves were fitted to the data (see Appendix C.2), this time for single experiments (no repeats at the same conductivities). The R-squared values for the fits mostly fell below 0.95, meaning that the data is not statistically significant, and these curves should merely be viewed as an indication of how curves might look if more data is gathered.

Figure 6.17 shows that from P3 to P7, the conductivity sweep curve moves from right to left, indicating decreasing cell polarisability, as was expected for ageing cells. However, P8 and P9 appear to show slightly increasing cell polarisability. To simplify the interpretation of the results, the crossover conductivity (i.e. the conductivity at which 50% of cells experience nDEP, and 50% experience pDEP) was plotted together with a fitted curve in Figure 6.18.

The results, if repeated consistently, would suggest that DPS cell overall cytoplasm conductivity decreases from P3 to P7, whereupon it starts to increase again up to P9. However, to be verified, these results would need to be repeated at each passage (at least n = 3), and ideally a comparison made between 3 or more donors.

6.5.1 Chapter conclusions

The focus of this chapter was on gauging the specificity of SAW-DEP for separating cell types. The most convincing data was that showing the separation of live and dead DPS cells, at 98% purity of both populations from a 1:1 mixture (Section 6.2). This is favourable compared with other cell separation methods in the literature; a review by Gao *et al.* 2013 ((222)) gives live/dead mammalian cell separation by DEP at 87% (live cells). The efficiency for MACS, the current 'gold standard' cell separation platform, ranges from 85% to 96% depending on

[1] At P8-P9 the growth rate of DPS cells slows considerably, making it harder and increasingly more time consuming to culture.

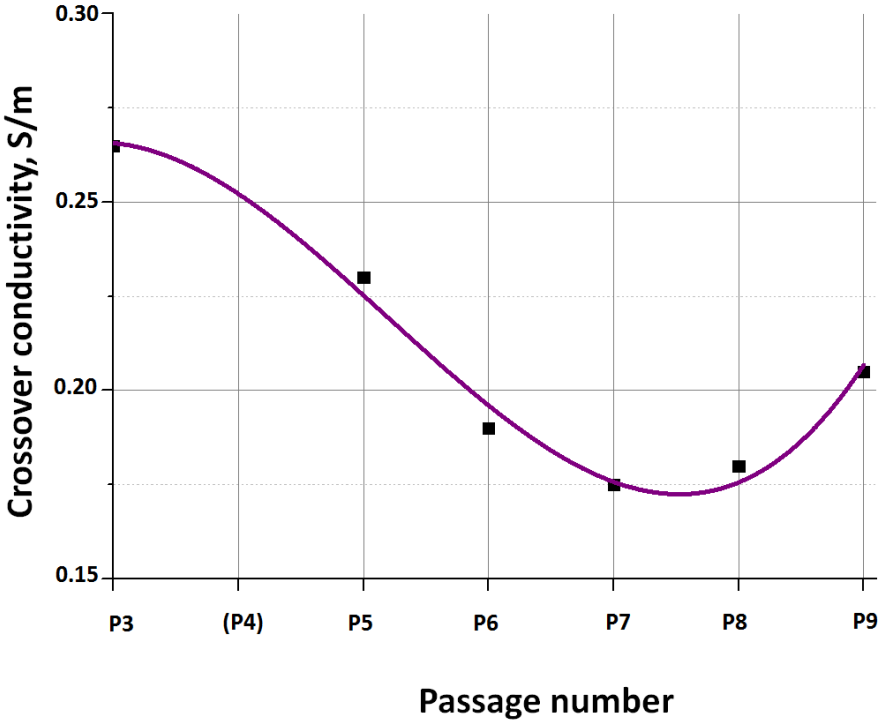

Figure 6.18: Crossover conductivity (the conductivity at which 50% of cells get nDEP/50% get pDEP) as a function of passage number. This is essentially plotting the points at which the curves in Figure 6.17 intersect the red (50% nDEP) line.

cell type and ligand binding strength (222).

While the separation efficiency for DPS cells and 16HBE cells is promising (Section 6.4.2), this result should not be analysed without being validated by further experimentation. This leads on to a shortcoming of this chapter, which is that the work separating live cell types gave very variable results. This is partly because time ran out, being conducted at the tail-end of the studentship, and inconsistency could perhaps be improved if experimental procedures were optimised. Nevertheless, the preliminary results also point to a possible inherent shortfall of DEP-selection based on cytoplasm conductivity, which is that there is a lot of variation in cytoplasm conductivity within cell types, even if average

conductivities are somewhat distinct between two cell types (at least those studied). The consequence of this is reduced specificity as the range of cytoplasm conductivities overlap between two cell types. Even so, better purity of the target cell can be achieved at the expense of recovery by raising or lowering the buffer conductivity used to exclude more of the non-target cell; thus, it is very possible that DEP (and SAW-DEP in particular) can achieve efficiencies approaching those of MACS for 16HBE cells and DPS cells, if the preliminary results are accurate.

Chapter 7

Conclusions and Outlook

This thesis concerns the development of a type of dielectrophoresis (DEP)-based technology known as SAW-DEP, from early proof-of-concept experiments to the separation and differentiation of clinically-relevant stem cells. The proceeding section (7.1) will summarise the key milestones discussed in the previous chapters. Following this, the advantages and limitations of SAW-DEP compared with traditional DEP methods shall be discussed (Section 7.2), after which will come a discussion on the suitability of SAW-DEP to be used to enrich live cells for autologous bone grafting procedures (Section 7.3.1), a key goal of this work. Finally, three separate branches of possible future directions for the work in this thesis will be briefly summarised (Section 7.3.2).

7.1 Summary of key achievements of thesis

7.1.1 Chapter 4

- By videoing the movement of latex beads (various sizes) in the device to map the force experienced at various regions within the microchannel, experimental data were found to closely match an analytical model for the electric field in a similar DEP system. This verified that shear horizontal surface acoustic wave (SH-SAW) devices could be used to produce a well-characterised DEP force on microparticles.

- To demonstrate the potential of SAW-DEP, a classic DEP experiment of separating live and dead yeast cells (103, 114, 124, 185, 187) was replicated using SAW-DEP, showing very precise and uniform separation of the two cell types (Figure 7.1).

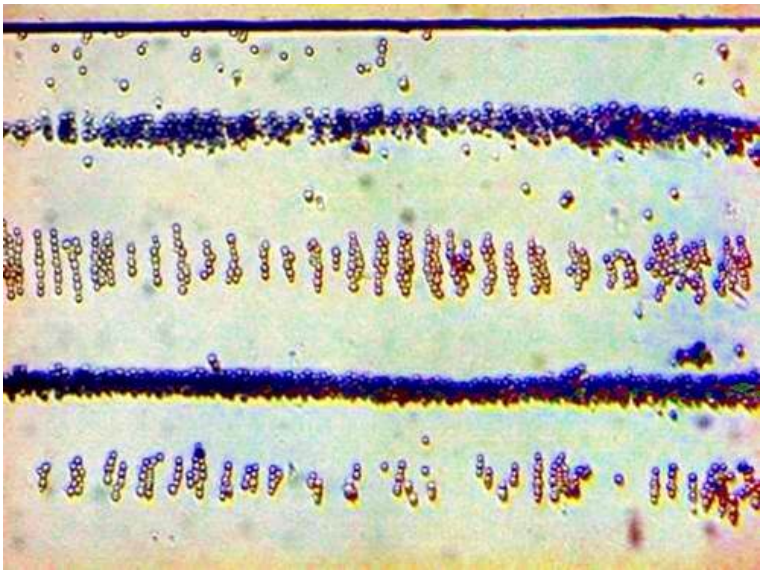

Figure 7.1: Microscope image of live and dead yeast cell separation (Section 4.5). The live yeast cells (white) can be seen to be clearly spatially separated from the dead yeast cells (blue), with both cell types arranged into precise, uniform lines.

7.1.2 Chapter 5

- A flow cell was designed and manufactured to allow mammalian cells to be delivered to the chip and subsequently extracted in a precise, controlled manner (Figure 7.3), with output of ~ 20,000 cells/minute.

- The viability of primary human mesenchymal stem cells (dental pulp stem cells) was tested after undergoing a SAW-DEP live cell enrichment procedure, designed to be similar to what could be used in a clinical setting. Statistical analysis showed that the SAW-DEP electric field did not cause cell viability to decrease significantly; however, a statistically-significant

drop in viability (from 96.7% to 91.3% was observed for cells held in DEP buffer rather than culture medium.

- The effect of DEP buffer composition was assessed, with the conclusion that adding 0.8-2% m/v BSA to a solution led to a significant increase in viability. An optimised buffer showed 93.7% cell viability, compared to 96.6% for a positive control (culture medium).
- Finally, undergoing SAW-DEP and all associated factors (shear stress of microfluidics, being held in DEP buffer) were shown to have no significant effect on the ability of DPS cells to undergoing osteogenic lineage differentiation.

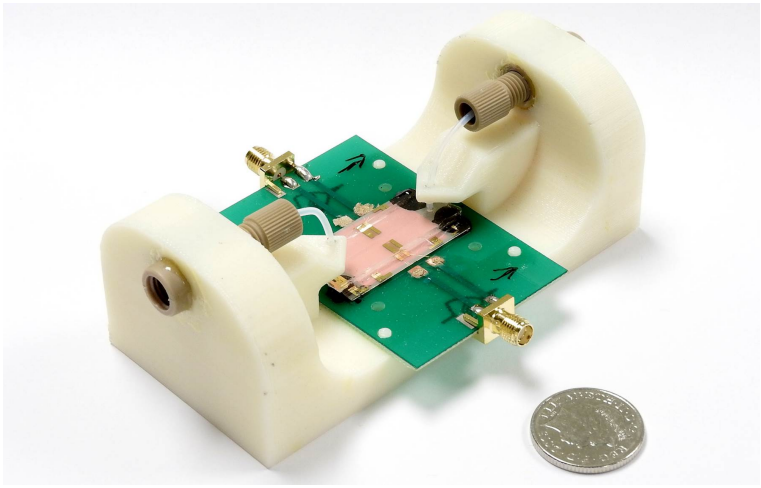

Figure 7.2: Photograph of the final flow cell iteration made during this work, included for illustrative purposes (from Section 5.2).

7.1.3 Chapter 6

- By tuning the conductivity of the fluid, SAW-DEP was shown to achieve very high fidelity separation of live and dead primary human cells (DPS cells), with negative and positive alignment regions containing 99% dead cells and 97% live cells, respectively (see Figure 6.1).

- 'Conductivity-stepping' was developed as a method to screen large numbers of cell populations for their DEP characteristics. Preliminary studies suggested differences between different cell lineages (DPS cells, MCF7 cells, and 16HBE cells) and differences between DPS cells of different passage number. This suggests it may be possible to use SAW-DEP to enrich certain cell-types from a heterogeneous sample of two or more of these cell types.

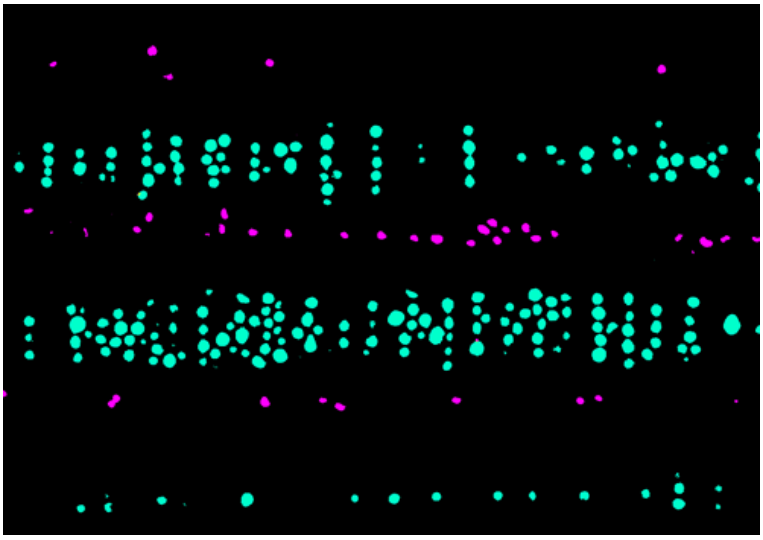

Figure 7.3: Microscope image of fluorescently-stained live cells (cyan) and dead cells (magenta), separated by SAW-DEP (from Section 6.2).

7.2 Summary of the advantages and limitations of SAW-DEP compared to other DEP methods

A full discussion of the shortfalls of traditional DEP methods that SAW-DEP was developed to address can be found in Literature Review 1.4. Below is a summary of key advantages that SAW-DEP has over traditional DEP approaches:

Advantages of SAW-DEP

1. *Continuous throughput* - Most DEP approaches involves at least one cell type being trapped at the electrodes by pDEP. These means that DEP separation must be carried out in batches that are limited by the size of the electrodes, such that they generally have low throughput (223). SAW-DEP, on the other hand, allows cells to be continously directed into separated channels, mainly due to the fact that electrodeless systems are less susceptible to cell-fouling. At a current flow rate of ~ 30,000 cells per minute (with 75% recovery), it is anticipated that this could be greatly improved by increasing the power input to the system (currently 1 mW) without having to increase the device' chip size.

2. *Conductive solutions* - While traditional DEP experiments must be perfomed in low-conductivity solutions (<0.03 S/m) to prevent Joule heating from the electrodes, the SAW-DEP field shows no signs of heating up to 10 S/m (Chapter 4.3.2). It must be noted, however, that device performance (i.e. time taken for cells to align) significantly decreases above ~ 0.3, although good alignment/separation can be observed up to 0.4 S/m and possibly higher. One key advantage of being able to use higher conductivity DEP buffer solutions is that more constituents can be added too ensure enhanced cell viability.

3. *Enhanced cell viability* - The viability of cells is expected to be far better in SAW-DEP systems than traditional DEP. This is due primarily due to points 1. (i.e. exposure to the electric field is brief), and 2. (i.e. more favourable cell buffer solutions can be formulated).

Two key disadvantages of SAW-DEP are also summarised below:

Limitations of SAW-DEP

1. *Device tunability* - The operating frequencing for a SAW-DEP device is relatively confined to a ~ 10% bandwidth around the device operating frequency (10 MHz and 20 MHz for the devices used in this work). The selectivity of

the device (i.e. to be used for a variety of cell types) can still be tuned by adjusting the conductivity of the buffer solution, however, this is thought to be more cumbersome than tuning the selectivity of traditional DEP devices, by simply modulating the applied frequency (which avoids having to prepare a variety of different buffers, etc).

2. *Selectivity* - On a related point, SAW-DEP can only practically be used on mammalian cells between 5 - 40 MHz. This is because below 5 MHz, the chip length would have to be greater than ~ 40 mm to accomodate larger IDTs, thus making it impractical from a fabrication/lab on a chip point of view. At 40 MHz, the wavelength (on $LiTaO_3$) is 100 µm, such that the separation between pDEP and nDEP is only 25 µm - roughly the diameter of a cell. The consequence of limiting devices to the 5 - 40 MHz range is that cells can be selected based on differences in cytoplasm conductivity (i.e. including cytoplasm-to-nucleus ratio), but not for other factors such cytoplasm permittivity and membrane capacitance which must be selected for at lower frequencies (214). This limits the cell types which can be seperated by DEP; for example, T lymphocytes and MDA231 breast cancer cells have similar cytoplasm conductivities, but distinct membrance capacitances, such that they can only be efficiently separated at lower frequencies (108).

7.3 Current status of the technology and future directions

7.3.1 Discussion on the suitability of SAW-DEP for autologous tissue grafting

In brief, this thesis has provided solid evidence to show that the SAW-DEP technology developed was capable of efficiently separating live and dead dental pulp stem cells (DPS cells), a mesenchymal stem cell similar to the ultimate goal of bone marrow stem cells (BMS cells). Furthermore, viability studies showed strong evidence that SAW-DEP did not adversely affect cells, although viability

could be improved, say, by improving the buffer composition and reducing the experiment time.

To reduce the experiment time, the sorting rate must be increased dramatically if the sorting is meant to be achieved within an 'intra-operative' timescale of <30 minutes; the typical number of cells used in cell therapeutics and grafts is 10 million - 1 billion (224). Current rates described in this work are on the order 900,000 cells per 30 minutes, recovering 675,000. Increasing the power coupling of the device (currently 1 mW) may allow much faster flow rates (as cells align at a greater force). Other approaches to improving throughput include using a wider channel and improving recovery by minimising fouling (for example, by functionalising devices with a defined PEG-layer, rather the current BSA-functionalisation approach).

7.3.2 Future work

Clinical applications - testing on mice

A grant was awarded to look in greater detail at the clinical applications of the SAW-DEP technology by using a mouse model to see if it could enhance grafting procedures. The proposed research is to transplant scaffolds into mice with a cranial defect. The scaffolds will be seeded with cells separated by SAW-DEP, and compared to those seeded with cells separated by MACS (currently considered a 'gold standard' for cell separation (223), Chapter 1.2.2).

7.3.3 Yeast viability counter

Another grant was awarded, based mainly on the results from Chapter 4.5, to make a commercial diagnostic device to probe the viability of yeast cultures in breweries. Breweries currently outsource diagnosing the viability of yeast cultures, which is done off-site by biotech firms which stain and count the number

of dead cells.

The grant was used to design an automated, mass-producible viability counter that could be used in-house with no expertise and no need for staining cells. The device consisted of a flow cell component, which can be seen in Figure 7.4, and an automated graphical user interface for simplified operation. This technology works by the user injecting a small sample of yeast suspension, whereupon the device automatically flows it to the SAW-DEP aperture and takes a picture of live and dead cell separation. A photograph is taken via a camera built into the device, and a computer algorithm counts the proportion of cells aligning in pDEP ('live') and nDEP ('dead') regions, to tell the user the % viability of cells.

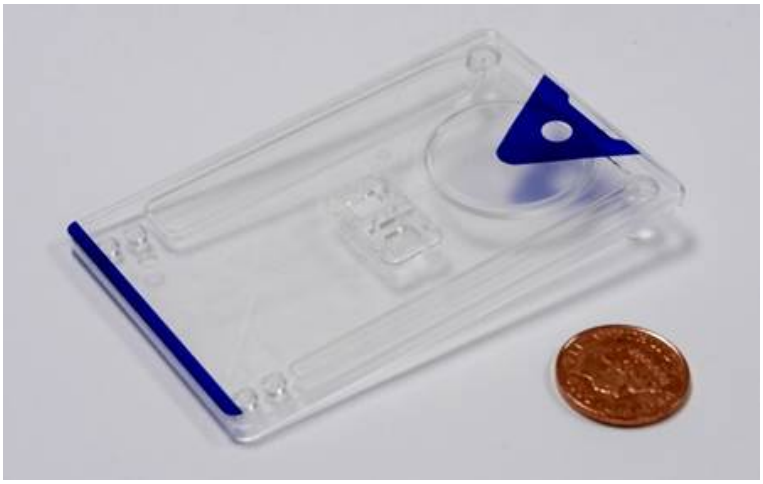

Figure 7.4: Photograph of injection-moulded flow cell used to assess yeast culture viability.

7.3.4 Device capability - high fidelity separation of other key cell types

While this was addressed to a certain extent in Chapter 6, the research presented here woulc do well to be supported by a comprehensive investigation into the range of cell types that can be selected for using SAW-DEP, starting with the

typical model cells used in DEP. These include live/dead cells, which are well covered here; however, future cell types to separate include blood cells (e.g. T-lymphocytes from red blood cells (108)), and cancerous from other cancerous or non-cancerous cells (108, 212).

Particularly relevant to the work presented here is the prospect of using SAW-DEP to separate stem cells from non-stem cells (i.e. which has many applications within regenerative medicine/cell therapies), and there is some work of DEP separation of stem cells in the literature that can be built on (106). Another opportunity relevant to this work is the prospect of separating mesenchymal stem cells (MSCs) from bone marrow aspirate, with MSCs only constituting 0.08%, and the rest being mainly blood cells ((23), Chapter 1.1.2). This is a key focus of a new PhD studentship that follows on from this work (225).

Appendix A

Supplementary information - multimedia

This Appendix describes each of the four short videos featured on the supplementary CD; each video is a different slide on the Powerpoint presentation.

A.1 Red blood cell alignment by SAW-DEP

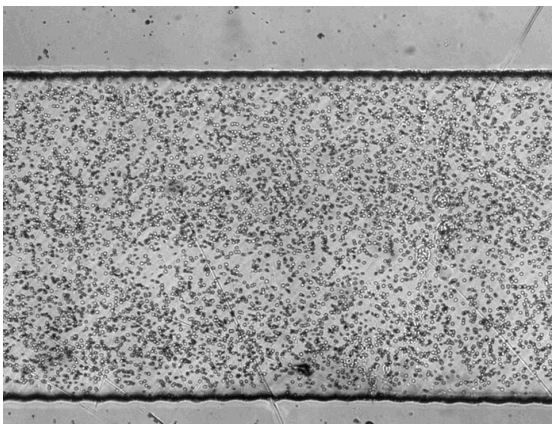

The video (in GIF format) shows red blood cells before and after turning the electric field on (1 mW applied power, 10 MHz device). It can be seen that most cells align immediately (<1 second) into pearl chains by positive DEP, although some cells take longer, presumably due to their being situated near zero-gradient regions (see Section 4.4) upon application of the SAW-DEP electric field. Red blood cells showed a slightly quicker DEP response than other mammalian cells studied, despite their smaller size (5 µm diameter compared with 15 µm diameter) - this

is presumably due to their high iron (Fe) content, making them more polarisable.

Red blood cells were supplied courtesy of Dr. Erica Watson from the Leeds Institute of Cancer and Pathology. For scale, the width of the microchannel (defined by thick black horizontal lines at the top and bottom of the frame) is 1 mm.

A.2 1 µm diameter latex beads aligning by SAW-DEP

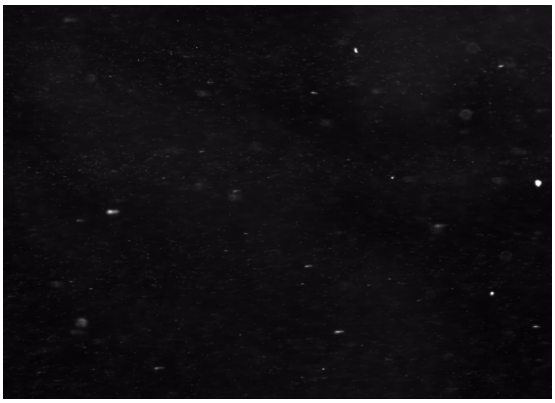

The video shows 1 µm latex beads aligning by negative DEP (1 mW applied power, 10 MHz device). For scale, the frame size is 0.65 mm x 0.85 mm; the spacing between the lines is ~ 200 µm.

A.3 Frequency-stepping with dental pulp stromal cells

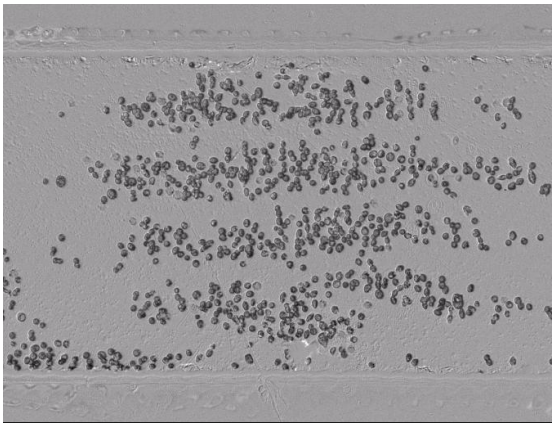

This video shows DPS cells trapped by positive DEP in a 10 MHz device (1 mW applied power). Every 1-2 seconds, the researcher changes the applied frequency within the 9.5-10.5 MHz range (for example, 9.6 MHz to 10.1 MHz, etc). For scale, the frame size is 1.3 x 1.7 mm.

A.4 Separation of live and dead dental pulp stromal cells

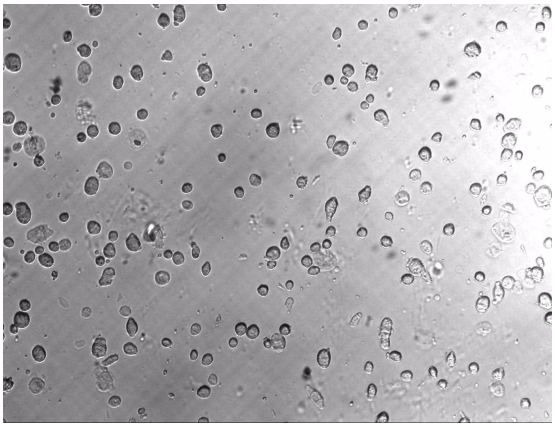

The video shows dental pulp stromal cells (DPS cells, unstained) being separated into live and dead cells in a 10 MHz device (1 mW applied power), at a x4-slowed frame rate. For scale, the frame size is 0.65 mm x 0.85 mm. The electric field is applied immediately after the video starts. The live cells can be distinguished because they are in focus (aligning at the bottom of the channel, nearest to the piezoelectric chip from which the electric field emanates) and so are a darker

colour, compared with the more translucent (due to being out of focus) dead cells.

Appendix B

Scripts

This Appendix features several scripts (four in Python and one in Java) used for calculations in this work.

B.1 CM factor for latex beads

This is the Python script used to calculate the CM factor for latex spheres, using equations from (149, 157).

```
#Script to plot FCM as a function of liquid conductivity.
    It can also plot FCM as a function of frequencing, by
    substituting Line 10 with Line 9, and Line 16 with Line
     15.

import numpy
import matplotlib.pyplot as plt


#General values

#freq = numpy.arange(1e3, 1e9, 1e3)
freq = 10e6 #Applied frequency
omega = 2*numpy.pi*freq

eps_0 = 8.854e-12 #vacuum permittivity
```

```
r = 25e-7 #radius of particle
#sig_m = numpy.arange(1e-5, 1.2, 1e-3) #conductivity of
    medium
sig_m = 5e-4
eps_p = 2.56*eps_0 #permittivity of particle
eps_m = 78*eps_0 #permittivity of medium
f_0 = 100e3
#-------------------------------------------------------

#sig_p = 0.0604

#Surface conductance



K_s = (r/4)*( - sig_m + (9*sig_m**2 - 4 * ( ( eps_p -
    eps_m)*(eps_p + 2*eps_m)*(2*numpy.pi*f_0)**2))**0.5)


#Particle conductivity

sig_p = (2*K_s)/r



#-------------------------------------------------------------




ceps_p = numpy.vectorize(complex)(eps_p,sig_p/omega)
ceps_m = numpy.vectorize(complex)(eps_m,sig_m/omega)

FCM = (ceps_p-ceps_m)/(ceps_p+2*ceps_m)


#-------------------------------------------------------------
```

```
# Plotting


plt.rc('font', **{'sans-serif' : 'Arial', 'family' : 'sans
    -serif'})
plt.plot(freq,FCM.real)

plt.hlines(0,1e3,1e9,linestyle='dashed')

plt.xlabel('Frequency, Hz')
plt.ylabel('CM Factor')
plt.title('DEP response of 1 micron diameter latex beads')
plt.show()

print K_s

print FCM
```

B.2 CM factor for yeast

This is the Python script used to calculate the CM factor for (live) yeast cells, using biophysical values from (162) (this paper also has values for dead cells which were used in this work).

```
import numpy
import matplotlib.pyplot as plt


# general values

freq = numpy.arange(1e4,1e9,1e5)
#freq = 1e7
omega = 2*numpy.pi*freq
vacperm = 8.854e-12
```

```
cond_med = 0.021
#cond_med = numpy.arange(0.001,2.0,0.001)



# r = radius, c = conductivity, e = permittivity 1, 2, 3 =
    cell wall, membrane, nucleus respectively

r1 = 3e-6
c1 = 140e-4
e1 = 60*vacperm
r2 = 2.78e-6
c2 = 2.5e-7
e2 = 6*vacperm
r3 = 2.772e-6
c3 = 2000e-4
e3 = 50*vacperm

e_med = 80*vacperm


#complex permittivities. NB numpy.vectorize takes two
   arrays and combines them to produce the real and
   imaginary parts of a complex number, respectively

eps1 = numpy.vectorize(complex)(e1,c1/omega)
eps2 = numpy.vectorize(complex)(e2, c2/omega)
eps3 =numpy.vectorize(complex)(e3, c3/omega)


#complex permittivity of the medium

eps_med = numpy.vectorize(complex)(e_med,cond_med/omega)


#complex permittivity of the particle

eps23 = eps2*((r2/r3)**3+2*((eps3-eps2)/(eps3+2*eps2)))/((
   r2/r3)**3-((eps3-eps2)/(eps3+2*eps2)))
```

```
eps_cell = eps1*((r1/r2)**3+2*((eps23-eps1)/(eps23+2*eps1)
    ))/((r1/r2)**3-((eps23-eps1)/(eps23+2*eps1)))


# finally, the clausius mossotti factor

FCM = (eps_cell-eps_med)/(eps_cell+2*eps_med)

# Found two X values which the root (f(x) = 0) is
    contained within
isPositive = (FCM[0].real > 0)
exactRoot = None # index of exact root (if it's actually
    found)
leftBound = 0 # index of the left bound on the root
rightBound = 0  # index of the right bound of the root
for i in range(1, len(cond_med)):
        if FCM[i].real == 0: # we've found the exact root
                exactRoot = i
                break
        elif FCM[i].real > 0: # real part is positive
                # We've passed through the root! Stop here
                if not isPositive:
                        rightBound = i
                        break
        else: # real part is negative
                if isPositive:
                        rightBound = i
                        break
        # Update left bound -- only gets called if root
            not found!
        leftBound = i
# Display left and right bounds of root, UNLESS EXACT ROOT
    FOUND
if exactRoot:
        print("Root:\n\tCondMed={} CMFactor={}".format(
            cond_med[exactRoot], FCM[exactRoot].real))
else:
        print("Left Bound:\n\tCondMed={} CMFactor={}".
            format(cond_med[leftBound], FCM[leftBound].real
            ))
```

```
        print("Right Bound:\n\tCondMed={} CMFactor={}".
            format(cond_med[rightBound], FCM[rightBound].
            real))


# Plotting

plt.plot(cond_med,FCM.real)
plt.xlabel('Medium conductivity, S/m')
plt.ylabel('CM Factor')
plt.title('Live Yeast cell CMF')
plt.show()
```

B.3 CM factor for mammalian cells

This is the Python script used to calculate the CM factor for mammalian cells. Mammalian cells were modelled using the erythrocyte biophysical values from (108) (the dominant value being the cytoplasm conductivity, 0.5 S/m - this was decreased for dead cells to fit the data.

```
#This script plots FCM as a function of liquid
    conductivity for two cell types (currently set to 'live
    ' and 'dead' generic mammalian cell).

import numpy
import matplotlib.pyplot as plt

plt.rcParams['axes.color_cycle'] = ['m', 'k', 'k']



vacperm = 8.854e-12

def mamcell_cap_model(cell_type,freq,cond_med,rad,memthick
    ,cap_mem,perm_cyt,cond_cyt):
```

```
#General values
        cond_cm = 3e-6
        omega = 2*numpy.pi*freq
        e_cyt = perm_cyt*vacperm
        g_mem = cond_cm/memthick
        perm_med = 80*vacperm

#complex permittivities. NB numpy.vectorize takes two
   arrays and combines them to produce the real and
   imaginary parts of a complex number, respectively


        comcap_mem = numpy.vectorize(complex)(cap_mem,
            g_mem/omega)
        comperm_cyt = numpy.vectorize(complex)(e_cyt,
            cond_cyt/omega)

#Complex permittivity of the cell and medium
        comperm_cell = (comcap_mem*rad*comperm_cyt)/(
            comcap_mem*rad+comperm_cyt)
        comperm_med = numpy.vectorize(complex)(perm_med,
            cond_med/omega)


#FCM calculation

        FCM = (comperm_cell-comperm_med)/(comperm_cell+2*
            comperm_med)


# Setting up

        plt.plot(cond_med,FCM.real,label=cell_type)

        return FCM.real


# Call the function

xValues = numpy.arange(0.00100,1.0,0.001)
```

```
#Reminder: def mamcell_cap_model(cell_type,freq,cond_med,
    rad,memthick,cap_mem,perm_cyt,cond_cyt):

a = mamcell_cap_model('Live cell',  9.75e6,xValues,7.5e
    -6,8e-9,9e-3,57,0.5)


#Identical to 'live' cell, but with lower cond_cyt

b = mamcell_cap_model('Dead cell',  9.75e6,xValues,7.5e
    -6,8e-9,9e-3,57,0.12)




#plt.xlabel('Medium conductivity, S/m')
#plt.ylabel('DEP response')
#plt.title('Breast cell DEP response @ 10 MHz')
#plt.axhline(0, color = 'black')


#plt.legend()
#plt.show()

#numDataPoints = len(xValues)
#for i in range(numDataPoints):
#        x = xValues[i]
#        print "%f,%f,%f" % (x, a[i], b[i])

plt.rc('font', **{'sans-serif' : 'Arial', 'family' : 'sans
    -serif'})


plt.hlines(0,0,0.5,linestyle='dashed')

plt.xlabel('Liquid conductivity, S/m')
plt.ylabel('DEP response')
```

```
#plt.title('DPSC DEP response @ 10 MHz')
plt.axhline(0, color = 'black')
plt.grid()

plt.legend()
plt.show()
```

B.4 Osmotic potential script

This is the Python script used to check the molarity remained between 300 and 330 mOsm/l when different DEP buffer solutions were made.

```
import numpy
import matplotlib.pyplot as plt

# Molarity calculations; % mass

BSA_mass = 20.00000
EDTA_mass = 0.2
sucrose_mass = 75
dextrose_mass = 3
NaCl_mass = 0.9 #lowish conductivity used earlier
HEPES_mass = 5.9575

BSA_M_mass = 68000
EDTA_M_mass =  292.24
sucrose_M_mass = 342.30
dextrose_M_mass = 180.16
NaCl_M_mass = 58.44
HEPES_M_mass = 238.3

BSA_M = BSA_mass/BSA_M_mass
EDTA_M = EDTA_mass/EDTA_M_mass
sucrose_M = sucrose_mass/sucrose_M_mass
dextrose_M = dextrose_mass/dextrose_M_mass
NaCl_M = NaCl_mass/NaCl_M_mass
HEPES_M = HEPES_mass/HEPES_M_mass
```

```
BSA_O = BSA_M
EDTA_O = EDTA_M
sucrose_O = sucrose_M
dextrose_O = dextrose_M
NaCl_O = NaCl_M*2
HEPES_O = HEPES_M

Buffer_O = BSA_O+EDTA_M+sucrose_O+dextrose_O+NaCl_O+
    HEPES_O

print(Buffer_O)
print "BSA"
print(BSA_M)
```

B.5 Java script to calculate DEP force based on .xml output files from Trackmate particle tracker

This is the script for a programme made by Christoph Wälti to calculate DEP force from experimental data with beads (see Chapter 4.4). After tracking the frame-by-frame trajectories of latex beads in a DEP system by Trackmate (an ImageJ plugin (165)), the .xml output file is read by the programme, which calculates the DEP force at every location in the video for every bead, using the equations for Newton's Second Law of Motion and Stoke's Drag, which it itself outputs as a .csv file.

```
package particletracking;

import java.io.File;
import javax.xml.parsers.DocumentBuilder;
import javax.xml.parsers.DocumentBuilderFactory;
import org.w3c.dom.Document;
import org.w3c.dom.Element;
```

```
import org.w3c.dom.Node;
import org.w3c.dom.NodeList;
import java.awt.BorderLayout;
import java.awt.Dimension;
import java.awt.GridLayout;
import java.awt.Toolkit;
import java.awt.event.ActionEvent;
import java.io.FileNotFoundException;
import java.io.PrintWriter;
import java.io.UnsupportedEncodingException;
import java.util.logging.Level;
import java.util.logging.Logger;
import javax.swing.AbstractAction;
import javax.swing.JButton;
import javax.swing.JFileChooser;
import javax.swing.JFrame;
import javax.swing.JOptionPane;
import javax.swing.JPanel;
import javax.swing.JTextField;
import javax.swing.UIManager;
import javax.swing.UnsupportedLookAndFeelException;
import org.jfree.chart.ChartFactory;
import org.jfree.chart.ChartPanel;
import org.jfree.chart.JFreeChart;
import org.jfree.chart.plot.PlotOrientation;
import org.jfree.data.xy.XYSeriesCollection;
import org.jfree.data.xy.XYSeries;

/**
 *
 * @author Chris
 */
public class ParticleTracking extends JPanel {

    // parameters which need adjusting

        // number of frame when SAW was switched on;
           frames before this are ignored
        static int tStart = 0;
        // minimum number of frames a trace must have to
           be considered; note, this includes the tStart
```

```
    frames as well (60)
static int minPoints = 60;
// viscosity of buffer
static double viscosity = 1e-3;          //Si
    units
// radius of particle in meters
static double particleRadius = 2.5e-6;
// density of particles; note, this probably doesn
    't matter very much as the total force is
    unlikly to be relevant
static double particleDensity = 1.05e3;  //kg/m3
// to convert the time-values from frames to
    seconds
static double tConversion = 0.0612; // in seconds/
    frame to convert t to s
// to convert the x and y-values from pixels to
    meters
static double xyConversion = 1.28e-6; // in m/
    pixel to convert x and y to m

// number of points used either side of the actual
     time point for fitting; fits t-wPoints to t+
    wPoints (10)
static int wPoints = 10;
// threshold by how much each fitted parameter can
     vary, otherwise point dismissed: not currently
     used (0.02)
static double aThresh = 0.02;

// arrangement for showing individual curves.
static int showCurvesCols = 3;
static int showCurvesRows = 2;

// Folder where track files (xml) are saved
final static String trackFolder = "/Users/Chris/
    Data/SAW-DEP Particle Tracking/";
// trackFolder = "D:\\Alban";

// Folder where force files (csv) are saved
final static String forceFolder = "/Users/Chris/
    Data/SAW-DEP Particle Tracking/";
```

```
        // forceFolder = "D:\\Alban";

// end of parameters which need adjusting



    /**
     * @param args the command line arguments
     */
    public interface LMfunc {

        public Object[] parameters();    // get the
           parameters

        public void parameters(Object[] param);  // set
           the parameters

        public double val(double[] x, double[] a);     //
           this gives the value at x

        public double grad(double[] x, double[] a, int a_k
           );       // this gives df/dAMP at pos x

        public double[][] testdata();
    }

    public static void main(String[] args) {




        double particleMass = particleDensity * 4 / 3 *
           3.1415 * Math.pow(particleRadius, 3);
        Object[] particleParameters = new Object[10];
        particleParameters[0] = viscosity;
        particleParameters[1] = particleRadius;
        particleParameters[2] = particleDensity;
        particleParameters[3] = particleMass;
        particleParameters[4] = tConversion;
        particleParameters[5] = xyConversion;
```

```
LMfunc f = new Quadratic();
double[][] data;
double[][] x;
//int nPts = 0;
//int nCols = 0;
boolean useTestData = false;

try {
    UIManager.setLookAndFeel(UIManager.
       getSystemLookAndFeelClassName());
} catch (ClassNotFoundException |
   InstantiationException | IllegalAccessException
    | UnsupportedLookAndFeelException ex) {
    Logger.getLogger(ParticleTracking.class.
       getName()).log(Level.SEVERE, null, ex);
}

try {

    JFileChooser fileChooser = new JFileChooser();
    System.setProperty("user.dir", trackFolder);
    fileChooser.setCurrentDirectory(new File(
       System.getProperty("user.dir")));
    int result = fileChooser.showOpenDialog(
       fileChooser);
    File fXmlFile = null;
    if (result == JFileChooser.APPROVE_OPTION) {
        fXmlFile = fileChooser.getSelectedFile();
    }
    DocumentBuilderFactory dbFactory =
       DocumentBuilderFactory.newInstance();
    DocumentBuilder dBuilder = dbFactory.
       newDocumentBuilder();
    Document doc = dBuilder.parse(fXmlFile);
    //optional, but recommended
    //read this - http://stackoverflow.com/
       questions/13786607/normalization-in-dom-
       parsing-with-java-how-does-it-work
    doc.getDocumentElement().normalize();
    // System.out.println("Root element :" + doc.
       getDocumentElement().getNodeName());
```

```
            JTextField particleDiameterTF = new JTextField
               ();
            particleDiameterTF.setText(Double.toString(
               particleRadius*2e6));
            Object[] message = {
                "Particle Radius (um):",
                   particleDiameterTF
            };

            int option = JOptionPane.showConfirmDialog(
               null, message, "Particles used",
               JOptionPane.OK_CANCEL_OPTION);
            if (option == JOptionPane.CANCEL_OPTION) {
                return;
            }
            particleRadius = Double.valueOf(
               particleDiameterTF.getText())/2*1e-6;
            particleParameters[1] = particleRadius;
            //System.out.println(particleRadius);

            NodeList nList = doc.getElementsByTagName("
               particle");
            System.out.println("Number of Tracks: " +
               nList.getLength());
            ParticleTrace[] traces = new ParticleTrace[
               nList.getLength()];

            // analyse all useful traces
            for (int iParticle = 0; iParticle < nList.
               getLength(); iParticle++) {
//              for (int iParticle = 0; iParticle < 100;
   iParticle++) {
                Node iNode = nList.item(iParticle);
                int nSpots = Integer.parseInt(((Element)
                   iNode).getAttribute("nSpots"));
                if (nSpots > minPoints) {
                    System.out.printf("Particle %d (nSpots
                       : %d)", iParticle, nSpots);
                    ParticleTrace iTrace = new
                       ParticleTrace(iParticle, nSpots,
```

```
                    tStart, particleParameters);
                iTrace.fitTrace(iNode, wPoints);
                traces[iParticle] = iTrace;
                System.out.printf(" ... analysed\n");
            }
        }

        // set up Jpanel for plotting charts etc
        JFrame frame = new JFrame("Particle Tracking")
            ;
        frame.setDefaultCloseOperation(JFrame.
            EXIT_ON_CLOSE);
        // show the menu containing the buttons for
            showing the traces, force, and for saving
            the file
        showMainMenu(0, showCurvesCols, showCurvesRows
            , nList.getLength(), traces, frame);

    } catch (Exception e) {
        e.printStackTrace();
    }

}



private static void showMainMenu(int iStart, int
    showCurvesCols, int showCurvesRows, int nParticles,
     ParticleTrace[] traces, JFrame frame) {
    frame.getContentPane().removeAll();
    frame.getContentPane().repaint();
    frame.revalidate();
    frame.setLayout(new BorderLayout(0, 5));

    JPanel panel = new JPanel();
    panel.setLayout(new GridLayout(1, 3));

    panel.add(createShowTraces(showCurvesCols,
        showCurvesRows, nParticles, traces, frame));
    panel.add(createShowFDEP(showCurvesCols,
        showCurvesRows, nParticles, traces, frame));
```

```
        panel.add(createSaveTraces(nParticles, traces,
            frame));
        //panel.setBounds(0, 0, 100, 20);

        frame.add(panel, BorderLayout.CENTER);
        frame.validate();
        frame.pack();
        //Dimension screenSize = Toolkit.getDefaultToolkit
            ().getScreenSize();
        //frame.setBounds(0, 0, screenSize.width,
            screenSize.height);
        frame.setVisible(true);
    }

    private static void plotCurves(int iStart, int
        showCurvesCols, int showCurvesRows, int nParticles,
        ParticleTrace[] traces, JFrame frame) {
        int nParticlesPlot = showCurvesCols *
            showCurvesRows;
        frame.getContentPane().removeAll();
        frame.getContentPane().repaint();
        frame.revalidate();
        frame.setLayout(new BorderLayout(0, 5));

        JPanel plotPanel = new JPanel();
        plotPanel.setLayout(new GridLayout(showCurvesRows,
            showCurvesCols));

        int k = 0;
        int i = iStart;
        while ((i < nParticles) && (k < nParticlesPlot)) {
//              for (int i=iStart; i<(iStart+nParticles); i
    ++) {
            ParticleTrace iTrace = traces[i];
            if (iTrace != null) {
                XYSeriesCollection dataset = new
                    XYSeriesCollection();
                XYSeries series1 = new XYSeries("data");
                for (int j = 0; j < iTrace.tData.length; j
                    ++) {
```

```
                series1.add(iTrace.tData[j], iTrace.
                    yData[j]*1e6);
            }
            dataset.addSeries(series1);
            XYSeries series2 = new XYSeries("fit");
            for (int j = 0; j < iTrace.tData.length; j
                ++) {
                series2.add(iTrace.tData[j], iTrace.
                    yfData[j]*1e6);
            }
            dataset.addSeries(series2);
            JFreeChart chart = ChartFactory.
                createScatterPlot("Particle" + i, "t (s
                )", "y(t) (um)", dataset,
                PlotOrientation.VERTICAL, true, true,
                true);
            ChartPanel chartPanel = new ChartPanel(
                chart);
            //chartPanel.add(chart,BorderLayout.CENTER
                );
            chartPanel.setLayout(new BorderLayout(0,
                5));
            chartPanel.setDomainZoomable(true);
            chartPanel.setMouseWheelEnabled(true);
            JPanel panel = new JPanel();
            panel.setLayout(new BorderLayout(0, 5));
            panel.add(chartPanel, BorderLayout.CENTER)
                ;
            JPanel controlPanel = new JPanel();
            controlPanel.add(createZoomOut(chartPanel)
                );
            controlPanel.add(createIgnore(i, traces));
            panel.add(controlPanel, BorderLayout.SOUTH
                );
            //frame.add(chartPanel);
            plotPanel.add(panel);
            k++;
        }
        i++;
    }
    frame.add(plotPanel, BorderLayout.CENTER);
```

```
        JPanel controlPanel = new JPanel();
        controlPanel.add(createShowMain(showCurvesCols,
            showCurvesRows, nParticles, traces, frame));
        if(i<nParticles) {
            controlPanel.add(createNextCurves(i,
                showCurvesCols, showCurvesRows, nParticles,
                 traces, frame));
        } else {
            controlPanel.add(createShowMain(showCurvesCols
                , showCurvesRows, nParticles, traces, frame
                ));
        }
        frame.add(controlPanel, BorderLayout.SOUTH);
        frame.validate();
        frame.pack();
        Dimension screenSize = Toolkit.getDefaultToolkit()
            .getScreenSize();
        frame.setBounds(0, 0, screenSize.width, screenSize
            .height);
        frame.setVisible(true);
    }

    private static void plotFDEP(int showCurvesCols, int
        showCurvesRows, int nParticles, ParticleTrace[]
        traces, JFrame frame) {
        double yMaxD = 0;
        double yMinD = 1e6;
        for (int iParticle = 0; iParticle < nParticles;
            iParticle++) {
            if (traces[iParticle] != null) {
                double yMaxThis = traces[iParticle].
                    getYmax();
                if (yMaxThis > yMaxD) {
                    yMaxD = yMaxThis;
                }
                double yMinThis = traces[iParticle].
                    getYmin();
                if (yMinThis < yMinD) {
                    yMinD = yMinThis;
                }
            }
```

```
}
int yMax = (int) Math.ceil(yMaxD);
int yMin = (int) Math.floor(yMinD);

System.out.println("Ymax=" + yMax + " pixels;
   Ymin=" + yMin+" pixels");
System.out.println("Ymax=" + yMax*traces[0].
   xyConversion*1e6 + " um;  Ymin=" + yMin*traces
   [0].xyConversion*1e6+" um");

int ySpread = yMax - yMin + 1;

System.out.println("ySpread " + ySpread);

double[] yForce = new double[ySpread];
double[] fForce = new double[ySpread];
double[] vForce = new double[ySpread];
double[] aForce = new double[ySpread];
double[] nForce = new double[ySpread];

for (int i = 0; i < ySpread; i++) {
    yForce[i] = (yMin + i) * traces[0].
       xyConversion;
    fForce[i] = 0;
    vForce[i] = 0;
    aForce[i] = 0;
    nForce[i] = 0;
}

for (int iParticle = 0; iParticle < nParticles;
   iParticle++) {
    if (traces[iParticle] != null) {
        for (int j = traces[iParticle].tStart; j <
            traces[iParticle].nSpots; j++) {
            int fIndex = (int) Math.floor((traces[
               iParticle].ypData[j] - yMin));  //
               note: yMin and yMax are in pixels,
               so use ypData
            if (fIndex < 0) {
                System.out.println("negative: " +
                   fIndex);
```

```
                }
                if (fIndex >= ySpread) {
                    System.out.println("too big");
                }
                fForce[fIndex] += traces[iParticle].
                    fDEPData[j];
                    // force in N
                vForce[fIndex] += traces[iParticle].
                    vData[j];
                    // v in m/s
                aForce[fIndex] += traces[iParticle].
                    aData[j];
                    // a in m/s^2
                nForce[fIndex]++;
            }
        }
    }

    for (int i = 0; i < ySpread; i++) {
        if(nForce[i]!=0) {
            fForce[i] = fForce[i] / nForce[i];
            vForce[i] = vForce[i] / nForce[i];
            aForce[i] = aForce[i] / nForce[i];
        }
    }

    frame.getContentPane().removeAll();
    frame.getContentPane().repaint();
    frame.revalidate();
    frame.setLayout(new BorderLayout(0, 5));

    XYSeriesCollection dataset = new
        XYSeriesCollection();
    XYSeries series1 = new XYSeries("");
    for (int i = 0; i < ySpread; i++) {
        if(nForce[i]!=0) {
            series1.add(yForce[i]*1e6, fForce[i]*1e12)
                ;
        }
    }
    dataset.addSeries(series1);
```

```
        JFreeChart chart = ChartFactory.createScatterPlot
            ("DEP Force", "y (um)", "FDEP(y) (pN)", dataset
            , PlotOrientation.VERTICAL, true, true, true);
        ChartPanel chartPanel = new ChartPanel(chart);
        chartPanel.setLayout(new BorderLayout(0, 5));
        chartPanel.setDomainZoomable(true);
        chartPanel.setMouseWheelEnabled(true);
        JPanel panel = new JPanel();
        panel.setLayout(new BorderLayout(0, 5));
        panel.add(chartPanel, BorderLayout.CENTER);
        JPanel controlPanel = new JPanel();
        controlPanel.add(createZoomOut(chartPanel));
        controlPanel.add(createShowMain(showCurvesCols,
            showCurvesRows, nParticles, traces, frame));
        controlPanel.add(createSaveForceCurves(ySpread,
            yForce, fForce, vForce, aForce, nForce));
        panel.add(controlPanel, BorderLayout.SOUTH);
        frame.add(panel);
        frame.validate();
        frame.pack();
        Dimension screenSize = Toolkit.getDefaultToolkit()
            .getScreenSize();
        frame.setBounds(0, 0, screenSize.width, screenSize
            .height);
        frame.setVisible(true);

    }

    private static void saveTraces(int nParticles,
        ParticleTrace[] traces, JFrame frame) {
            // export fitted traces to csv file
            File file = null;
            JFileChooser fileChooser = new JFileChooser();
            System.setProperty("user.dir", forceFolder);
            fileChooser.setCurrentDirectory(new File(
                System.getProperty("user.dir")));
            fileChooser.setSelectedFile(new File("
                ParticleTraces.csv"));
            if (fileChooser.showSaveDialog(fileChooser) ==
                JFileChooser.APPROVE_OPTION) {
                file = fileChooser.getSelectedFile();
```

```
        }

        PrintWriter writer = null;
        try {
            writer = new PrintWriter(file, "UTF-8");
        } catch (FileNotFoundException |
           UnsupportedEncodingException ex) {
            Logger.getLogger(ParticleTracking.class.
               getName()).log(Level.SEVERE, null, ex);
        }
        //PrintWriter writer = new PrintWriter("
           ParticleTrackingData.csv", "UTF-8");
        writer.println("PartNo,FrameNo(t),x,y,yFit,
           vFit,vFitFit,aFitFit,Fdrag,FTotal,FDEP\n");

        for (int iParticle = 0; iParticle < nParticles
           ; iParticle++) {
            if (traces[iParticle] != null) {
                traces[iParticle].writeOutputFile(
                   writer);
            }
        }
        writer.close();

}

private static void saveForceCurves(int ySpread,
   double[] yForce, double[] fForce, double[] vForce,
   double[] aForce, double[] nForce) {
        // export fitted traces to csv file

        JTextField particleDiameter = new JTextField()
           ;
        JTextField appliedPower = new JTextField();
        JTextField repeatNumber = new JTextField();
        particleDiameter.setText(Integer.toString((int
           )Math.floor(particleRadius*2e6+0.1)));
        Object[] message = {
            "Particle Diameter (um):",
               particleDiameter,
            "Applied Power (dB):", appliedPower,
```

```
    "Repetition Number:", repeatNumber
};

int option = JOptionPane.showConfirmDialog(
   null, message, "Experiment Settings",
   JOptionPane.OK_CANCEL_OPTION);
if (option == JOptionPane.CANCEL_OPTION) {
    return;
}
String expId = particleDiameter.getText()+"um_
   "+appliedPower.getText()+"dB_"+repeatNumber
   .getText();

File file = null;
JFileChooser fileChooser = new JFileChooser();
System.setProperty("user.dir", forceFolder);
fileChooser.setCurrentDirectory(new File(
   System.getProperty("user.dir")));
fileChooser.setSelectedFile(new File("
   ForceCurve_"+expId+".csv"));
if (fileChooser.showSaveDialog(fileChooser) ==
    JFileChooser.APPROVE_OPTION) {
    file = fileChooser.getSelectedFile();
}

PrintWriter writer = null;
try {
    writer = new PrintWriter(file, "UTF-8");
} catch (FileNotFoundException |
   UnsupportedEncodingException ex) {
    Logger.getLogger(ParticleTracking.class.
       getName()).log(Level.SEVERE, null, ex);
}
//PrintWriter writer = new PrintWriter("
   ParticleTrackingData.csv", "UTF-8");

writer.println("y (m) ["+expId+"],FDEP (N) ["+
   expId+"],v (m/s) ["+expId+"],a (m/s2) ["+
   expId+"]");

for (int i = 0; i < ySpread; i++) {
```

```
            if(nForce[i]!=0) {    //
                writer.println(yForce[i] + "," +
                   fForce[i] + "," + vForce[i] + "," +
                    aForce[i]);
            }
        }
        writer.close();

}


private static JButton createZoomOut(final ChartPanel
   chartPanel) {
    final JButton auto = new JButton(new
       AbstractAction("Reset Zoom") {

        @Override
        public void actionPerformed(ActionEvent e) {
            chartPanel.restoreAutoBounds();
        }
    });
    auto.setBounds(10, 10, 10, 10);
    return auto;
}

private static JButton createShowTraces(final int
   showCurvesCols, final int showCurvesRows, final int
    nParticles, final ParticleTrace[] traces, final
   JFrame frame) {
    final JButton auto = new JButton(new
       AbstractAction("Show Traces") {

        @Override
        public void actionPerformed(ActionEvent e) {
            plotCurves(0, showCurvesCols,
               showCurvesRows, nParticles, traces,
               frame);
        }
    });
    auto.setBounds(10, 10, 10, 10);
    return auto;
```

```
}

private static JButton createShowFDEP(final int
   showCurvesCols, final int showCurvesRows, final int
    nParticles, final ParticleTrace[] traces, final
   JFrame frame) {

    final JButton auto = new JButton(new
       AbstractAction("Work out FDEP") {

        @Override
        public void actionPerformed(ActionEvent e) {
            plotFDEP(showCurvesCols, showCurvesRows,
               nParticles, traces, frame);
        }

    });
    auto.setBounds(10, 10, 10, 10);
    return auto;
}

private static JButton createSaveTraces(final int
   nParticles, final ParticleTrace[] traces, final
   JFrame frame) {

    final JButton auto = new JButton(new
       AbstractAction("Save Traces") {

        @Override
        public void actionPerformed(ActionEvent e) {
            saveTraces(nParticles, traces, frame);
        }

    });
    auto.setBounds(10, 10, 10, 10);
    return auto;
}

private static JButton createIgnore(final int
   ignoreTrace, final ParticleTrace[] traces) {
    //final JButton auto = null;
```

```
        final JButton auto = new JButton(new
            AbstractAction("Ignore Trace") {

                @Override
                public void actionPerformed(ActionEvent e) {
                    traces[ignoreTrace] = null;
                }

        });
        auto.setBounds(10, 10, 10, 10);
        return auto;
    }

    private static JButton createShowMain(final int
        showCurvesCols, final int showCurvesRows, final int
         nParticles, final ParticleTrace[] traces, final
        JFrame frame) {
        final JButton auto = new JButton(new
            AbstractAction("Show Main Menu") {

                @Override
                public void actionPerformed(ActionEvent e) {
                    showMainMenu(0, showCurvesCols,
                        showCurvesRows, nParticles, traces,
                        frame);
                }
        });
        auto.setBounds(10, 10, 10, 10);
        return auto;
    }

    private static JButton createNextCurves(final int
        iStart, final int showCurvesCols, final int
        showCurvesRows, final int nParticles, final
        ParticleTrace[] traces, final JFrame frame) {
        final JButton auto = new JButton(new
            AbstractAction("Next ...") {

                @Override
                public void actionPerformed(ActionEvent e) {
```

```
                plotCurves(iStart, showCurvesCols,
                    showCurvesRows, nParticles, traces,
                    frame);
            }
        });
        auto.setBounds(10, 10, 10, 10);
        return auto;
    }

    private static JButton createSaveForceCurves(final int
        ySpread, final double[] yForce, final double[]
       fForce, final double[] vForce, final double[]
       aForce, final double[] nForce) {
        final JButton auto = new JButton(new
           AbstractAction("Export Force Curves") {

            @Override
            public void actionPerformed(ActionEvent e) {
                saveForceCurves(ySpread, yForce, fForce,
                    vForce, aForce, nForce);
            }
        });
        auto.setBounds(10, 10, 10, 10);
        return auto;
    }

}
```

Appendix C

Supplementary data

C.1 Fitted curves for DEP force measurements of latex beads at various power levels

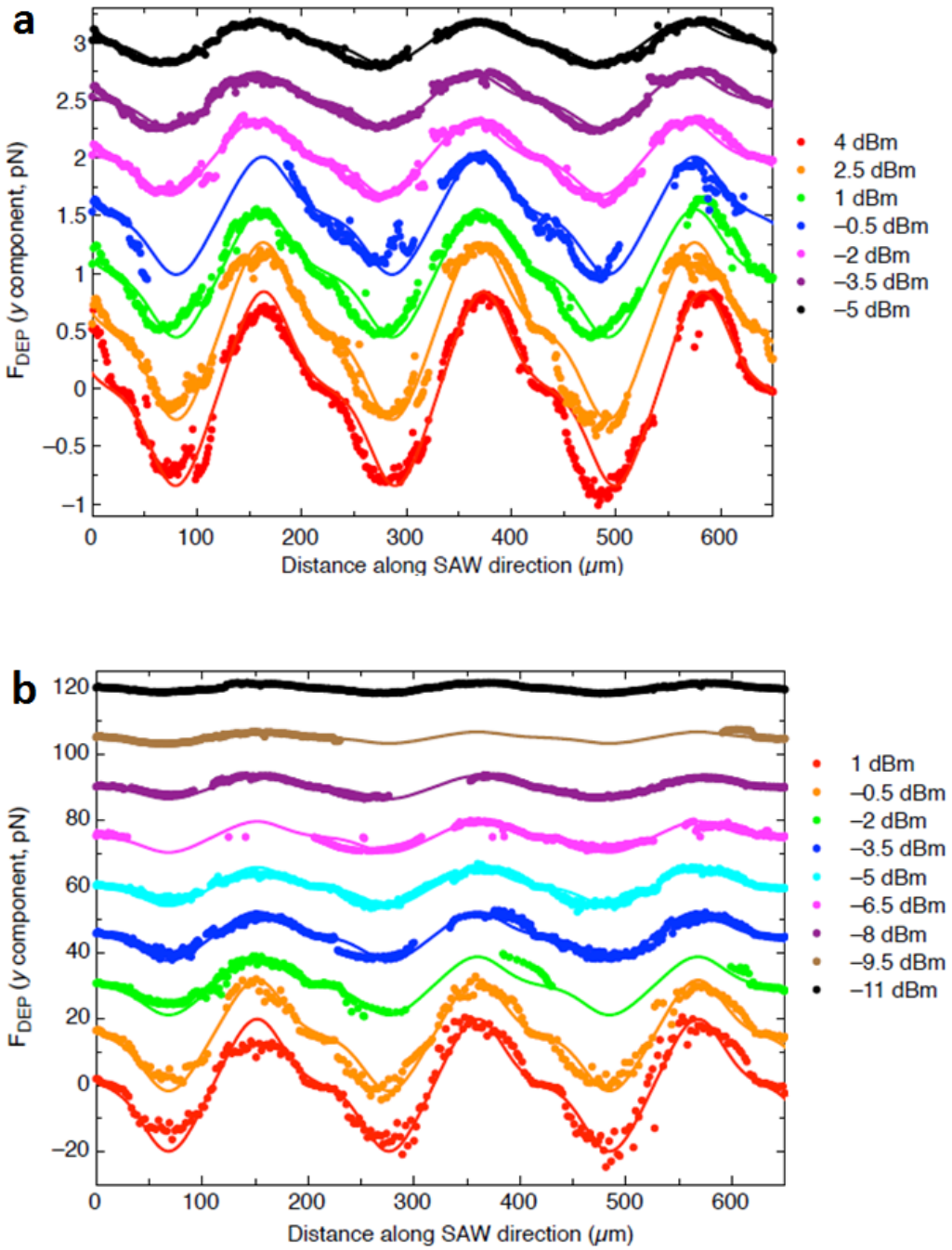

Figure C.1: Force measurements from tracking movement of 3 µm beads (**a**) and 10 µm beads (**b**) at various positions along the SAW standing wave, for various power input levels (different colours).

C.2 Fitted curves with raw datapoints for conductivity sweeps of DPS cells as a function of passage number

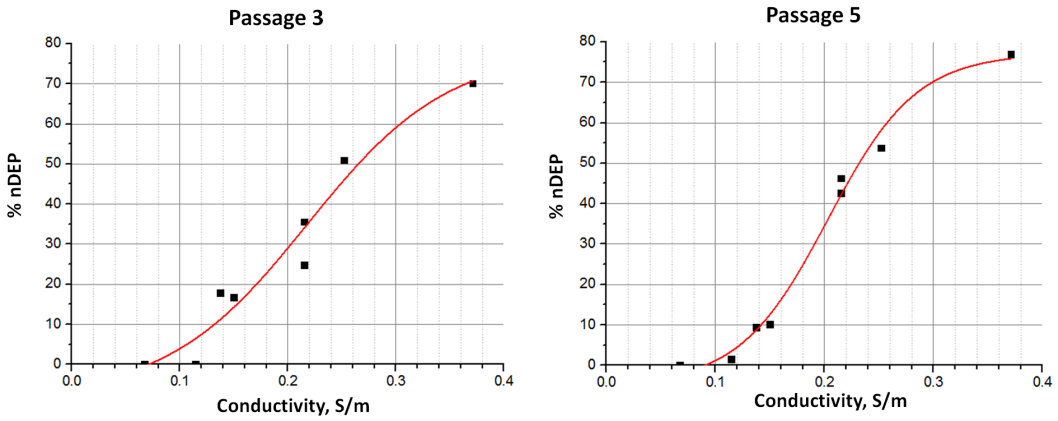

Figure C.2: Fitted curves with raw datapoints for conductivity sweeps of dental pulp stromal cells (DPS cells), for cells at Passage 3 and 5 (Section 6.5). The graphs show that as the liquid conductivity is increased (at 10 MHz frequency), a progressively higher proportion of DPS cells experience nDEP, as their polarisability becomes lower relative to that of the liquid. The conductivities (x-axis) at which the red line passes through the point nDEP = 50% (y-axis) was used to plot Figure 6.18 in the main text.

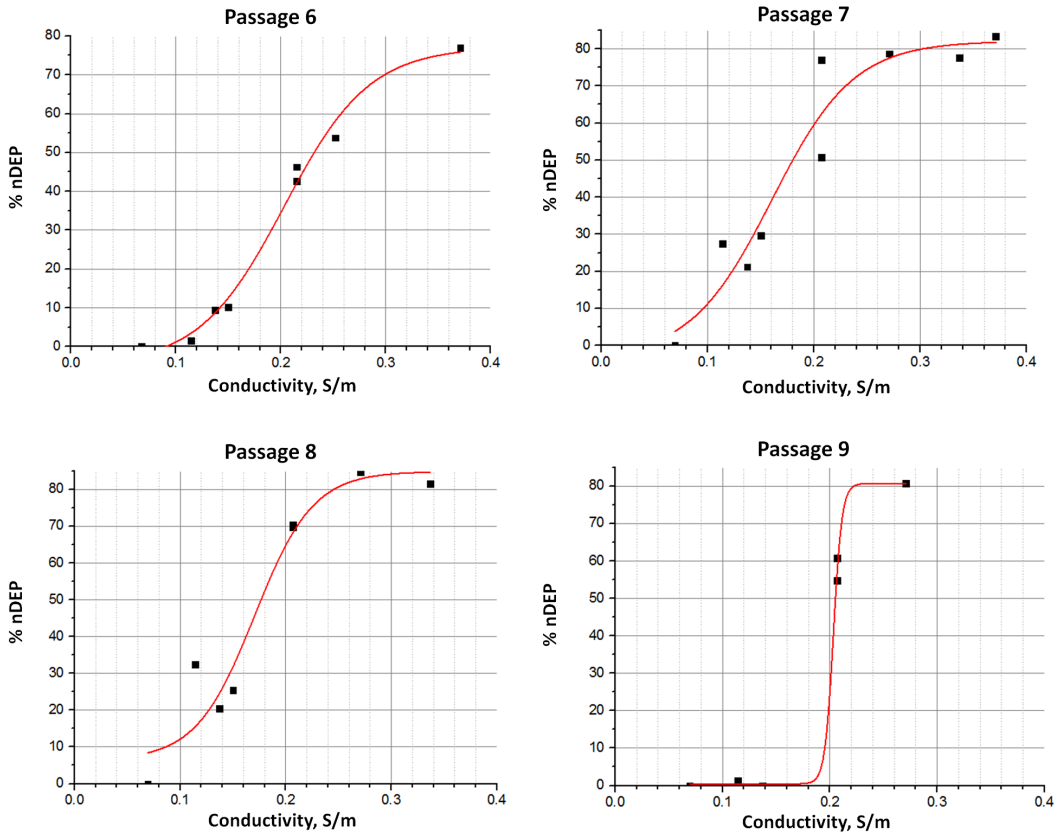

Figure C.3: Fitted curves with raw datapoints for conductivity sweeps of dental pulp stromal cells (DPS cells), for cells at Passage 6-9 (Section 6.5). The graphs show that as the liquid conductivity is increased (at 10 MHz frequency), a progressively higher proportion of DPS cells experience nDEP, as their polarisability becomes lower relative to that of the liquid. The conductivities (x-axis) at which the red line passes through the point nDEP = 50% (y-axis) was used to plot Figure 6.18 in the main text.

References

[1] Rob Jepras and Steve Ludbrook. Evolution of flow cytometry as a drug screening platform. Spring 13. http://www.ddw-online.com/enabling-technologies/p211493-evolution-of-flow-cytometry-as-a-drug-screening-platform\-spring-13.html, 2013. [Online; accessed 9-May-2016]. 2

[2] LB To, DN Haylock, PJ Simmons, and CA Juttner. The biology and clinical uses of blood stem cells. *Blood*, 89(7):2233–2258, 1997. 3

[3] Newsbeat (BBC). Rules on when gay men can give blood to be reconsidered. http://www.bbc.co.uk/newsbeat/article/34938123/rules-on-when-gay-men-can-give-blood-to-be-reconsidered, 2015. [Online; accessed 9-May-2016]. 15, 3

[4] WebMD. Bone Marrow Aspiration and Biopsy. http://www.webmd.com/cancer/bone-marrow-aspiration-and-biopsy-facedown-position, 2014. [Online; accessed 9-May-2016]. 15, 3

[5] Fergus Walsh. Paralysed man walks again after cell transplant. http://www.bbc.co.uk/news/health-29645760, 2016. [Online; accessed 9-May-2016]. 15, 3, 4

[6] Signature Smile. Wisdom teeth removal. http://www.woodfordsmile.com/wisdom-tooth-removal-woodford/, 2016. [Online; accessed 10-April-2017]. 15, 3

[7] Bokyung Park, Keon Hee Yoo, and Changsung Kim. Hematopoietic stem cell expansion and generation: the ways to make a breakthrough. *Blood research*, 50(4):194–203, 2015. 3

[8] Christof Stamm, Bernd Westphal, Hans-Dieter Kleine, Michael Petzsch, Christian Kittner, Heiko Klinge, Carl Schümichen, Christoph A Nienaber, Mathias Freund, and Gustav Steinhoff. Autologous bone-marrow stem-cell transplantation for myocardial regeneration. *The Lancet*, 361(9351):45–46, 2003. 3

[9] L.B. To, D.N. Haylock, P.J. Simmons, and C.A. Juttner. The Journal of The American Society of Hematology. 89(7), 1997. 3

[10] Pawel Tabakow, Wlodzimierz Jarmundowicz, Bogdan Czapiga, Wojciech Fortuna, Ryszard Miedzybrodzki, Marcin Czyz, Juliusz Huber, Dariusz Szarek, Stefan Okurowski, Pawel Szewczyk, et al. Transplantation of autologous olfactory ensheathing cells in complete human spinal cord injury. *Cell transplantation*, 22(9):1591–1612, 2013. 4

[11] Pravin D Potdar and Yogita D Jethmalani. Human dental pulp stem cells: Applications in future regenerative medicine. *World journal of stem cells*, 7(5):839, 2015. 4, 223

[12] Cader Dental Practise. Dental Implants. http://dolgellau-smiledesign.co.uk/dental-implants/, 2016. [Online; accessed 06-January-2016]. 15, 5

[13] BracedLife. Minerva plaster body cast with double shoulder spica. https://www.youtube.com/watch?v=YmJ1ipTzsEk, 2016. [Online; accessed 06-January-2016]. 15, 5

[14] K Hosking. Massive bone loss around the knee - the orthopaedic oncological perspective. *SA Orthopaedic Journal*, 11:26 – 32, 01 2012. ISSN 1681-150X. URL http://www.scielo.org.za/scielo.php?script=sci_arttext&pid=S1681-150X2012000400004&nrm=iso. 15, 5

[15] Brian Krans and William A MD Morrison. What Is a Bone Graft? http://www.healthline.com/health/bone-graft#Overview1, 2015. [Online; accessed 9-May-2016]. 4

[16] Peter V. Giannoudis, Haralambos Dinopoulos, and Eleftherios Tsiridis. Bone substitutes: An update. *Injury*, 36(3, Supplement):S20 – S27, 2005. ISSN 0020-1383. doi: http://dx.doi.org/10.1016/j.injury.2005.07.029. URL http://www.sciencedirect.com/science/article/pii/S0020138305002871. Proceedings from the 1st European Clinical Symposium on Bone and Tissue Regeneration 27-28 November 2004. 4, 5

[17] MA Saghiri, A Asatourian, F Garcia-Godoy, and N Sheibani. The role of angiogenesis in implant dentistry part ii: The effect of bone-grafting and barrier membrane materials on angiogenesis. *Medicina oral, patologia oral y cirugia bucal*, page 0, 2016. 5

[18] Clayton R Perry. Bone repair techniques, bone graft, and bone graft substitutes. *Clinical orthopaedics and related research*, 360:71–86, 1999. 5

[19] Richard L Davis, Benjamin C Taylor, Nathan Johnson, Jason R Ferrel, and Joaquin Castaneda. Retrograde versus antegrade femoral bone graft harvesting using the reamer–irrigator–aspirator. *Journal of orthopaedic trauma*, 29(8):370–372, 2015. 5

[20] Feng Li, Changlin Zhou, Liang Xu, Shuqing Tao, Jingyi Zhao, and Qun Gu. Effect of stem cell therapy on bone mineral density: A meta-analysis of preclinical studies in animal models of osteoporosis. *PloS one*, 11(2): e0149400, 2016. 5

[21] Yong-Gon Koh, Yun-Jin Choi, Sae-Kwang Kwon, Yong-Sang Kim, and Jee-Eun Yeo. Clinical results and second-look arthroscopic findings after treatment with adipose-derived stem cells for knee osteoarthritis. *Knee Surgery, Sports Traumatology, Arthroscopy*, 23(5):1308–1316, 2015. 5

[22] DBCLS. Iliac crest 03 - anterior view. https://commons.wikimedia.org/wiki/File:Iliac_crest_03_-_anterior_view.png, 2015. [Online; accessed 06-January-2016]. 15, 6

[23] Jing Li, Wilfred Hing-Sang Wong, Shing Chan, James Chor-San Chim, Kenneth Man-Chee Cheung, Tsz-Leung Lee, Wing-Yan Au, Shau-Yin Ha, Albert Kwok-Wei Lie, Yu-Lung Lau, et al. Factors affecting mesenchymal stromal cells yield from bone marrow aspiration. *Chinese Journal of Cancer Research*, 23(1):43–48, 2011. 6, 271

[24] J Torres, A Lopes, MA Lopes, M Gutierres, AT Cabral, MH Fernandes, E Monteiro, CF van Eck, and JD Santos. The benefit of a human bone marrow stem cells concentrate in addition to an inorganic scaffold for bone regeneration: an in vitro study. *BioMed research international*, 2015, 2015. 6

[25] Patrik Brundin, Jenny Karlsson, Mia Emgård, Gabriele S. Kaminski Schierle, Oskar Hansson, Åsa Petersén, and Roger F Castilho. Improving the Survival of Grafted Dopaminergic Neurons: A Review Over Current Approaches. *Cell Transplantation*, 9:179–195, 2000. 6

[26] Patrik Brundin, Roger a Barker, and Malin Parmar. *Neural grafting in Parkinson's disease Problems and possibilities.*, volume 184. Elsevier B.V., January 2010. doi: 10.1016/S0079-6123(10)84014-2. URL http://www.ncbi.nlm.nih.gov/pubmed/20887880. 6

[27] Alexandre S Raposo do Amaral, Rena L Pawlick, Erika Rodrigues, Flavia Costal, Andrew Pepper, Flávio H Ferreira Galvão, Maria Lucia Correa-Giannella, and a M James Shapiro. Glutathione ethyl ester supplementation during pancreatic islet isolation improves viability and transplant outcomes in a murine marginal islet mass model. *PloS one*, 8 (2):e55288, January 2013. ISSN 1932-6203. doi: 10.1371/journal.pone.0055288. URL http://www.pubmedcentral.nih.gov/articlerender.fcgi?artid=3570543&tool=pmcentrez&rendertype=abstract. 6

[28] Hirohito Ichii, Atsushi Miki, Toshiyuki Yamamoto, Ruth D Molano, Scott Barker, Atsuyoshi Mita, Rayner Rodriguez-Diaz, Dagmar

Klein, Ricardo Pastori, Rodolfo Alejandro, Luca Inverardi, Antonello Pileggi, and Camillo Ricordi. Characterization of pancreatic ductal cells in human islet preparations. *Laboratory investigation; a journal of technical methods and pathology*, 88(11):1167–77, November 2008. ISSN 1530-0307. doi: 10.1038/labinvest.2008.87. URL http://www.pubmedcentral.nih.gov/articlerender.fcgi?artid=3793849&tool=pmcentrez&rendertype=abstract. 6

[29] Rene D Largo, Laurent a H Tchang, Valentina Mele, Arnaud Scherberich, Yves Harder, Reto Wettstein, and Dirk J Schaefer. Efficacy, safety and complications of autologous fat grafting to healthy breast tissue: a systematic review. *Journal of plastic, reconstructive & aesthetic surgery : JPRAS*, 67(4):437–48, April 2014. ISSN 1878-0539. doi: 10.1016/j.bjps.2013.11.011. URL http://www.ncbi.nlm.nih.gov/pubmed/24394754. 6

[30] Richard J Miron, Reinhard Gruber, Erik Hedbom, Nikola Saulacic, Yufeng Zhang, Anton Sculean, Dieter D Bosshardt, and Daniel Buser. Impact of bone harvesting techniques on cell viability and the release of growth factors of autografts. *Clinical implant dentistry and related research*, 15(4):481–9, August 2013. ISSN 1708-8208. doi: 10.1111/j.1708-8208.2012.00440.x. URL http://www.ncbi.nlm.nih.gov/pubmed/22375920. 6, 7

[31] Hubert T Kim, Margie S Teng, and Alexis C Dang. Chondrocyte apoptosis: implications for osteochondral allograft transplantation. *Clinical orthopaedics and related research*, 466(8):1819–25, August 2008. ISSN 1528-1132. doi: 10.1007/s11999-008-0304-6. URL http://www.pubmedcentral.nih.gov/articlerender.fcgi?artid=2584268&tool=pmcentrez&rendertype=abstract. 7

[32] Peter J Evans, Anthony Miniaci, and Mark B Hurtig. Manual punch versus power harvesting of osteochondral grafts. *Arthroscopy : the journal of arthroscopic & related surgery : official publication of the Arthroscopy Association of North America and the International Arthroscopy Association*, 20(3):306–10, March 2004. ISSN 1526-3231. doi: 10.1016/j.arthro.2004.01.012. URL http://www.ncbi.nlm.nih.gov/pubmed/15007320. 7

[33] A Dwenger, J Strassburger, and W Schwerdtfeger. [regulation (ec) no. 1394/2007 on advanced therapy medicinal products: Incorporation into national law]. *Bundesgesundheitsblatt, Gesundheitsforschung, Gesundheitsschutz*, 53(1):14–19, 2010. 7

[34] Richard G Miller and RAf Phillips. Separation of cells by velocity sedimentation. *Journal of cellular physiology*, 73(3):191–201, 1969. 9, 200

[35] Alvin Zipursky, Eric Bow, Rama S Seshadri, and Elizabeth J Brown. Leukocyte density and volume in normal subjects and in patients with acute lymphoblastic leukemia. *Blood*, 48(3):361–371, 1976. 10

[36] William H Grover, Andrea K Bryan, Monica Diez-Silva, Subra Suresh, John M Higgins, and Scott R Manalis. Measuring single-cell density. *Proceedings of the National Academy of Sciences*, 108(27):10992–10996, 2011. 10

[37] Debdatta Basu and Rajendra Kulkarni. Overview of blood components and their preparation. *Indian journal of anaesthesia*, 58(5):529, 2014. 10

[38] ED Harlow, David Lane, et al. A laboratory manual. *New York: Cold Spring Harbor Laboratory*, page 579, 1988. 11

[39] Karen Cheung, Shady Gawad, and Philippe Renaud. Impedance spectroscopy flow cytometry: on-chip label-free cell differentiation. *Cytometry Part A*, 65(2):124–132, 2005. 11

[40] Daniel R Gossett, Westbrook M Weaver, Albert J Mach, Soojung Claire Hur, Henry Tat Kwong Tse, Wonhee Lee, Hamed Amini, and Dino Di Carlo. Label-free cell separation and sorting in microfluidic systems. *Analytical and bioanalytical chemistry*, 397(8):3249–3267, 2010. 17, 11, 26, 27, 38

[41] Miltenyi Biotec. CD34 MicroBead Kit. `https://www.miltenyibiotec.com/~/media/Images/Products/Import/0001400/IM0001498.ashx?force=1`, 2016. [Online; accessed 10-May-2016]. 12

[42] Adam Davison and Liz Straszynski. Leeds Institute of Molecular Medicine Flow Cytometry Core Facility Users Guide. Obtained courtesy of Dr Adam Davison, 2015. [Obtained courtesy of Dr Adam Davison]. 16, 13

[43] Cleveland Clinic. Innovations in Male Infertility Research. https://www.clevelandclinic.org/reproductiveresearchcenter/info/innomaleinf_5.html, 2008. [[Online; accessed 12-May-2016]. 16, 14

[44] Matthew J Tomlinson, Sophie Tomlinson, Xuebin B Yang, and Jennifer Kirkham. Cell separation: Terminology and practical considerations. *Journal of tissue engineering*, 4:2041731412472690, January 2013. ISSN 2041-7314. doi: 10.1177/2041731412472690. URL http://www.pubmedcentral.nih.gov/articlerender.fcgi?artid=3578272&tool=pmcentrez&rendertype=abstract. 14, 16

[45] Miltenyi Biotec. Manual cell separation. http://www.miltenyibiotec.com/en/products-and-services/macs-cell-separation/manual-cell-separation.aspx, 2016. [[Online; accessed 12-May-2016]. 14

[46] A Willasch, S Eing, G Weber, S Kuci, G Schneider, J Soerensen, A Jarisch, E Rettinger, U Koehl, T Klingebiel, et al. Enrichment of cell subpopulations applying automated macs technique: purity, recovery and applicability for pcr-based chimerism analysis. *Bone marrow transplantation*, 45(1):181–189, 2010. 15

[47] Miltenyi Biotec. Sorting out the benefits. https://www.miltenyibiotec.com/~/media/Files/Navigation/Cell%20Separation/Sorting_out_the_Facts.ashx, 2011. [[Online; accessed 12-May-2016]. 15

[48] David S Hage. Affinity chromatography: a review of clinical applications. *Clinical chemistry*, 45(5):593–615, 1999. 16

[49] Ashok Kumar and Akshay Srivastava. Cell separation using cryogel-based affinity chromatography. *Nature protocols*, 5(11):1737–1747, 2010. 16, 17

[50] Paul T Sharpe. *Methods of cell separation*, volume 18. Elsevier, 1988. 16

[51] S Gronthos, J Brahim, W Li, LW Fisher, N Cherman, A Boyde, P DenBesten, P Gehron Robey, and S Shi. Stem cell properties of human dental pulp stem cells. *Journal of dental research*, 81(8):531–535, 2002. 16

[52] Nowruz Delirezh, Ehsan Shojaeefar, Parva Parvin, and Behnaz Asadi. Comparison the effects of two monocyte isolation methods, plastic adherence and magnetic activated cell sorting methods, on phagocytic activity of generated dendritic cells. *Cell journal*, 15(3):218–223, 2012. 16

[53] Kenichi Nagase, Ayaka Kimura, Tatsuya Shimizu, Katsuhisa Matsuura, Masayuki Yamato, Naoya Takeda, and Teruo Okano. Dynamically cell separating thermo-functional biointerfaces with densely packed polymer brushes. *Journal of Materials Chemistry*, 22(37):19514–19522, 2012. 18

[54] Samuel H Sigal, Shlomo Brill, Lola M Reid, Isabel Zvibel, Sanjeev Gupta, Douglas Hixson, Ronald Faris, and Patricia A Holst. Characterization and enrichment of fetal rat hepatoblasts by immunoadsorption (panning) and fluorescence-activated cell sorting. *Hepatology*, 19(4):999–1006, 1994. 18

[55] UC San Diego. Multichannel Magnetic Cell Sorting. http://beweb.ucsd.edu/courses/senior-design/projects/2010/project_14/design-goals-alternatives.html, 2015. [Online; accessed 09-January-2016]. 16, 18

[56] David Holmes, Nicolas G Green, and Hywel Morgan. Microdevices for dielectrophoretic flow-through cell separation. *Engineering in Medicine and Biology Magazine, IEEE*, 22(6):85–90, 2003. 21, 40, 18, 49, 50, 51, 138, 201, 202, 216, 220, 221

[57] Microfluidic Future. MICROFLUIDICS? WHAT'S THAT? A BEGINNER'S GUIDE. http://www.microfluidicfuture.com/blog/microfluidics-a-beginners-guide, 2011. [[Online; accessed 12-May-2016]. 16, 19

[58] ETHZurich. de Mello group homepage. https://demellogroup.ethz.ch/en/index, 2016. [Online; accessed 08-January-2016]. 19, 20

[59] Sara Rodriguez-Mozaz, Maria J Lopez de Alda, and Damià Barceló. Biosensors as useful tools for environmental analysis and monitoring. *Analytical and bioanalytical chemistry*, 386(4):1025–1041, 2006. 19

[60] Chong H Ahn, Jin-Woo Choi, Gregory Beaucage, Joseph H Nevin, Jeong-Bong Lee, Aniruddha Puntambekar, and Jae Y Lee. Disposable smart lab on a chip for point-of-care clinical diagnostics. *Proceedings of the IEEE*, 92 (1):154–173, 2004. 19

[61] Robert R Schaller. Moore's law: past, present and future. *Spectrum, IEEE*, 34(6):52–59, 1997. 19

[62] George Brewer. *Electron-beam technology in microelectronic fabrication*. Elsevier, 2012. 19

[63] Yuksel Temiz, Robert D Lovchik, Govind V Kaigala, and Emmanuel Delamarche. Lab-on-a-chip devices: How to close and plug the lab? *Microelectronic Engineering*, 132:156–175, 2015. 20

[64] Travis D Boone, Z Hugh Fan, Herbert H Hooper, Antonio J Ricco, Hongdong Tan, and Stephen J Williams. Peer reviewed: plastic advances microfluidic devices. *Analytical chemistry*, 74(3):78–A, 2002. 20

[65] George M Whitesides. The origins and the future of microfluidics. *Nature*, 442(7101):368–73, July 2006. ISSN 1476-4687. doi: 10.1038/nature05058. URL http://www.ncbi.nlm.nih.gov/pubmed/16871203. 20

[66] Paul Yager, Gonzalo J Domingo, and John Gerdes. Point-of-care diagnostics for global health. *Annu. Rev. Biomed. Eng.*, 10:107–144, 2008. 21

[67] Wentao Su, Xinghua Gao, Lei Jiang, and Jianhua Qin. Microfluidic platform towards point-of-care diagnostics in infectious diseases. *Journal of Chromatography A*, 1377:13–26, 2015. 21

[68] The Economist. Theranos: Blood sports. http://www.economist.com/news/business/21697273-pressure-mounting-startup-has-tried-shake-up-lab-test-market-blood 2016. [Online; accessed 12-May-2016]. 21

[69] Matther Herper. From $4.5 Billion To Nothing: Forbes Revises Estimated Net Worth Of Theranos Founder Elizabeth Holmes. http://www.forbes.com/sites/matthewherper/2016/06/01/from-4-5-billion-to-nothing-forbes-revises-estimated-net-worth-of-theranos- 2016. [Online; accessed 10-April-2017]. 21

[70] Reed Abelson. Theranos to Close Labs and Lay Off 340 Workers. https://www.nytimes.com/2016/10/06/business/theranos-to-close-labs-and-lay-off-340-workers.html?_r=0, 2016. [Online; accessed 10-April-2017]. 21

[71] Dickinson Becton and Company. BD Veritor System. http://www.bd.com/ds/veritorsystem/systemoverview.asp, 2016. [Online; accessed 12-May-2016]. 16, 21

[72] Anne Y Fu, Charles Spence, Axel Scherer, Frances H Arnold, and Stephen R Quake. A microfabricated fluorescence-activated cell sorter. *Nature biotechnology*, 17(11):1109–1111, 1999. 17, 22, 23

[73] Menake E Piyasena and Steven W Graves. The intersection of flow cytometry with microfluidics and microfabrication. *Lab on a Chip*, 14(6): 1044–1059, 2014. 22

[74] howpublished = "http://www.marketsandmarkets.com/ResearchInsight/flow-cytometry-market.asp" year = 2016 note = "[Online; accessed 13-May-2016]" Rohan, title = Becton, Dickinson and Company and Beckman Coulter, Inc. Command More Than 50% of the Global Flow Cytometry Market. 24

[75] howpublished = "https://www.bdbiosciences.com/us/instruments/research/cell-sorters/bd-facsjazz/m/1349554/overview" year = 2016 note = "[Online; accessed 13-May-2016]" BD Biosciences, title = BD FACSJazz. 17, 24

[76] title = Sorting Made Simpler howpublished = "http://www.the-scientist.com/?articles.view/articleNo/41513/title/

Sorting-Made-Simpler/" year = 2014 note = "[Online; accessed 13-May-2016]" Yandell, Kate. 24

[77] T Chianea, NE Assidjo, and PJP Cardot. Sedimentation field-flow-fractionation: emergence of a new cell separation methodology. *Talanta*, 51(5):835–847, 2000. 24, 25

[78] howpublished = "http://www.postnova.com/general-theory.html" year = 2016 note = "[Online; accessed 13-January-2016]" Postnova, title = General Theory about Field-Flow Fractionation. 17, 25

[79] J Calvin Giddings, FJ Yang, and Marcus N Myers. Flow-field-flow fractionation: a versatile new separation method. *Science*, 193(4259):1244–1245, 1976. 25

[80] Karin D Caldwell, Zhi-Qing Cheng, Peter Hradecky, and J Calvin Giddings. Separation of human and animal cells by steric field-flow fractionation. *Cell biophysics*, 6(4):233–251, 1984. 25

[81] Adel K Afifi, Ronald Arly Bergman, and Paul M Heidger. *Atlas of Microscopic Anatomy: A Functional Approach: Companion to Histology and Neuroanatomy*. University of Iowa, 1999. 26

[82] Siyang Zheng, Henry Lin, Jing-Quan Liu, Marija Balic, Ram Datar, Richard J Cote, and Yu-Chong Tai. Membrane microfilter device for selective capture, electrolysis and genomic analysis of human circulating tumor cells. *Journal of Chromatography A*, 1162(2):154–161, 2007. 26

[83] Masumi Yamada and Minoru Seki. Hydrodynamic filtration for on-chip particle concentration and classification utilizing microfluidics. *Lab on a Chip*, 5(11):1233–1239, 2005. 17, 27

[84] Howard A Stone, Abraham D Stroock, and Armand Ajdari. Engineering flows in small devices: microfluidics toward a lab-on-a-chip. *Annu. Rev. Fluid Mech.*, 36:381–411, 2004. 27

[85] Ali Asgar S Bhagat, Hansen Bow, Han Wei Hou, Swee Jin Tan, Jongyoon Han, and Chwee Teck Lim. Microfluidics for cell separation. *Medical & biological engineering & computing*, 48(10):999–1014, 2010. 28

[86] Masumi Yamada, Megumi Nakashima, and Minoru Seki. Pinched flow fractionation: continuous size separation of particles utilizing a laminar flow profile in a pinched microchannel. *Analytical chemistry*, 76(18):5465–5471, 2004. 28

[87] Steven Block. An introduction to optical tweezers. https://blocklab.stanford.edu/optical_tweezers.html, 2015. [Online; accessed 12-July-2017]. 28

[88] Jeffrey R Moffitt, Yann R Chemla, Steven B Smith, and Carlos Bustamante. Recent advances in optical tweezers. *Biochemistry*, 77(1):205, 2008. 28

[89] Axel Hochstetter, Eric Stellamanns, Siddharth Deshpande, Sravanti Uppaluri, Markus Engstler, and Thomas Pfohl. Microfluidics-based single cell analysis reveals drug-dependent motility changes in trypanosomes. *Lab on a Chip*, 15(8):1961–1968, 2015. 28

[90] howpublished = "https://en.wikipedia.org/wiki/Optical_tweezers#/media/File:Optical_trap_principle.svg" year = 2013 note = "[Online; accessed 13-January-2016]" Locke83, title = Optical Tweezers. 18, 29

[91] Xiaolin Wang, Shuxun Chen, Marco Kong, Zuankai Wang, Kevin D Costa, Ronald a Li, and Dong Sun. Enhanced cell sorting and manipulation with combined optical tweezer and microfluidic chip technologies. *Lab on a chip*, 11(21):3656–62, November 2011. ISSN 1473-0189. doi: 10.1039/c1lc20653b. URL http://www.ncbi.nlm.nih.gov/pubmed/21918752. 28

[92] MP MacDonald, GC Spalding, and Kishan Dholakia. Microfluidic sorting in an optical lattice. *Nature*, 426(6965):421–424, 2003. 18, 29, 30

[93] L Paterson, E Papagiakoumou, G Milne, V Garcés-Chávez, SA Tatarkova, W Sibbett, FJ Gunn-Moore, PE Bryant, AC Riches, and K Dholakia. Light-induced cell separation in a tailored optical landscape. *Applied Physics Letters*, 87(12):123901, 2005. 29

[94] Christopher Rowland Hill, Jeff C Bamber, and Gail Haar. *Physical principles of medical ultrasonics*, volume 2. Wiley Online Library, 2004. 30

[95] James Friend and Leslie Y Yeo. Microscale acoustofluidics: Microfluidics driven via acoustics and ultrasonics. *Reviews of Modern Physics*, 83(2):647, 2011. 30

[96] J F Spengler and W T Coakley. Ultrasonic trap to monitor morphology and stability of developing microparticle aggregates. *Langmuir*, 19 (9):3635–3642, 2003. doi: 10.1021/la026798c. URL <GotoISI>://WOS:000182467100012. 18, 30, 31

[97] John William Strutt. On waves propagated along the plane surface of an elastic solid. *Proceedings of the London Mathematical Society*, 17(1):4–11, 1885. 31

[98] Keiiti Aki and Paul G Richards. *Quantitative seismology*, volume 1. 2002. 31

[99] David P Morgan. History of saw devices. In *Frequency Control Symposium, 1998. Proceedings of the 1998 IEEE International*, pages 439–460. IEEE, 1998. 31

[100] C D Wood, S D Evans, J E Cunningham, R O'Rorke, C Walti, and A G Davies. Alignment of particles in microfluidic systems using standing surface acoustic waves. *Applied Physics Letters*, 92(4), 2008. doi: 10.1063/1.2838748. URL <GotoISI>://WOS:000252860400126. 33, 161

[101] Jinjie Shi, Hua Huang, Zak Stratton, Yiping Huang, and Tony Jun Huang. Continuous particle separation in a microfluidic channel via standing surface acoustic waves (SSAW). *Lab on a Chip*, 9(23):3354–3359, 2009. doi: 10.1039/b915113c. URL <GotoISI>://WOS:000271647400005. 18, 33, 51, 161

[102] Ronald Pethig. Review articledielectrophoresis: status of the theory, technology, and applications. *Biomicrofluidics*, 4(2):022811, 2010. 19, 20, 21, 42, 37, 41, 43, 44, 45, 51, 54, 77, 246

[103] Saurin Patel, Daniel Showers, Pallavi Vedantam, Tzuen-Rong Tzeng, Shizhi Qian, and Xiangchun Xuan. Microfluidic separation of live and dead yeast cells using reservoir-based dielectrophoresis. *Biomicrofluidics*, 6(3):34102, 2012. doi: 10.1063/1.4732800. URL <GotoISI>://MEDLINE:23853679. 39, 94, 127, 129, 186, 187, 264

[104] JS Crane and AH Pohl. *Journal of the Electrochemical Society*, 115:584 – 586, 1968. 39

[105] ZR Gagnon. Cellular dielectrophoresis: applications to the characterisation, manipulation, separation and patterning of cells. *Electrophoresis*, 32:2466–2487, 2011. 39

[106] Hongjun Song, Jenna M Rosano, Yi Wang, Charles J Garson, Balabhaskar Prabhakarpandian, Kapil Pant, George J Klarmann, Alan Perantoni, Luis M Alvarez, and Eva Lai. Continuous-flow sorting of stem cells and differentiation products based on dielectrophoresis. *Lab on a Chip*, 15 (5):1320–1328, 2015. 39, 245, 246, 271

[107] M Alshareef, N Metrakos, EJ Perez, F Azer, F Yang, X Yang, and G Wang. Separation of tumor cells dielectrophoresis-based microfluidic chip. *Biomicrofluidics*, 7, 2013. 39, 201, 202

[108] F F Becker, X B Wang, Y Huang, R Pethig, J Vykoukal, and P R Gascoyne. Separation of human breast cancer cells from blood by differential dielectric affinity. *Proceedings of the National Academy of Sciences of the United States of America*, 92(3):860–4, January 1995. ISSN 0027-8424. URL http://www.pubmedcentral.nih.gov/articlerender.fcgi?artid=42720&tool=pmcentrez&rendertype=abstract. 27, 42, 39, 90, 91, 93, 245, 246, 247, 268, 271, 281

[109] Yi Lu, Tingting Liu, Ariana C Lamanda, Mandy LY Sin, Vincent Gau, Joseph C Liao, and Pak Kin Wong. Ac electrokinetics of physiological fluids for biomedical applications. *Journal of laboratory automation*, 20(6): 611–620, 2015. 39

[110] Srinivasu Valagerahally Puttaswamy, Shilpa Sivashankar, Rong-Jhe Chen, Chung-Kuang Chin, Hwan-You Chang, and Cheng Hsien Liu. Enhanced cell viability and cell adhesion using low conductivity medium for negative dielectrophoretic cell patterning. *Biotechnology journal*, 5(10):1005–1015, 2010. 39, 204, 205

[111] Hadi Shafiee, John L Caldwell, Michael B Sano, and Rafael V Davalos. Contactless dielectrophoresis: a new technique for cell manipulation. *Biomedical microdevices*, 11(5):997–1006, 2009. 22, 40, 39, 55, 56, 220, 221

[112] AH Pohl. The motion and precipitation of suspensoids in divergent electric fields. *Journal of Applied Physics*, 22, 1951. 41

[113] Herbert Ackland Pohl and HA Pohl. *Dielectrophoresis: the behavior of neutral matter in nonuniform electric fields*, volume 80. Cambridge university press Cambridge, 1978. 41

[114] Herbert A Pohl and Ira Hawk. Separation of living and dead cells by dielectrophoresis. *Science*, 152(3722):647–649, 1966. 19, 41, 186, 264

[115] H. Morgan and N.G. Green. Ac electrokinetics: colloids and nanoparticles, 2003. URL `http://eprints.gla.ac.uk/33024/`. 41, 42, 43, 44, 46, 47, 77, 85, 90, 170

[116] H Morgan, MP Hughes, and NG Green. Separation of submicron bioparticles by dielectrophoresis. *Biophysical Journal*, 77, 1999. 42

[117] HG Green and H Morgan. Dielectrophoresis of submicrometer latex spheres. 1. experimental results. *Journal of Physical Chemistry B*, 103:41–50, 1999. 42

[118] NG Green, H Morgan, and JJ Milner. Manipulation and trapping of sub-micron bioparticles using dielectrophoresis. *Journal of Biochemical and Biophysical Methods*, 35:89–102, 1997. 42

[119] NG Green and H Moran. Dielectrophoretic separation of nano-particles. *Journal of Physics D - Applied Physics*, 30:L41–L44, 1997. 42

[120] Xiao-Bo Wang, Jun Yang, Ying Huang, Jody Vykoukal, Frederick F Becker, and Peter RC Gascoyne. Cell separation by dielectrophoretic field-flow-fractionation. *Analytical Chemistry*, 72(4):832–839, 2000. 21, 42, 48, 49

[121] Jun Yang, Ying Huang, Xiao-Bo Wang, Frederick F Becker, and Peter RC Gascoyne. Enrichment of putative stem cells from adipose tissue using dielectrophoretic field-flow fractionation. *Analytical Chemistry*, 71(5):911–918, 1999. 42, 48

[122] Jody Vykoukal, Daynene M Vykoukal, Susanne Freyberg, Eckhard U Alt, and Peter RC Gascoyne. Enrichment of putative stem cells from adipose tissue using dielectrophoretic field-flow fractionation. *Lab on a Chip*, 8(8): 1386–1393, 2008. 40, 42, 48, 138, 216, 217, 220, 221

[123] Gerard H Markx, Ronald Pethig, and Juliette Rousselet. The dielectrophoretic levitation of latex beads, with reference to field-flow fractionation. *Journal of Physics D: Applied Physics*, 30(17):2470–2477, September 1997. ISSN 0022-3727. doi: 10.1088/0022-3727/30/17/013. URL http://stacks.iop.org/0022-3727/30/i=17/a=013?key=crossref.fe28e61c97b6ee73c6771075e856cbaa. 42

[124] Gerard H Markx, Mark S Talary, and Ronald Pethig. Separation of viable and non-viable yeast using dielectrophoresis. *Journal of Biotechnology*, 32 (1):29–37, 1994. 42, 186, 264

[125] Ronald Pethig, Ying Huang, Xiao-Bo Wang, and Julian PH Burt. Positive and negative dielectrophoretic collection of colloidal particles using interdigitated castellated microelectrodes. *Journal of Physics D: Applied Physics*, 25(5):881, 1992. 42, 43

[126] Gerard H Markx, Penelope A Dyda, and Ronald Pethig. Dielectrophoretic separation of bacteria using a conductivity gradient. *Journal of biotechnology*, 51(2):175–180, 1996. 42, 44

[127] Tomoyuki Yasukawa, Masato Suzuki, Hitoshi Shiku, and Tomokazu Matsue. Control of the microparticle position in the channel based on dielectrophoresis. *Sensors and Actuators B: Chemical*, 142(1):400–403, 2009. 20, 45, 46

[128] F Yang, H Yang, X amd Jiang, W.M Butler, and G Wang. 20, 47

[129] Rolf Hagedorn, Günter Fuhr, Torsten Müller, and Jan Gimsa. Traveling-wave dielectrophoresis of microparticles. *Electrophoresis*, 13(1):49–54, 1992. 46

[130] Hywel Morgan, Nicolas G Green, MP Hughes, W Monaghan, and TC Tan. Large-area travelling-wave dielectrophoresis particle separator. *Journal of micromechanics and Microengineering*, 7(2):65, 1997. 46

[131] L Cui and H Morgan. Design and fabrication of travelling wave dielectrophoresis structures. *Journal of Micromechanics and Microengineering*, 10(1):72, 2000. 20, 46, 47, 48

[132] Hywel Morgan, Alberto García Izquierdo, David Bakewell, Nicolas G Green, and Antonio Ramos. The dielectrophoretic and travelling wave forces generated by interdigitated electrode arrays: analytical solution using fourier series. *Journal of Physics D: Applied Physics*, 34(10):1553, 2001. 46, 170, 172

[133] Li Cui, David Holmes, and Hywel Morgan. The dielectrophoretic levitation and separation of latex beads in microchips. *Electrophoresis*, 22(18):3893–3901, 2001. 46

[134] Stefan Fiedler, Stephen G Shirley, Thomas Schnelle, and Günter Fuhr. Dielectrophoretic sorting of particles and cells in a microsystem. *Analytical chemistry*, 70(9):1909–1915, 1998. 49, 51

[135] David Holmes, Nicolas G Green, and Hywel Morgan. Microdevices for dielectrophoretic flow-through cell separation. *IEEE Engineering in Medicine and Biology Magazine*, 22(6):85–90, 2003. 21, 49, 50, 51

[136] Xiangchun Xuan, Junjie Zhu, and Christopher Church. Particle focusing in microfluidic devices. *Microfluidics and nanofluidics*, 9(1):1–16, 2010. 49

[137] Jason G Kralj, Michael TW Lis, Martin A Schmidt, and Klavs F Jensen. Continuous dielectrophoretic size-based particle sorting. *Analytical chemistry*, 78(14):5019–5025, 2006. 51

[138] Il Doh and Young-Ho Cho. A continuous cell separation chip using hydrodynamic dielectrophoresis (dep) process. *Sensors and Actuators A: Physical*, 121(1):59–65, 2005. 21, 52

[139] Youlan Li, Colin Dalton, H John Crabtree, Gregory Nilsson, and Karan VIS Kaler. Continuous dielectrophoretic cell separation microfluidic device. *Lab on a Chip*, 7(2):239–248, 2007. 21, 53, 54

[140] Youlan Li and Karan VIS Kaler. Dielectrophoretic fluidic cell fractionation system. *Analytica Chimica Acta*, 507(1):151–161, 2004. 53

[141] Chia-Fu Chou, Jonas O Tegenfeldt, Olgica Bakajin, Shirley S Chan, Edward C Cox, Nicholas Darnton, Thomas Duke, and Robert H Austin. Electrodeless dielectrophoresis of single-and double-stranded dna. *Biophysical Journal*, 83(4):2170–2179, 2002. 22, 54, 55

[142] Chia-Fu Chou and Frederic Zenhausern. Electrodeless dielectrophoresis for micro total analysis systems. *Engineering in Medicine and Biology Magazine, IEEE*, 22(6):62–67, 2003. 54

[143] Hadi Shafiee, Michael B Sano, Erin a Henslee, John L Caldwell, and Rafael V Davalos. Selective isolation of live/dead cells using contactless dielectrophoresis (cDEP). *Lab on a chip*, 10(4):438–45, February 2010. ISSN 1473-0197. doi: 10.1039/b920590j. URL http://www.ncbi.nlm.nih.gov/pubmed/20126683. 56, 138, 149, 201, 202, 216

[144] Chia-Chern Chen, Po-Hsiu Lin, and Chen-Kuei Chung. Microfluidic chip for plasma separation from undiluted human whole blood samples using low voltage contactless dielectrophoresis and capillary force. *Lab on a Chip*, 14 (12):1996–2001, 2014. 56

[145] Yuchao Chen, Xiaoyun Ding, Sz-Chin Steven Lin, Shikuan Yang, Po-Hsun Huang, Nitesh Nama, Yanhui Zhao, Ahmad Ahsan Nawaz, Feng Guo, Wei Wang, et al. Tunable nanowire patterning using standing surface acoustic waves. *ACS nano*, 7(4):3306–3314, 2013. 22, 58, 59, 60, 161

[146] Leslie Y Yeo and James R Friend. Surface acoustic wave microfluidics. *Annual Review of Fluid Mechanics*, 46:379–406, 2014. 58

[147] XH Kong, Ch Deneke, H Schmidt, DJ Thurmer, HX Ji, M Bauer, and OG Schmidt. Surface acoustic wave mediated dielectrophoretic alignment of rolled-up microtubes in microfluidic systems. *Applied Physics Letters*, 96 (13):134105, 2010. 22, 59

[148] Kerstin Länge, Bastian E Rapp, and Michael Rapp. Surface acoustic wave biosensors: a review. *Analytical and bioanalytical chemistry*, 391(5):1509–1519, 2008. 60

[149] Alban J Smith, Richard D ORorke, Akshay Kale, Roberts Rimsa, Matthew J Tomlinson, Jennifer Kirkham, A Giles Davies, Christoph Wälti, and Christopher D Wood. Rapid cell separation with minimal manipulation for autologous cell therapies. *Scientific Reports*, 7, 2017. 23, 62, 239, 276

[150] No Jimnez. Wave simulations. http://www.nojigon.webs.upv.es/simulations_waves.php, 2017. [Online; accessed 21-June-2017]. 23, 64

[151] Richard O'Rorke. The spatial control of particles in microfluidic systems using surface acoustic waves, 2010. URL www.summon.com. 23, 66

[152] James Friend and Leslie Y. Yeo. Microscale acoustofluidics: Microfluidics driven via acoustics and ultrasonics. *Reviews of Modern Physics*, 83(2): 647–704, June 2011. ISSN 0034-6861. doi: 10.1103/RevModPhys.83.647. URL http://link.aps.org/doi/10.1103/RevModPhys.83.647. 68

[153] Thirumalai Kannan. Finite element analysis of surface acoustic wave resonators, 2006. URL http://www.collectionscanada.gc.ca/obj/s4/f2/dsk3/SSU/TC-SSU-07022006160413.pdf. 68, 76

[154] B.A. Auld and B.A. Auld. *Acoustic fields and waves in solids*. Number v. 1 in Acoustic Fields and Waves in Solids. Wiley, 1973. ISBN 9780471037026. URL http://books.google.co.uk/books?id=9_wzAQAAIAAJ. 68

[155] David Morgan. Surface acoustic wave filters. *Amsterdam: Elsevier*, 2007. 68

[156] David Holmes. *Advanced dielectrophoretic cell separation systems*. PhD thesis, University of Glascow, 2003. 77

[157] Mp Hughes, H Morgan, and Mf Flynn. The Dielectrophoretic Behavior of Submicron Latex Spheres: Influence of Surface Conductance. *Journal of colloid and interface science*, 220(2):454–457, December 1999. ISSN 1095-7103. doi: 10.1006/jcis.1999.6542. URL http://www.ncbi.nlm.nih.gov/pubmed/10607465. 88, 124, 276

[158] Chun-Ping Jen and Wei-Fu Chen. An insulator-based dielectrophoretic microdevice for the simultaneous filtration and focusing of biological cells. *Biomicrofluidics*, 5(4):44105–4410511, December 2011. ISSN 1932-1058. doi: 10.1063/1.3658644. URL http://www.pubmedcentral.nih.gov/articlerender.fcgi?artid=3364804&tool=pmcentrez&rendertype=abstract. 91

[159] Michael D Vahey and Joel Voldman. High-throughput cell and particle characterization using isodielectric separation. *Analytical chemistry*, 81(7): 2446–2455, 2009. 27, 93, 249

[160] Helen M Coley, Fatima H Labeed, Hilary Thomas, and Michael P Hughes. Biophysical characterization of mdr breast cancer cell lines reveals the cytoplasm is critical in determining drug sensitivity. *Biochimica et Biophysica Acta (BBA)-General Subjects*, 1770(4):601–608, 2007. 27, 93, 249

[161] David Holmes. *Advanced dielectrophoretic cell separation systems*. PhD thesis, University of Glascow, 2003. 92

[162] S Patel, D Showers, P Vedantam, TR Tzeng, S Qian, and X Xuan. Microfluidic separation of live and dead yeast cells using reservoid-based dielectrophoresis. *Biomicrofluidics*, 6, 2012. 96, 278

[163] Clean Air Technology Inc. What is a cleanroom? http://www.cleanairtechnology.com/cleanroom-classifications-class.php, 2018. [Online; accessed 12-March-2018]. 98

[164] Germán Comina, Anke Suska, and Daniel Filippini. Pdms lab-on-a-chip fabrication using 3d printed templates. *Lab on a Chip*, 14(2):424–430, 2014. 118

[165] Jean-Yves Tinevez, Nick Perry, Johannes Schindelin, Genevieve M Hoopes, Gregory D Reynolds, Emmanuel Laplantine, Sebastian Y Bednarek, Spencer L Shorte, and Kevin W Eliceiri. Trackmate: An open and extensible platform for single-particle tracking. *Methods*, 2016. 30, 36, 127, 128, 170, 178, 285

[166] Jean-Yves Tinevez. Getting started with TrackMate. http://imagej.net/Getting_started_with_TrackMate, 2013. [Online; accessed 23-Februrary-2017]. 127

[167] S a Altman, L Randers, and G Rao. Comparison of trypan blue dye exclusion and fluorometric assays for mammalian cell viability determinations. *Biotechnology progress*, 9(6):671–4, 1999. ISSN 8756-7938. doi: 10.1021/bp00024a017. URL http://www.ncbi.nlm.nih.gov/pubmed/7764357. 131

[168] John R Masters and Glyn N Stacey. Changing medium and passaging cell lines. *Nature protocols*, 2(9):2276–2284, 2007. 134

[169] S Gronthos, M Mankani, J Brahim, P G Robey, and S Shi. Postnatal human dental pulp stem cells (DPSCs) in vitro and in vivo. *Proceedings of the National Academy of Sciences of the United States of America*, 97(25):13625–30, December 2000. ISSN 0027-8424. doi: 10.1073/pnas.240309797. URL http://www.pubmedcentral.nih.gov/articlerender.fcgi?artid=17626&tool=pmcentrez&rendertype=abstract. 135

[170] Sigma-Aldrich. Product Information: Mimumum Essential Medium Eagle (MEM). http://www.sigmaaldrich.com/content/dam/sigma-aldrich/docs/Sigma/Formulation/m4655for.pdf, 2016. [Online; accessed 24-Februrary-2017]. 138, 216

[171] AP Mazzoleni, BF Sisken, and RL Kahler. Conductivity values of tissue culture medium from 20 c to 40 c. *Bioelectromagnetics*, 7(1):95–99, 1986. 138, 216

[172] Sigma-Aldrich. Product Information: Dulbeccos Phosphate Buffered Saline. http://www.sigmaaldrich.com/content/dam/sigma-aldrich/docs/Sigma/Formulation/d8537for.pdf, 2014. [Online; accessed 24-Februrary-2017]. 138, 216

[173] ZMF. LSR II. http://www.medunigraz.at/zmf/1243, 2015. [Online; accessed 11-Februrary-2016]. 31, 38, 140, 208

[174] Andor. Spectral Flow Cytometry. http://www.andor.com/learning-academy/spectral-flow-cytometry-an-introduction-to-spectral-flow-c 2017. [Online; accessed 24-Februrary-2017]. 31, 140

[175] PD Cook. Plate Reader. https://en.wikipedia.org/wiki/Plate_reader, 2012. [Online; accessed 24-Februrary-2017]. 32, 145

[176] Klaus Hoffmeier. Chemical Structure of Propidium Iodide. https://commons.wikimedia.org/wiki/File:Propidium_iodide.png, 2007. [Online; accessed 25-Februrary-2017]. 32, 148

[177] NEUROtiker. Structure of Calcein (Fluorexon). https://commons.wikimedia.org/wiki/File:Calcein.svg, 2008. [Online; accessed 25-Februrary-2017]. 32, 148

[178] Soul Guidance. Resonance by Standing Waves. http://www.soul-guidance.com/lft/resonance.htm, 2017. [Online; accessed 25-August-2017]. 34, 162

[179] Samuel K Sia and George M Whitesides. Microfluidic devices fabricated in poly(dimethylsiloxane) for biological studies. *Electrophoresis*, 24(21):3563–76, November 2003. ISSN 0173-0835. doi: 10.1002/elps.200305584. URL http://www.ncbi.nlm.nih.gov/pubmed/14613181. 164, 196

[180] Jeremy J Hawkes and W Terence Coakley. Force field particle filter, combining ultrasound standing waves and laminar flow. *Sensors and Actuators B: Chemical*, 75(3):213–222, 2001. 169

[181] Joel Voldman, Rebecca A Braff, Mehmet Toner, Martha L Gray, and Martin A Schmidt. Holding forces of single-particle dielectrophoretic traps. *Biophysical Journal*, 80(1):531–542, 2001. 169

[182] Joel Voldman. Electrical forces for microscale cell manipulation. *Annu. Rev. Biomed. Eng.*, 8:425–454, 2006. 169

[183] Johan Nilsson, Mikael Evander, Björn Hammarström, and Thomas Laurell. Review of cell and particle trapping in microfluidic systems. *Analytica chimica acta*, 649(2):141–157, 2009. 169

[184] Jin-Yu Shao. Measuring piconewton forces and its application in cellular and molecular biomechanics. *Advances in Biomechanics*, pages 47–51, 2001. 169

[185] Ying Huang, Ralph Holzel, Ronald Pethig, and Xiao-B Wang. Differences in the ac electrodynamics of viable and non-viable yeast cells determined through combined dielectrophoresis and electrorotation studies. *Physics in medicine and biology*, 37(7):1499, 1992. 170, 186, 264

[186] Nicolas G Green, Antonio Ramos, and Hywel Morgan. Numerical solution of the dielectrophoretic and travelling wave forces for interdigitated electrode arrays using the finite element method. *Journal of Electrostatics*, 56(2): 235–254, 2002. 170

[187] Zachary Gagnon, Jill Mazur, and Hsueh-Chia Chang. Glutaraldehyde enhanced dielectrophoretic yeast cell separation. *Biomicrofluidics*, 3(4):44108, January 2009. ISSN 1932-1058. doi: 10.1063/1.3257857. URL http://www.pubmedcentral.nih.gov/articlerender.fcgi?artid=2835288&tool=pmcentrez&rendertype=abstract. 186, 264

[188] Zachary Gagnon, Jill Mazur, and Hsueh-Chia Chang. Integrated ac electrokinetic cell separation in a closed-loop device. *Lab on a Chip*, 10(6): 718–726, 2010. 36, 187

[189] a Docoslis, N Kalogerakis, and L a Behie. Dielectrophoretic forces can be safely used to retain viable cells in perfusion cultures of animal cells. *Cytotechnology*, 30(1-3):133–42, July 1999. ISSN 0920-9069. doi: 10.1023/A:1008050809217. URL http://www.pubmedcentral.nih.gov/articlerender.fcgi?artid=3449951&tool=pmcentrez&rendertype=abstract. 201, 202

[190] Steffen Archer, Tong-Tong Li, A Tudor Evans, Stephen T Britland, and Hywel Morgan. Cell reactions to dielectrophoretic manipulation. *Biochemical and biophysical research communications*, 257(3):687–698, 1999. 204

[191] DA Mower, David W Peckham, Vivian A Illera, Justin K Fishbaugh, Laura L Stunz, and Robert F Ashman. Decreased membrane phospholipid packing and decreased cell size precede dna cleavage in mature mouse b cell apoptosis. *The Journal of Immunology*, 152(10):4832–4842, 1994. 210

[192] Merck Sigma-Aldrich. RPMI-1640 Medium. http://www.sigmaaldrich.com/catalog/product/sigma/r0883?lang=en&region=GB, 2017. [Online; accessed 07-August-2017]. 216

[193] Thermofisher Scientific. HEPES Use in Cell Culture. https://www.thermofisher.com/uk/en/home/life-science/cell-culture/mammalian-cell-culture/reagents/hepes.html#, 2017. [Online; accessed 17-May-2017]. 218

[194] Geoffrey L Francis. Albumin and mammalian cell culture: implications for biotechnology applications. *Cytotechnology*, 62(1):1–16, 2010. 219, 220

[195] Expressions (RMBIO). Comparison of FBS and Other Bovine Serums. https://www.rmbio.com/comparison-of-fbs-and-other-bovine-serums, 2017. [Online; accessed 17-May-2017]. 220

[196] Sciencell. Human Bone Marrow-derived Mesenchymal Stem Cells. http://www.sciencellonline.com/human-bone-marrow-derived-mesenchymal-stem-cells.html, 2017. [Online; accessed 18-May-2017]. 40, 224

[197] Sciencell. Human Osteoblasts-femoral. https://www.sciencellonline.com/products-services/primary-cells/human-osteoblasts-femoral.html, 2017. [Online; accessed 18-May-2017]. 40, 224

[198] Sciencell. Rat Schwann Cells. http://www.sciencellonline.com/products-services/primary-cells/animal/rat/rat-schwann-cells.html, 2017. [Online; accessed 18-May-2017]. 40, 224

[199] Anand Mohan Prasad and Giuseppe Inesi. Effects of thapsigargin and phenylephrine on calcineurin and protein kinase c signaling functions in cardiac myocytes. *American Journal of Physiology-Cell Physiology*, 296(5): C992–C1002, 2009. 40, 224

[200] Sciencell. Human Hepatic Stellate Cells. https://www.sciencellonline.com/human-hepatic-stellate-cells.html, 2017. [Online; accessed 18-May-2017]. 40, 224

[201] Interactive Biology. Bones: A Brief Review on its Functions, Types, Structure and Development. http://www.interactive-biology.com/3810/bones-a-brief-review-on-its-functions-types-structure-and-development/, 2017. [Online; accessed 18-May-2017]. 40, 224

[202] Tanya Lewis. Human Brain: Facts, Functions & Anatomy. http://www.livescience.com/29365-human-brain.html, 2017. [Online; accessed 18-May-2017]. 40, 224

[203] Patrick Lynch. Heart. https://en.wikipedia.org/wiki/Heart, 2017. [Online; accessed 18-May-2017]. 40, 224

[204] MedlinePlus. Liver Diseases. https://medlineplus.gov/liverdiseases.html, 2017. [Online; accessed 18-May-2017]. 40, 224

[205] Matthew J Tomlinson, Caitriona Dennis, Xuebin B Yang, and Jennifer Kirkham. Tissue non-specific alkaline phosphatase production by human dental pulp stromal cells is enhanced by high density cell culture. *Cell and tissue research*, 361(2):529–540, 2015. 40, 223, 225, 226

[206] ThermoFisher Scientific. StemPro Osteogenesis Differentiation Kit. https://www.thermofisher.com/order/catalog/product/A1007201, 2017. [Online; accessed 18-May-2017]. 226

[207] Ellis E Golub and Kathleen Boesze-Battaglia. The role of alkaline phosphatase in mineralization. *Current Opinion in Orthopaedics*, 18(5):444–448, 2007. 226

[208] Sigma Aldrich. Alkaline Phosphatase kit procedure. https://www.sigmaaldrich.com/content/dam/sigma-aldrich/docs/Sigma/General_Information/1/85.pdf, 2014. [Online; accessed 29-Februrary-2016]. 227

[209] Mi-Hye Choi, Woo-Chang Noh, Jin-Woo Park, Jae-Mok Lee, and Jo-Young Suh. Gene expression pattern during osteogenic differentiation of human periodontal ligament cells in vitro. *Journal of periodontal & implant science*, 41(4):167–175, 2011. 228

[210] Bettina Lindroos, Shayne Boucher, Lucas Chase, Hannu Kuokkanen, Heini Huhtala, Riina Haataja, Mohan Vemuri, Riitta Suuronen, and Susanna Miettinen. Serum-free, xeno-free culture media maintain the proliferation rate and multipotentiality of adipose stem cells in vitro. *Cytotherapy*, 11 (7):958–972, 2009. 230

[211] A Brauer, T Pohlemann, and W Metzger. Osteogenic differentiation of immature osteoblasts: interplay of cell culture media and supplements. *Biotechnic & Histochemistry*, 91(3):161–169, 2016. 231

[212] Ronald Pethig. Reviewwhere is dielectrophoresis (dep) going? *Journal of The Electrochemical Society*, 164(5):B3049–B3055, 2017. 245, 271

[213] Gerard H Markx and Christopher L Davey. The dielectric properties of biological cells at radiofrequencies: applications in biotechnology. *Enzyme and Microbial Technology*, 25(3):161–171, 1999. 245

[214] Ronald R Pethig. *Dielectrophoresis: Theory, Methodology and Biological Applications*. John Wiley & Sons, 2017. 246, 249, 268

[215] Aristides Docoslis, Nicolas Kalogerakis, Leo A Behie, and Karan VIS Kaler. A novel dielectrophoresis-based device for the selective retention of viable cells in cell culture media. *Biotechnology and bioengineering*, 54(3):239–250, 1997. 246

[216] Unyoung Kim, Chih-Wen Shu, Karen Y Dane, Patrick S Daugherty, Jean YJ Wang, and HT Soh. Selection of mammalian cells based on their cell-cycle phase using dielectrophoresis. *Proceedings of the National Academy of Sciences*, 104(52):20708–20712, 2007. 246

[217] Waqas Nawaz. Epithelium, cells,tissues & histology . https://www.slideshare.net/vicky14381/epithelium-cellstissues-histology, 2017. [Online; accessed 29-May-2017]. 43, 251

[218] Linda W Engel and Nathaniel A Young. Human breast carcinoma cells in continuous culture: a review. *Cancer research*, 38(11 Part 2):4327–4339, 1978. 249

[219] Ying Qu, Bingchen Han, Bowen Gao, Shikha Bose, Yiping Gong, Kolja Wawrowsky, Armando E Giuliano, Dhruv Sareen, and Xiaojiang Cui. Differentiation of human induced pluripotent stem cells to mammary-like organoids. *Stem cell reports*, 8(2):205–215, 2017. 249

[220] Ronald Pethig, Anoop Menachery, Steve Pells, and Paul De Sousa. Dielectrophoresis: a review of applications for stem cell research. *BioMed Research International*, 2010, 2010. 44, 258, 259

[221] John J Correia and H William Detrich III. *Biophysical Tools for Biologists: In Vivo Techniques*, volume 89. Academic Press, 2009. 258

[222] Yan Gao, Wenjie Li, and Dimitri Pappas. Recent advances in microfluidic cell separations. *Analyst*, 138(17):4714–4721, 2013. 260, 261

[223] Michael P Hughes. Fifty years of dielectrophoretic cell separation technology. *Biomicrofluidics*, 10(3):032801, 2016. 267, 269

[224] C. Van Blitterswijk and J. De Boer. *Tissue Engineering*. Academic Press Series in Biomedical Engineering. Elsevier Science, 2014. ISBN 9780124202108. URL https://books.google.co.uk/books?id=Dsw6BAAAQBAJ. 269

[225] Africa Smith de Diego. Rapid label-free separation of stromal cell populations for autologous cell therapy in musculoskeletal disease. Master's thesis, University of Leeds, UK, 2017. 271